Experimental and Analytical Study on Reduction of Residual Stresses and Distortion During Welding in High Strength Steel

By

CHIRDPUN VITOORAPORN

B.Eng. (Mech.), Chulalongkorn University, 1983

M.S. Naval Architecture and Marine Engineering, M.I.T., 1986

Submitted to the Department of Ocean Engineering in Partial Fulfillment of the Requirements for the Degree of

Doctor of Philosophy

in

Naval Architecture and Marine Engineering

at the

Massachusetts Institute of Technology

January 1990

Copyright © Massachusetts Institute of Technology, 1990. All rights reserved.

Signature of Author _____
Department of Ocean Engineering
January 9, 1990

Certified by _____
Professor Koichi Masubuchi
Thesis Supervisor

Accepted by _____
Professor A. Douglas Carmichael
Chairman, Graduate Thesis Committee

MAR 22 1990

Experimental and Analytical Study on Reduction of Residual Stresses and Distortion During Welding in High Strength Steel

By

CHIRDPUN VITOORAPORN

Submitted to the Department of Ocean Engineering on January 9, 1990
in partial fulfillment of the requirements for the degree of

Doctor of Philosophy in Naval Architecture and Marine Engineering

Abstract

Residual stresses developed during the fabrication of welded structures are the main factor that causes detrimental effects on the quality of the service behavior of a welded structure. They create cracks, porosity and other types of defects. Distortion which occurs as well during welding creates the mismatch problem especially on the parts that need to be joined. Many attempts have been made so far to reduce these residual stresses and distortion. Most of them, however, are done before or after welding is completed. Since these residual stresses and distortion are developed during welding, it is effective to control and reduce them during the welding process.

In this thesis, a side heating technique, which was used successfully in controlling metal movement during butt welding in low carbon steel, was used to reduce residual stresses and distortion during bead-on-edge welding in high strength steel, i.e., HY-100 and HY-130. The objective was to investigate the general usefulness of such a technique to other types of material as well as other types of applications. A series of experiments was performed during the course of this investigation. It was found from experiments that by placing the side heating torch along with the welding arc and heating the specimen in the wide region away from the weld line to a moderate temperature (200°F) the residual stresses and distortion could be effectively reduced. The reduction of distortion achieved for HY-130 and HY-100 ranged from 44% to 48%. Longitudinal residual stresses could be reduced 23%-34% for HY-130 and HY-100. Transverse residual stresses were reduced 23%-29% for HY-130 and HY-100. It was found that with side heating, the cooling rate and the strain rate decreased in the weldment after the welding was completed. Uniform temperature distribution throughout the specimen was reached in a shorter time when side heating was performed. Results from the experiments also indicated the possibility for using of such a technique to control and reduce residual stresses and distortion during welding in in-process control.

Both analytical and numerical approaches were used to analyze physical

quantities involved in the welding phenomena. A three dimensional finite heat source model with the modification to include the side heating effect was developed to determine the temperature distribution. A finite element model for the welding process was developed and run on ADINA to analyze the transient strains, distortion, and residual stresses. The results showed good agreement with the experimental results. The plastic zone was found to be narrower when side heating was provided. Even though the numerical approach provides a good accuracy in determining physical quantities, it consumes a great deal of time for determining solutions. Therefore, it is difficult to implement such an approach in the in-process control of welding. An approach which can provide a solution time that is fast enough to be employed in the in-process control of welding is desired.

By applying the low temperature localized stress relief to the weldment when it cools down, residual stresses and distortion can be further reduced. The analysis revealed also that the low temperature localized stress relief can be effective when it is performed near or on the weld line.

Thesis Supervisor: Professor Koichi Masubuchi
Title: Kawasaki Professor of Engineering

Acknowledgments

I would like to express my sincere appreciation to Prof. Masubuchi for his supervision and support during the course of this project. His help during my most difficult time is something that cannot be expressed in words. I would also like to thank the members of my thesis committee who patiently advised and kindly supported me throughout this thesis; to Prof. Wierzbicki, for his enthusiasm and suggestions which helped me to deeply understand the problem, to Prof. Pian, for his generosity and comments on the thesis.

Special thanks and appreciation go to my colleague, Lt. Commander Richard Allen Bass of the U.S. Navy, who worked alongside me during the experimental part of this study; to Mr. Anthony Zona, lab technician, for his helpful advice and quick response for any equipment needed in performing the experiments; to Mike Aliosi, Remo, and the rest of the staff at the Laboratory For Nuclear Science in Building 20 for cutting our test pieces, teaching us about milling and fabricating the adjustable torch holder used in the experiments.

My most special thanks go to my Mom and Dad who have been patiently waiting and supporting me during my study, to my beloved Nuj for making time here the most memorable one for me.

Table of Contents

Abstract 2
Acknowledgments 4
Table of Contents 5
List of Figures 7
List of Tables 13

1. Introduction 14
1.1 General Discussion of Residual Stresses and Distortion in Welded Structures 15
1.2 Control and Reduction of Residual Stresses and Distortion 20
1.3 Research Objective 22

2. Experimental Synopsis 24
2.1 Experimental Description 24
2.2 Material Characteristics of Low Carbon Steel 25
2.2.1 General Characteristics 25
2.2.2 Low Carbon Steel Description 25
2.3 Material Characteristics of HY-100 and HY-130 29
2.3.1 General Characteristics 29
2.3.2 HY-100 Description 29
2.3.3 HY-130 Description 33
2.4 Heat Source for Side Heating 38
2.5 Experiment Set-Up 41
2.5.1 Specimen 41
2.5.2 Welding and Side Heating Devices 42
2.5.3 Thermocouple and Strain Gage 48
2.5.4 Data Acquisition System 49
2.5.5 Experimental Results 54
2.5.5.1 Bead-on-Edge Welding Without Side Heating 54
2.5.5.2 Bead-on-Edge Welding With Side Heating 73
2.6 Summary 103

3. Analytical and Numerical Treatment of Heat Flow 104
3.1 Introduction 104
3.2 Analytical Treatment on Heat Flow Analysis 106
3.2.1 Literature Review 106
3.3 Heat Input 113
3.4 Side Heating Heat Input 118
3.5 Three-Dimensional Finite Heat Source Model 122
3.5.1 Governing Equation 122
3.5.2 Heat Input Model for the Welding Torch and Side Heating Torch 125
3.5.3 Boundary Conditions 128
3.5.3.1 Case Without Side Heating 128
3.5.3.2 Case With Side Heating 129

3.5.4 Linearization on Boundary Conditions 130
3.5.5 Solution Procedure 132
3.5.5.1 Case Without Side Heating 132
3.5.5.2 Case With Side Heating 133
3.6 Numerical Treatment on Heat Flow Analysis 146
3.6.1 Literature Review 146
3.6.2 Finite Element Procedure 148
3.6.2.1 Boundary Conditions 148
3.6.2.2 Step-By-Step Time Integration 149
3.6.3 Weld Model 149
3.6.3.1 Boundary Conditions 150
3.6.3.2 Material Properties 151
3.6.3.3 Heat Input 151
3.7 Comparison of Results 155
3.8 Summary 163

4. Analytical and Numerical Treatment of Stress-Strain-Distortion 164

4.1 Introduction 164
4.2 Literature Review 165
4.3 One-Dimensional Analysis 166
4.4 Finite Element Formulation 175
4.4.1 Governing Equation 175
4.4.2 Thermo-Elastic-Plastic and Creep Model 176
4.5 Weld Model Using the FEM 180
4.5.1 Boundary Condition 180
4.5.2 Material Properties 181
4.5.3 Solution Procedure 182
4.6 Comparison of the Results 183
4.7 Summary 209

5. Concept on Reduction of Residual Stress and Distortion 210

5.1 Introduction 210
5.2 Distortion in Weldment in Various Materials 210
5.3 Maximum Longitudinal Strain in Weldments of Various Materials 213
5.4 Size of Plastic Zone 214
5.5 Low Temperature Localized Stress Relief 219
5.6 Summary 230

6. Conclusion and Future Study 231

Appendix A. Data Acquisition Program 234

List of Figures

Figure 1-1:	Weldment Configuretion for Butt Welding	1.1
Figure 1-2:	Four Parts of Weld Subjected to Different Thermal Histories	1.1
Figure 1-3:	Typical Distribution of Residual Stresses in Butt Weld	1.1
Figure 1-4:	Various Types of Weld Distortion	1.1
Figure 2-1:	Types of Side Heating Source	2.4
Figure 2-2:	Calculated Distribution of Residual Stress	2.4
Figure 2-3:	Size of Specimen	2.5.1
Figure 2-4:	Arrangement of GMA Welding and Side Heating Devices	2.5.2
Figure 2-5:	Configuration of Welding Torch and Side Heating Torch	2.5.2
Figure 2-6:	Side View of Weld Arrangement	2.5.2
Figure 2-7:	Strain Gage and Temperature Characteristic	2.5.3
Figure 2-8:	HP 3852A Mainframe Front Panel	2.5.4
Figure 2-9:	HP 3852A Mainframe Rear Panel	2.5.4
Figure 2-10:	Schematic Diagram for Data Acquisition System	2.5.4
Figure 2-11:	Thermocouple and Strain Gage Arrangement	2.5.5.1
Figure 2-12:	Temperature Profile for Low Carbon Steel	2.5.5.1
Figure 2-13:	Temperature Profile for HY-100	2.5.5.1
Figure 2-14:	Temperature Profile for HY-130	2.5.5.1
Figure 2-15:	Transient Longitudinal Strain Profile for Low Carbon Steel	2.5.5.1
Figure 2-16:	Transient Longitudinal Strain Profile for HY-100	2.5.5.1
Figure 2-17:	Transient Longitudinal Strain Profile for HY-130	2.5.5.1
Figure 2-18:	Transient Transverse Strain Profile for Low Carbon Steel	2.5.5.1
Figure 2-19:	Transient Transverse Strain Profile for HY-100	2.5.5.1
Figure 2-20:	Transient Transverse Strain Profile for HY-130	2.5.5.1
Figure 2-21:	Transient Longitudinal Strain Profile for Low Carbon Steel	2.5.5.1
Figure 2-22:	Transient Longitudinal Strain Profile for HY-100	2.5.5.1
Figure 2-23:	Transient Longitudinal Strain Profile for HY-130	2.5.5.1
Figure 2-24:	Transient Transverse Strain Profile for Low Carbon Steel	2.5.5.1
Figure 2-25:	Transient Transverse Strain Profile for HY-100	2.5.5.1
Figure 2-26:	Transient Transverse Strain Profile for HY-130	2.5.5.1
Figure 2-27:	Distortion Profile of Low Carbon Steel	2.5.5.1
Figure 2-28:	Distortion Profile of HY-100	2.5.5.1
Figure 2-29:	Distortion Profile of HY-130	2.5.5.1
Figure 2-30:	Longitudinal Residual Stress Distribution for Low Carbon Steel	2.5.5.1
Figure 2-31:	Longitudinal Residual Stress Distribution for HY-100	2.5.5.1
Figure 2-32:	Longitudinal Residual Stress Distribution for HY-130	2.5.5.1
Figure 2-33:	Transverse Residual Stress Distribution for Low Carbon Steel	2.5.5.1
Figure 2-34:	Transverse Residual Stress Distribution for HY-100	2.5.5.1
Figure 2-35:	Transverse Residual Stress Distribution for HY-130	2.5.5.1

Figure 2-36:	Side Heating Flame Configuration	2.5.5.2
Figure 2-37:	Distortion Profile due to Side Heating Source for Low Carbon Steel	2.5.5.2
Figure 2-38:	Distortion Profile due to Side Heating Source for HY-100	2.5.5.2
Figure 2-39:	Distortion Profile due to Side Heating Source for HY-130	2.5.5.2
Figure 2-40:	Distortion Profile for Low Carbon Steel	2.5.5.2
Figure 2-41:	Distortion Profile for HY-100	2.5.5.2
Figure 2-42:	Distortion Profile for HY-130	2.5.5.2
Figure 2-43:	Distortion Profile for Low Carbon Steel	2.5.5.2
Figure 2-44:	Distortion Profile for HY-100	2.5.5.2
Figure 2-45:	Distortion Profile for HY-130	2.5.5.2
Figure 2-46:	Distortion Profile for Low Carbon Steel	2.5.5.2
Figure 2-47:	Distortion Profile for HY-100	2.5.5.2
Figure 2-48:	Distortion Profile for HY-130	2.5.5.2
Figure 2-49:	Comparison of Distortion for Low Carbon Steel	2.5.5.2
Figure 2-50:	Comparison of Distortion for HY-100	2.5.5.2
Figure 2-51:	Comparison of Distortion for HY-130	2.5.5.2
Figure 2-52:	Comparison of Distortion for Low Carbon Steel	2.5.5.2
Figure 2-53:	Comparison of Distortion for HY-100	2.5.5.2
Figure 2-54:	Comparison of Distortion for HY-130	2.5.5.2
Figure 2-55:	Comparison of Distortion for Low Carbon Steel	2.5.5.2
Figure 2-56:	Comparison of Distortion for HY-100	2.5.5.2
Figure 2-57:	Comparison of Distortion for HY-130	2.5.5.2
Figure 2-58:	Temperature Profile for Low Carbon Steel	2.5.5.2
Figure 2-59:	Temperature Profile for HY-100	2.5.5.2
Figure 2-60:	Temperature Profile for HY-130	2.5.5.2
Figure 2-61:	Transient Longitudinal Strain Profile for Low Carbon Steel	2.5.5.2
Figure 2-62:	Transient Longitudinal Strain Profile for HY-100	2.5.5.2
Figure 2-63:	Transient Longitudinal Strain Profile for HY-130	2.5.5.2
Figure 2-64:	Transient Transverse Strain Profile for Low Carbon Steel	2.5.5.2
Figure 2-65:	Transient Transverse Strain Profile for HY-100	2.5.5.2
Figure 2-66:	Transient Transverse Strain Profile for HY-130	2.5.5.2
Figure 2-67:	Transient Longitudinal Strain Profile for Low Carbon Steel	2.5.5.2
Figure 2-68:	Transient Longitudinal Strain Profile for HY-100	2.5.5.2
Figure 2-69:	Transient Longitudinal Strain Profile for HY-130	2.5.5.2
Figure 2-70:	Transient Transverse Strain Profile for Low Carbon Steel	2.5.5.2
Figure 2-71:	Transient Transverse Strain Profile for HY-100	2.5.5.2
Figure 2-72:	Transient Transverse Strain Profile for HY-130	2.5.5.2
Figure 2-73:	Longitudinal Residual Stress Distribution for Low Carbon Steel	2.5.5.2
Figure 2-74:	Longitudinal Residual Stress Distribution for HY-100	2.5.5.2
Figure 2-75:	Longitudinal Residual Stress Distribution for HY-130	2.5.5.2
Figure 2-76:	Transverse Residual Stress Distribution for Low Carbon Steel	2.5.5.2
Figure 2-77:	Transverse Residual Stress Distribution for HY-100	2.5.5.2

Figure 2-78:	Transverse Residual Stress Distribution for HY-130	2.5.5.2
Figure 3-1:	Two-Dimensional Heat Flow : Thin Plate	3.2.1
Figure 3-2:	Three-Dimensional Heat Flow : Semi-infinite Plate	3.2.1
Figure 3-3:	Superposition of Heat Sources	3.2.1
Figure 3-4:	Gaussian Radial Heat Flux Distribution	3.3
Figure 3-5:	Effective Power and Efficiency of the Oxyacetylene Flame versus Acetylene Consumption	3.4
Figure 3-6:	Schematic Representation for Welding with Side Heating	3.5.2
Figure 3-7:	Schematic Representation of Geometry for Boundary Condition	3.5.2
Figure 3-8:	Superposition Used for Inner Solution	3.5.5.2
Figure 3-9:	Boundary Conditions for ϕ_I^i	3.5.5.2
Figure 3-10:	Boundary Conditions for ϕ_{II}^i	3.5.5.2
Figure 3-11:	Superposition Used for Outer Solution	3.5.5.2
Figure 3-12:	Boundary Condition for ϕ_I^o	3.5.5.2
Figure 3-13:	Boundary Conditions for ϕ_{II}^o	3.5.5.2
Figure 3-14:	Welding Heat Source Distribution	3.6.3.3
Figure 3-15:	Side Heating Heat Source Distribution	3.6.3.3
Figure 3-16:	Finite Element Mesh for Temperature Analysis	3.6.3.3
Figure 3-17:	Comparison of Temperature History -Calculation Prediction .vs. Experiment Data -for Low Carbon Steel	3.7
Figure 3-18:	Comparison of Temperature History -Calculation Prediction .vs. Experiment Data -for Low Carbon Steel	3.7
Figure 3-19:	Comparison of Temperature History -Calculation Prediction .vs. Experiment Data -for HY-100	3.7
Figure 3-20:	Comparison of Temperature History -Calculation Prediction .vs. Experiment Data -for HY-100	3.7
Figure 3-21:	Comparison of Temperature History -Calculation Prediction .vs. Experiment Data -for HY-130	3.7
Figure 3-22:	Comparison of Temperature History -Calculation Prediction .vs. Experiment Data -for HY-130	3.7
Figure 3-23:	Comparison of Temperature History -Calculation Prediction .vs. Experiment Data -for Low Carbon Steel (Side Heating)	3.7
Figure 3-24:	Comparison of Temperature History -Calculation Prediction .vs. Experiment Data -for Low Carbon Steel (Side Heating)	3.7
Figure 3-25:	Comparison of Temperature History -Calculation Prediction .vs. Experiment Data -for HY-100 (Side Heating)	3.7
Figure 3-26:	Comparison of Temperature History -Calculation Prediction .vs. Experiment Data -for HY-100 (Side Heating)	3.7
Figure 3-27:	Comparison of Temperature History -Calculation Prediction .vs. Experiment Data -for HY-130 (Side Heating)	3.7
Figure 3-28:	Comparison of Temperature History -Calculation Prediction .vs. Experiment Data -for HY-130 (Side Heating)	3.7
Figure 4-1:	Stripped Element for One-dimensional Calculation	4.3
Figure 4-2:	Temperature Distribution on One Dimensional Model	4.3
Figure 4-3:	Bilinear Stress-strain Relation	4.3
Figure 4-4:	Plastic Strain Estimation	4.3
Figure 4-5:	Loading and Unloading	4.3

Figure 4-6:	Procedure of Calculating Transient Deformation at Mid-length	4.3
Figure 4-7:	Typical 2-D Plane Stress Field	4.5.1
Figure 4-8:	Finite Element Mesh and Boundary Conditions	4.5.1
Figure 4-9:	Comparison of Distortion --Calculation .vs. Experiment for Low Carbon Steel	4.6
Figure 4-10:	Comparison of Distortion --Calculation .vs. Experiment for HY-100	4.6
Figure 4-11:	Comparison of Distortion --Calculation .vs. Experiment for HY-130	4.6
Figure 4-12:	Comparison of Distortion - Calculation .vs. Experiment for Low Carbon Steel (Ahead)	4.6
Figure 4-13:	Comparison of Distortion --Calculation .vs. Experiment for HY-100 (Ahead)	4.6
Figure 4-14:	Comparison of Distortion --Calculation .vs. Experiment for HY-130 (Ahead)	4.6
Figure 4-15:	Comparison of Distortion --Calculation .vs. Experiment for Low Carbon Steel (Along)	4.6
Figure 4-16:	Comparison of Distortion --Calculation .vs. Experiment for HY-100 (Along)	4.6
Figure 4-17:	Comparison of Distortion --Calculation .vs. Experiment for HY-130 (Along)	4.6
Figure 4-18:	Comparison of Distortion --Calculation .vs. Experiment for Low Carbon Steel (Behind)	4.6
Figure 4-19:	Comparison of Distortion --Calculation .vs. Experiment for HY-100 (Behind)	4.6
Figure 4-20:	Comparison of Distortion --Calculation .vs. Experiment for HY-130 (Behind)	4.6
Figure 4-21:	Comparison of Longitudinal Strain Profile --Calculation .vs. Experiment for Low Carbon Steel at 1.00 inch	4.6
Figure 4-22:	Comparison of Longitudinal Strain Profile --Calculation .vs. Experiment for Low Carbon Steel at 4.00 inches	4.6
Figure 4-23:	Comparison of Transverse Strain Profile --Calculation .vs. Experiment for Low Carbon Steel at 1.25 inches	4.6
Figure 4-24:	Comparison of Transverse Strain Profile --Calculation .vs. Experiment for Low Carbon Steel at 4.25 inches	4.6
Figure 4-25:	Comparison of Longitudinal Strain Profile --Calculation .vs. Experiment for HY-100 at 1.00 inch	4.6
Figure 4-26:	Comparison of Longitudinal Strain Profile --Calculation .vs. Experiment for HY-100 at 4.00 inches	4.6
Figure 4-27:	Comparison of Transverse Strain Profile --Calculation .vs. Experiment for HY-100 at 1.25 inches	4.6
Figure 4-28:	Comparison of Transverse Strain Profile --Calculation .vs. Experiment for HY-100 at 4.25 inches	4.6
Figure 4-29:	Comparison of Longitudinal Strain Profile --Calculation .vs. Experiment for HY-130 at 1.00 inch	4.6
Figure 4-30:	Comparison of Longitudinal Strain Profile --Calculation .vs. Experiment for HY-130 at 4.00 inches	4.6
Figure 4-31:	Comparison of Transverse Strain Profile --Calculation .vs. Experiment for HY-130 at 1.25 inches	4.6
Figure 4-32:	Comparison of Transverse Strain Profile --Calculation .vs. Experiment for HY-130 at 4.25 inches	4.6

Figure 4-33:	Comparison of Longitudinal Strain Profile --Calculation .vs. Experiment for Low Carbon Steel at 1.00 inch (Side Heating)	4.6
Figure 4-34:	Comparison of Longitudinal Strain Profile --Calculation .vs. Experiment for Low Carbon Steel at 4.00 inches (Side Heating)	4.6
Figure 4-35:	Comparison of Transverse Strain Profile --Calculation .vs. Experiment for Low Carbon Steel at 1.25 inches (Side Heating)	4.6
Figure 4-36:	Comparison of Transverse Strain Profile --Calculation .vs. Experiment for Low Carbon Steel at 4.25 inches (Side Heating)	4.6
Figure 4-37:	Comparison of Longitudinal Strain Profile --Calculation .vs. Experiment for HY-100 at 1.00 inch (Side Heating)	4.6
Figure 4-38:	Comparison of Longitudinal Strain Profile --Calculation .vs. Experiment for HY-100 at 4.00 inches (Side Heating)	4.6
Figure 4-39:	Comparison of Transverse Strain Profile --Calculation .vs. Experiment for HY-100 at 1.25 inches (Side Heating)	4.6
Figure 4-40:	Comparison of Transverse Strain Profile --Calculation .vs. Experiment for HY-100 at 4.25 inches (Side Heating)	4.6
Figure 4-41:	Comparison of Longitudinal Strain Profile --Calculation .vs. Experiment for HY-130 at 1.00 inch (Side Heating)	4.6
Figure 4-42:	Comparison of Longitudinal Strain Profile --Calculation .vs. Experiment for HY-130 at 4.00 inches (Side Heating)	4.6
Figure 4-43:	Comparison of Transverse Strain Profile --Calculation .vs. Experiment for HY-130 at 1.25 inches (Side Heating)	4.6
Figure 4-44:	Comparison of Transverse Strain Profile --Calculation .vs. Experiment for HY-130 at 4.25 inches (Side Heating)	4.6
Figure 4-45:	Comparison of Longitudinal Residual Stress -- Calculation .vs. Experiment for Low Carbon Steel	4.6
Figure 4-46:	Comparison of Transverse Residual Stress --Calculation .vs. Experiment for Low Carbon Steel	4.6
Figure 4-47:	Comparison of Longitudinal Residual Stress -- Calculation .vs. Experiment for HY-100	4.6
Figure 4-48:	Comparison of Transverse Residual Stress --Calculation .vs. Experiment for HY-100	4.6
Figure 4-49:	Comparison of Longitudinal Residual Stress -- Calculation .vs. Experiment for HY-130	4.6
Figure 4-50:	Comparison of Transverse Residual Stress --Calculation .vs. Experiment for HY-130	4.6
Figure 4-51:	Comparison of Longitudinal Residual Stress -- Calculation .vs. Experiment for Low Carbon Steel (Side Heating)	4.6
Figure 4-52:	Comparison of Transverse Residual Stress --Calculation .vs. Experiment for Low Carbon Steel (Side Heating)	4.6
Figure 4-53:	Comparison of Longitudinal Residual Stress -- Calculation .vs. Experiment for HY-100 (Side Heating)	4.6
Figure 4-54:	Comparison of Transverse Residual Stress --Calculation .vs. Experiment for HY-100 (Side Heating)	4.6
Figure 4-55:	Comparison of Longitudinal Residual Stress -- Calculation .vs. Experiment for HY-130 (Side Heating)	4.6
Figure 4-56:	Comparison of Transverse Residual Stress --Calculation .vs. Experiment for HY-130 (Side Heating)	4.6

Figure 5-1:	Distortion Comparison	5.2
Figure 5-2:	Yield Stresses at Elevated Temperature	5.2
Figure 5-3:	Maximum Longitudinal Strain observed at 1 inch from weld line	5.3
Figure 5-4:	Development of Plastic Zone for the Case without Side Heating	5.4
Figure 5-5:	Development of Plastic Zone for the Case with Side Heating	5.4
Figure 5-6:	Temperature Profile for Preheating	5.5
Figure 5-7:	Temperature Profile during Low Temperature Treatment at 0.5 inches from the weld line for no side heating case	5.5
Figure 5-8:	Temperature Profile during Low Temperature Treatment at 0.5 inches from the weld line for side heating case	5.5
Figure 5-9:	Temperature Profile during Low Temperature Treatment at 3.5 inches from the weld line for side heating case	5.5
Figure 5-10:	Comparison of Distortion Profile between the Side Heating Case and Preheating Case	5.5
Figure 5-11:	Comparison of Distortion Profile	5.5
Figure 5-12:	Comparison of Longitudinal Residual Stress I	5.5
Figure 5-13:	Comparison of Longitudinal Residual Stress II	5.5
Figure 5-14:	Comparison of Transverse Residual Stress I	5.5
Figure 5-15:	Comparison of Transverse Residual Stress II	5.5
Figure 5-16:	Temperature Profile during Low Temperature Treatment	5.5
Figure 5-17:	Distortion Profile during Low Temperature Treatment	5.5
Figure 5-18:	Comparison of Longitudinal Residual Stress	5.5
Figure 5-19:	Comparison of Transverse Residual Stress	5.5

List of Tables

Table 2-I:	Low Carbon Steel Chemical Composition, percent	2.2.2
Table 2-II:	Low Carbon Steel Specified Mechanical Properties	2.2.2
Table 2-III:	Physical Properties of Low Carbon Steel	2.2.2
Table 2-IV:	Mechani l Properties of Low Carbon Steel	2.2.2
Table 2-V:	HY-100 Chemical Composition, percent	2.3.2
Table 2-VI:	HY-100 Specified Mechanical Properties	2.3.2
Table 2-VII:	Physical Properties of HY - 100	2.3.2
Table 2-VIII:	Mechanical Properties of HY - 100	2.3.2
Table 2-IX:	HY-130 Chemical Composition, percent	2.3.3
Table 2-X:	HY-130 Specified Mechanical Properties	2.3.3
Table 2-XI:	Physical Properties of HY - 130	2.3.3
Table 2-XII:	Mechanical Properties of HY - 130	2.3.3
Table 2-XIII:	Contents of Consumables of HY-130	2.3.3
Table 2-XIV:	Specification of Deltaweld 650	2.5.2
Table 3-I:	Values of Arc Efficiency for Various Processes	3.3
Table 3-II:	Experimental Values for the Concentration Coefficient	3.3
Table 3-III:	Thermal Characteristic of Oxyacetylene Flame of Standard Torches	3.4
Table 3-IV:	Flame Efficiencies and Heat Distribution of Various Gas Flame	3.4
Table 3-V:	Convection coefficient h	3.6.3.1
Table 5-I:	Distortion at Mid-Length	5.2

Chapter 1

Introduction

The welding process has been used extensively in the fabrication of many structures, including ships, airplanes, buildings, bridges, pressure vessels, etc. It provides many advantages over other joining techniques such as riveting, casting, and forging. To name only a few, it provides excellent mechanical properties, air and water tightness, and good joining efficiency.

There are, however, various problems such as residual stresses and shape distortion associated with the construction of welded structures. When a material is being welded, it experiences local heat due to the welding heat source. The temperature field inside the weldment is not uniform and changes as the welding progresses. The welding heat cycle gives rise to a complex strain field in the weld metal and in the base metal regions near the weld. These strains, along with the plastic upsetting, create the residual stresses that remain after the welding is completed. In addition, shrinkage and distortion are also produced. Residual stresses and distortion are highly undesirable in welding technology. Thermal stresses during welding often cause cracking. High tensile residual stresses near the weld may lead to a fracture of the weldment. Compressive residual stresses in the base plate, often combined with distortion, may reduce its buckling strength. If distortion occurs in the parts of complex structures that need to be joined, a mismatch problem takes place. The mismatch increases the possibility of the weld defect. Furthermore, if the parts are forced into alignment and joined, stress is locked into the structures. This results in the strength reduction of the joint under either static loads or cyclical loadings. In some extreme cases it may be necessary to remove distortion completely before joining. However, correcting unacceptable distortion is extremely costly and in some cases impossible.

1.1 General Discussion of Residual Stresses and Distortion in Welded Structures

A typical physical phenomenon of a butt weld is shown in Fig. 1-1. A welding arc is traveling with a speed v between two plates causing them to coalesce by providing filler metal. The four parts of the weld that are subjected to different thermal histories are shown in Fig. 1-2. Part one constitutes the filler metal which is deposited in a molten state and solidifies as cooling begins. Part two is the part of the joint that melts and resolidifies during cooling. Both of these parts define the weld metal. Part three is the heat affected zone defined as that part of the joint in which the maximum temperature reached is above that in the first part but below the solidus temperature. Part four is the base metal [50].

The residual stresses in a welded joint are caused by the contraction of the weld metal and the plastic deformation produced in the base metal region near the weld. Residual stresses in a welded joint are classified as "residual welding stress" which occurs in a joint free from any external constraint and "reaction stress" (or "locked-in stress"), which is induced by an external constraint. By far, the most extensive studies on residual stress have been done on weldments in steel, especially in low carbon steel. Some data have been generated in high strength steels, stainless steels, aluminum alloys, and titanium alloys. Most of the studies have been made on arc welded joints, especially butt welds [3] [26] [29] [37] [45] [47] [63].

A typical distribution of residual stresses in a butt weld is shown in Fig. 1-3. The stresses of concern are those parallel to the weld direction, σ_x, and those transverse to the weld direction, σ_y. The distribution of the residual stress σ_x along a line transverse to the weld (YY) is shown in Fig. 1-3b. Tensile stresses of high magnitude are produced in the region of the weld. These stresses taper off rapidly and become compressive at a distance of several times the width of the weld. The stress distribution is characterized by two parameters: (1) the

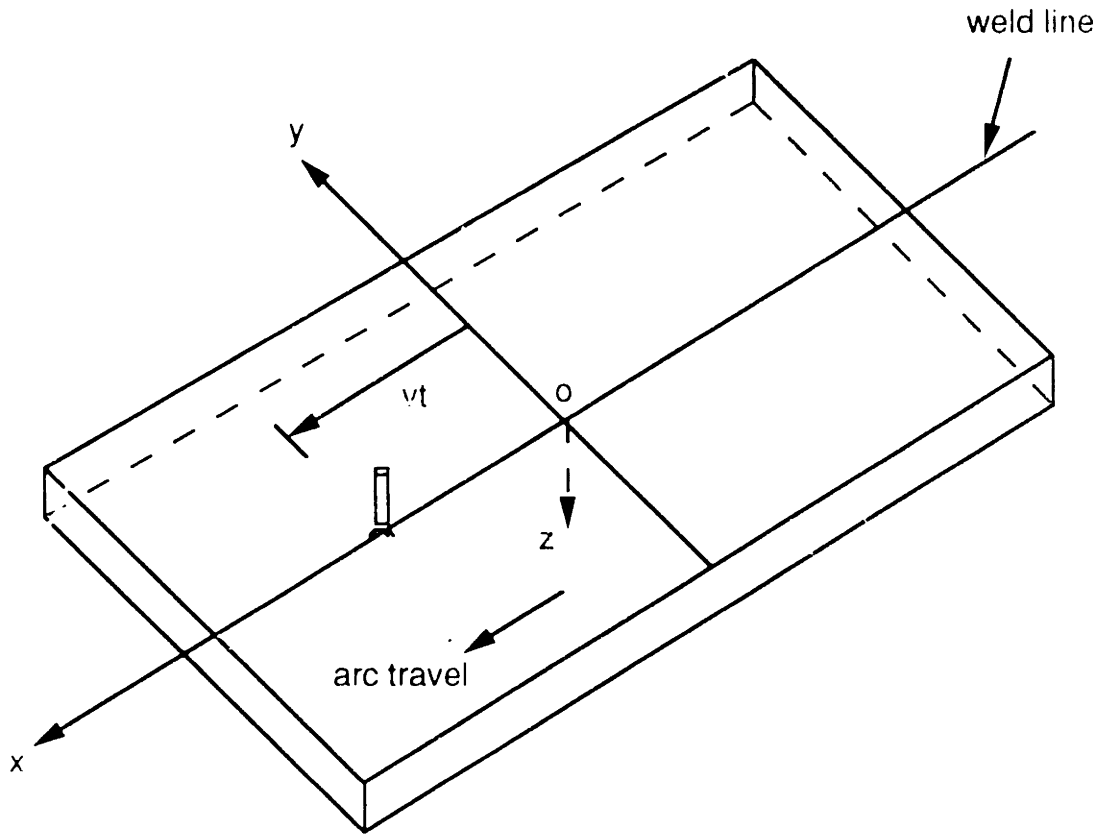

Figure 1-1: Weldment Configuration for Butt Welding

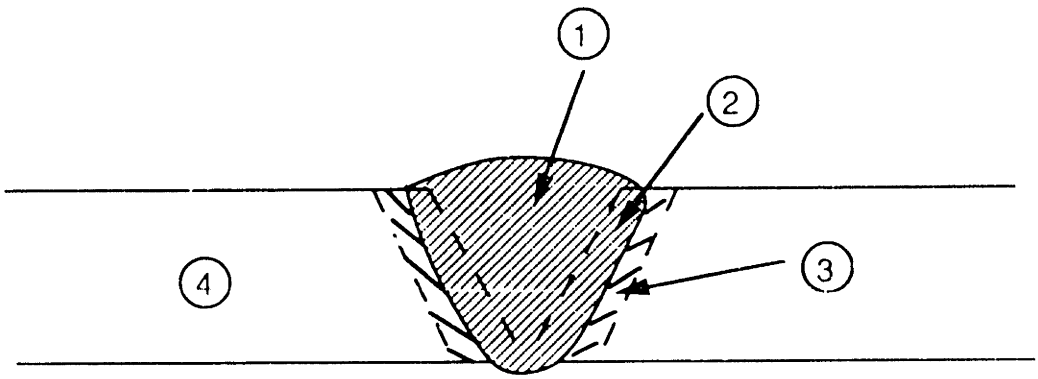

1 , 2 Weld Metal

3 Heat Affected Zone

4 Base Metal

Figure 1-2: Four Parts of Weld Subjected to Different Thermal Histories

maximum stress at the weld region σ_m, and (2) the width of the tension zone of residual stress b. The weld metal and heat affected zone try to shrink in the direction of the weld and the adjacent plate material prevents this shrinkage. The distribution of the residual stress σ_y along the length of the weld (XX) is shown in curve 1 in Fig. 1-3c. Tensile stresses of relatively low magnitude are produced in the middle part of the joint and compressive stresses are observed at the end of the joint. If the lateral contraction of the joint is restrained by an external constraint such as a series of springs, the distribution of σ_y is as shown by curve 2 in Fig. 1-3c. Tensile stresses, approximately uniform along the weld, are added as the reaction stress. An external constraint, however, has little influence on the distribution of σ_x residual stresses.

The magnitude and distribution of residual stresses in a weld are determined by:

1.) Expansion and contraction characteristics of the base metal and the weld metal during the welding thermal cycle.

2.) Temperature versus yield strength relationship of the base metal and the weld metal.

Research on a low carbon steel weldment has shown that the maximum residual stress σ_x is as high as the yield strength of the weldment. For some high strength steel weldments, it was found that the maximum residual stress is considerably lower than the yield strength. For example, in the study of the heat treated SAE 4340 steel, the maximum residual stresses were around 50,000 to 80,000 psi considerably less than the yield strength of the weld metal (about 150,000 psi) and the base metal (224,000 psi). For a titanium-alloy weldment, it was found that the maximum residual stresses ranged from 35,000 to 85,000 psi, depending upon the type of base metal and welding processes [47].

The distortion found in fabricated structures is caused by three fundamental dimensional changes that occur during welding:

1.) Transverse shrinkage that occurs perpendicular to the weld line.

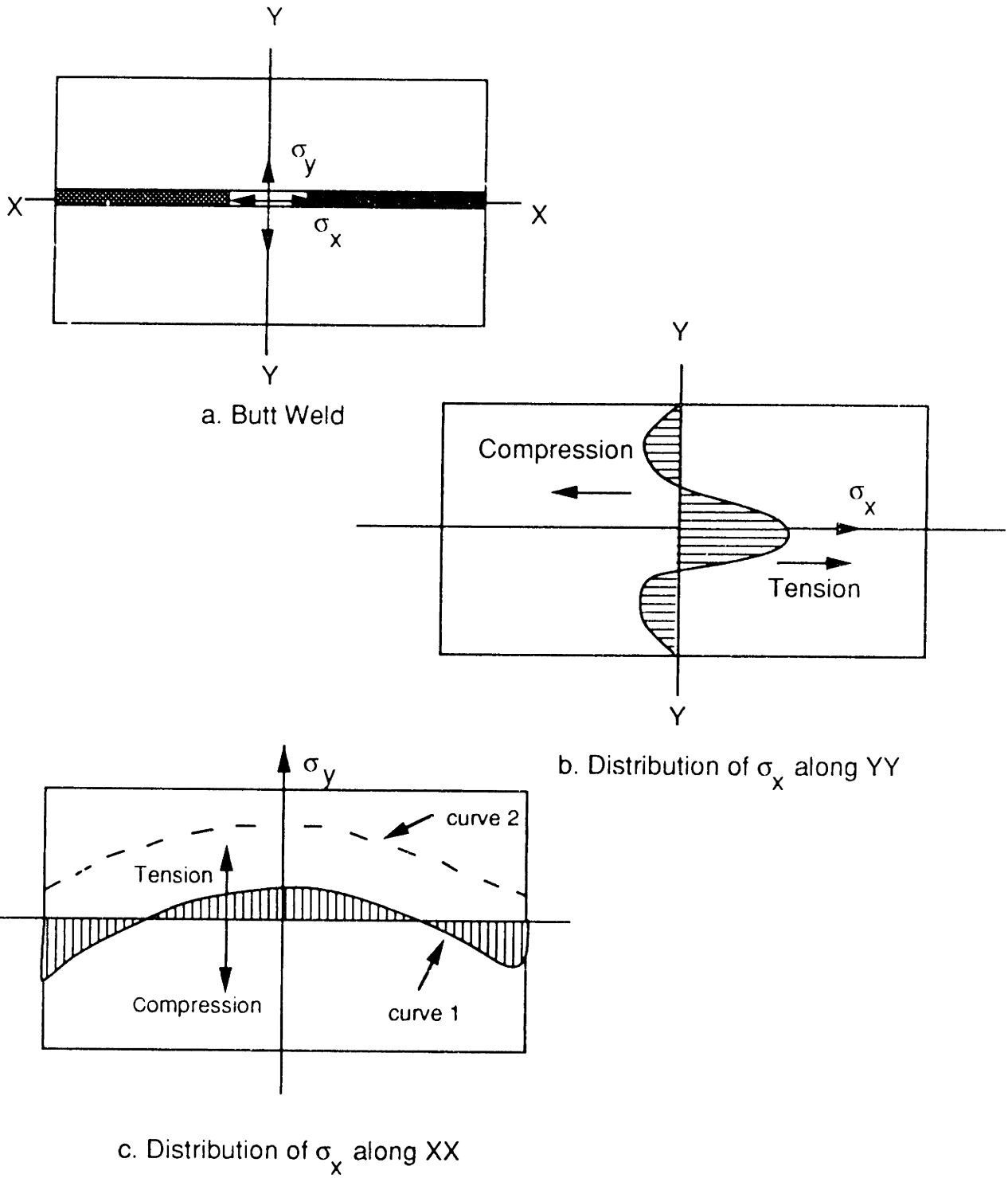

Figure 1-3: Typical Distribution of Residual Stresses in Butt Weld

2.) Longitudinal shrinkage that occurs parallel to the weld line.

3.) An angular change that consists of rotation around the weld line.

These dimensional changes are shown in Fig. 1-4 and are classified by their appearance as follows:

a.) Transverse shrinkage: Shrinkage perpendicular to the weld line.

b.) Angular change: A non uniform thermal distribution in the thickness direction causes distortion close to the weld line.

c.) Rotational distortion: Angular distortion in the plane of the plate due to thermal expansion.

d.) Longitudinal shrinkage: Shrinkage in the direction of the weld line.

e.) Longitudinal bending distortion: Distortion in a plane through the weld line and perpendicular to the plate.

f.) Buckling distortion: Thermal compressive stresses which cause instability when the plates are thin.

Shrinkage and distortion that occur during the fabrication of actual structures are far more complex than those shown in Fig. 1-4. For example, when a long butt joint is welded by the step-back sequence, the transverse shrinkage is not uniform along the weld as shown in Fig. 1-4a. When longitudinal shrinkage occurs in a fillet welded joint, the joint will bend longitudinally unless the weld line is located along the neutral axis of the joint. Whether or not a joint is restrained externally will also affect the magnitude and form of distortion.

1.2 Control and Reduction of Residual Stresses and Distortion

As mentioned earlier in this chapter, residual stresses and distortion during fabrication and service bring about vital consequences, most of which are detrimental. There is always a strong interest in the industry for developing efficient means for controlling and reducing these undesirable effects. In the past, several methods have been proposed and are currently in use, aiming at

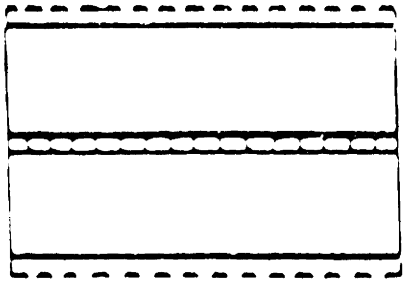

a. Transverse Shrinkage

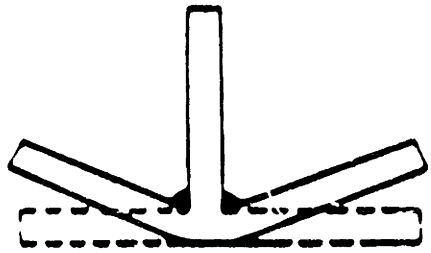

b. Angular change

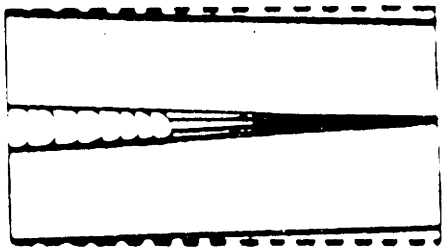

c. Rotational Distortion

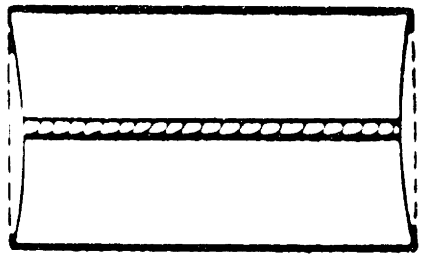

d. Longitudinal Shrinkage

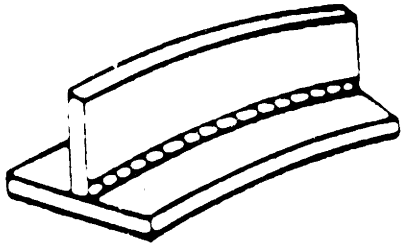

e. Longitudinal Bending Distortion

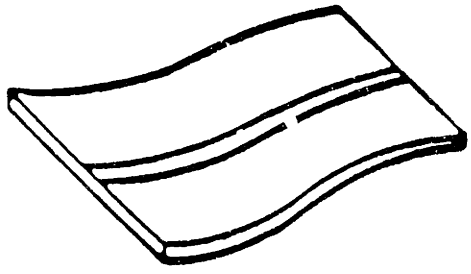

f. Buckling Distortion

Figure 1-4: Various Types of Weld Distortion

reducing residual stresses and distortion. These methods include both mechanical and thermal treatments such as pre-heating, pre-deformation, vibrating, flattening, etc. However, these methods are applied only after or before welding and are arranged as special operations in the manufacturing procedure. All of them need special installation. This results in increasing cost and variable quality of welded structures. It is believed that the most effective method of reducing residual stresses and distortion is to perform a proper action during welding while non elastic strains that cause the stresses and distortion are being formed. This concept was proposed by Prof. Masubuchi as a result of many years of experience involving a number of research programs [5] [12] [13] [16] [44].

Since it takes considerable time (on the order of 30 minutes or even longer) after welding is completed or before a weldment cools down completely to fully develop residual stresses, it is too late to try to effectively alter residual stresses by doing something after welding is completed.

1.3 Research Objective

In the course of the research program at M.I.T., directed by Prof. Masubuchi, it has been found that in-process control and reduction of residual stresses and distortion is indeed very effective in controlling and reducing residual stresses and distortion. However, the research efforts thus far have covered only two types of experiments:

a.) Control of mismatch during butt welding.

b.) Control of residual stresses and radial distortion during girth welding of pipes.

A question arises as to whether or not the concept of in-process control and reduction of residual stresses and distortion can be extended to other types of weldments as well as to different types of materials. For example, it is

effective to use side heating technique to control the metal movement in a butt weld of low carbon steel while side cooling is more effective in controlling the metal movement in a butt weld of aluminum. The objective of this thesis is to give an answer to the above questions.

In this thesis, study is undertaken on the use of side heating technique to reduce residual stresses and distortion during bead-on-edge welding of high strength steel. Side heating is used as a secondary heat source to provide thermal stresses that counteract those produced by the welding arc. The following research tasks were completed in order to further prove the advantage of the side heating technique.

1.) Survey of literature and review of industrial practice on methods of reducing residual stresses and distortion in weldments.

2.) Perform a series of experiments with and without side heating on low carbon steel, HY-100, and HY-130 to collect necessary data.

3.) Develop an analytical heat flow analysis with and without side heating effect and implement the analysis into computer.

4.) Perform a preliminary stress-strain analysis using one-dimension analysis and implement into computer.

5.) Analyze and compare the results obtained in task no.2,3,and 4.

6.) Perform numerical analysis of heat flow with and without side heating using the finite element model.

7.) Develop a finite element model for welding application to perform numerical analysis of two-dimension stress-strain analysis.

8.) Analyze and compare the results obtained from task no. 2, 3, 4, 6 and 7.

9.) Develop a novel concept of reducing residual stresses and distortion based on the knowledge developed during this research.

Chapter 2

Experimental Synopsis

2.1 Experimental Description

The welding experiments were carried out on three different materials, namely low carbon steel, HY-100, and HY-130. Experiments consisted of two phases. In the first phase, ie., the control phase, the welding process was performed on each specimen of low carbon steel, HY-100, and HY-130 without providing additional side heating. These specimens were bead-on-edge welds using the gas metal arc welding process. Temperature changes and strain changes during welding were measured by thermocouples and strain gages, respectively. These thermocouples and strain gages were mounted on specimen surfaces. Data from thermocouples and strain gages were processed through a data acquisition system. Distortion during welding and after welding was measured on three different positions along the weldment by three dial gages which were attached to the lower part of each specimen. After welding was completed, the specimens were left to cool down to room temperature before they were cut to measure residual stresses using the stress relaxation method. The objective of this phase is to establish temperature, transient strain and distortion profiles for all three steels and to provide based lines for residual stresses for these steels that were welded without side heating.

The second phase was to weld these three types of steels along with additional side heating. The same physical quantities were measured as in the first phase. Location of side heating was varied in the weld line direction to find the most appropriate location of side heating that would provide good reduction in residual stresses and distortion.

The following sections in this chapter discuss in further detail the

characteristics of material, the type and appropriate location of side heating source used in this experiment, the experimental set up as well as experimental results.

2.2 Material Characteristics of Low Carbon Steel

2.2.1 General Characteristics

Low carbon steels are widely used for ocean engineering structures. Typically, a ferrous metal with a carbon content of less than 0.3% is defined as a low carbon steel. It has the ability to stand rough treatment and abuse. Low carbon steel can be welded by any of the welding processes.

2.2.2 Low Carbon Steel Description

Low carbon steel used in this investigation is an ABS class B type steel. The specified chemical composition is shown in Table 2-I [40].

Table 2-I: Low Carbon Steel Chemical Composition, percent

C	Mn	P	S
0.21 max.	0.80-1.10	0.05 max.	0.05 max.

The mechanical properties of low carbon steel are shown in Table 2-II [40].

Table 2-II: Low Carbon Steel Specified Mechanical Properties

Yield Strength	36 ksi
Tensile Strength 0.2%	58 ksi
Reduction of Area	60-70%
Elongation in 8 in.	28%
A Charpy-V-notch impact energy absorption	50 - 80 ft.lbs.

The material properties of low carbon steel at elevated temperature are shown in Tables 2-III and 2-IV [48].

Table 2-III: Physical Properties of Low Carbon Steel

θ	70	200	400	600	800	1000	1200	1400	1600	1800	2000	2200	2400	2600
κ	20.02	20.88	21.29	21.01	20.68	19.49	20.06	14.91	15.29	15.68	15.25	16.38	16.69	16.99
c	0.102	0.110	0.120	0.132	0.148	0.166	0.178	0.190	0.173	0.156	0.156	0.156	0.156	0.156
ρ	0.284	0.283	0.282	0.280	0.279	0.277	0.276	0.275	0.275	0.275	0.275	0.275	0.275	0.275
α	6.55	6.55	6.97	7.35	7.75	8.06	8.50	8.15	6.95	7.00	7.23	7.30	7.50	7.50

Nomenclature

θ = temperature (°F)

κ = thermal conductivity (Btu/hr.ft.°F)

c = specific heat (Btu/lbm °F)

ρ = density (lbm/in**3)

α = thermal expansion coefficient (in/in °F x 10e-6)

Table 2-IV: Mechanical Properties of Low Carbon Steel

θ	70	200	400	600	800	1000	1200	1400	1600	1800	2000	2200	2400	2600
σ_y	36.0	32.0	29.0	25.0	22.0	17.0	14.2	6.0	3.0	1.0	0.8	0.7	0.1	0.0
E	30.00	29.60	28.80	27.70	26.00	22.70	14.00	5.00	4.20	3.00	2.10	1.20	0.30	0 0
E_t	1.60	1.58	1.54	1.48	1.39	1.21	0.75	0.27	0.23	0.16	0.11	0.06	0.01	0.0
ν	0.3	0.308	0.324	0.338	0.349	0.369	0.376	0.384	0.391	0.415	0.423	0.447	0.465	0.464

Nomenclature

θ = temperature ($^{\circ}$F)

σ_y = yield stress (ksi)

E = Young's moduius (ksi x 10e+3)

E_t = tangent modulus (ksi x 10e+3)

ν = Poisson's ratio

2.3 Material Characteristics of HY-100 and HY-130

2.3.1 General Characteristics

HY-100 and HY-130 were developed as an upgrading of the HY-80 Class of Naval Hull-Construction Alloys. Both of them are weldable, high strength, quenched and tempered steel plates made according to the restrictive practice common to the production of armor plate steel. Their superior notch toughness and ductility at high strength level make them suitable for dynamic loading situations and/or low temperature service.

2.3.2 HY-100 Description

HY-100 is similar to HY-80 in concept since only minor adjustments to the composition and heat treatment are made to permit the attainment of the 100 ksi minimum yield strength level. HY-100 is characterized by a superior level of notch toughness and ductility for a steel of this strength level. The specified chemical composition is shown in Table 2-V [40].

Table 2-V: HY-100 Chemical Composition, percent

C	Mn	P	S	Si	Ni	Cr	Mo
0.12 0.20	0.10 0.40	0.025 max	0.025 max.	0.15 0.35	2.25 3.50	1.00 1.80	0.20 0.60

The mechanical properties of HY-100 in the as-received quenched and tempered condition are shown in Table 2-VI [31].

Table 2-VI: HY-100 Specified Mechanical Properties

Min. Yield Strength	100 ksi
Min Tensile Strength [0.2%]	110 ksi
Reduction of area	55% longitudinally
	50% transversely
Elongation in 2 in.[50.8 mm]	17% for 0.5 in. thick plate
A Charpy -V-notch impact energy absorption at -120 °F [-84 °C]	
	50 ft.lbs for 0.5. in. thick plate

The availability of material properties for HY-100 at elevated temperatures is at best scant, if not nonexistent. These properties, such as thermal conductivity, specific heat, Young's modulus, etc, are necessary for the calculation of temperature, strains and stresses. This is due to the fact that during the welding cycle the material experiences temperatures ranging from room to melting temperature; and it is well established that all material properties exhibit severe changes within that range. This left us with no other alternative but to approximate the elevated temperature properties from the available properties of material with similar chemical compositions through an averaging process. In this study the material properties of HY-80 were chosen and interpolated for HY-100. The physical and mechanical properties of HY-100 at elevated temperatures are shown in Tables 2-VII and 2-VIII [26].

Table 2-VII: Physical Properties of HY - 100

θ	70	200	400	600	800	1000	1200	1400	1600	1800	2000	2200	2400	2600
κ	19.38	20.40	21.51	21.80	21.18	19.50	17.09	14.91	15.32	15.69	16.03	16.37	16.72	16.80
c	0.107	0.110	0.118	0.126	0.136	0.148	0.168	0.354	0.168	0.156	0.155	0.153	0.153	0.153
ρ	0.284	0.283	0.282	0.280	0.279	0.278	0.276	0.275	0.275	0.275	0.275	0.275	0.275	0.275
α	6.50	6.65	6.95	7.25	7.60	8.05	8.50	8.15	6.95	7.00	7.23	7.45	7.45	7.45

Nomenclature

θ = temperature (°F)

κ = thermal conductivity (Btu/hr.ft.°F)

c = specific heat (Btu/lbm °F)

ρ = density (lbm/in**3)

α = thermal expansion coefficient (in/in°F x 10e-6)

Table 2-VIII: Mechanical Properties of HY - 100

θ	70	200	400	600	800	1000	1200	1400	1600	1800	2000	2200	2400	2600
σ_y	100.0	99.2	97.6	93.6	86.4	70.0	46.4	24.5	11.0	5.8	3.5	1.2	0.2	0.0
E	30.30	29.60	28.30	27.50	25.80	22.30	12.90	5.30	4.20	3.10	2.10	1.40	0.30	0.0
E_t	1.60	1.59	1.54	1.48	1.40	1.20	0.75	0.27	0.23	0.16	0.11	0.06	0.0	0.0
ν	0.3	0.308	0.324	0.338	0.349	0.369	0.376	0.384	0.391	0.415	0.423	0.447	0.465	0.464

Nomenclature

θ = temperature (°F)

σ_y = yield stress (ksi)

E = Young's modulus (ksi x 10e+3)

E_t = tangent modulus (ksi x 10e+3)

ν = Poisson's ratio

Fabrication practices of HY-100 do not differ significantly from those used for HY-80. The 20 ksi increase in minimum yield strength can result in reduced machinability (approximately 50% in relation to A36 Steel) and slightly less formability commensurate with the 5% reduction in the minimum reduction in area requirement. The same MIL-SPEC specification for HY-80 is used for HY-100 with slight differences in composition and production process.

2.3.3 HY-130 Description

HY-130 was developed in the early sixties under the contract that was placed with the US Steel Co. by the U.S. Navy for the systematic development of a steel with a minimum yield strength in the 130 to 150 ksi range and of associated welding procedures and consumables. Table 2-IX provides the chemical composition of HY-130 [50].

Table 2-IX: HY-130 Chemical Composition, percent

C	Mn	Si	Ni	Cr	Mo	V	S	P	Ti	Cu
0.08-0.12	0.60-0.90	0.20-0.35	4.75-5.25	0.40-0.70	0.30-0.65	0.05-0.10	0.01 max.	0.01 max.	0.02 max.	0.2 max

The mechanical properties of HY-130 in the as-received quenched and tempered condition are shown in Table 2-X [50].

Table 2-X: HY-130 Specified Mechanical Properties

Min Yield Strength	130 ksi
Min Tensile Strength [0.2%]	143 ksi
Reduction of area	55% longitudinally
	53% transversely
Elongation in 2 in.[50.8 mm.]	24% for 0.5 in. thick plate.
A Charpy-V-notch impact energy absorption at 0 °F	
	60 ft.lbs for 0.5 in. thick plate.

The temperature dependence of material properties for HY-130 is shown in Tables 2-XI and 2-XII. These values were taken from [50]. It should be noted here that not all the data presented in Tables 2-XI and 2-XII came from experimental measurements, especially for the data in the range of high temperatures. This is due to the great difficulties encountered in the measurement of properties at elevated temperatures. In such cases the data for high temperature range are approximated through careful interpolation or by an educated guess. For example, the thermal conductivity data for HY-130 were available up to a temperature of 1400 °F. From this temperature and up to solidus (2600 °F), a linear increasing thermal conductivity was assumed. Heat is conducted through metals by two distinct mechanisms: one involves the transfer of thermal energy by the free electrons in the metal; the other results from the coupling together of the vibrations of the atom in the crystal. Both contributions are expected to result in an increase in thermal conductivity at high temperature [11].

Table 2-XI: Physical Properties of HY - 130

θ	70	200	400	600	800	1000	1200	1400	1600	1800	2000	2200	2400	2600
κ	20.03	20.90	21.30	21.03	20.70	19.50	17.60	14.90	15.30	15.70	16.00	16.40	16.70	17.00
c	.0.102	0.110	0.120	0.132	0.148	0.166	0.190	0.354	0.168	0.156	0.156	0.156	0.156	0.156
ρ	0.284	0.283	0.282	0.280	0.279	0.277	0.276	0.275	0.275	0.275	0.275	0.275	0.275	0.275
α	---	6.55	6.97	7.35	7.75	8.06	8.23	8.15	6.95	7.00	7.18	7.30	7.45	7.50

Nomenclature

θ = temperature (°F)

κ = thermal conductivity (Btu/hr.ft.°F)

c = specific heat (Btu/lbm°F)

ρ = density (lbm/in**3)

α = average thermal expansion coefficient (in/in°F x 10e-6)

Table 2-XII: Mechanical Properties of HY - 130

θ	70	200	400	600	800	1000	1200	1400	1600	1800	2000	2200	2400	2600
σ_y	138.0	135.5	126.7	117.0	106.0	85.0	49.0	24.5	11.0	5.8	4.0	2.0	1.0	0.0
E	30.00	29.60	28.8	27.7	26.0	22.7	14.0	5.0	4.0	3.0	2.0	1.20	0.40	0.0
E_t	1.60	1.58	1.54	1.48	1.40	1.20	0.75	0.27	0.23	0.16	0.11	0.06	0.02	0.0
ν	0.3	0.308	0.321	0.334	0.346	0.359	0.372	0.384	0.397	0.410	0.422	0.435	0.447	0.454

Nomenclature

θ = temperature (°F)

σ_y = yield stress (ksi)

E = Young's modulus (ksi x 10e+3)

E_t = tangent modulus (ksi x 10e+3)

ν = Poisson's ratio

Consumables for welding HY-130 have been developed for both shield metal arc (SMA) and gas metal arc (GMA) welding. The Navy specification for a low-hydrogen type E14018 electrode is recommended to be used with SMA. The AX-140 developed by Airco and the Navy specification MIL-140s are used with GMA. Table 2-XIII [50] shows the analysis of consumables for welding HY-130 type steel.

Table 2-XIII: Contents of Consumables of HY-130

Element	MIL-14018	AX-140	MIL-140s
C	0.1 max.	0.07-0.11	0.12 max.
Mn	0.75-1.35	1.70-2.00	1.5-2.0
Si	0.65 max.	0.25-0.45	0.3-0.5
S	0.010 max.	~0.007	0.010 max.
P	0.013	~0.006	0.010 max.
Cr	0.35-1.20	0.85-1.20	0.65-1.05
Mo	0.30-0.90	0.50-0.60	0.40-1.00
Ni	3.10-3.90	2.00-2.50	1.05-3.10
Al	-	~0.018	0.04 max.
Ti	-	~0.010	0.04 max.
Zr	-		0.04 max.
Cu	-		0.15 max.

If one compares the amount of content in the consumables with the chemical composition (Table 2-IX) of HY-130, it can be seen that the carbon content of the consumables is below that of the base metal because of carbon's

tendency to cause cracking. Similarly the manganese content is relatively high because it imparts toughness. Nickel content is lowered to avoid cracking known to be caused by high nickel content. Chromium content is raised for increased hardenability. HY-130 also has a high strength to weight ratio, about 473, similar to aluminum. Therefore, it may be used in place of aluminum where weight is critical and light weight with high strength is desired.

2.4 Heat Source for Side Heating

There are two types of heat sources for side heating to be considered. One is concentrated heat source and the other is distributed heat source. Concentrated side heating with the same magnitude of heat source as welding itself can prevent the thermal distortion of the weldment during bead-on-edge weld due to the symmetry condition. Even though it is effective in controlling the during process distortion it also has some unavoidable adverse effects. First, this technique needs exactly the same heat input as the welding itself. This high heat input will cause the material degradation of the weldment, especially for quenched and tempered steel like HY-100 and HY-130. Second, due to the high concentrated side heating source, there will be melting and solidification processes where the heat is applied, just as in welding itself. This melting and solidification processes will cause high residual stresses comparable with those of welding itself.

Side heating with distributed heat source operates according to the same basic principle as does concentrated side heating. It creates counter thermal stresses against those produced by the weld arc. The difference is that with the distributed side heating, melting and resultant residual stresses beneath the side heating are much less than those created by concentrated side heating. This is due to lower heating temperature. The material degradation will also be much less for the same reason. Figure 2-1 shows the basic concept of both concentrated side heating and distributed side heating.

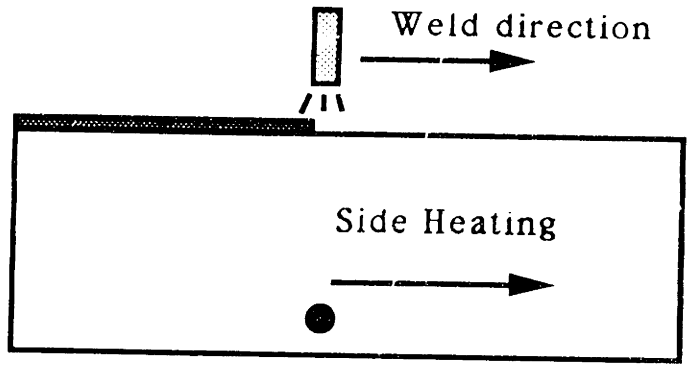

a. Concentrated Side Heating Method

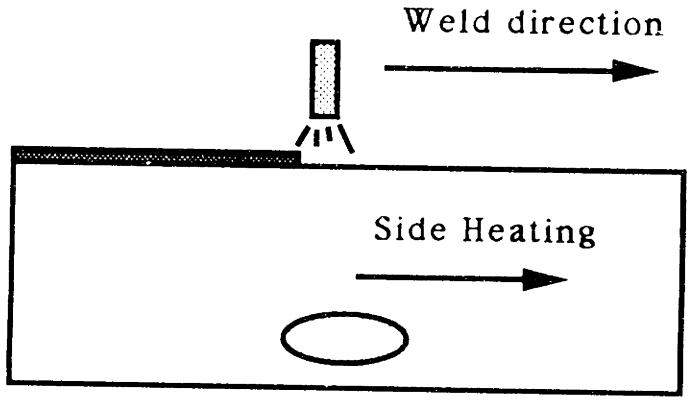

b. Distributed Side Heating Method

Figure 2-1: Types of Side Heating Source

Figure 2-2 shows the calculated longitudinal residual stresses, occurring along the lateral distance from the weld caused by both welding and side heating. If the side heating is concentrated (k large) it causes residual stresses. Therefore, the plate has two peak residual stresses as a result of welding and side heating. This is obviously undesirable. If the side heating is less concentrated (k small), it causes no additional residual stresses. From these results we can see that side heating with low heat input in a wide region is the most appropriate way. By using this method, a significant amount of counter balancing action can be exerted without producing additional residual stresses. This gives the initial idea of how to perform the experiment to prove the effectiveness of side heating. Another question is the position of the side heating torch so as to effectively reduce residual stresses and distortion. Should it be placed ahead of the welding torch, along with the welding torch or even behind the welding torch? This is one of the tasks that needs to be accomplished in this study.

In Chang's [13] study of reducing the root gap change during butt welding with side heating, he tried different distributed side heating sources, such as electric heating pad and oxyacetylene torch. He then concluded that distributed side heating by oxyacetylene flame is an effective heat source. This oxyacetylene flame can provide enough thermal effect; at the same time heat fluxes from the torch are widely distributed enough to be effective and not to leave any material degradation or residual stresses. In his study an oxyacetylene torch flame was used to heat a very wide range of the plate up to 200 degree F or over. This temperature is moderate enough not to provide additional residual stresses. As a result of this study, an oxyacetylene torch was then employed as a side heating source in this investigation.

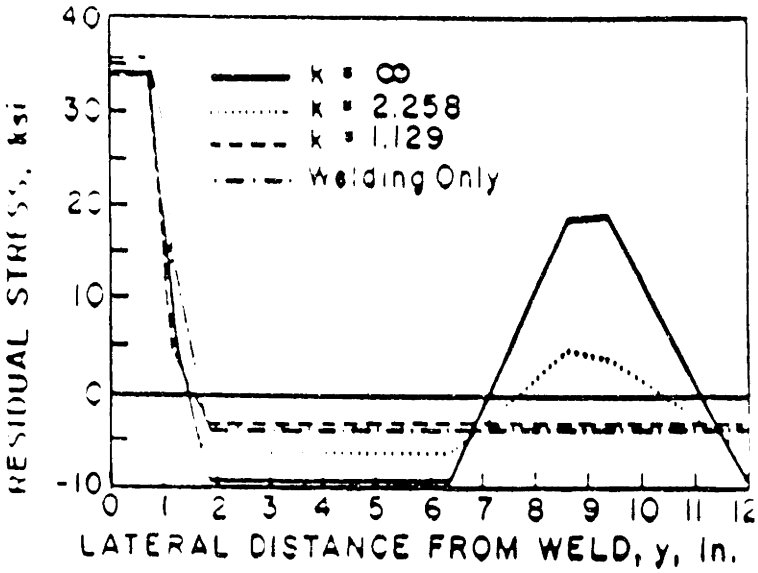

Figure 2-2: Calculated Distribution of Residual Stress

2.5 Experiment Set-Up

2.5.1 Specimen

Low carbon steel was used as a control specimen and for comparative purposes to verify the result obtained on the high strength steels, HY-100 and HY-130. The HY-100 and HY-130 were obtained from the David Taylor Naval Research Center in Annapolis, Maryland. The dimension of each test piece was 18"x5.5" and 0.5 in. thick (Fig. 2-3). This dimension was selected according to De Garmo [17] to ensure that it could contain residual stresses as high as those that exist in actual structures. In preparing these test pieces, care was taken to ensure that they were all cut along the rolling direction of the plate. This was to avoid any creation of residual stresses that might happen during the cutting process. In addition, the edges of each test piece were milled to remove flame

hardened edges where needed. Cooling water was provided during milling to keep the plate cool. Cutting and milling were done using the facility in the M.I.T. Machine Shop. To obtain the best experimental results, all of each specimen had to be chemically clean and free of all grease, oil, scale or oxidation. The following steps were taken to ensure this.

Surface Preparation

1.) Removal of all foreign matters (oil, paint, oxide, scale, etc.) from surfaces using an electric disc sanding wheel, leaving the surface smooth. This was done very carefully, especially for HY-130 which has very thick paint over its surface, since it could heat up the plate.

2.) Once the surfaces were smooth; they were cleaned with acetone to remove residue. Then they were sprayed with the thin film coating to keep them from rust and other form of oxidation until they were used.

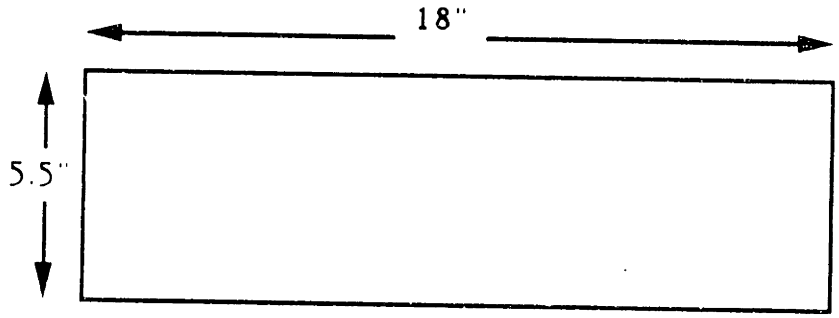

Figure 2-3: Size of Specimen

2.5.2 Welding and Side Heating Devices

The arrangement of gas metal arc welding devices and an oxyacetylene torch heating device is shown in Fig. 2-4 schematically.

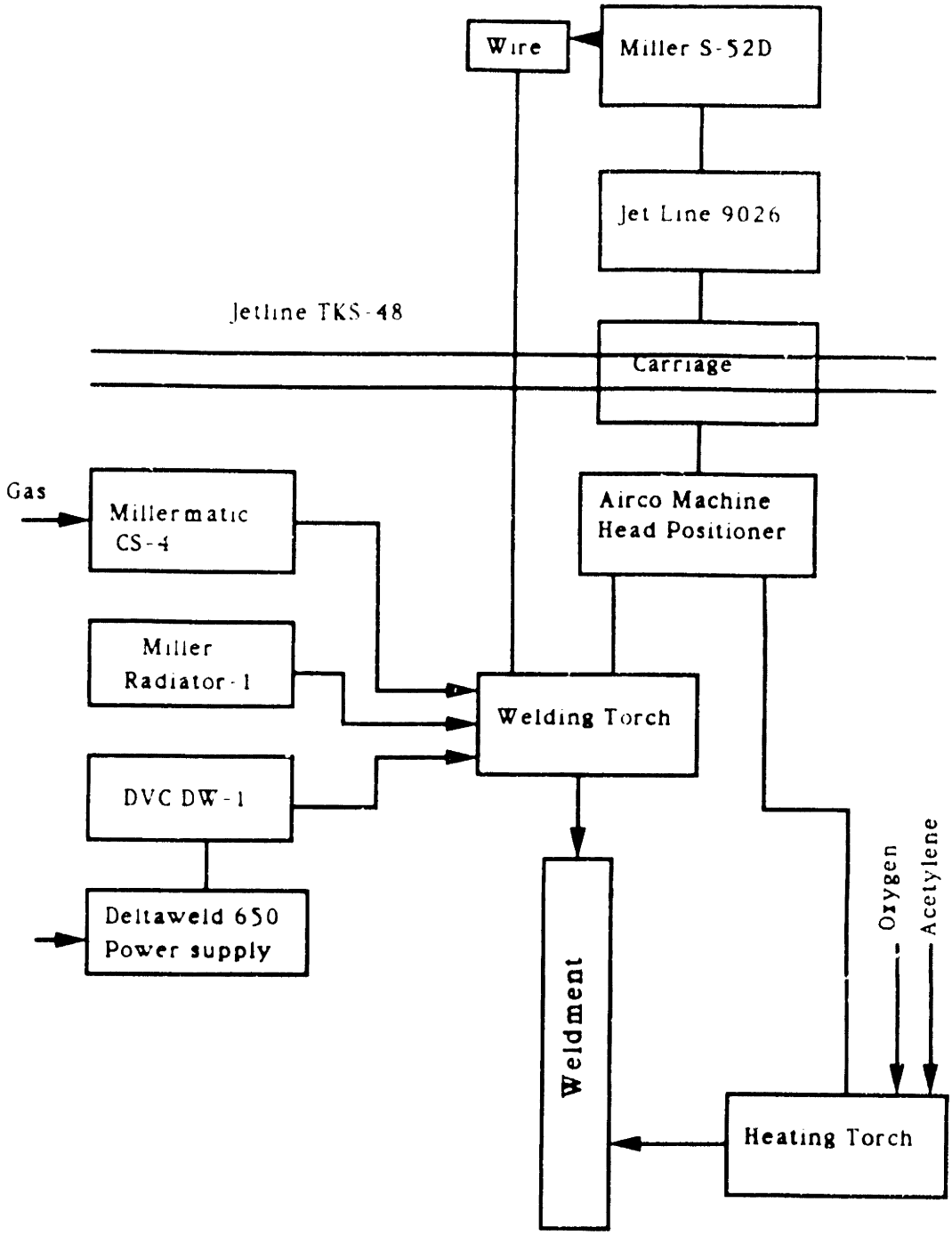

Figure 2-4: Arrangement of GMA Welding and Side Heating Devices

A Deltaweld 650 three phase constant potential dc arc welding power source with solid state control was used. It produces dc weld current and is designed to be used in conjunction with the Gas Metal Arc Welding process. The unit is capable of compensating for variation in line voltage up to 10%. The specification of this unit is shown in Table 2-XIV.

Table 2-XIV: Specification of Deltaweld 650

Rated welding current amperes at 100% duty cycle	Voltage range	Max. open circuit voltage	Input at rated load output 60 Hz Three-Phase			
			Amperes at			
			200v	230v	460v	575v
650 Amp 44 Volt	14-44	52	120	104	52	40

Filler wire was supplied by a Millermatic S-54D. This unit is a digital wire feeder that is designed to be used with a constant potential welding power source. The digital wire feeder maintains constant wire feed speed regardless of line or load variation. This unit can handle electrode wire from 0.030" to 1/8" in diameter with speed ranges from 50-785 inches per minute. A Miller DVC DW-1 remote digital voltage controller was used to preselect and monitor the output voltage of the Deltaweld 650 power supply through a feedback control mechanism. The unit can maintain the preset voltage during welding even in the presence of line and load variations within the capability of the Deltaweld 650 welding power source. A Millermatic CS-4 Controller acts as a timer and control point during weld initiation and termination. Different conditions at weld initiation and termination may be obtained by selecting parameters such as run-in speed, pre- and post-flow time of shielding gas, spot weld and burn back time.

A Miller Radiator -1 cooling system was incorporated into the Miller welding system to provide a means of controlling the temperature of the welding torch during continuous operation.

The Miller S-54D, Miller DVC DW-1 and Millermatic CS-4 are all positioned on the travel carriage which is located on the travelling beam of the Jetline TKS-48. The travel carriage provides a means of controlling both the direction and magnitude of the electrode travel speed. The system incorporates a DC voltage controlled motor, mounted on a traveling beam. The motor drives a carriage on wheels along a gear track via a sprocket on the drive shaft. The system does not contain a feed back loop. Travel rate which ranges from 0.85-150 inches per minute is determined by varying a rheostat on the front panel of the Jetline 9026 carriage speed control box. Weld direction is controlled by reversing the polarity across the DC drive motor via a switch on the control box.

The additional carriage was built and attached to the original carriage to carry the heating torch while the original carriage carried the welding torch (see Fig. 2-5). The position of the heating torch can be adjusted by sliding the additional carriage up and down or left and right. Additional bolts and nuts were used to place the heating torch ahead or behind the welding torch (see Fig. 2-6). An Airco machine head positioner was used to position the welding torch.

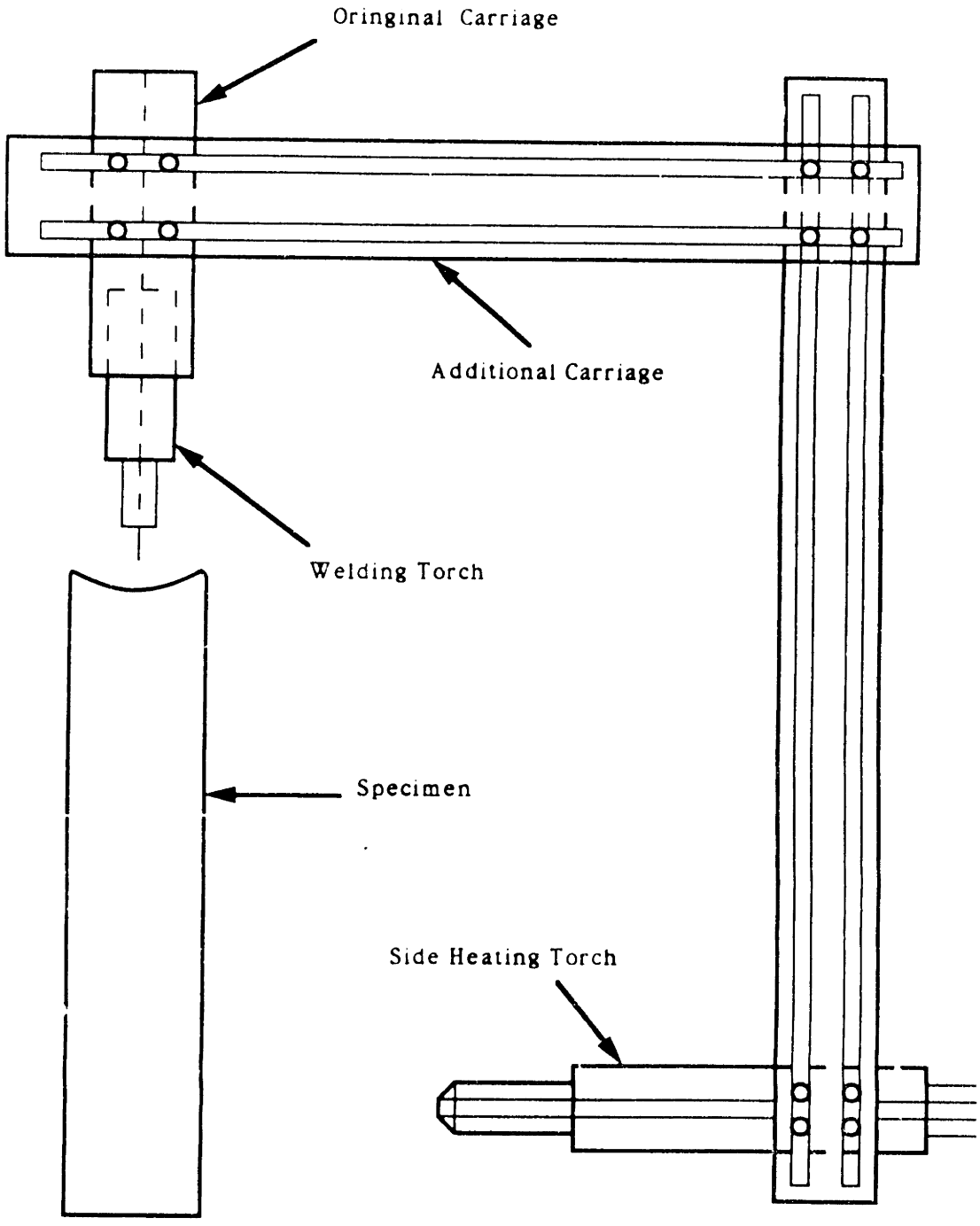

Figure 2-5: Configuration of Welding Torch and Side Heating Torch

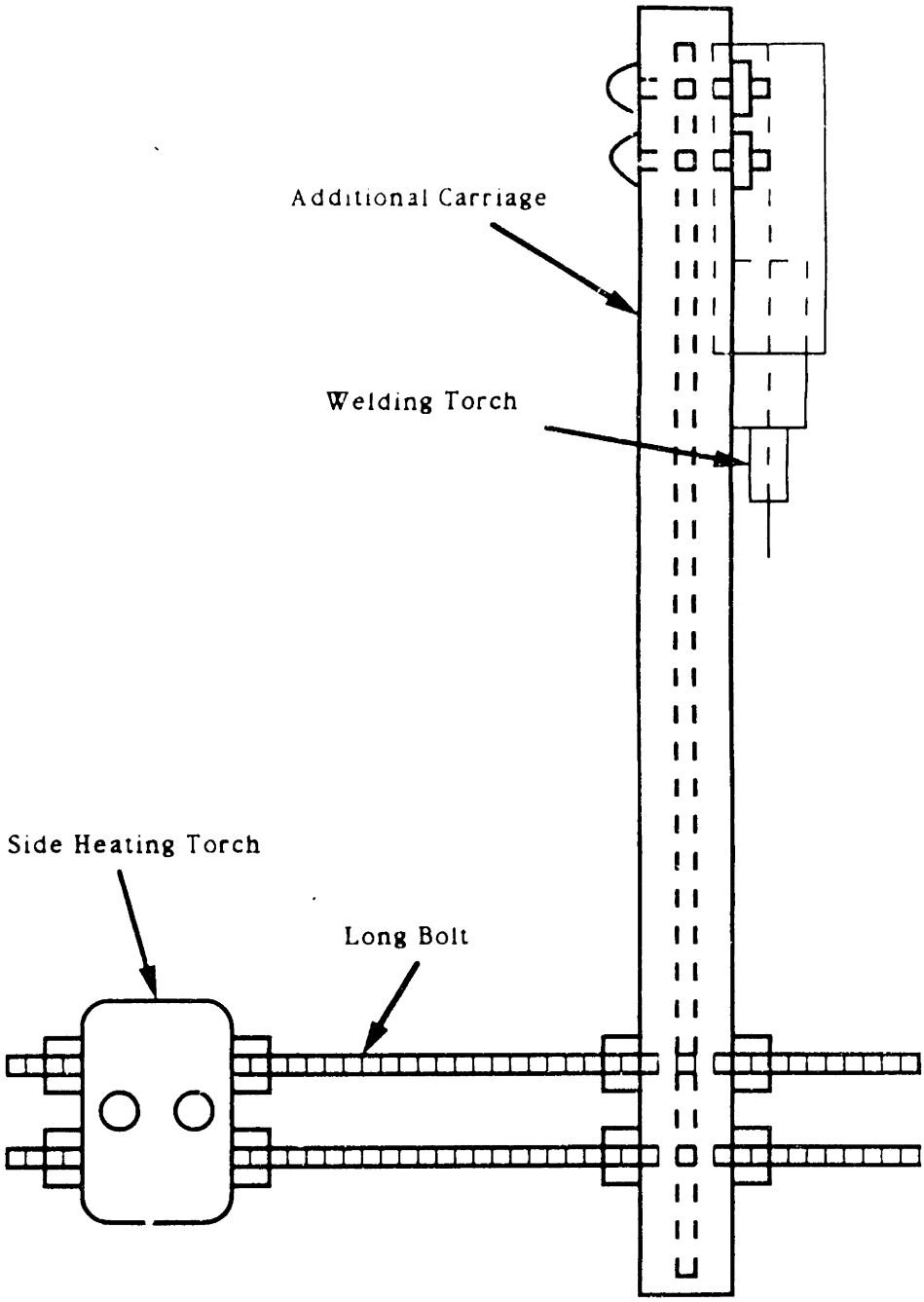

Figure 2-6: Side View of Weld Arrangement

The oxyacetylene torch used for side heating is the Airco style 4 separable type tip with an equal pressure mixer. This style number of torch provides a bulbous flame. It is normally used for light production welding and general light duty welding and brazing.

2.5.3 Thermocouple and Strain Gage

The type of strain gage selected for this investigation was XY11: two measured grids in x and y direction with 350 ohms and 0.35% error. The gage factor for this strain gage is 1.97 with 1% error. The strain gage was manufactured by Hottinger Baldwin Messtechnik Co. (HBM). It is recommended for use on steel. Since the specimens used in the experiment are only one half inch thick, this gage is considered adequate for use when compared with other special residual stress types of strain gage. Figure 2-7 shows the physical configuration of this strain gage as well as the temperature characteristic of this gage. A Z-70 quick drying room temperature curing cement was used for mounting the strain gages as recommended.

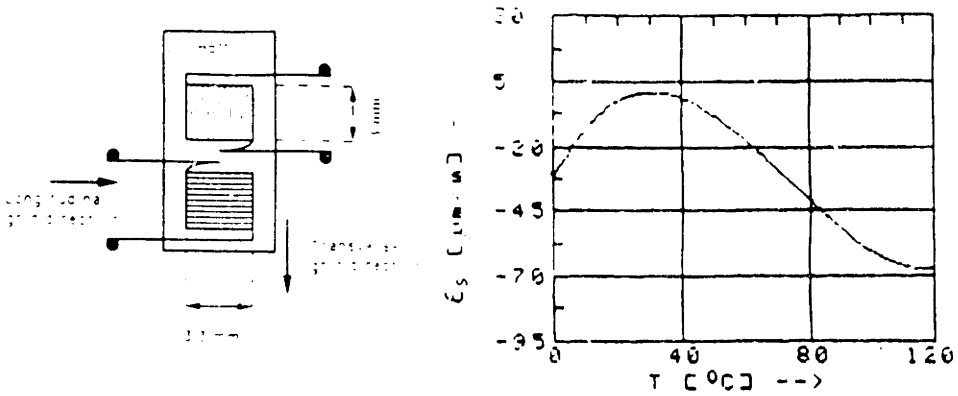

Figure 2-7: Strain Gage and Temperature Characteristic

Thermocouple type K (Cromel-Alumel) was selected to use in this experiment. It has a high temperature range from 0 °C to 1370 °C. The OMEGA Engineering type OST probe termination thermocouples with a standard 12" length and 1/8" diameter probe were ordered from the OMEGA Engineering Co. to use in this experiment. This thermocouple has a connector configuration which provides minimum error in carrying signals. Moreover, it is very simple to mount on the specimen. OMEGA BOND 101 Epoxy adhesive was used to mount these thermocouples. This adhesive has a high thermal conductivity and requires only room temperature cure. Strain gages and thermocouples were mounted on the specimen and were covered with Dow Corning 3140 RTV Coating to prevent any electrical interference and foreign matters. Glass tapes were placed over this RTV to prevent the welding flame. Both strain gages and thermocouples were connected to the data acquisition system via single conductor shielded cables and thermocouple type K compensation wires, respectively.

2.5.4 Data Acquisition System

The HP 3852A Data Acquisition and Control System was used to measure and receive signals from thermocouples and strain gages. This system was newly purchased to use in this experiment in the Ocean Engineering Welding System Laboratory. Much thought was given to the purchasing of this system. The main concern was that the system should be able to work in the welding environment which included a high noise level, high open voltage, high vibration, spark and electric shock effects, as well as dirty environment. The system receives signals through the channels of various plug-in accessories or transducers. These devices then convert physical signals into electric signals for HP 3852A to measure. A system clock built in to drive HP 3852A has a 1 msec resolution and allows data to be time-stamped and events to be timed. Figure 2-8 and Fig. 2-9 show the configuration of this system.

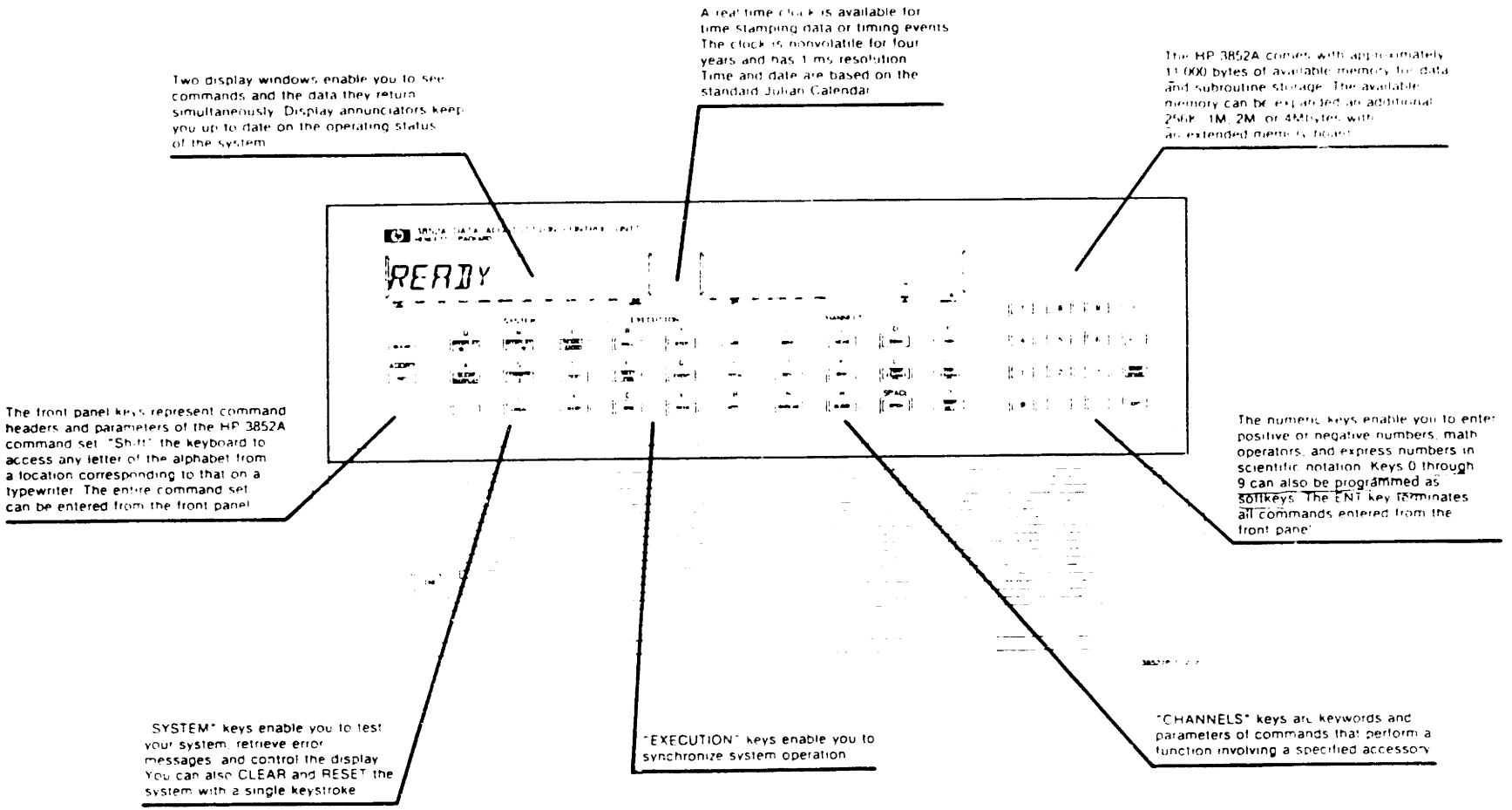

Figure 2-8: HP 3852A Mainframe Front Panel

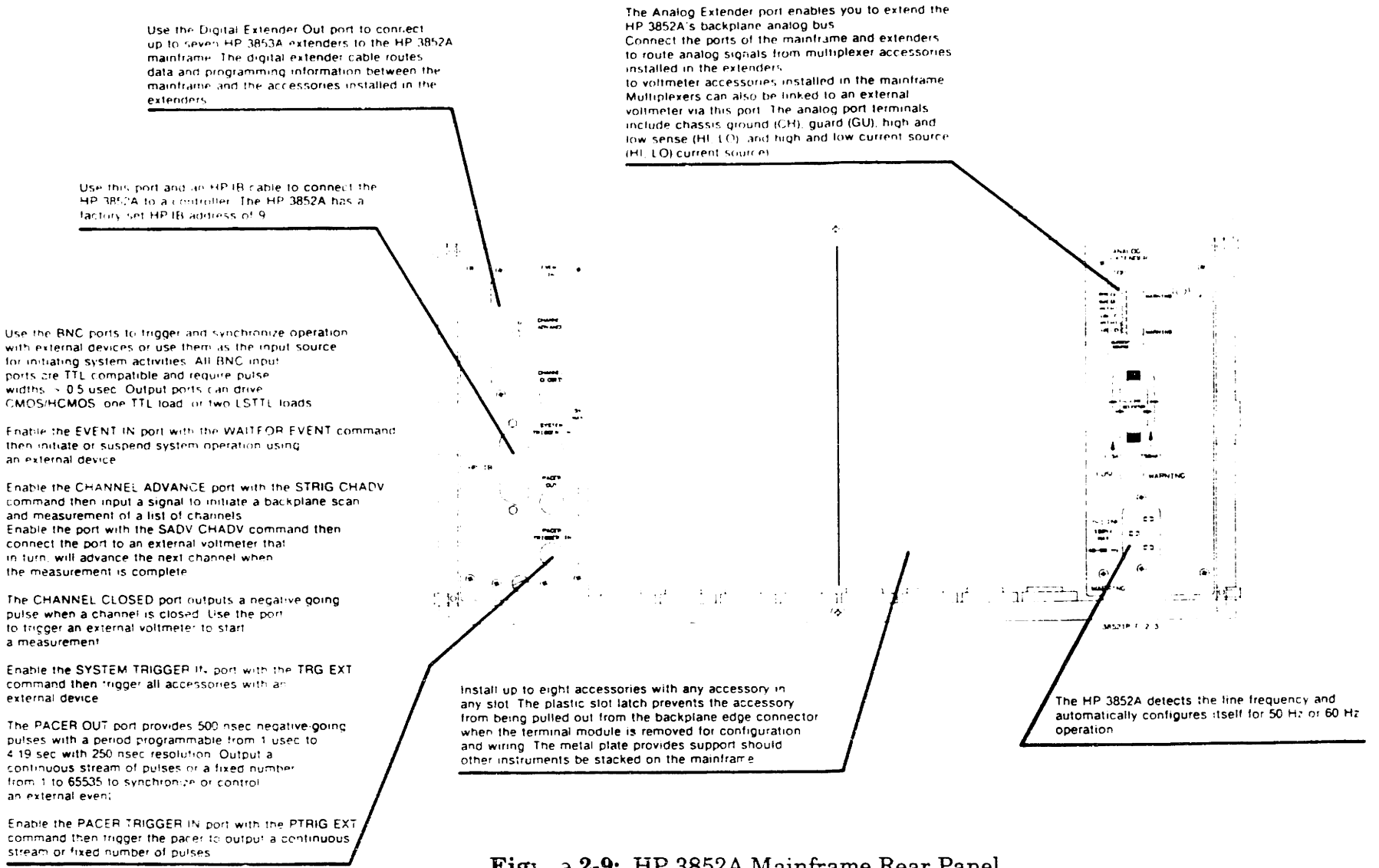

Figure 2-9: HP 3852A Mainframe Rear Panel

Three plug-in accessories were used, namely HP 44708A, HP 44718A, and HP 44701A. The HP 44708A multiplexer accessory was used for temperature measurement. Up to 20 thermocouple measurements can be made in HP 44708A. Strain measurement was made through the HP 44718A. This unit is a 10 bridge 350 ohms static strain gage relay multiplexer. It can provide up to 10 channels for strain measurement. It does not require any bridge adjustment balance which can cause errors in strain measurement. Another advantage is that the strain accuracy is independent of long term bridge excitation voltage changes because the unit will automatically measure and include this excitation voltage in the strain calculation. HP 44701A is a 5 1/2 to 3 1/2 digit integrating voltmeter. The unit is used along with HP 44708A and HP 44718A to make temperature and strain measurements. All the measurement signals from thermocouples and strain gages will first go to HP 44708A and HP 44718A respectively. The returned signals from these two units are in the form of voltage difference which will go to HP 44701A for temperature and strain calculation. The calculation data are temperature in °C and strain in microstrain.

To perform any measurement, the HP 3852A needs to be instructed by a set of commands to control the measurement directly. This can be done through a controller or on the HP 3852A itself. In this investigation the AT&T PC 6300 computer (IBM PC XT compatible) is used as a controller. The communication between HP 3852A and AT&T PC 6300 is done over the HP-IB cable. The HP Basic Language Processor Board was installed inside the AT&T PC 6300. This board is used to create a data acquisition program to enable communication between HP 3852A and AT&T PC 6300. A data acquisition program was written especially for use in this experiment using Advanced Basic Language supported by the HP Basic Language Processor Board. Details of the program are listed in Appendix A. This program first instructs HP 3852A to make an initial measurement and then waits for a start command. When the welding process starts, the program will send commands to HP 3852A to take measurements

during and after welding. At the same time it will receive the measurement data back from HP 3852A and store these data in an output file. Fig. 2-10 shows the schematic diagram of the system

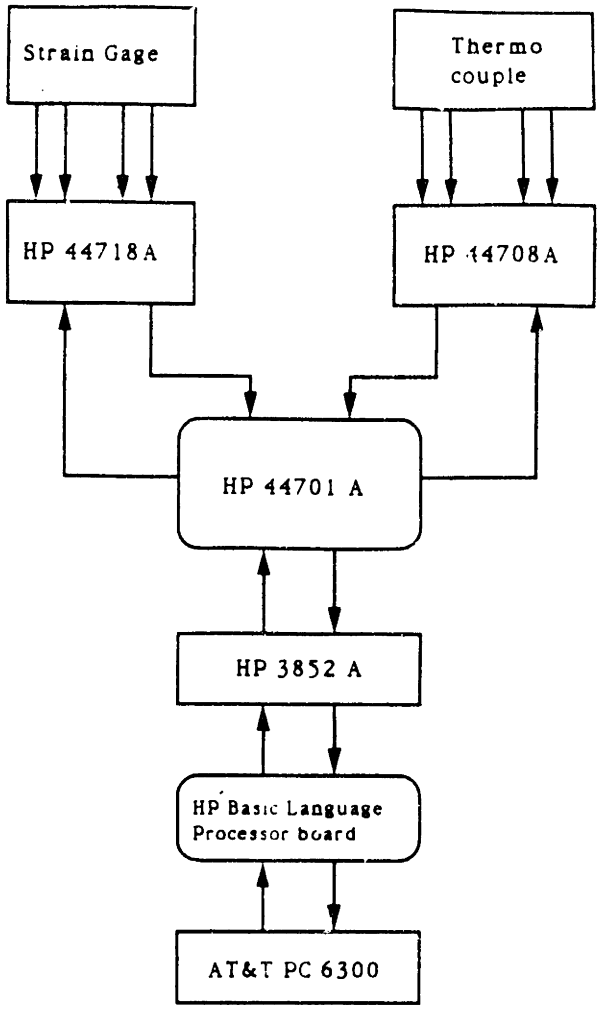

Figure 2-10: Schematic Diagram for Data Acquisition System

2.5.5 Experimental Results

The first three experiments were conducted on two low carbon steel plates with 12"x5.5" and 18"x5.5", 0.5 inches in thickness and one HY-130 steel plate with 12"x6", 0.5 inches in thickness. This set of experiments was performed to establish appropriate welding conditions and welding machine settings for a further series of experiments. In addition, we also wanted to test and verify the newly acquired Data Acquisition and Control System as well as the data acquisition program. The problem we encountered in this set of experiments was that we did not get a proper bead-on-edge weld on the specimen. After careful investigation, it was found that the problem could be solved by ensuring that the welding torch was properly aligned with the edge of the plate. The data acquisition program had problems with the recorded time that was needed to acquire data from thermocouples and strain gages. It was debugged and re-run on the third experiment of this set. This time it ran smoothly. After this set of experiments another set of three experiments was conducted.

2.5.5.1 Bead-on-Edge Welding Without Side Heating

This set of experiments was conducted on low carbon steel, HY-100, and HY-130 without providing additional side heating. Four strain gages and four thermocouples were mounted on the surface of each experiment as shown in Fig. 2-11.

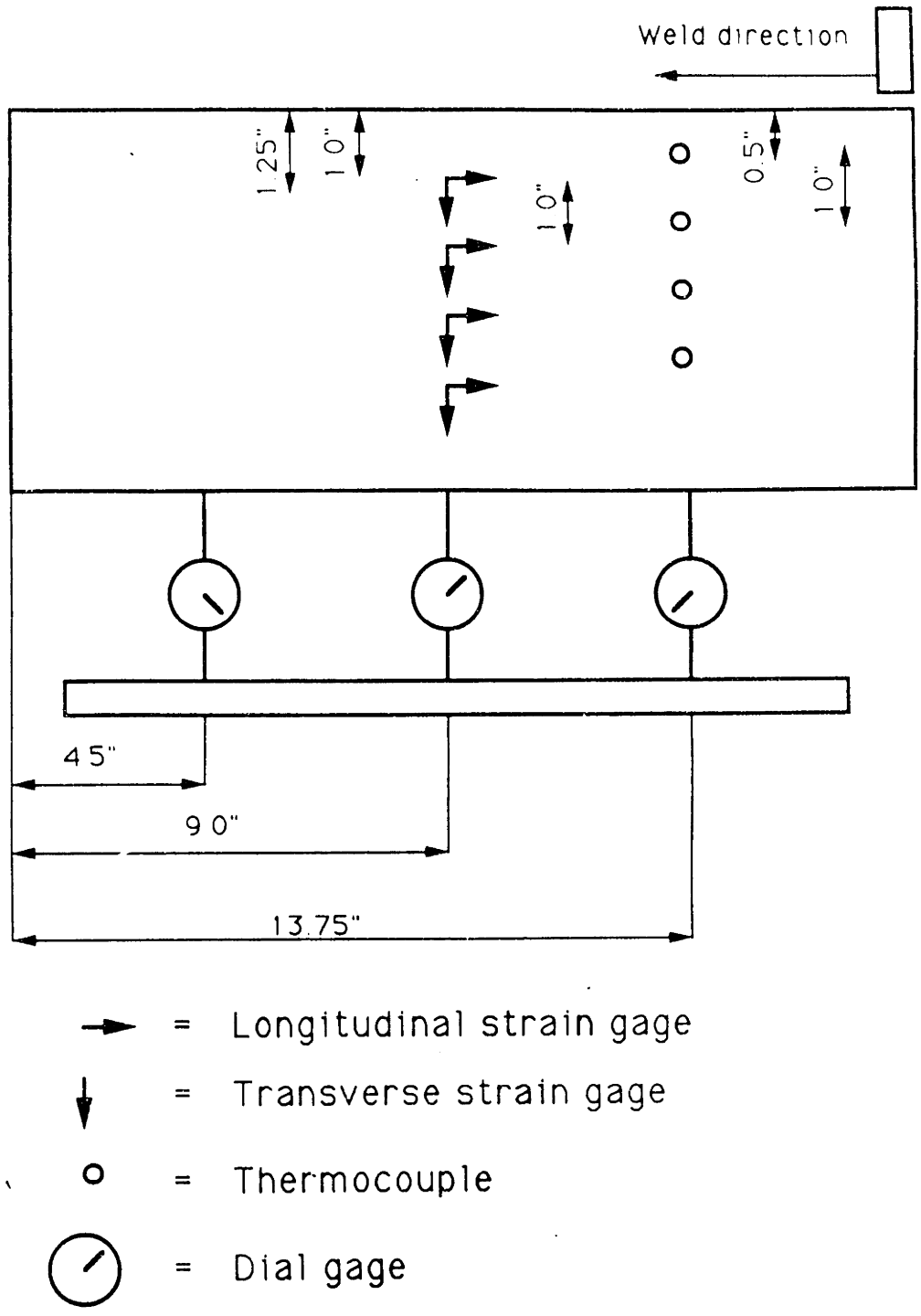

Figure 2-11: Thermocouple and Strain Gage Arrangement

Three dials gages were placed at the lower part of the specimen to read the distortion at three different locations as shown in Fig. 2-11. The welding conditions and settings for the Millermatic Gas Metal Arc Semi Automatic Welding machine were as follows:

Material	Low carbon steel, HY-100, HY-130
Dimension	18"x5.5" with 0.5 inches thick
Filler wire	E70S
Transfer Type	Spray
Gas Flow Rate	30 cfh of Argon 98%, 2% O_2

Millermatic Semi Automatic Welding Machine Setting

Pre-Flow Time	1 sec.
Run-in Speed	20 sec.

(Causing a selected wire feed rate to be maintained from the completion of pre-flow time to arc initiation)

Welding Mode	Continuous
Time Range	High (2.5 -5 sec.)
Burn Back Time	0.05 sec.

(Controlling the amount of time weld power is available at the electrode wire after stop feeding wire)

Post Flow Time	2 sec.
Miller DVC DW-1	25 Volts
Wire feed speed	375 inches per minute

Carriage Control

Type of Control	Manual
Weld Speed	0.200 inches per second
Polarity	DCRP
Power Supply	25 V/ 230 Amp.

(Ampere is the average value reading during welding)

After the welding process was completed, these specimens were left to cool

down to room temperature to ensure full development of residual stresses. Then all of the specimens were cut to measure the residual stresses using stress relaxation technique. This technique is based upon the principle that strains created during unloading are elastic even when the material has undergone plastic deformation. Therefore, it is possible to determine residual stresses without knowing the history of the material. These residual stresses were calculated from the difference between the measured strain before and after cutting. The 2-D plane stress problem was assumed and only the in-plane deformation was considered. Based on these assumptions, the following formulas were used to calculate residual stresses:

$$\sigma_x = -\frac{E}{1-\nu^2}(\varepsilon_x + \nu\varepsilon_y) \tag{2.1}$$

$$\sigma_y = -\frac{E}{1-\nu^2}(\varepsilon_y + \nu\varepsilon_x) \tag{2.2}$$

where

$\varepsilon_x = -\varepsilon_x'$

$\varepsilon_y = -\varepsilon_y'$

ε_x' and ε_y' are elastic strain components of the residual stress.

E = Young's modulus.

ν = Poisson's ratio.

Figures 2-12 to 2-14 show the temperature profile observed at four measuring points along the width of the plate for low carbon steel, HY-100, and HY-130. The arc passed the mid-length of the specimen 30 seconds after the welding was begun and completed the pass in 60 seconds. The horizontal coordinate represents time in seconds from the commencement of the welding process. The vertical coordinate is the temperature value in °C. Near the weld line (0.5 inches) the temperature is around 300-350 °C. A rapid cooling rate can be observed in this region. A slow cooling rate can be observed away from the weld line. No dramatic increases of temperature occurred in this region during the welding process. Below 100 °C the difference in the cooling rate at different

locations is almost negligible for low carbon steel but there is a slight difference for HY-100 and HY-130. After 500 seconds, the temperature distribution has become more or less uniform throughout the plate.

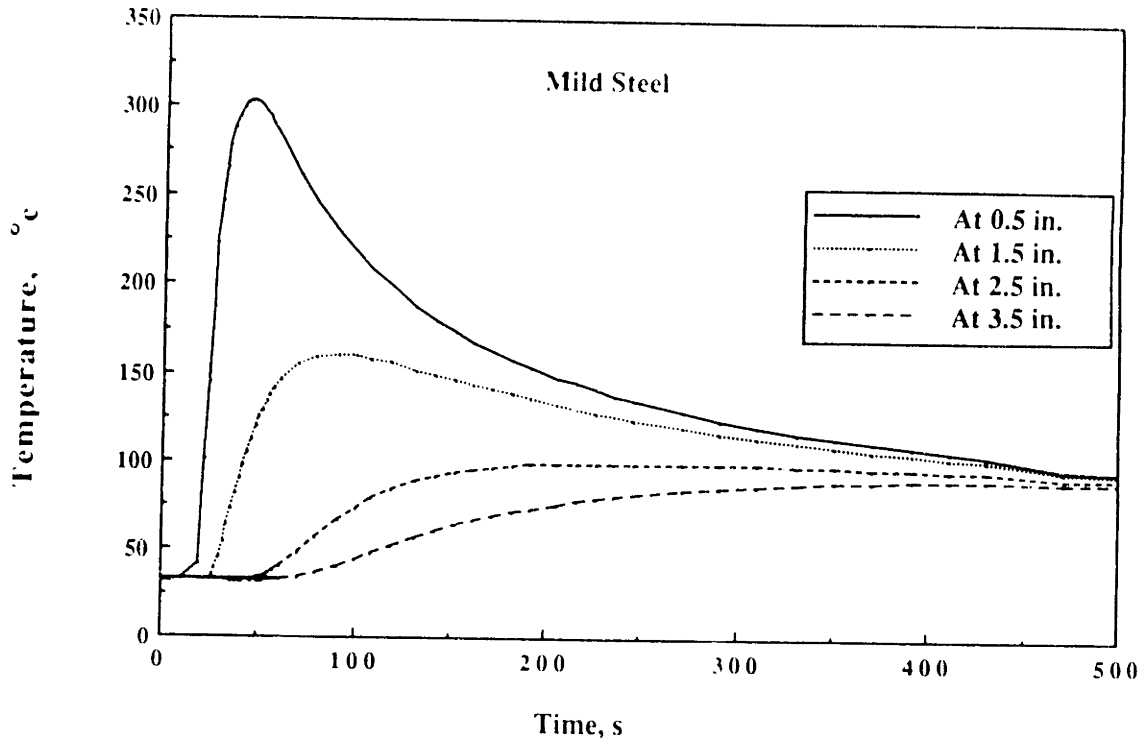

Figure 2-12: Temperature Profile for Low Carbon Steel

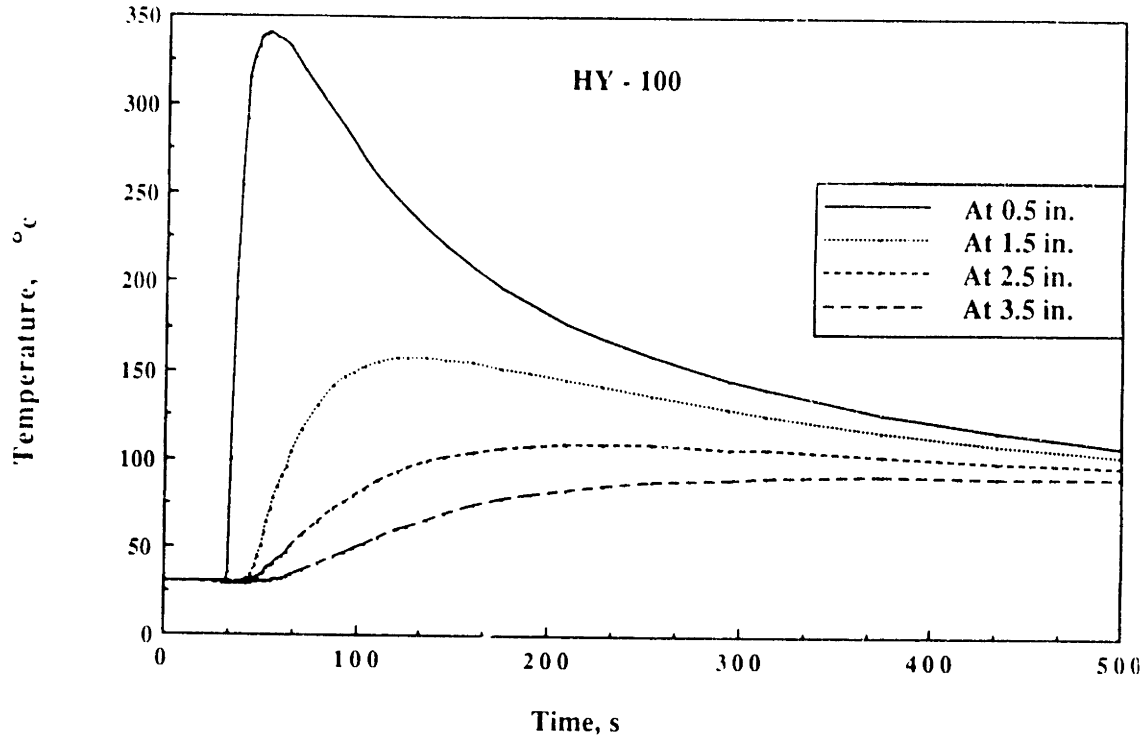

Figure 2-13: Temperature Profile for HY-100

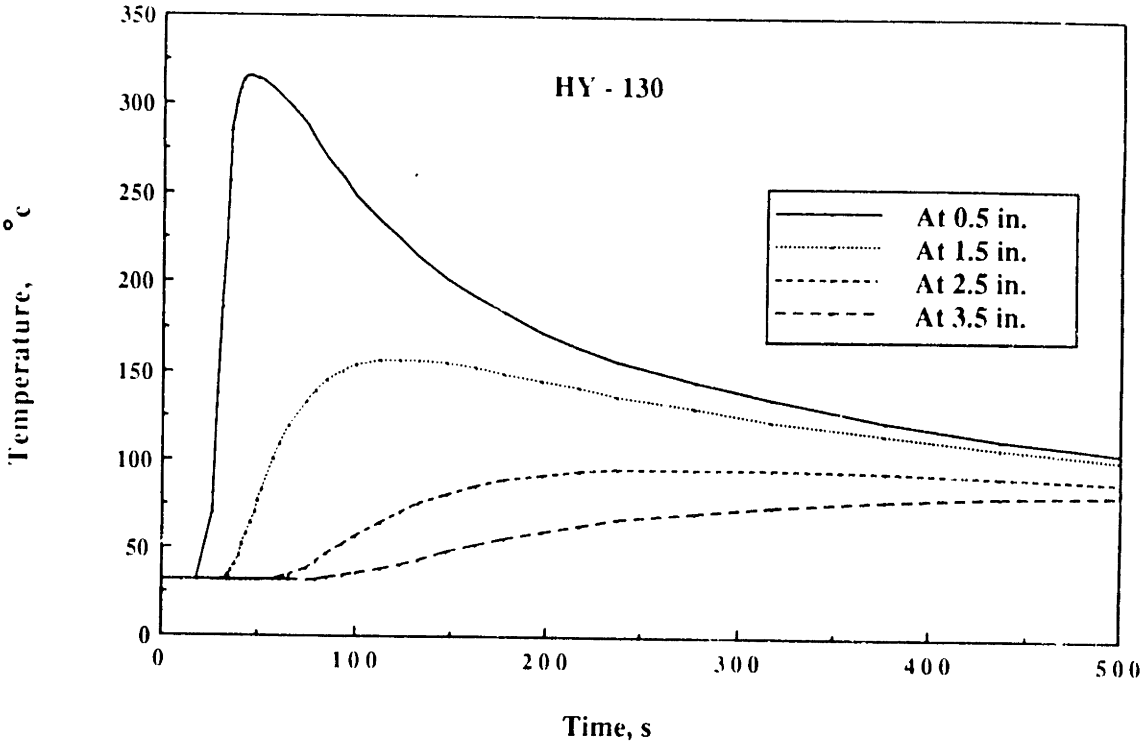

Figure 2-14: Temperature Profile for HY-130

The history of both longitudinal and transverse strain distribution observed at eight measuring points along the width of the plate is shown in Figs. 2-15 to 2-20. The horizontal coordinate is the log scale time in seconds while the vertical coordinate is the linear scale for strain in microstrain. The overall observed time for running the Data Acquisition and Control System to collect these data is 8 hours. Figures 2-21 to 2-26 show the longitudinal and transverse strain profile up to the time when differences between the cooling rate at different locations is small. A large strain change can be observed near the weld line. At locations away from the weld line the strain becomes uniform when the temperature distribution becomes uniform. The order of strain for both longitudinal and transverse strain near the weld line is about 1,500 and 1,400 microstrain for low carbon steel, 1,800 and 1,500 microstrain for HY-100, and 1,850 and 1,250 microstrain for HY-130 respectively.

For low carbon steel, on gage #1, at 1 inch from the weld line, tensile longitudinal strains were produced when the welding arc approached the gage. These strains later changed to compressive after the specimen was cooled down to room temperature. Similar phenomena occurred to the transverse strain. Compressive transverse strains were observed at 2.25 inches and 3.25 inches from the weld line as the welding arc approached the gages. These strains later changed into tensile transverse strains. Similar behavior of strain history also occurred to HY-100. For HY-130, a large compressive transverse strain occurred at 1.25 inches away from the weld line and then changed into tensile transverse strain.

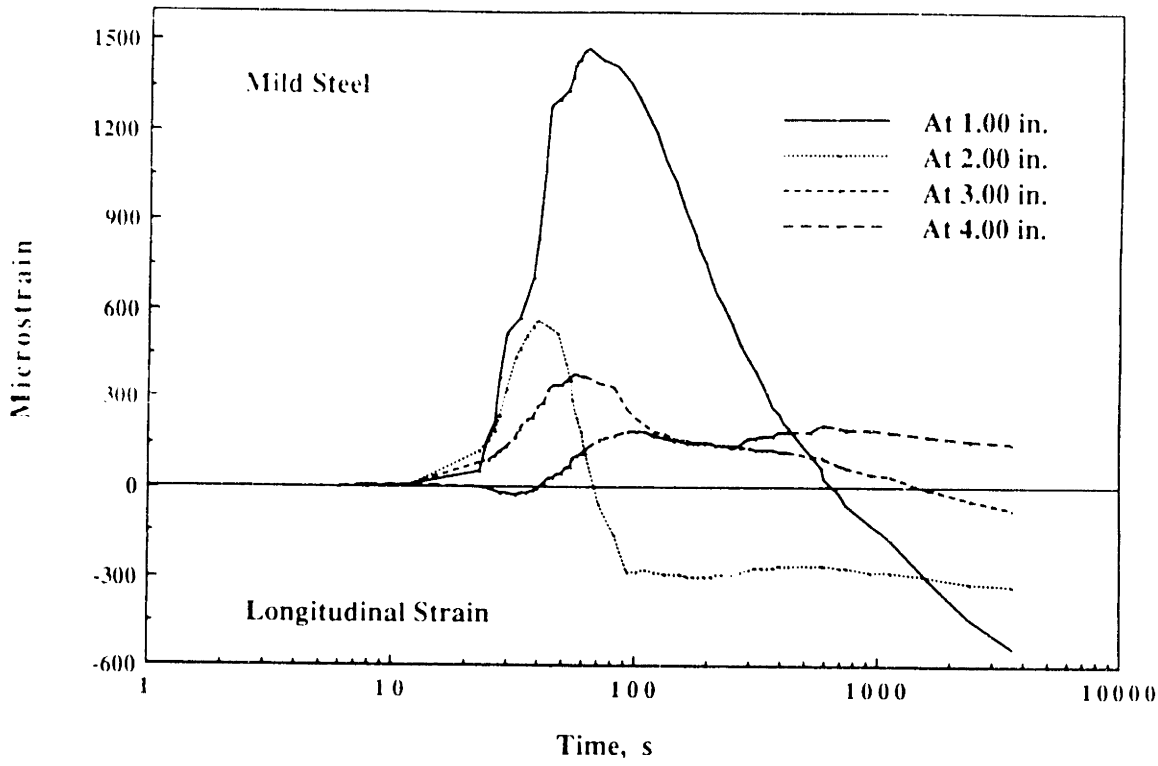

Figure 2-15: Transient Longitudinal Strain Profile for Low Carbon Steel

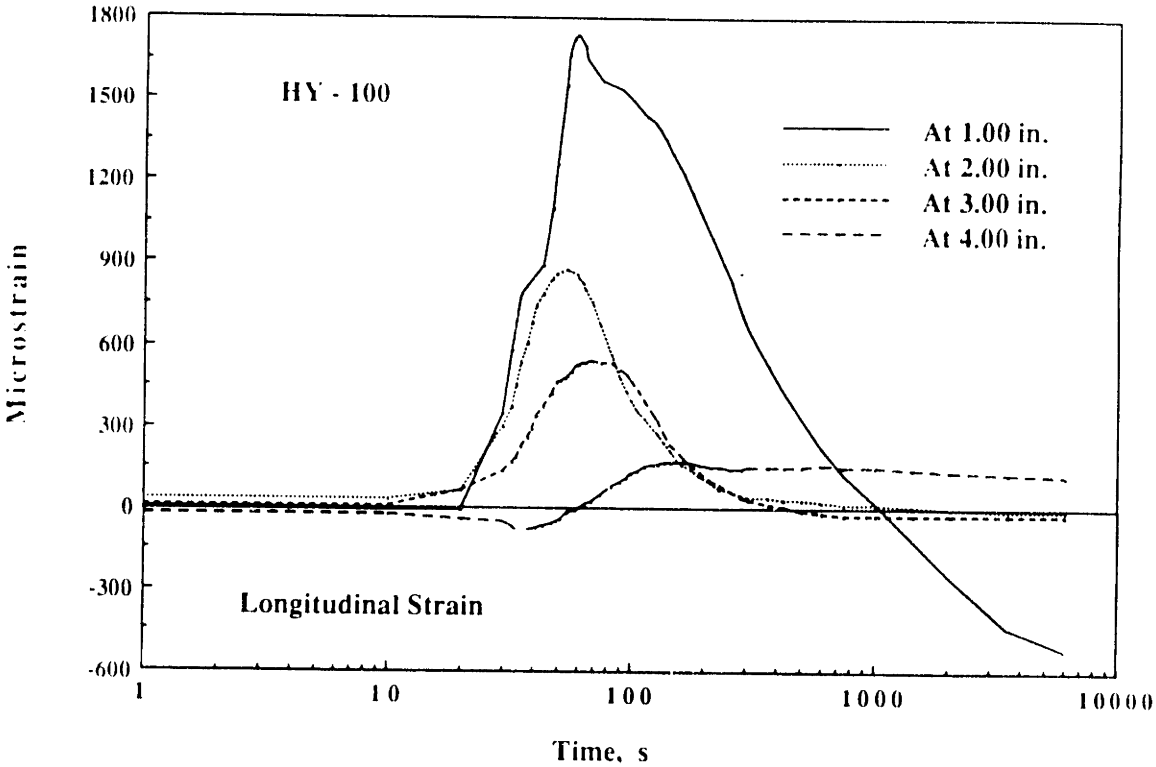

Figure 2-16: Transient Longitudinal Strain Profile for HY-100

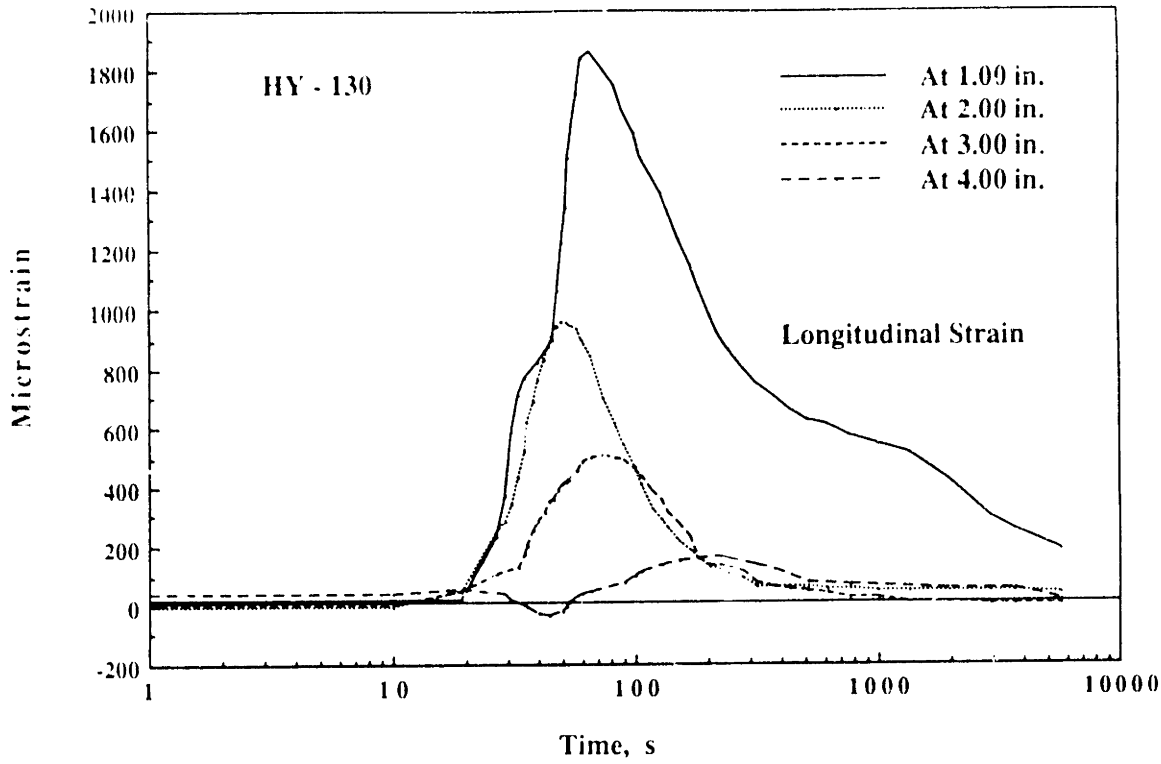

Figure 2-17: Transient Longitudinal Strain Profile for HY-130

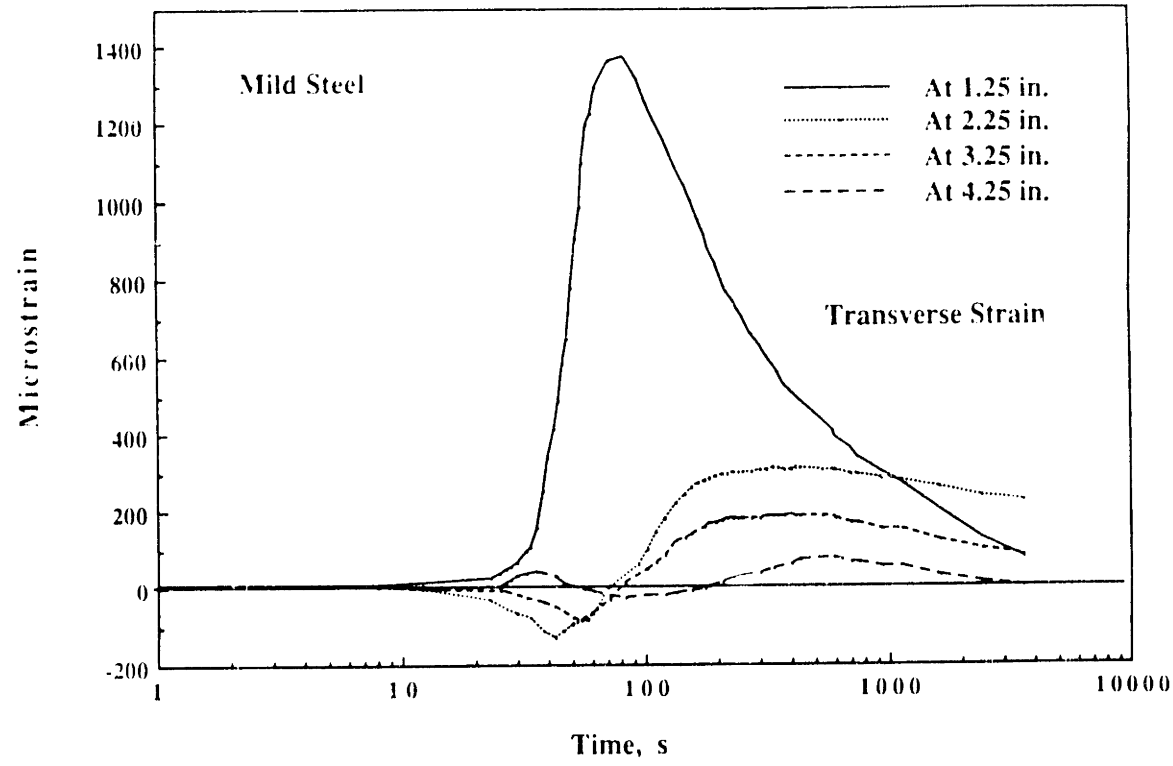

Figure 2-18: Transient Transverse Strain Profile for Low Carbon Steel

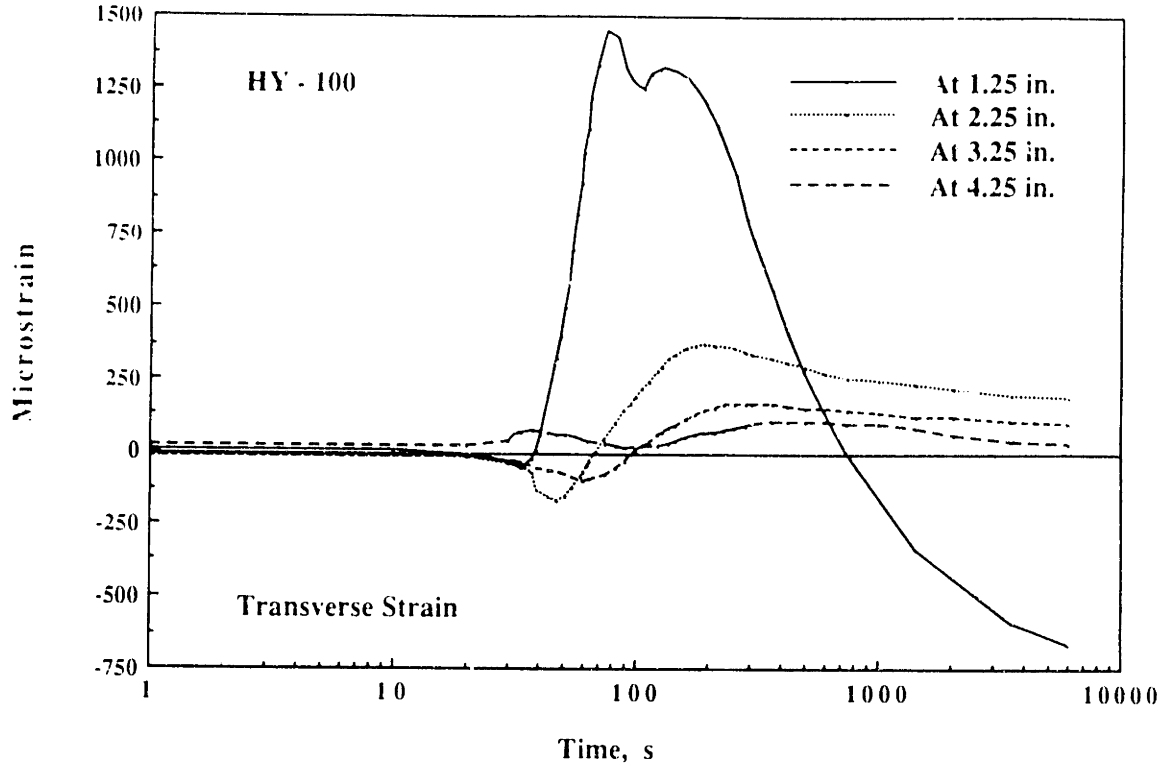

Figure 2-19: Transient Transverse Strain Profile for HY-100

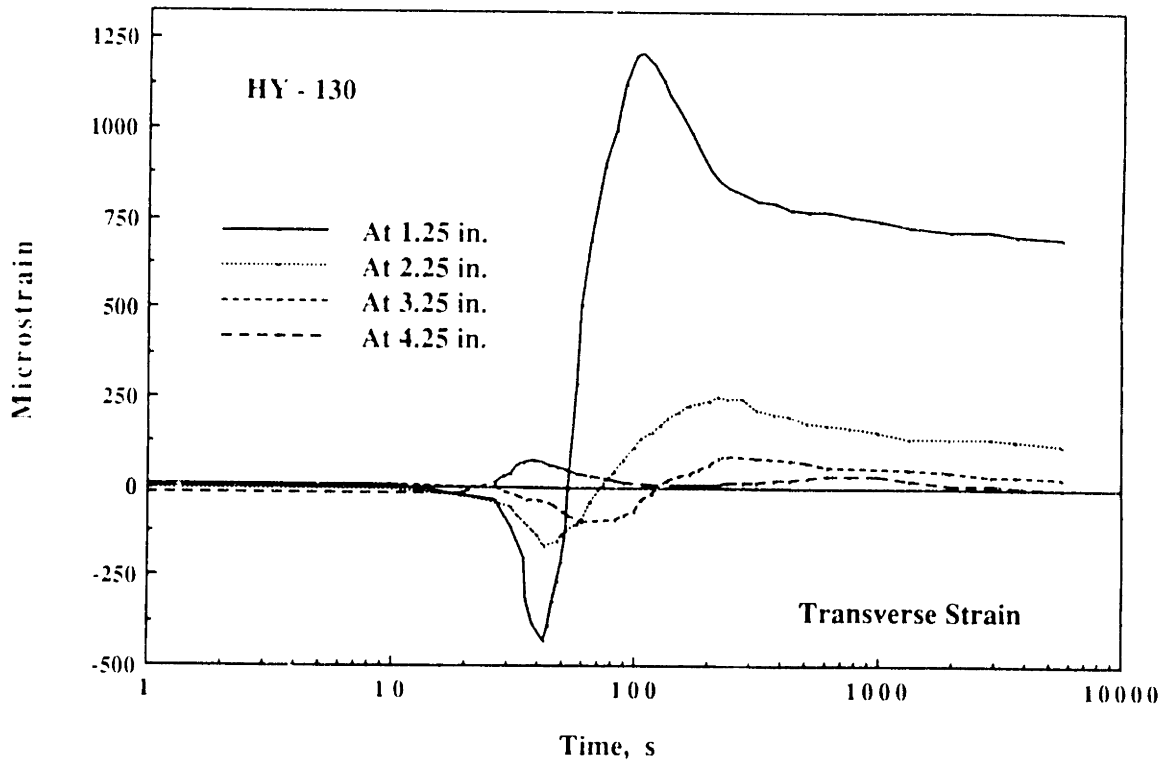

Figure 2-20: Transient Transverse Strain Profile for HY-130

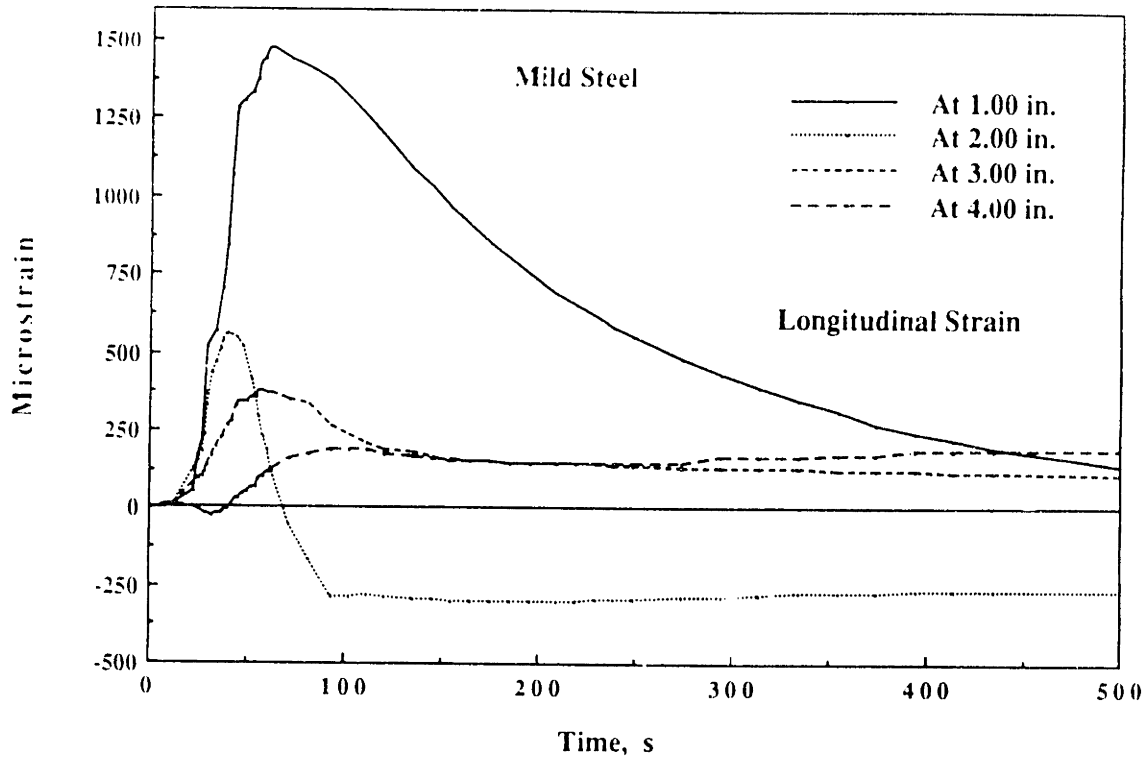

Figure 2-21: Transient Longitudinal Strain Profile for Low Carbon Steel

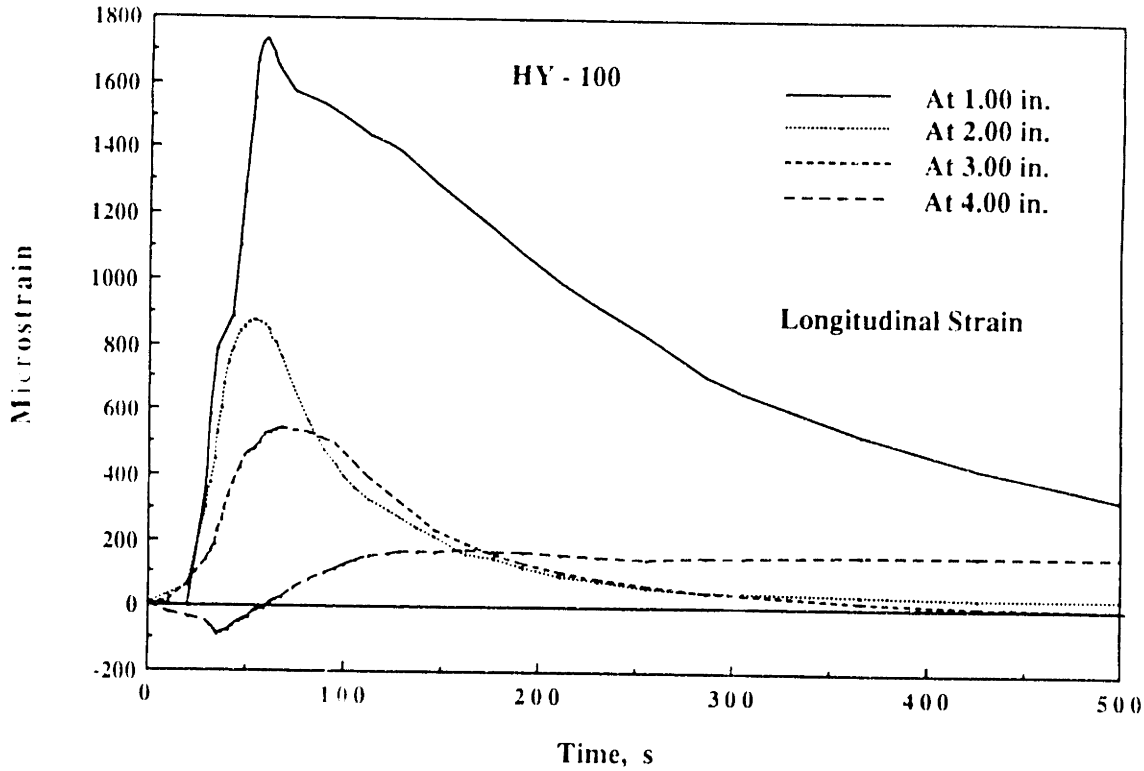

Figure 2-22: Transient Longitudinal Strain Profile for HY-100

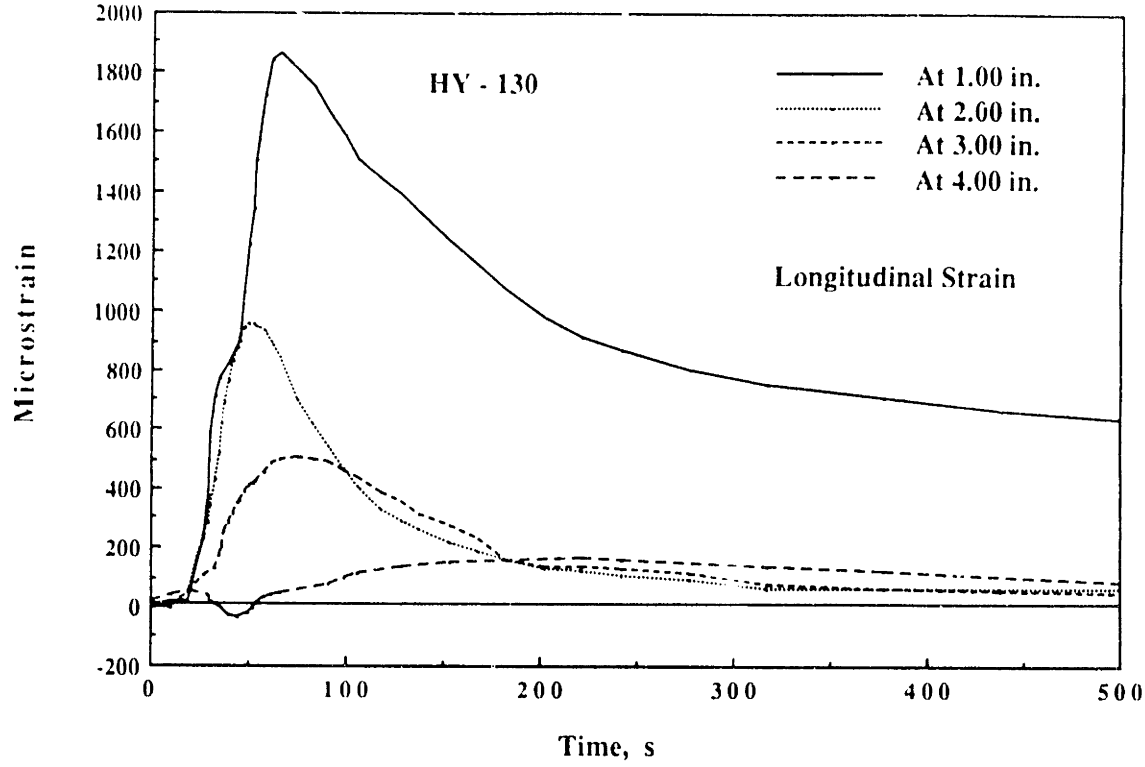

Figure 2-23: Transient Longitudinal Strain Profile for HY-130

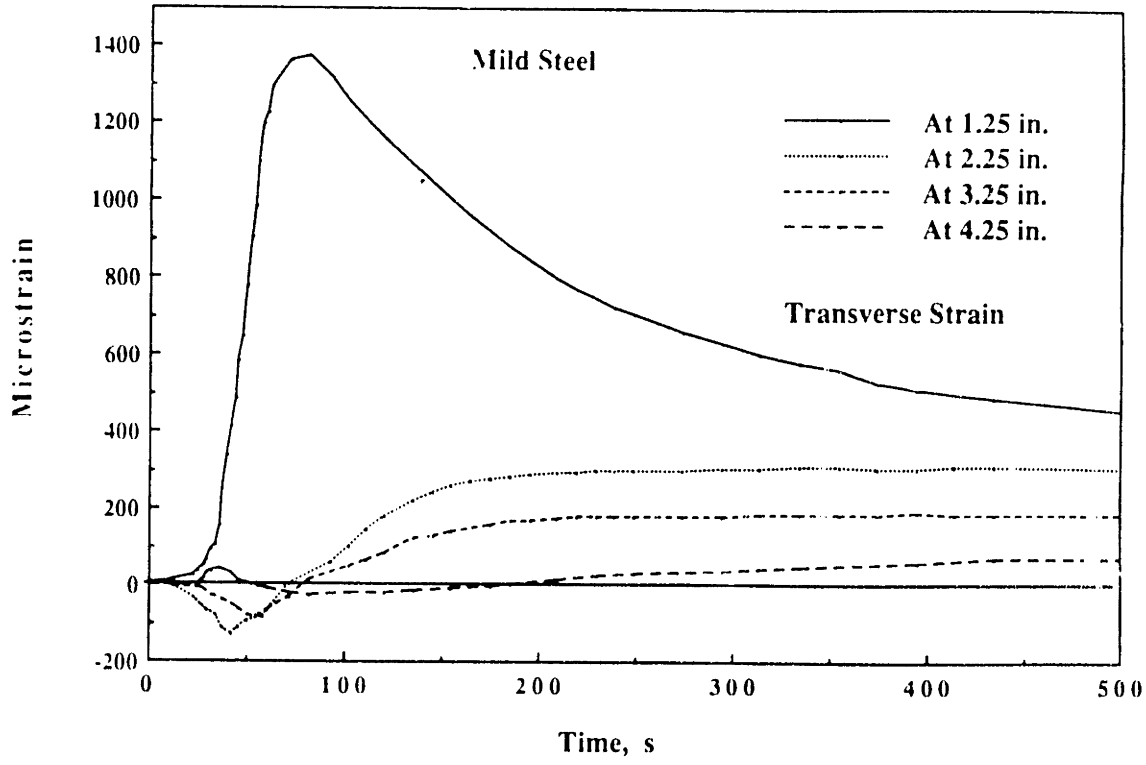

Figure 2-24: Transient Transverse Strain Profile for Low Carbon Steel

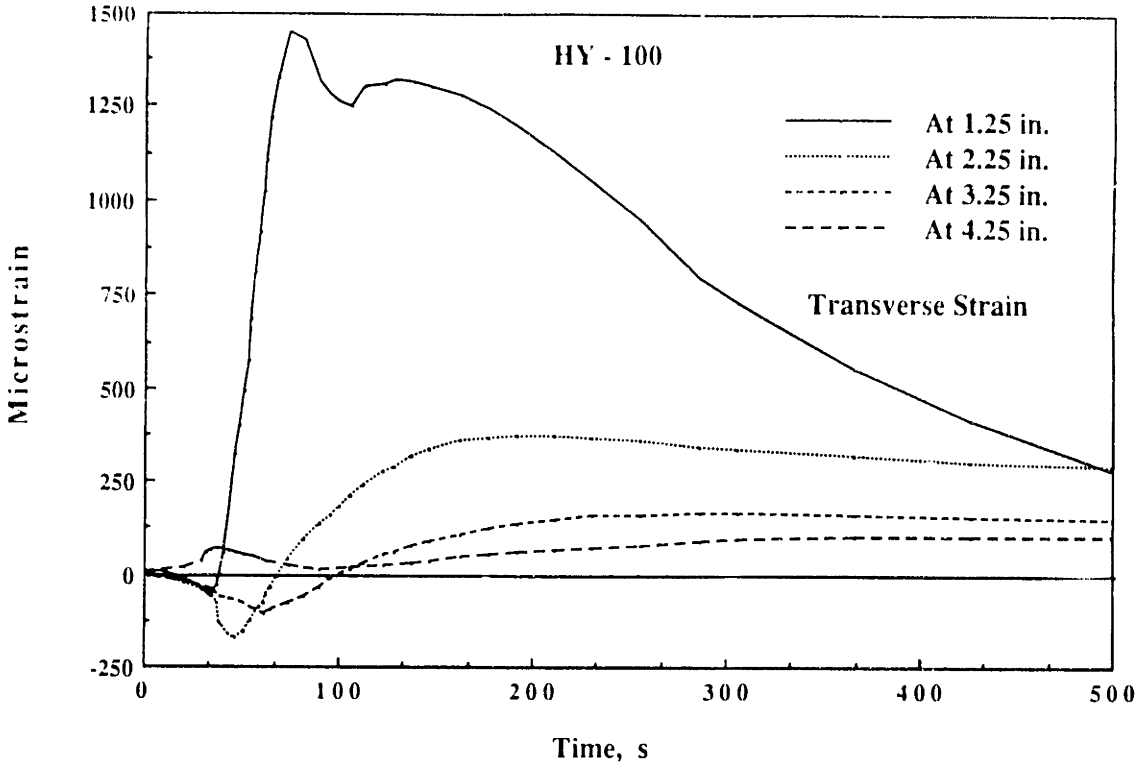

Figure 2-25: Transient Transverse Strain Profile for HY-100

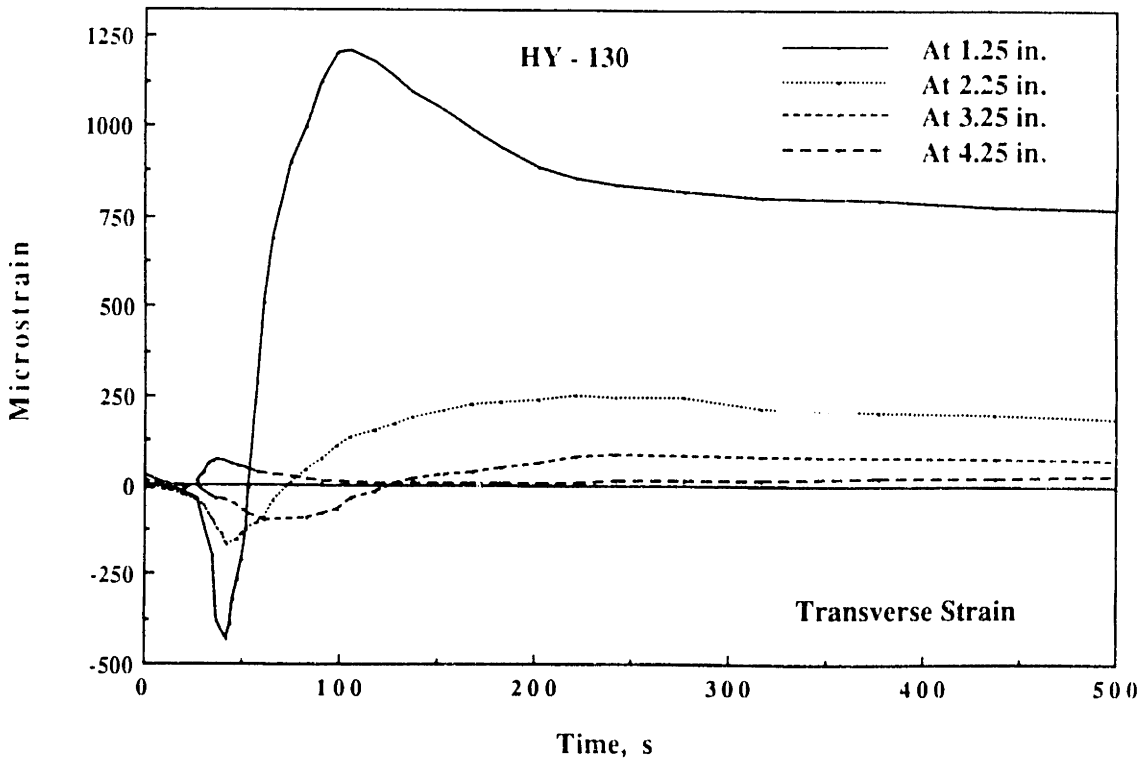

Figure 2-26: Transient Transverse Strain Profile for HY-130

The distortion history is shown in Figs. 2-27 to 2-29 for low carbon steel, HY-100, and HY-130 at three different locations. The bending behavior of the specimen can be described from these figures as follows. At the early stage of welding the specimen bent upward. This was due to expansion at the upper part from the welding heat source. After the welding was completed, the specimen cooled down and the weld metal shrank along the entire weld length. It then bent downward and continue to bend through its original position. This phenomenon suggests that a method of reducing distortion could be devised. There are differences in maximum magnitude of distortion during welding and after it is completed. Low carbon steel has lower distortion during welding than HY-100 and HY-130 but higher distortion than HY-100 and HY-130 when the plate cools down. This also suggests that it should be easier to control distortion during welding for low carbon steel than it is for HY-100 and HY-130. Low carbon steel also has a higher rate of change of distortion after welding than HY-100 and HY-130. Therefore, any action to control distortion after welding has to take place in a shorter time for low carbon steel than for HY-100 and HY-130.

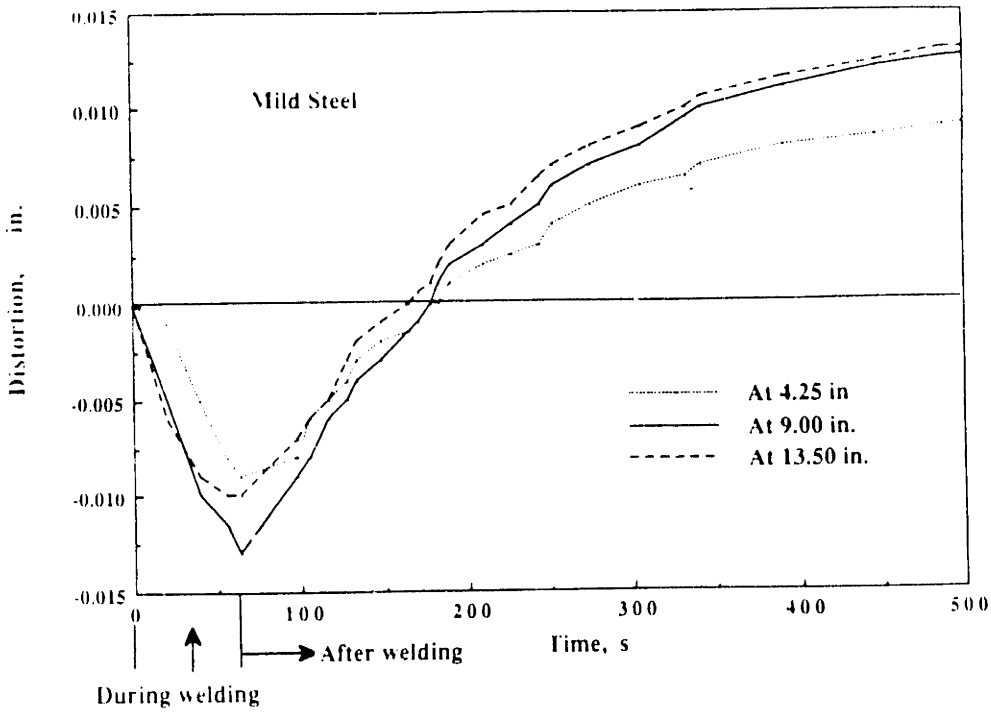

Figure 2-27: Distortion Profile of Low Carbon Steel

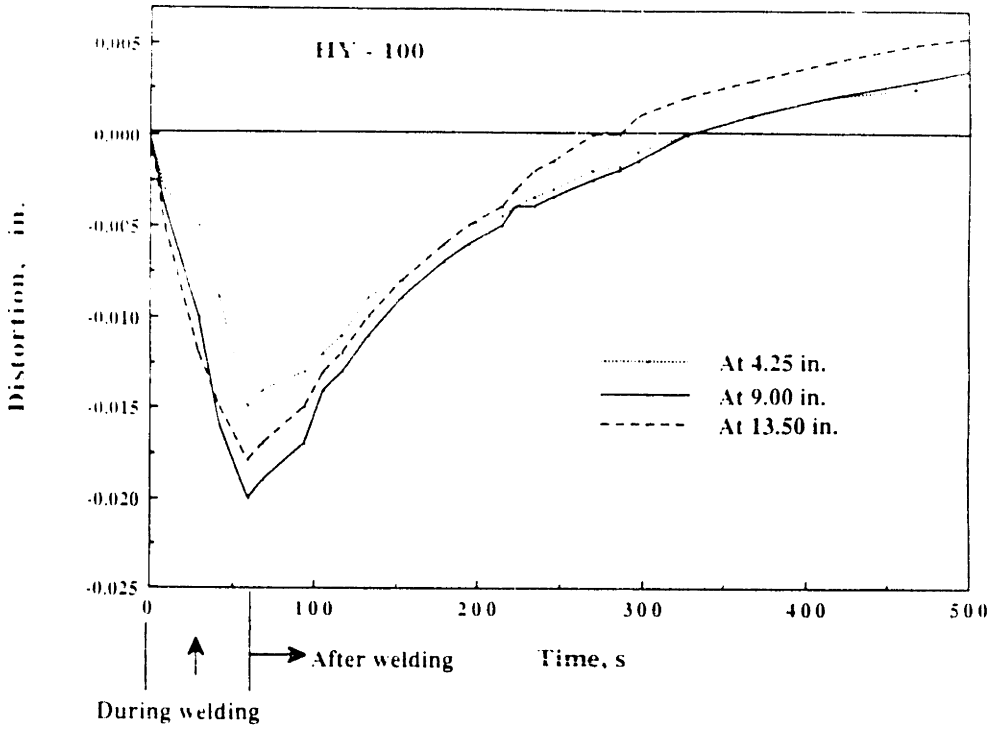

Figure 2-28: Distortion Profile of HY-100

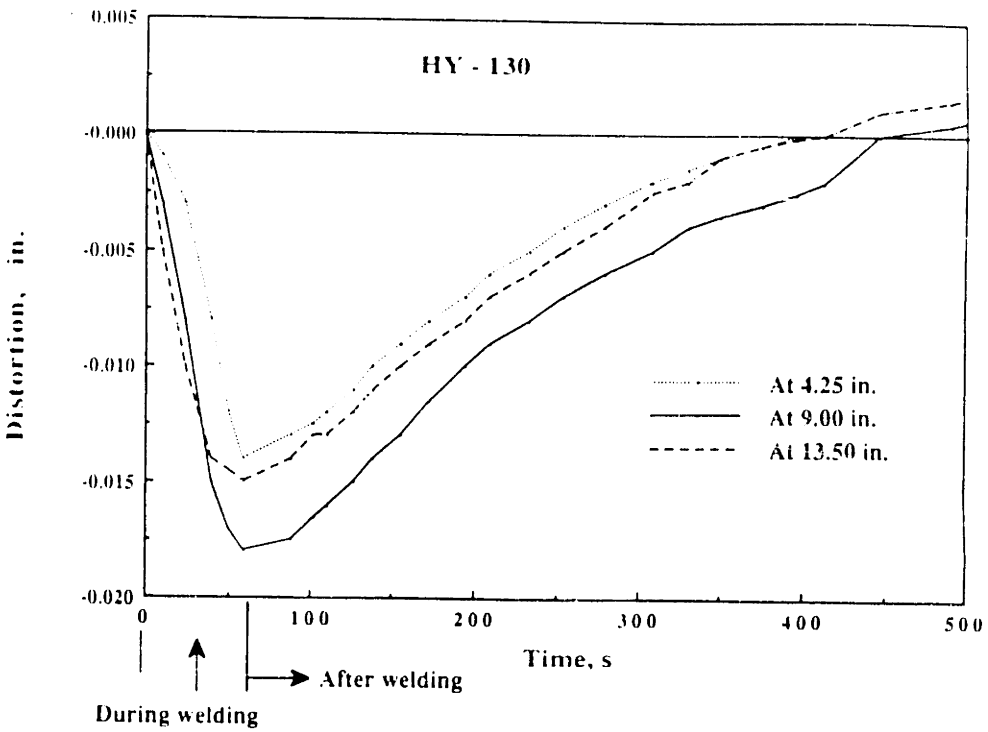

Figure 2-29: Distortion Profile of HY-130

The residual stress distribution along the width of the plate at eight measuring points is shown in Figs. 2-30 to 2-35. The longitudinal residual stress distribution shown in Figs. 2-30 to 2-32 can be interpreted as resulting from the shrinkage of the weld which causes high tensile residual stress in regions near the weld and moderately low compressive residual stresses in regions away from the weld. A higher magnitude of longitudinal residual stress occurs in HY-100 and HY-130 than in low carbon steel. This longitudinal residual stress can get as high as the yield strength in mild steel or 50-60% of the yield strength in HY-100 and HY-130 at locations very close to the weld line.

The transverse residual stress distribution is shown in Figs. 2-33 to 2-35. For low carbon steel one can observe the compressive residual stress near the weld line and the tensile residual stress away from the weld line. This is the opposite of what happens for the longitudinal residual stress. For HY-100 and HY-130 the tensile residual stresses are observed in the region near the weld line and compressive residual stress occurs away from the weld. The magnitudes of these transverse residual stresses are much less than those of longitudinal stresses.

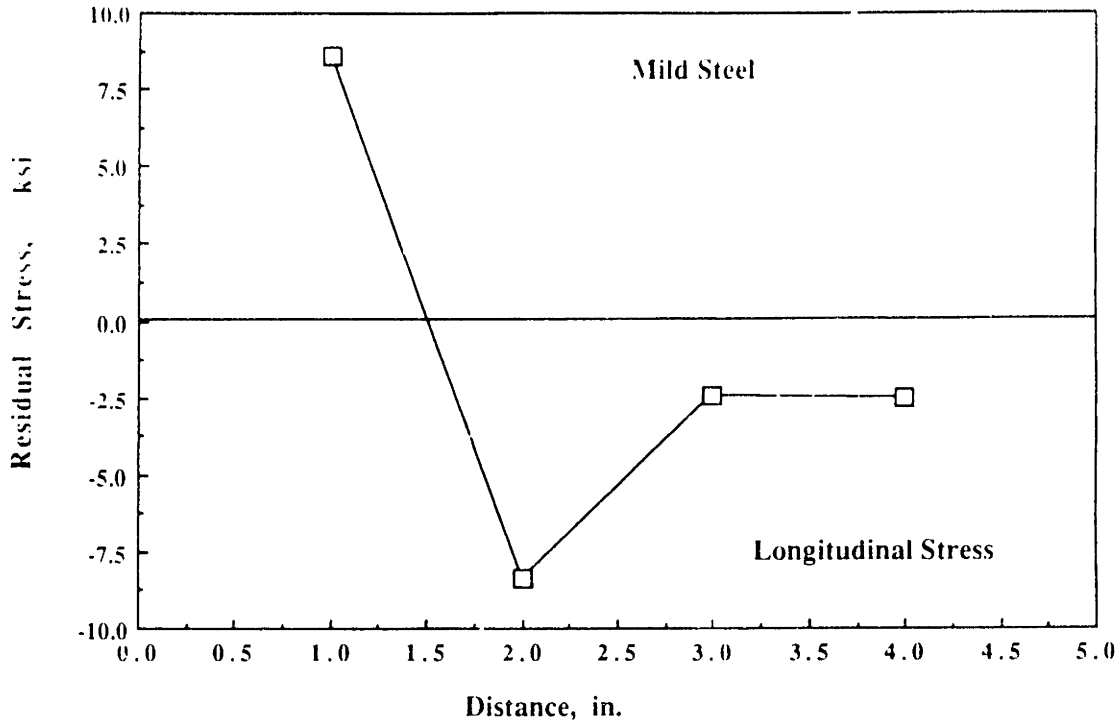

Figure 2-30: Longitudinal Residual Stress Distribution for Low Carbon Steel

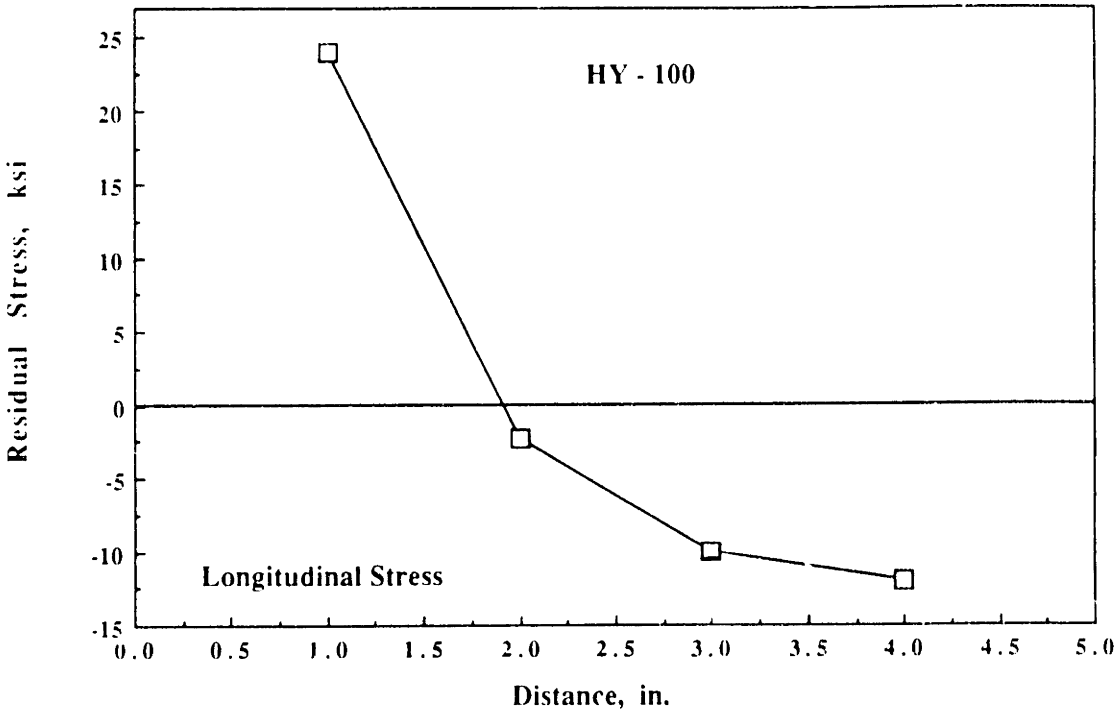

Figure 2-31: Longitudinal Residual Stress Distribution for HY-100

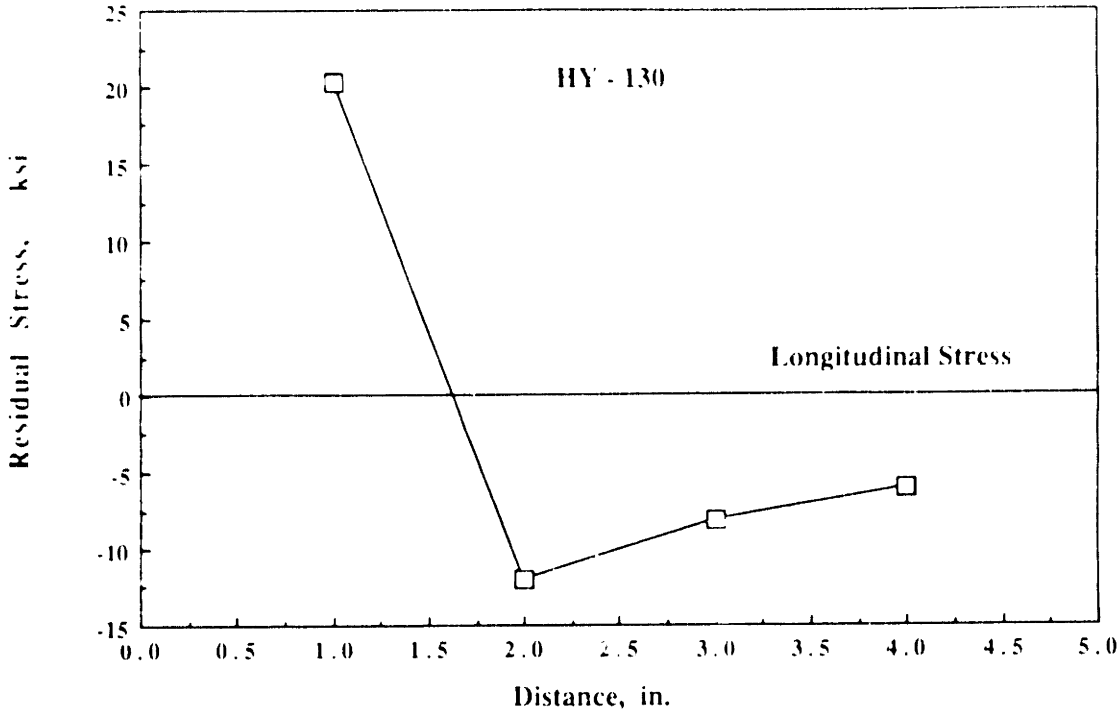

Figure 2-32: Longitudinal Residual Stress Distribution for HY-130

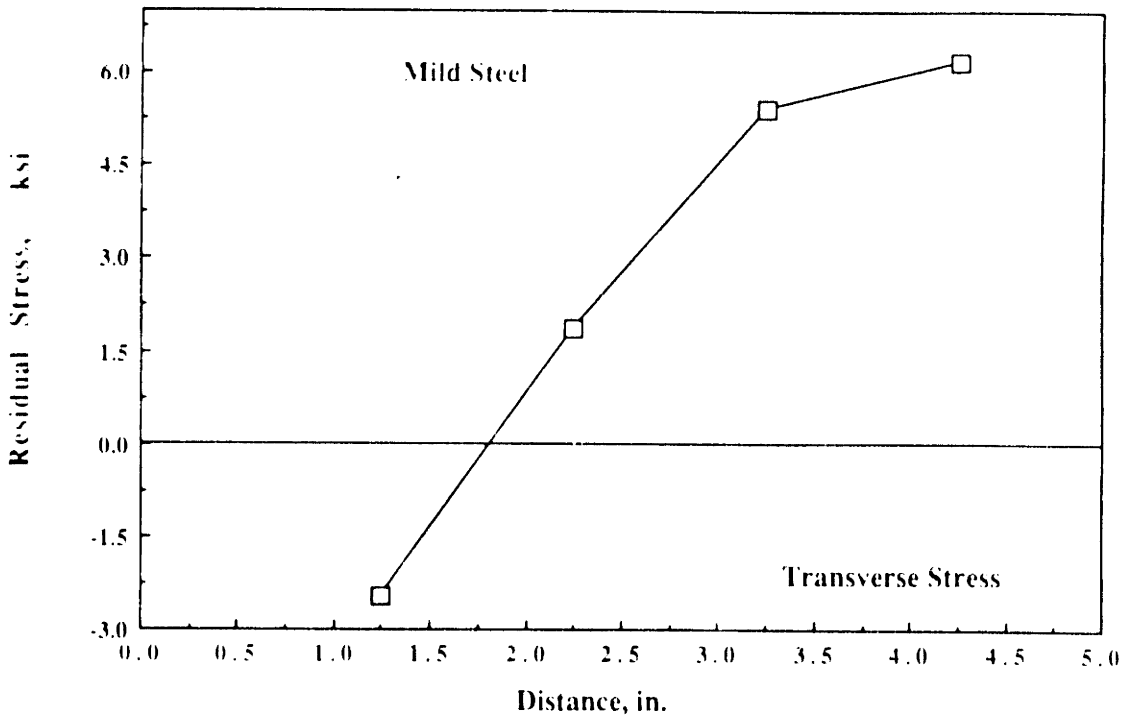

Figure 2-33: Transverse Residual Stress Distribution for Low Carbon Steel

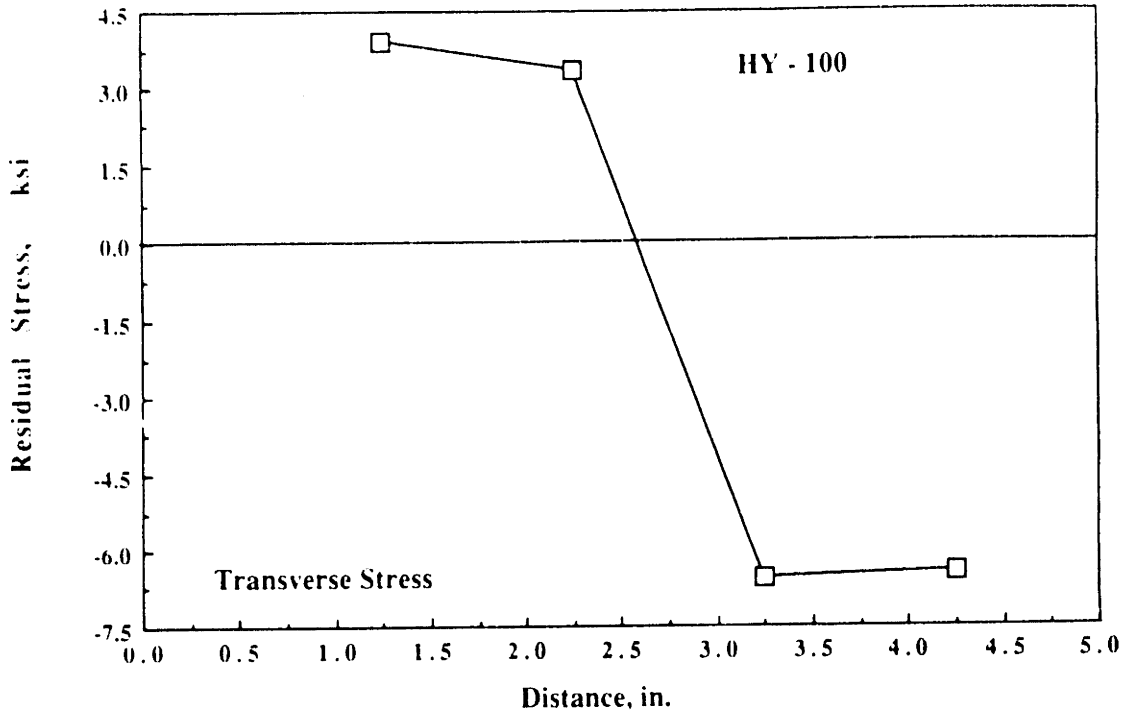

Figure 2-34: Transverse Residual Stress Distribution for HY-100

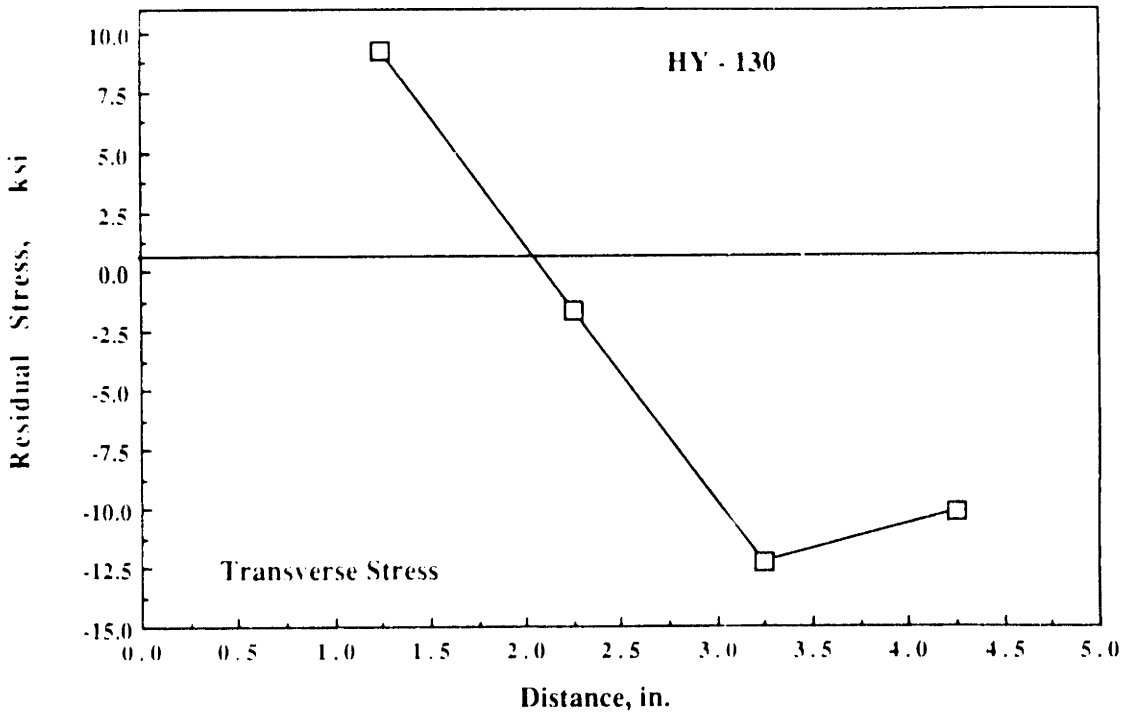

Figure 2-35: Transverse Residual Stress Distribution for HY-130

2.5.5.2 Bead-on-Edge Welding With Side Heating

Residual stresses and distortion are very closely related phenomena. This can be explained as follows. During heating and cooling in the welding cycle, thermal strain occurs in the weld metal and base metal regions near the weld. The strains produced during the heating arc are accompanied by plastic upsetting. The stresses resulting from these strains add up and react to produce internal forces that cause bending, buckling or rotation. The resulting displacements are called distortion. This distortion can provide an insight which is useful in understanding the state of residual stresses. The next set of experiments was done with side heating and only distortion was measured. The conclusion drawn from this set of experiments was used to establish the final set in this investigation.

Three experiments were conducted on the same three types of steel. In these experiments no welding pass was performed. The side heating torch was used to heat the lower part of the specimen to study the effects of side heating on the specimen. The side heating flame was adjusted to heat the specimen up to 200 °F. The temperature lacquer (Tempo-Lac) was used to indicate the desired temperature. The following is the setting for the side heating:

Side Heating Set-Up

1. Acetylene tank pressure	3 psi
2. Oxygen tank pressure	8 psi
3. Flame Torch Adjustment	1/2" cone, 2" feather
4. Lateral position of the torch	1" from the specimen
5. Vertical position of the torch	4" from the upper part of the specimen
6. Torch Speed	0.300 inches per second

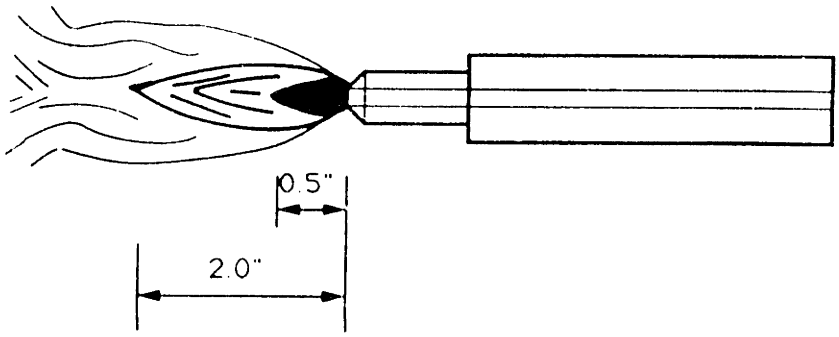

Figure 2-36: Side Heating Flame Configuration

Figures 2-37 to 2-39 show the distortion resulting from the side heating torch. The bending behavior of the specimen was opposite to the bending behavior resulting from the welding torch. The specimen started to bend downward as the side heating torch began to heat the specimen. After the side heating process was completed and the specimen began to cool down, it started to bend back to its original position. From this behavior it was clear that the side heating technique could be used to reduce distortion and hence residual stresses during welding.

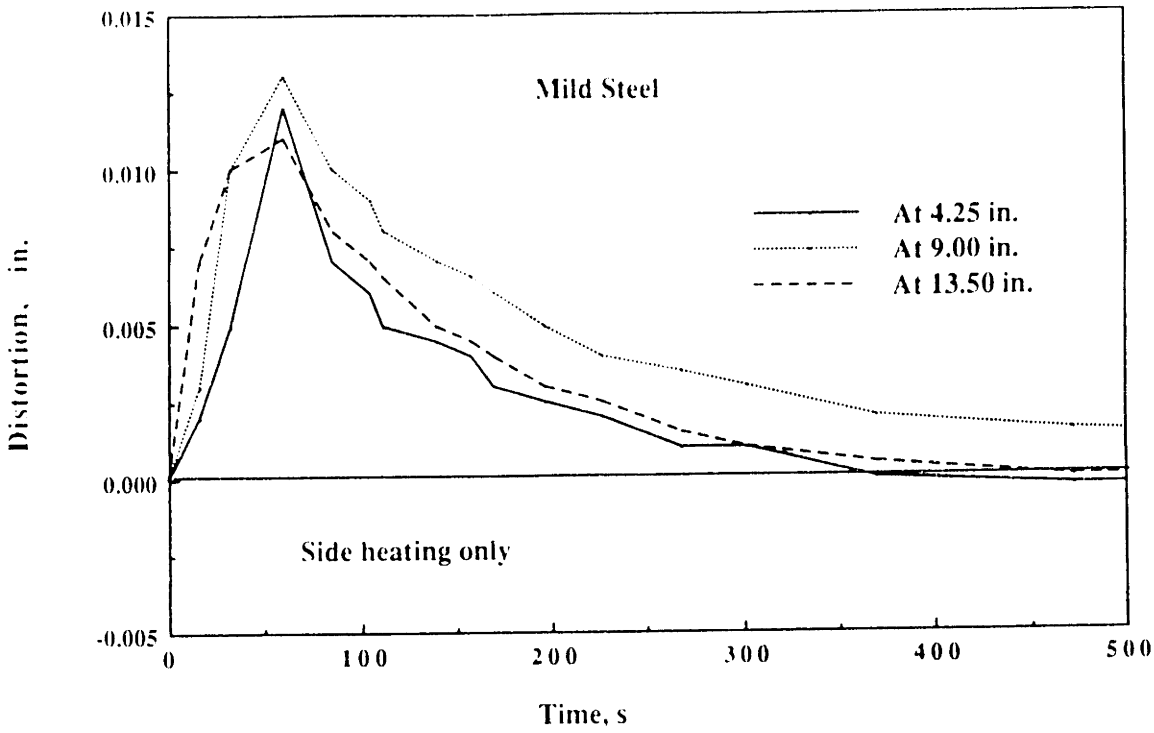

Figure 2-37: Distortion Profile due to Side Heating Source for Low Carbon Steel

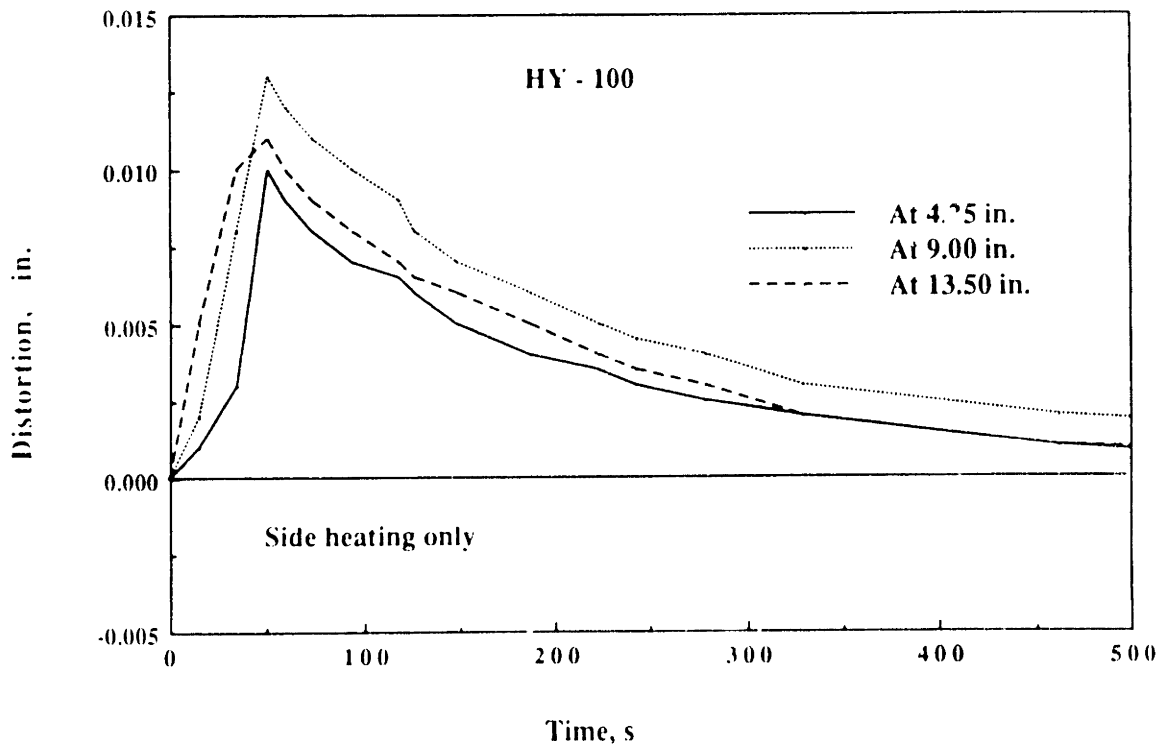

Figure 2-38: Distortion Profile due to Side Heating Source for HY-100

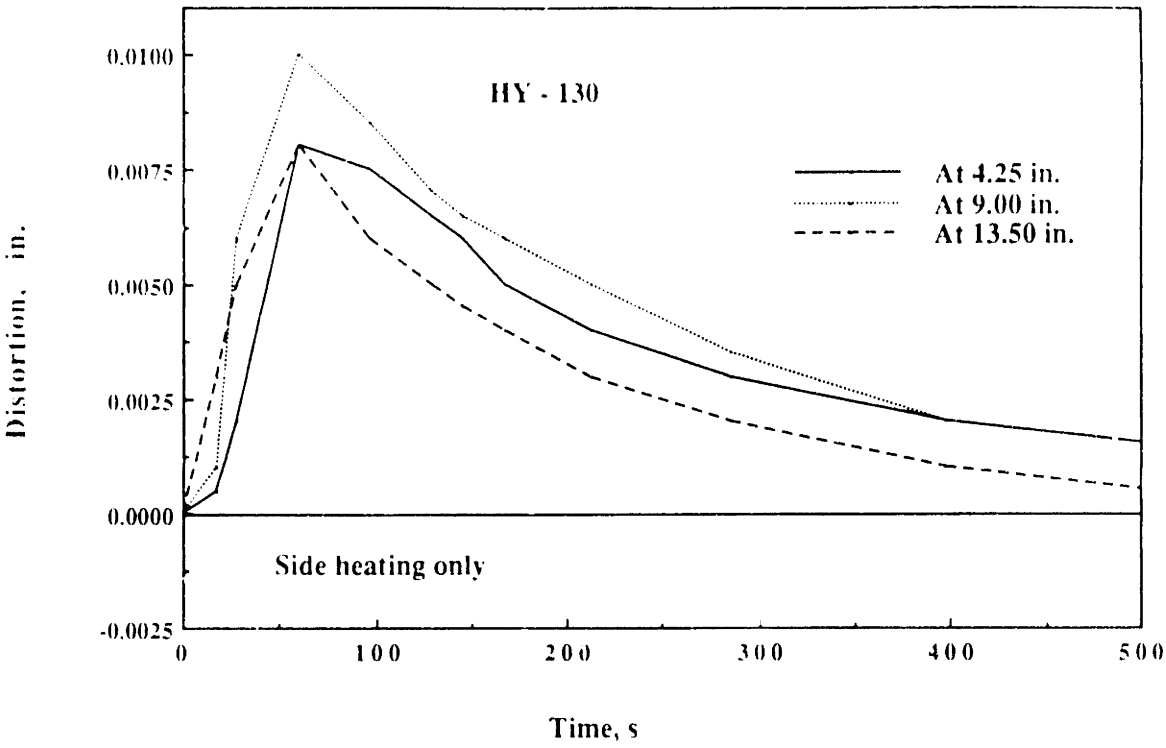

Figure 2-39: Distortion Profile due to Side Heating Source for HY-130

The next task was to find the proper position of the side heating torch to provide the optimum reduction in distortion and residual stresses. In this investigation we were concerned with the position in the parallel direction to the welding torch. Three different positions were considered here: ahead of, behind, and along with the welding arc.

Nine experiments were conducted on three types of steel. The first three were performed by placing the side heating torch 9 inches ahead of the welding torch; this was equivalent to 30 seconds before the welding process started. The next three were performed by placing the side heating torch 9 inches behind the welding torch. This was equivalent to 30 seconds after the welding process started. The last three experiments were performed by placing the side heating torch along with the welding torch. Therefore, these two processes started at the same time.

Figures 2-40 to 2-42 show the distortion resulting from welding with the side heating torch ahead of the welding arc. The specimen experienced complex bending behavior. It first started to bend downward due to the effect from side heating heat source. When the welding torch started to weld the specimen, it started to bend upward. This meant that these two heat sources produced counteractive effect which reacted upon the specimen. When the welding torch started, it immediately dominated the bending behavior of the specimen due to the stronger heat source. Even though it appeared that by doing this the distortion could be reduced as much as 60% for low carbon steel, and 22%-25% for HY-100 and HY-130, it is not desirable for welding fabrication. The complex bending behavior can cause difficulty during welding in real structures.

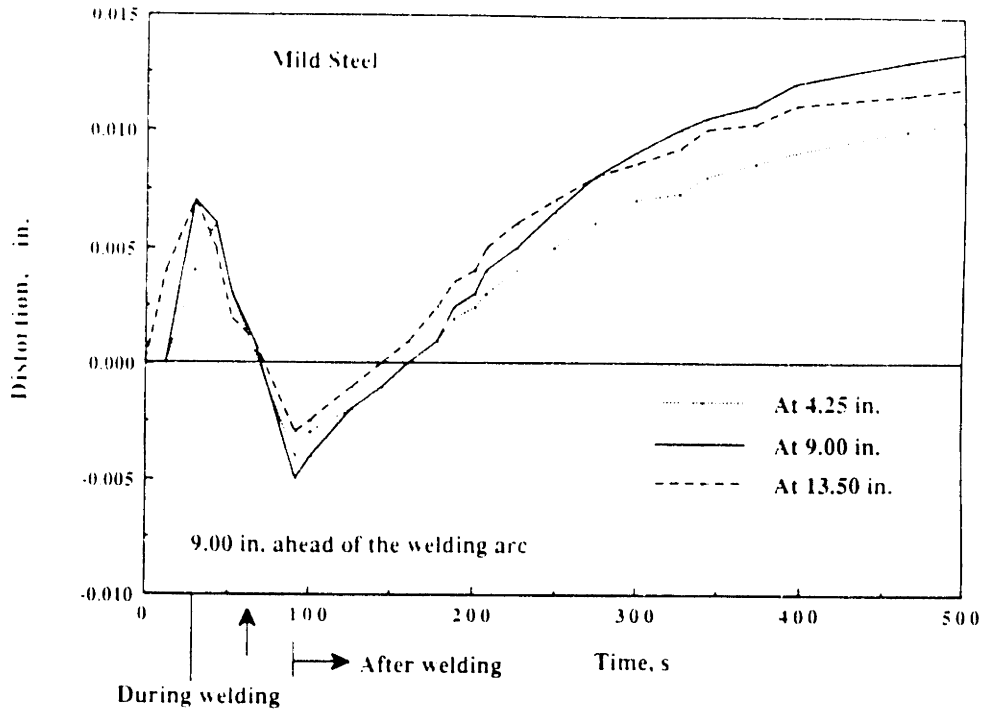

Figure 2-40: Distortion Profile for Low Carbon Steel

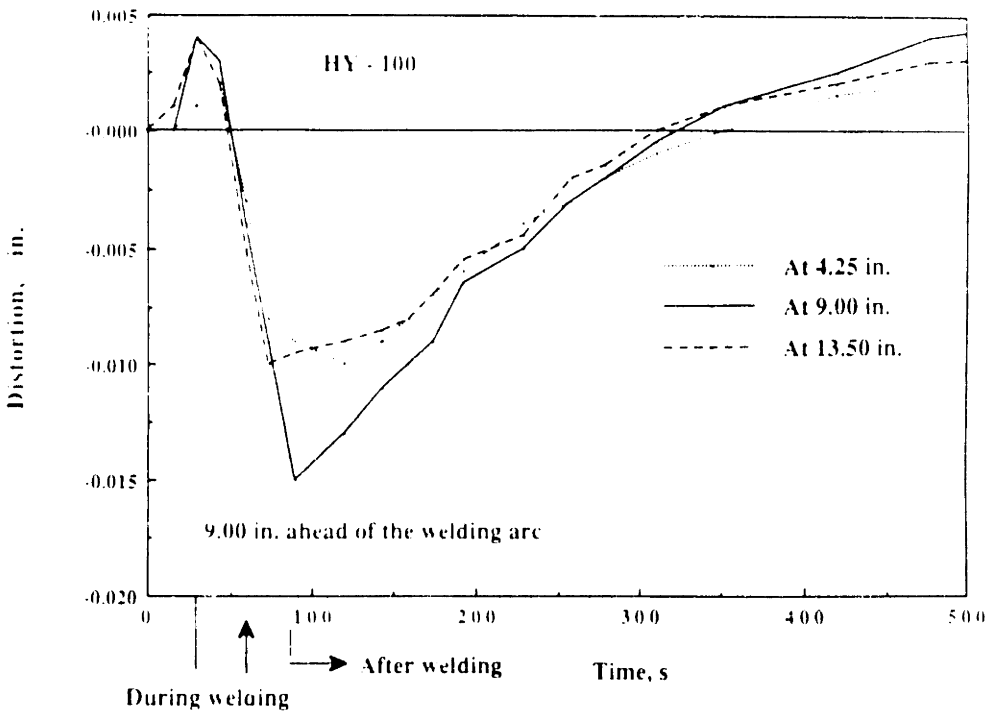

Figure 2-41: Distortion Profile for HY-100

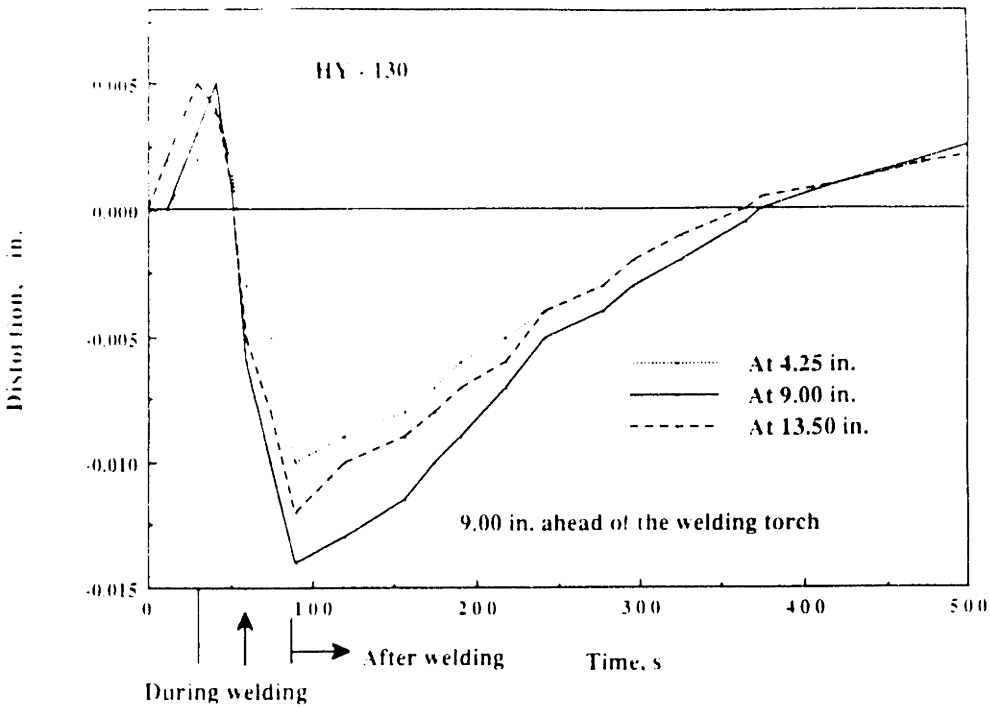

Figure 2-42: Distortion Profile for HY-130

Figures 2-43 to 2-45 show the distortion behavior of the specimen when the side heating torch was placed behind the welding torch. The distortion behavior is the same as it is when there is no side heating torch except that the magnitude of distortion is smaller. This is because the effect from the welding torch is so strong that even after the side heating torch started to heat the specimen it could not totally overcome the effect from the welding torch. However, it could reduce the magnitude of the distortion by as much as 20% for low carbon steel, and 16%-20% for HY-130 and HY-100. Placing the side heating torch behind the welding torch did not create any complex bending behavior during welding. However, it could not reduce distortion as much as placing the side heating torch ahead of the welding torch. The amount of distortion reduction is therefore considerably less, especially for low carbon steel.

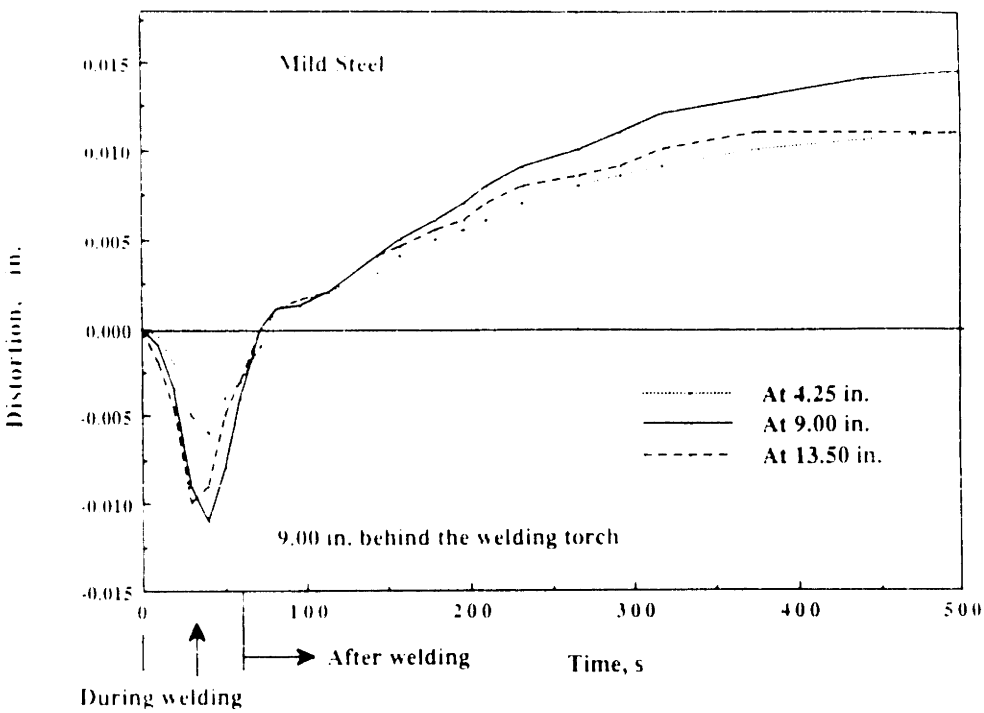

Figure 2-43: Distortion Profile for Low Carbon Steel

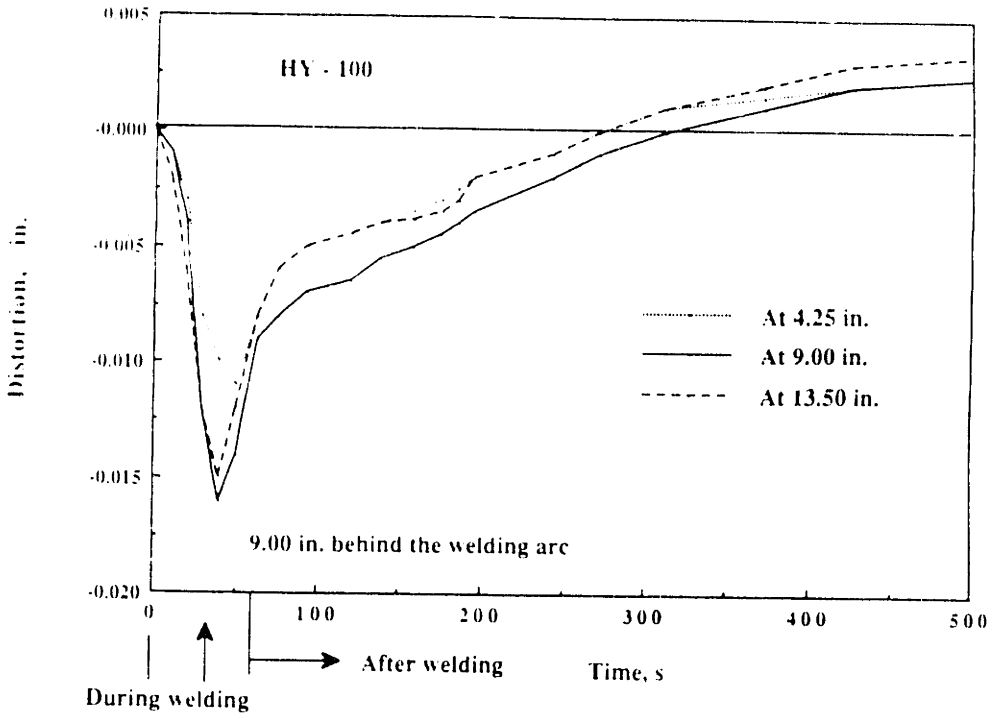

Figure 2-44: Distortion Profile for HY-100

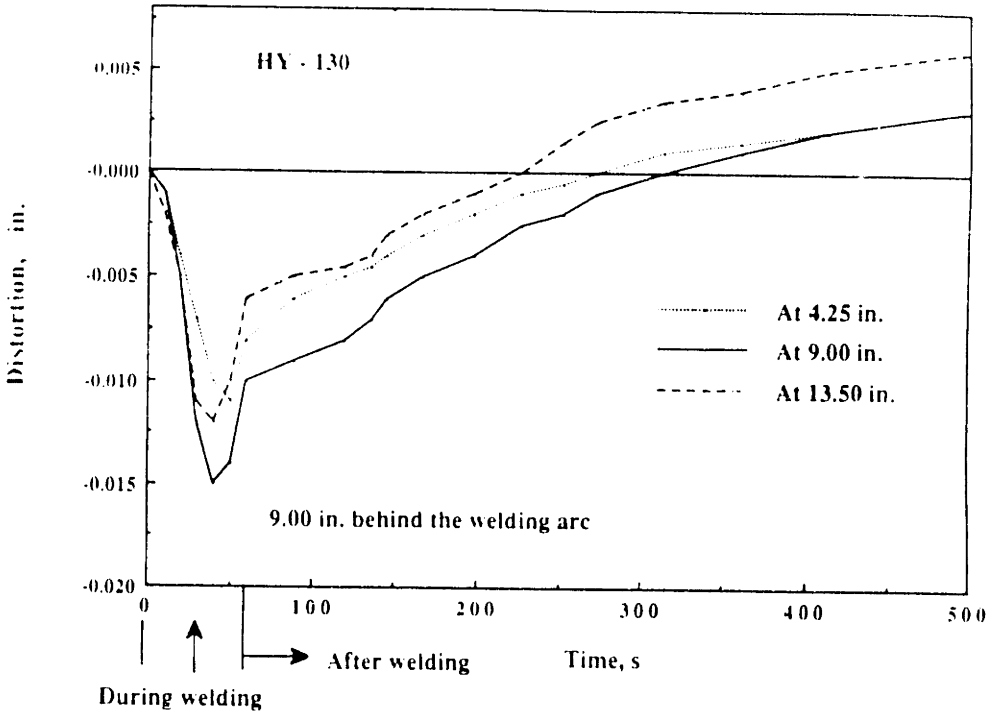

Figure 2-45: Distortion Profile for HY-130

Figures 2-46 to 2-48 show the distortion behavior of the specimen when the side heating torch was placed along with the welding arc. The bending behavior is similar to that when no side heating was provided except that the magnitude of distortion is much smaller. The effect from side heating in this situation directly counteracts to the effect from the welding torch, resulting in reduced distortion. The reduced distortion is as high as 58% for low carbon steel, and 44%-48% for HY-130 and HY-100. Figures 2-49 to 2-57 show the comparison of the distortion referred to the previous discussion at three different locations along the length of each specimen.

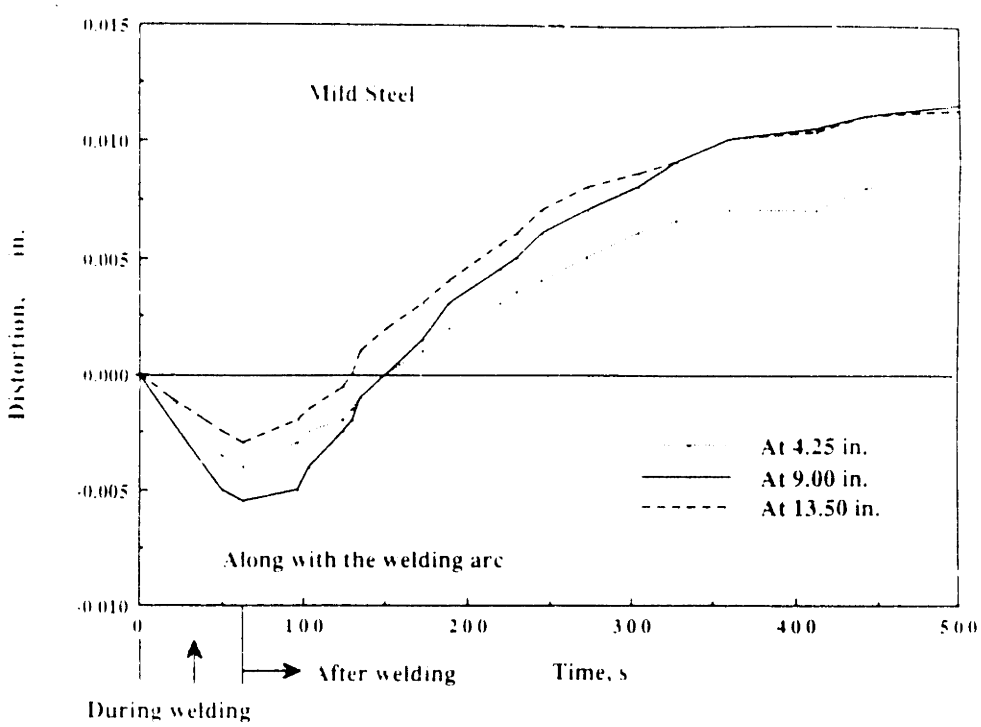

Figure 2-46: Distortion Profile for Low Carbon Steel

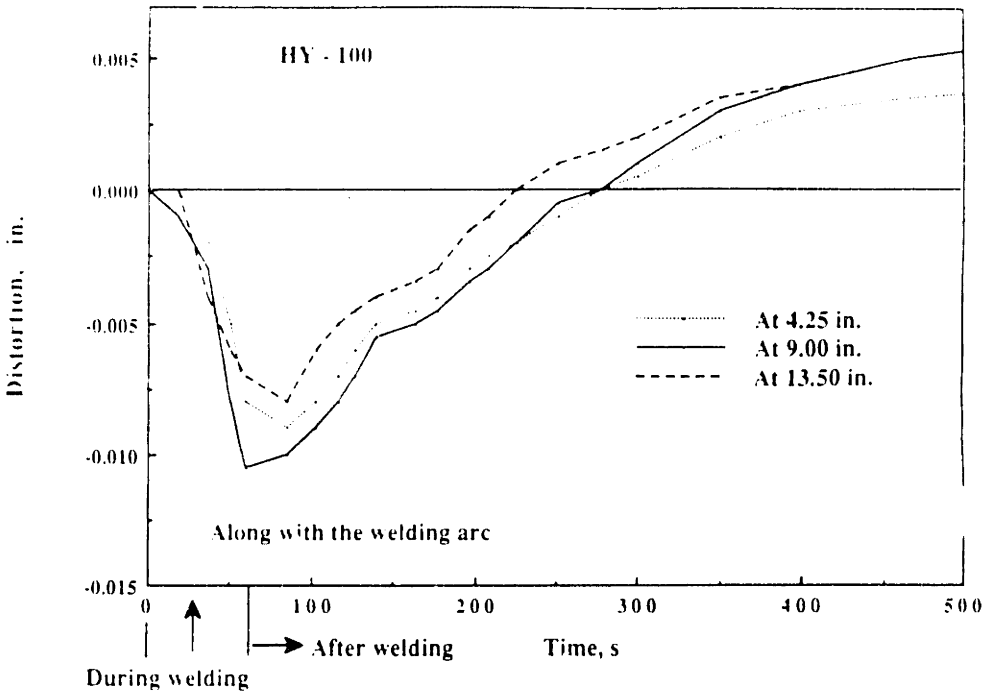

Figure 2-47: Distortion Profile for HY-100

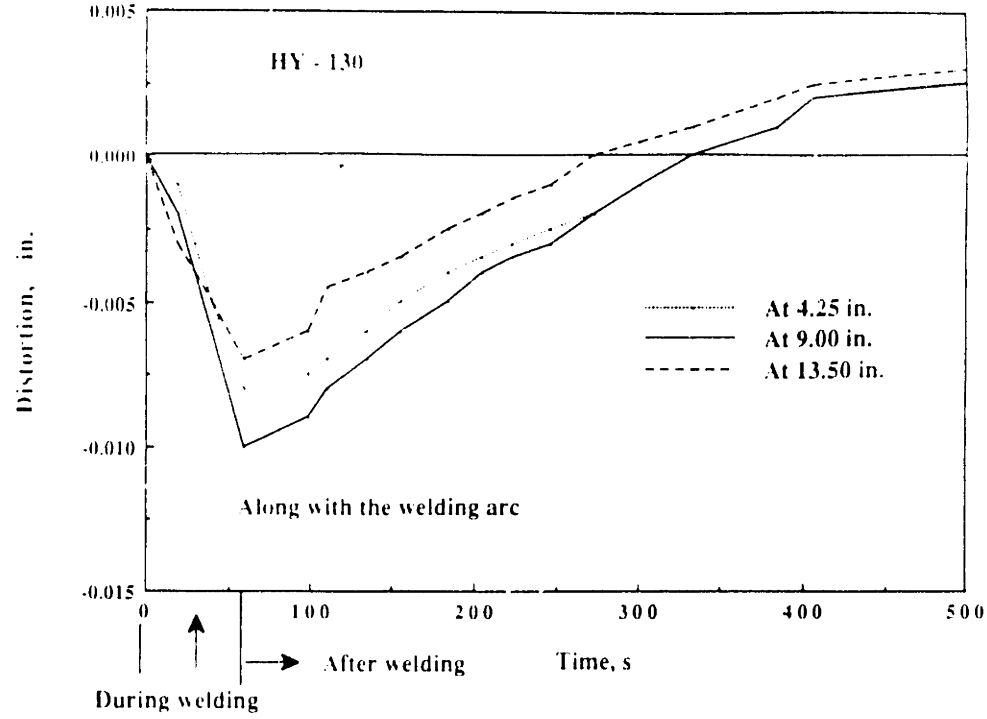

Figure 2-48: Distortion Profile for HY-130

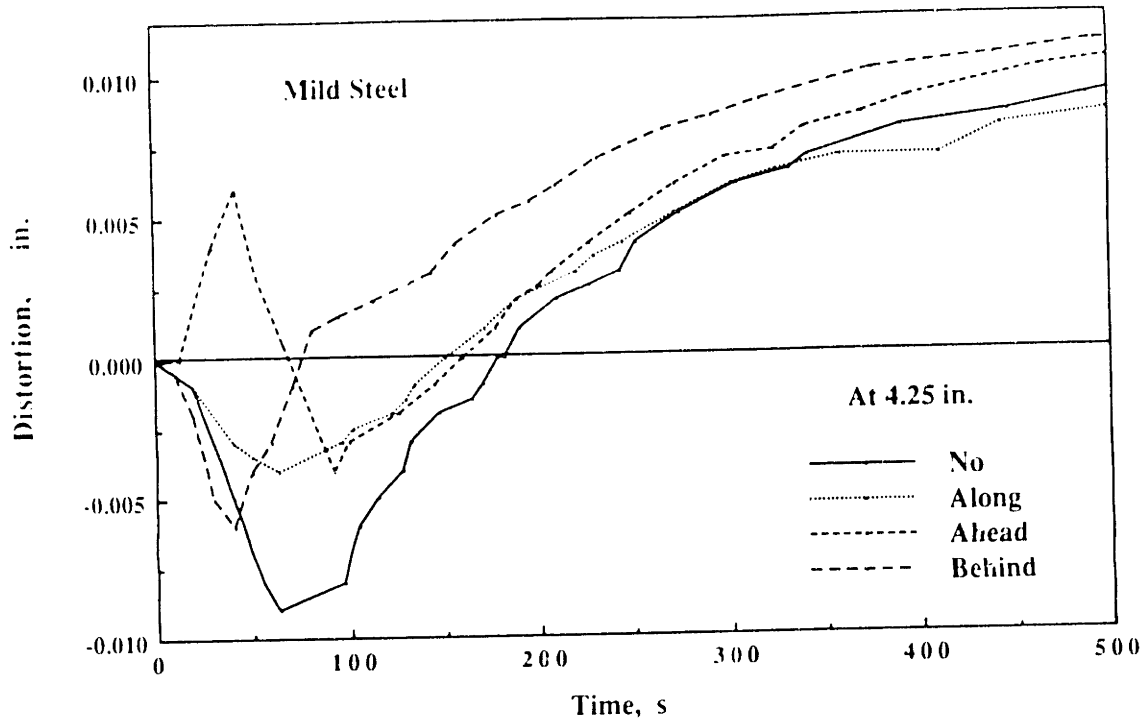

Figure 2-49: Comparison of Distortion for Low Carbon Steel

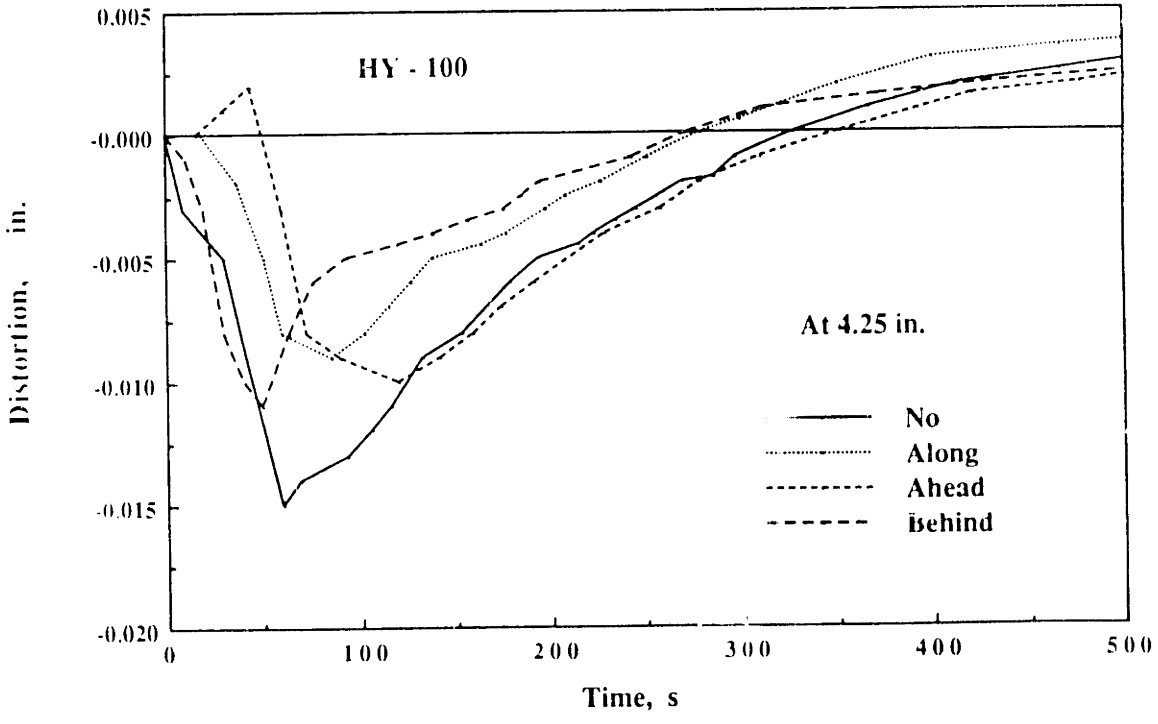

Figure 2-50: Comparison of Distortion for HY-100

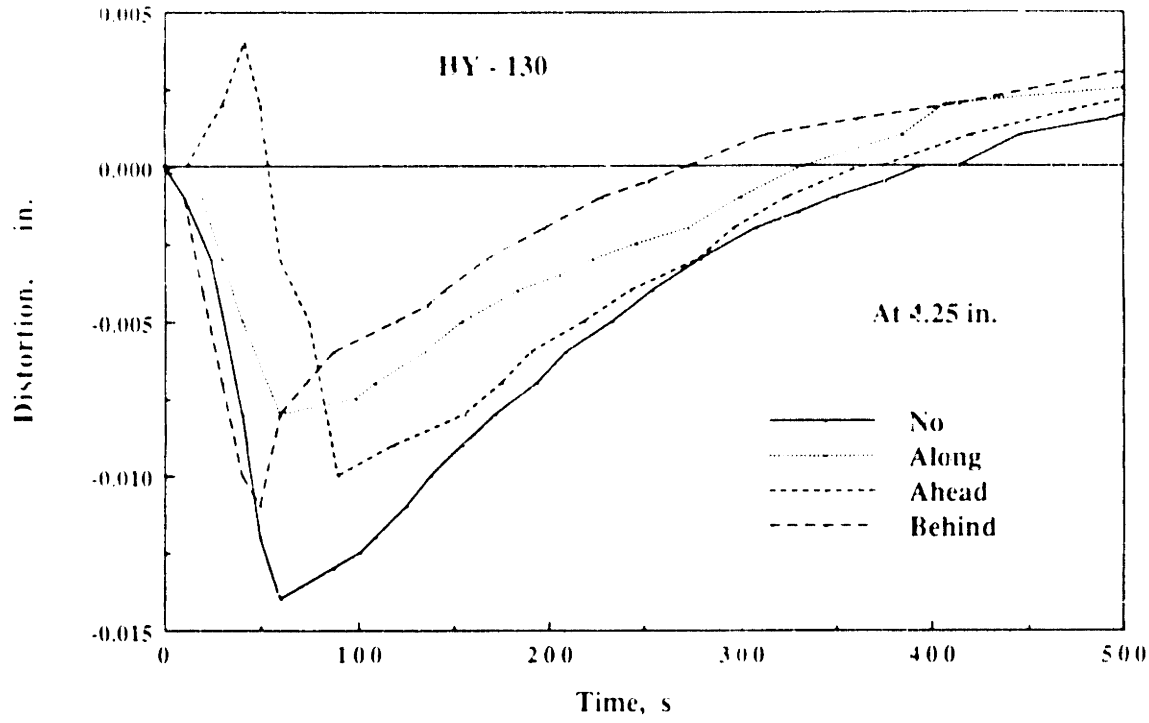

Figure 2-51: Comparison of Distortion for HY-130

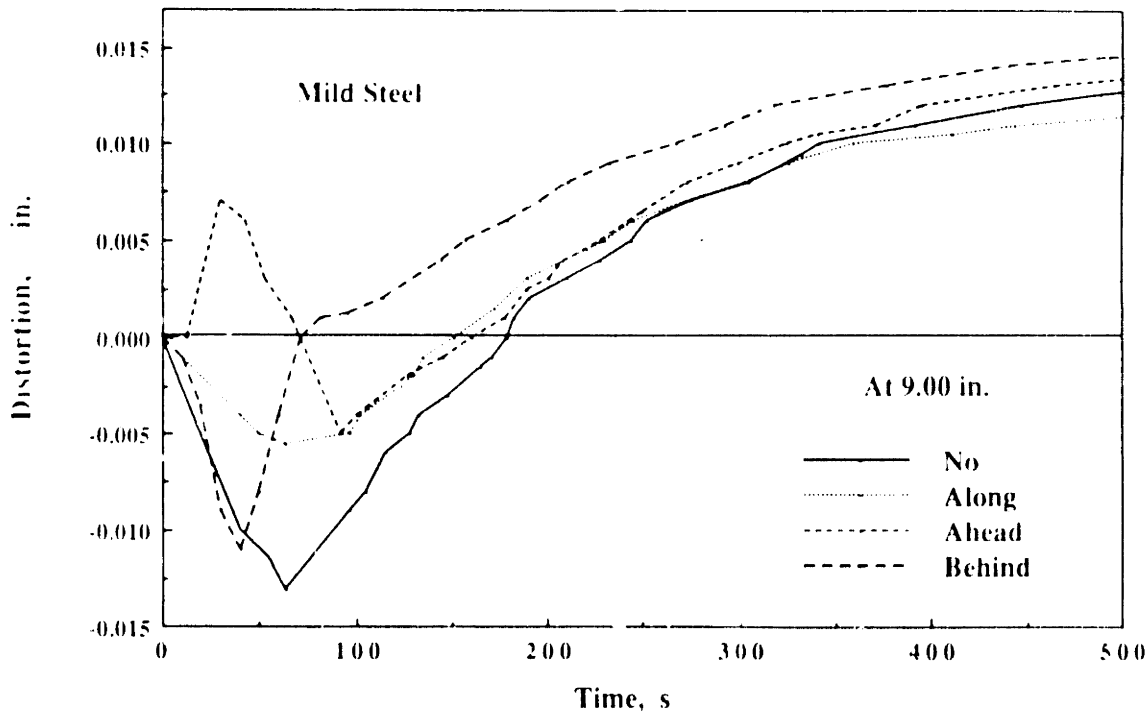

Figure 2-52: Comparison of Distortion for Low Carbon Steel

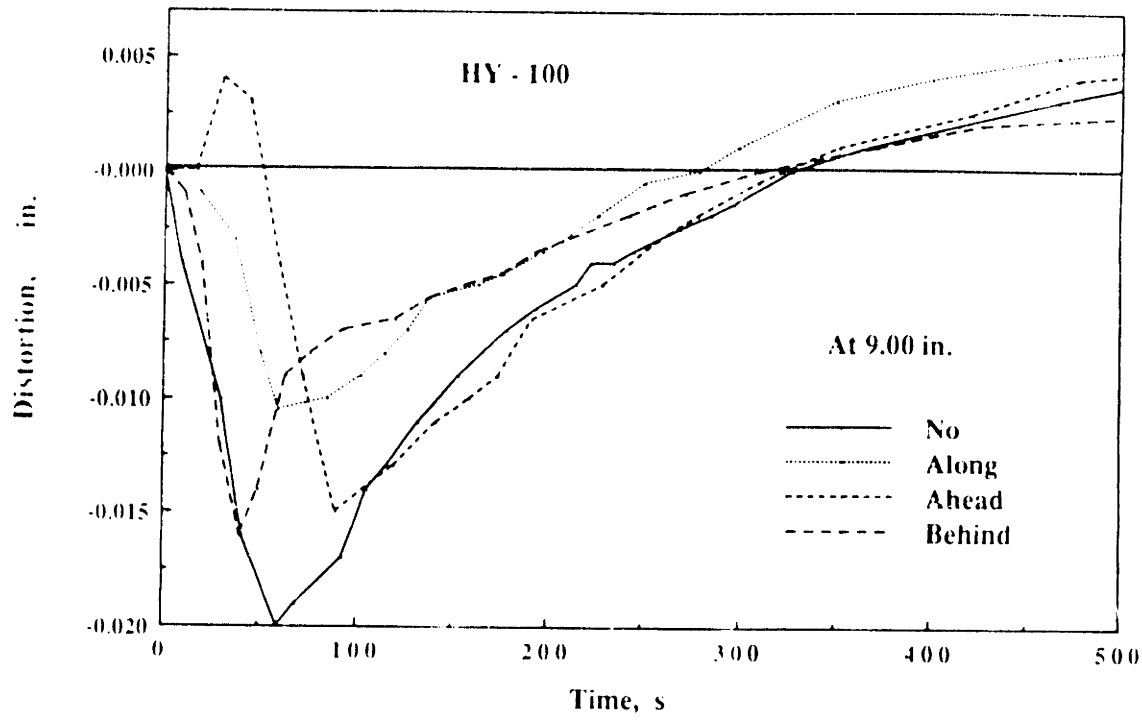

Figure 2-53: Comparison of Distortion for HY-100

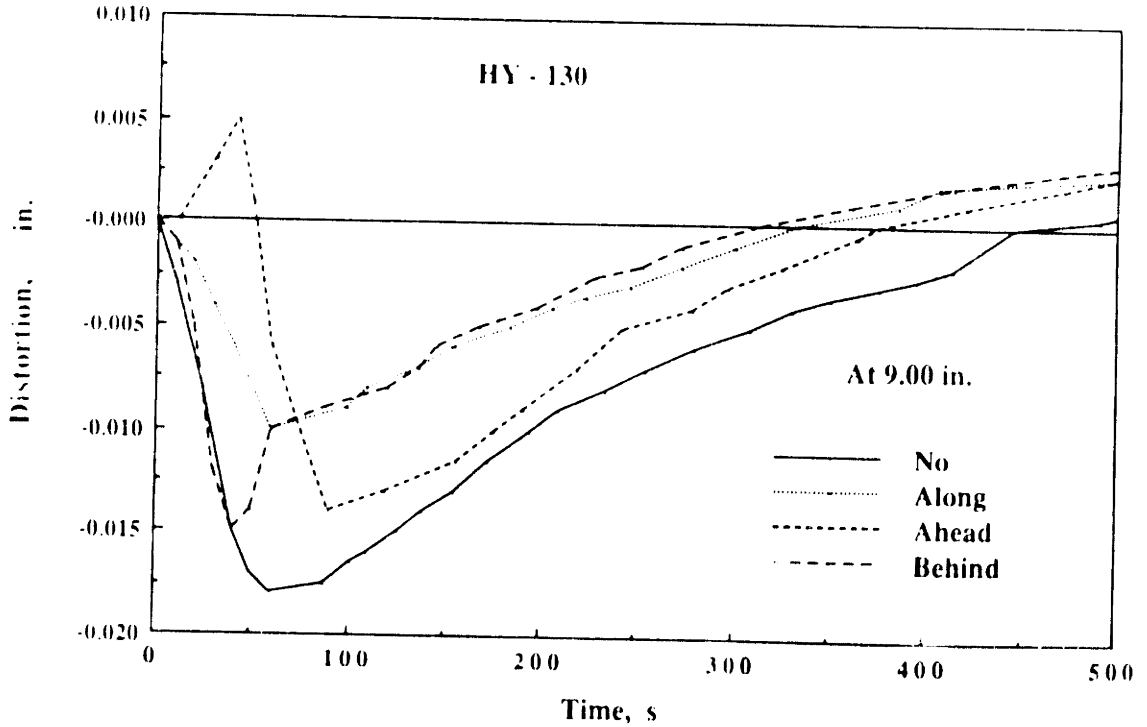

Figure 2-54: Comparison of Distortion for HY-130

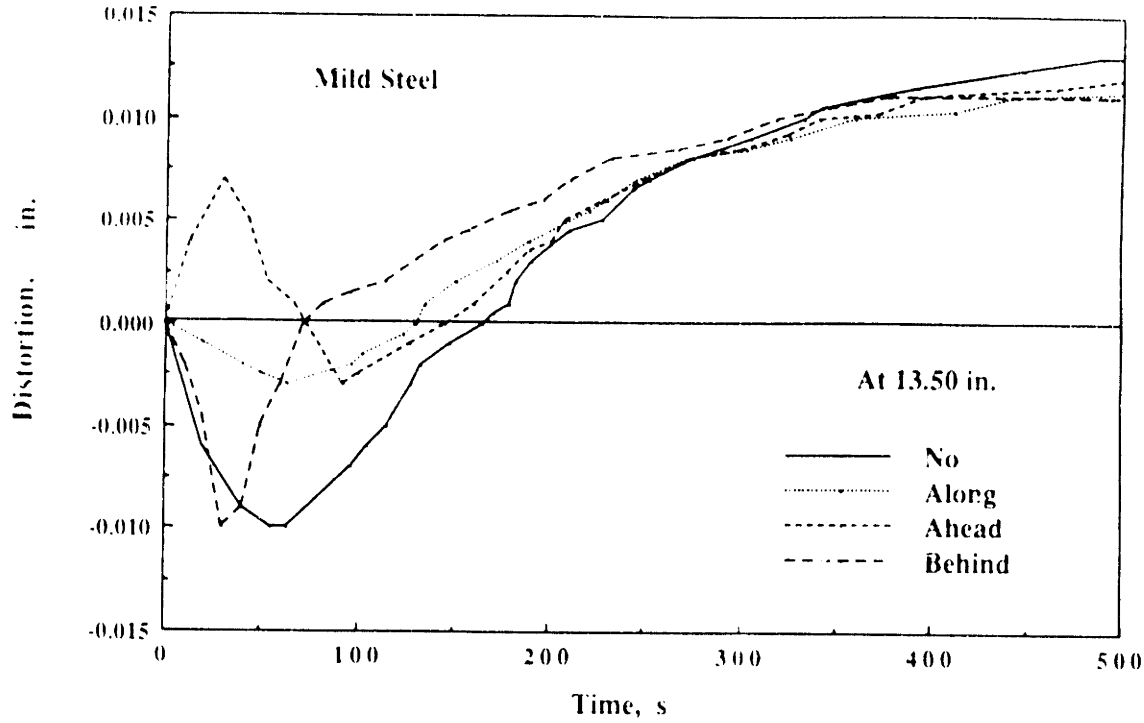

Figure 2-55: Comparison of Distortion for Low Carbon Steel

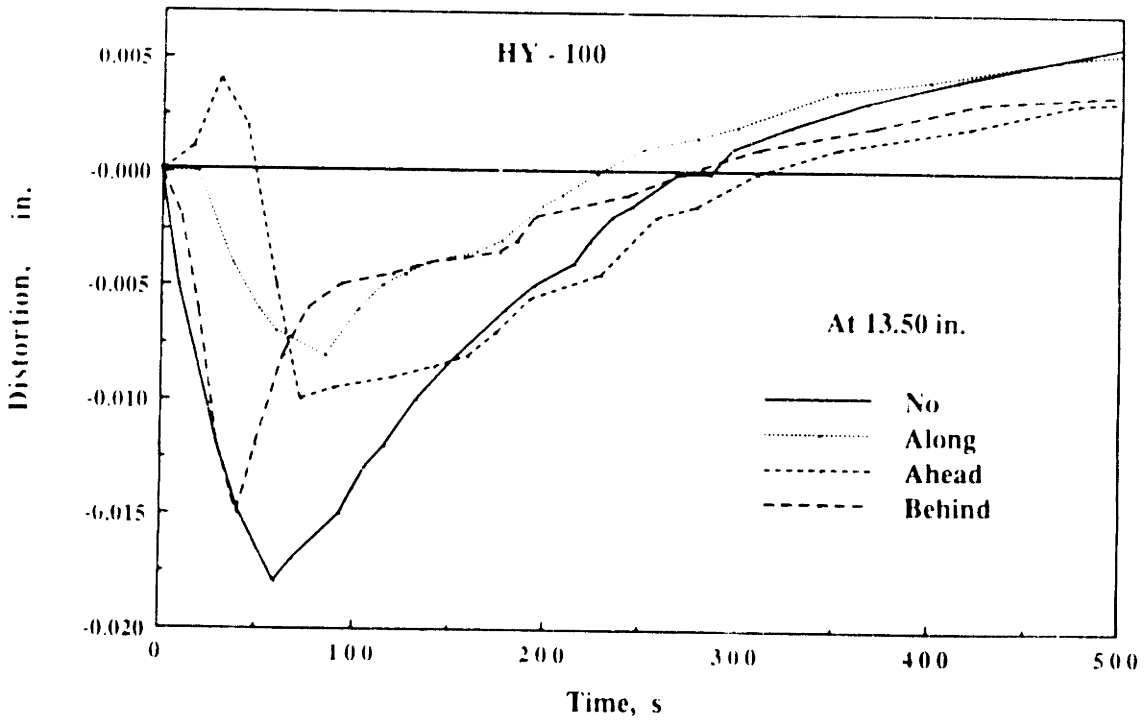

Figure 2-56: Comparison of Distortion for HY-100

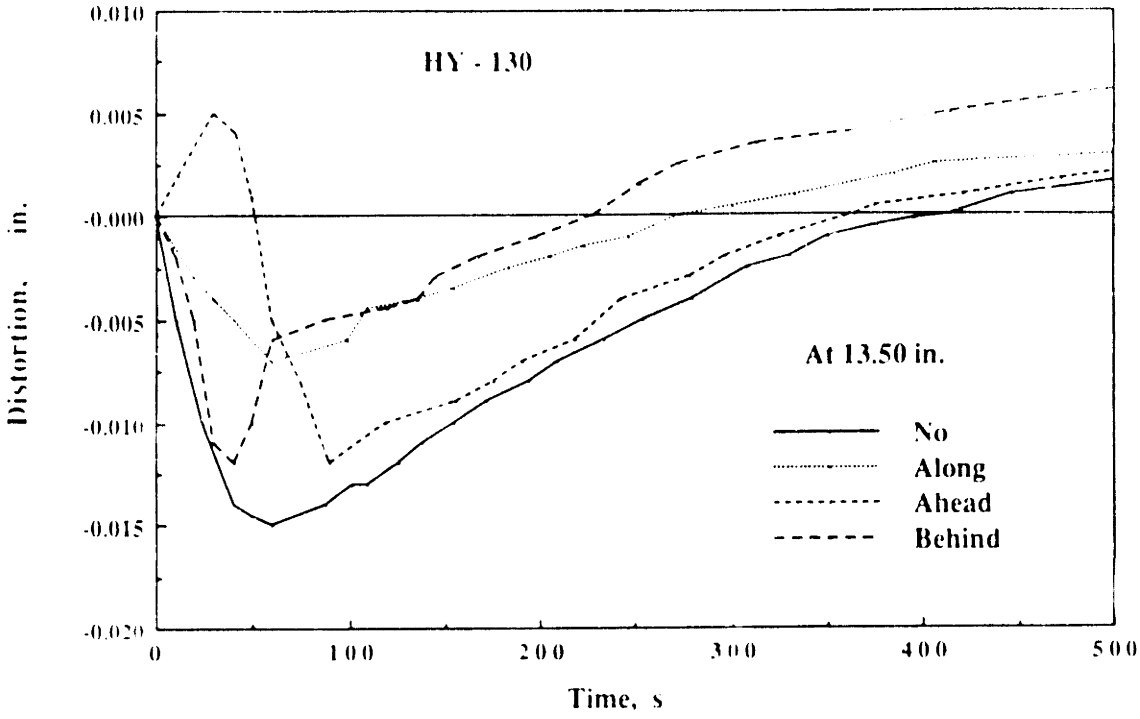

Figure 2-57: Comparison of Distortion for HY-130

It can be concluded that placing the side heating torch along with the welding arc can provide the most reasonable reduction in distortion without creating any complex or undesirable distortion behavior during welding. As mentioned earlier in this section, residual stresses and distortion are closely related phenomena. Therefore, it is logically enough to expect the most reasonable reduction in residual stresses by providing side heating along with the welding arc.

The next three experiments were conducted with the side heating torch placed along with the welding torch to measure residual stresses. These stresses were then compared with those from the previous experiments that were done without providing side heating.

Four thermocouples and four strain gages were mounted on each specimen to measure temperature and strain change. The welding condition and setting for the Millermatic Gas Metal Arc Semi Automatic Welding machine as well as the side heating process were as follows:

Material	Low carbon steel, HY-100, HY-130
Dimension	12"x5.5" with 0.5 inches thick
Filler wire	E70S
Transfer Type	Spray
Gas Flow Rate	30 cfh of Argon 98%, 2% O_2
<u>Millermatic Semi Automatic Welding Machine Setting</u>	
Pre-Flow Time	1 sec.
Run-in Speed	20 sec.
Welding Mode	Continuous
Time Range	High (2.5 -5 sec.)
Burn Back Time	0.05 sec.
Post Flow Time	2 sec.
Miller DVC DW-1	25 Volts
Wire feed speed	375 inches per minute

Carriage Control

Type of Control	Manual
Weld Speed	0.300 inches per second
Polarity	DCRP
Power Supply	25 V/ 230 Amp.

(Ampere is the average value reading during welding)

Side Heating Set-Up

1. Acetylene tank pressure	3 psi
2. Oxygen tank pressure	8 psi
3. Flame Torch Adjustment	1/2" cone, 2" feather
4. Lateral position of the torch	1" from the specimen
5. Vertical position of the torch	4" from the upper part of the specimen
6. Longitudinal position of the torch	Match to the welding arc
7. Torch Speed	0.300 inches per second

After welding was completed and specimens cooled down they were cut to measure residual stresses as in the previous experiments.

Figures 2-58 to 2-60 show the temperature distribution during and after welding. As one can observe, the temperature 3.25 inches away from the weld line experienced a dramatic increase. This was due to the side heating heat source which was provided near that location. The cooling rate was slower than it was without side heating; i.e., at 500 seconds the temperature over the specimen was about 25°C (45°F) higher than it was without side heating. The magnitude of temperature near the weld was roughly the same as it was without side heating except for HY-100, where the position of the thermocouple was moved 1/4" away from the original position due to some technical problems when it was mounted.

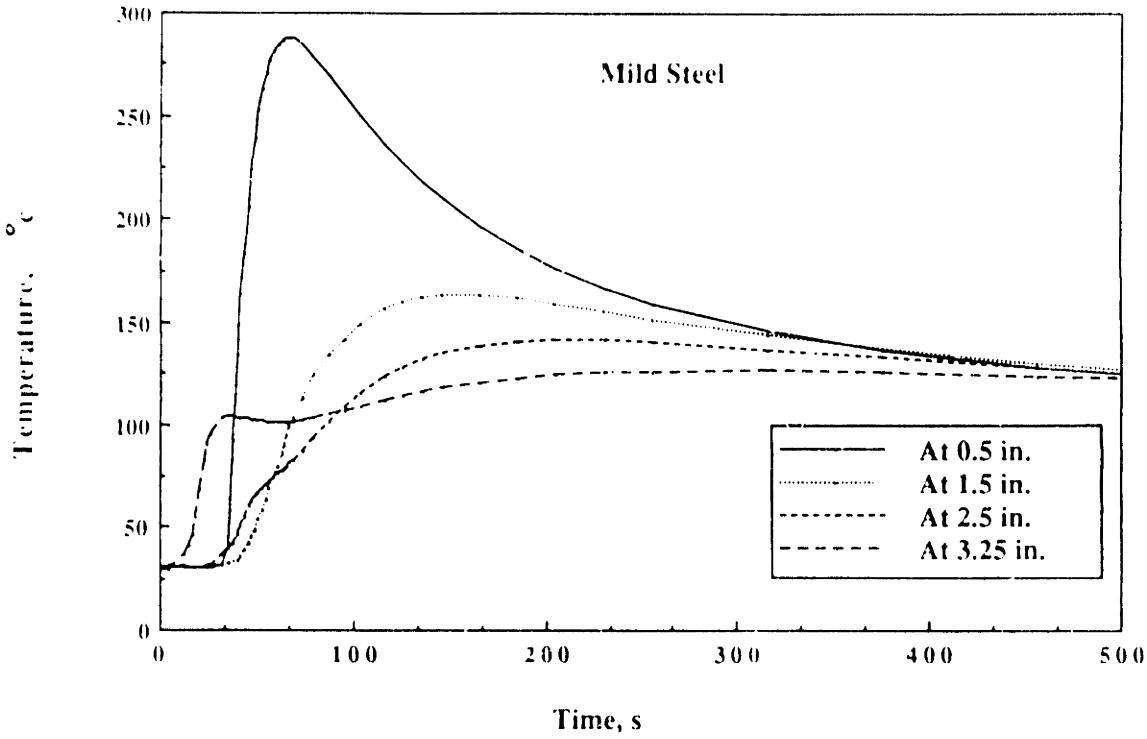

Figure 2-58: Temperature Profile for Low Carbon Steel

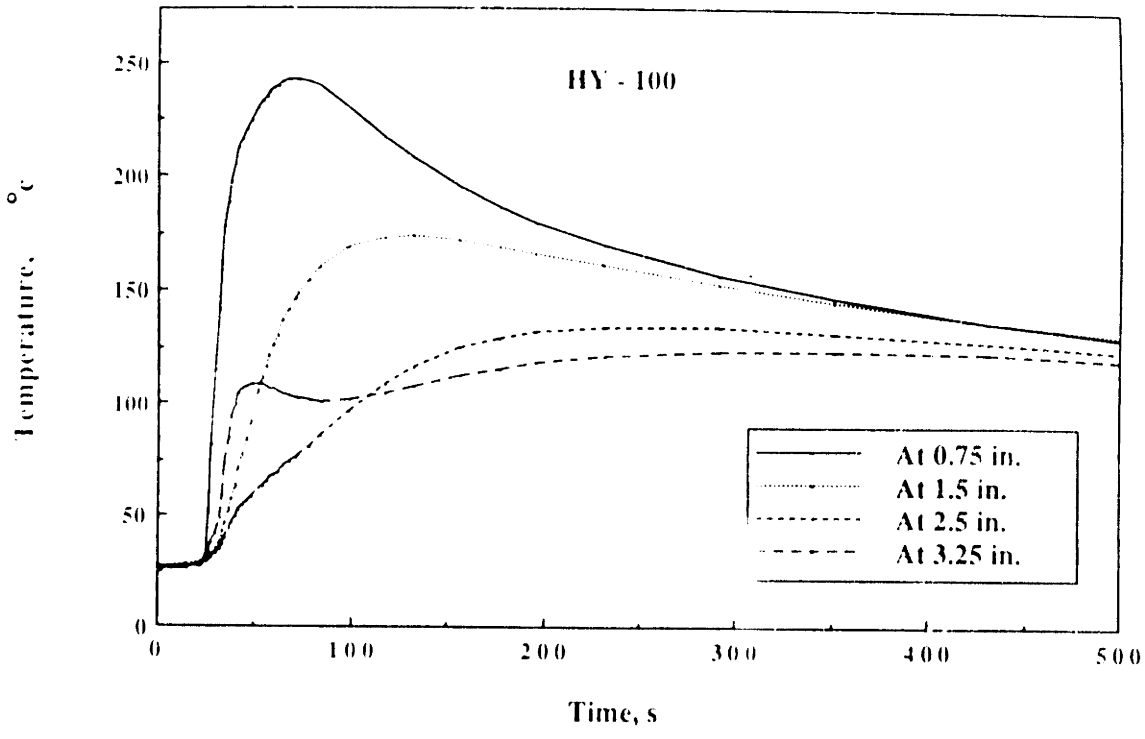

Figure 2-59: Temperature Profile for HY-100

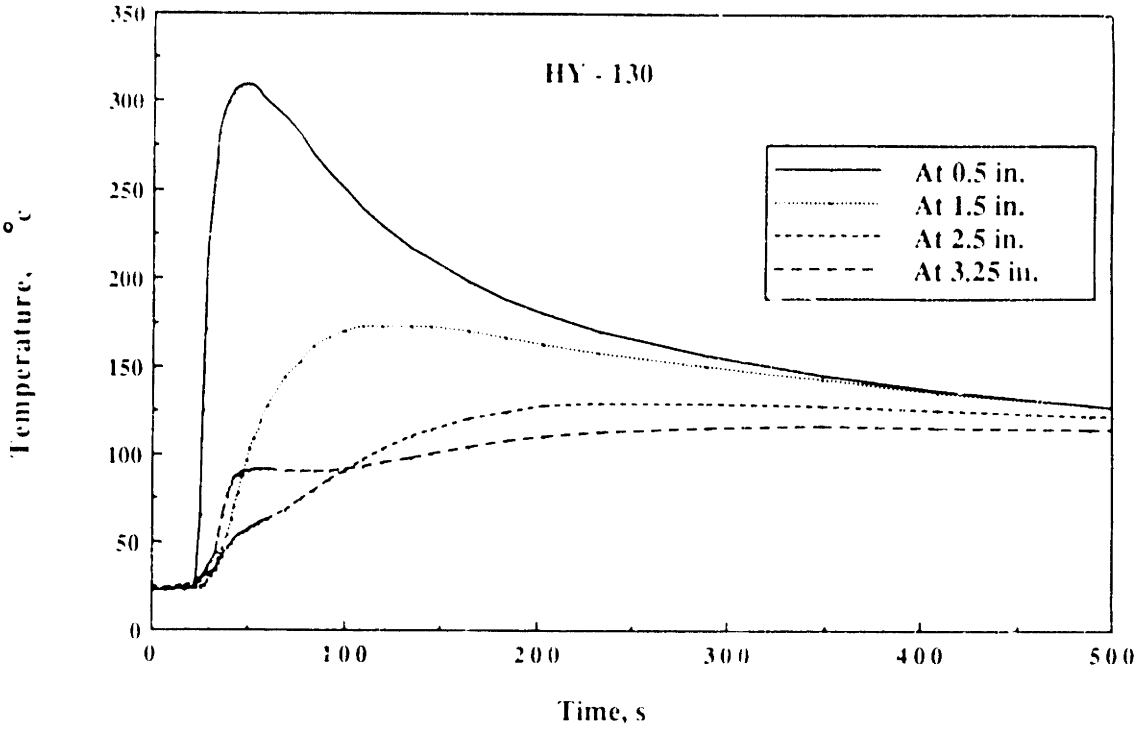

Figure 2-60: Temperature Profile for HY-130

Figures 2-61 to 2-63 show the longitudinal strain history of low carbon steel, HY-100 and HY-130. The tensile longitudinal strain developed near the weld line at the start of the welding process and then changed into compressive strain when the specimen cooled down. The increase of strain during welding can be clearly observed both at the position near the weld line (1 inch) and far away from the weld line (4 inches) when compared with strain observed in cases without side heating. The magnitude of the strain near the weld line was around 2,500 microstrain for low carbon steel, 2,200 microstrain for HY-100 and HY-130. These increases in magnitude of strain indicate that the rate of change in strain during welding is higher than that of the previous experiments without side heating. For the transverse strain, shown in Figs. 2-64 to 2-66, the increase in strain during welding happened largely at the location away from the weld line (4 inches). Compressive transverse strain developed at the start of the welding process then changed into tensile transverse strain during welding. After welding was completed it tended to change to compressive strain. Figs. 2-67 to 2-72 show more detail of strain history for both longitudinal and transverse strain up to the time when the temperature was uniform throughout the specimen. From these figures it was clear that the side heating technique provided an impact on the strain change during welding and after welding. This was mainly due to the change in the cooling rate throughout the specimen which was caused by the side heating heat source. Hence, it altered the strains while they were being formed.

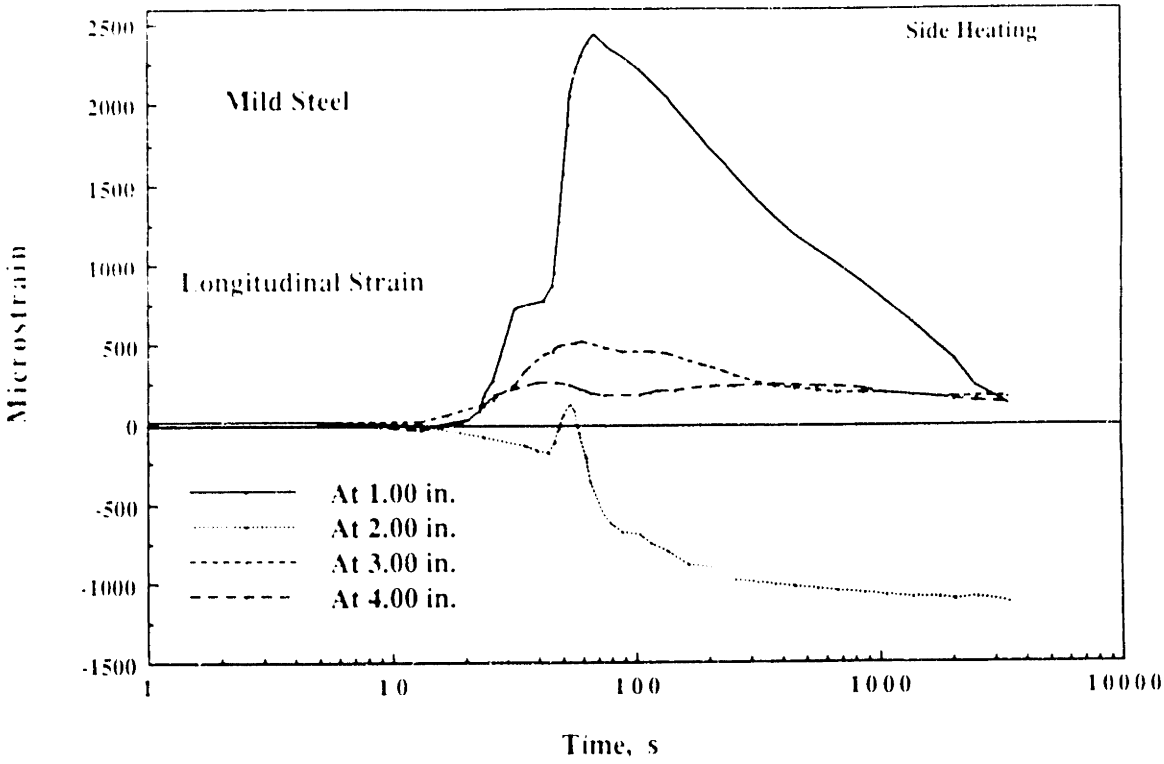

Figure 2-61: Transient Longitudinal Strain Profile for Low Carbon Steel

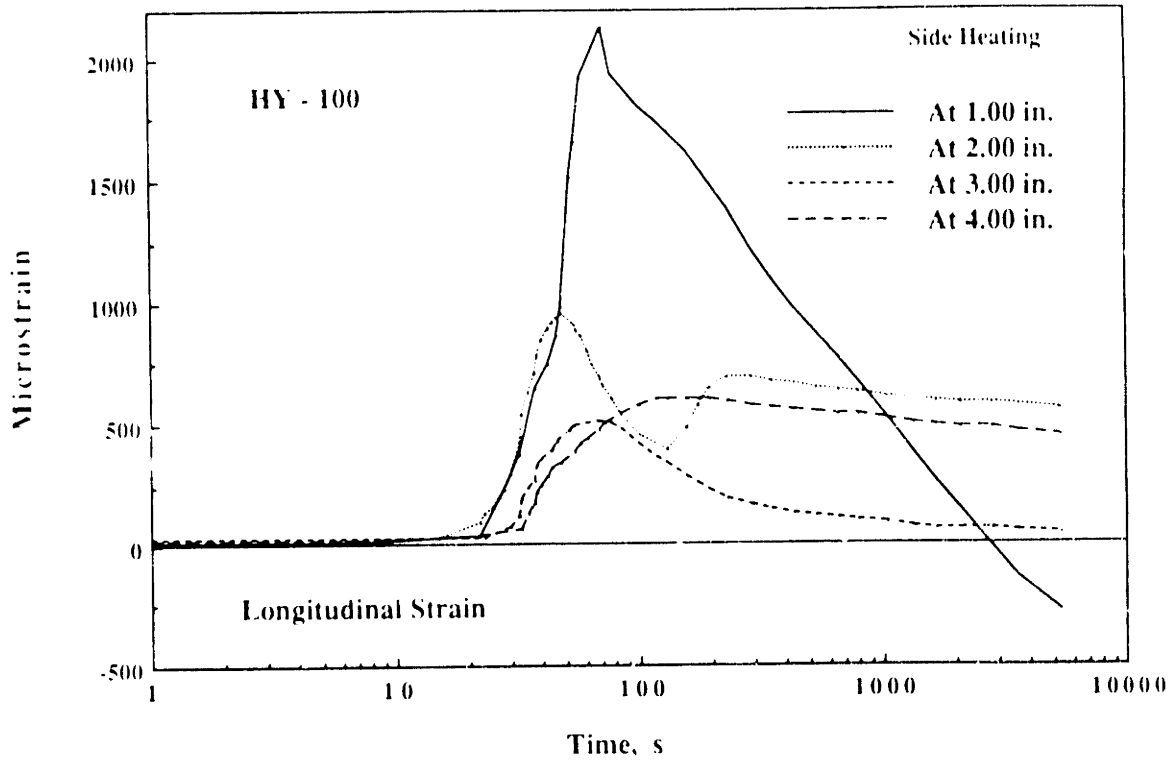

Figure 2-62: Transient Longitudinal Strain Profile for HY-100

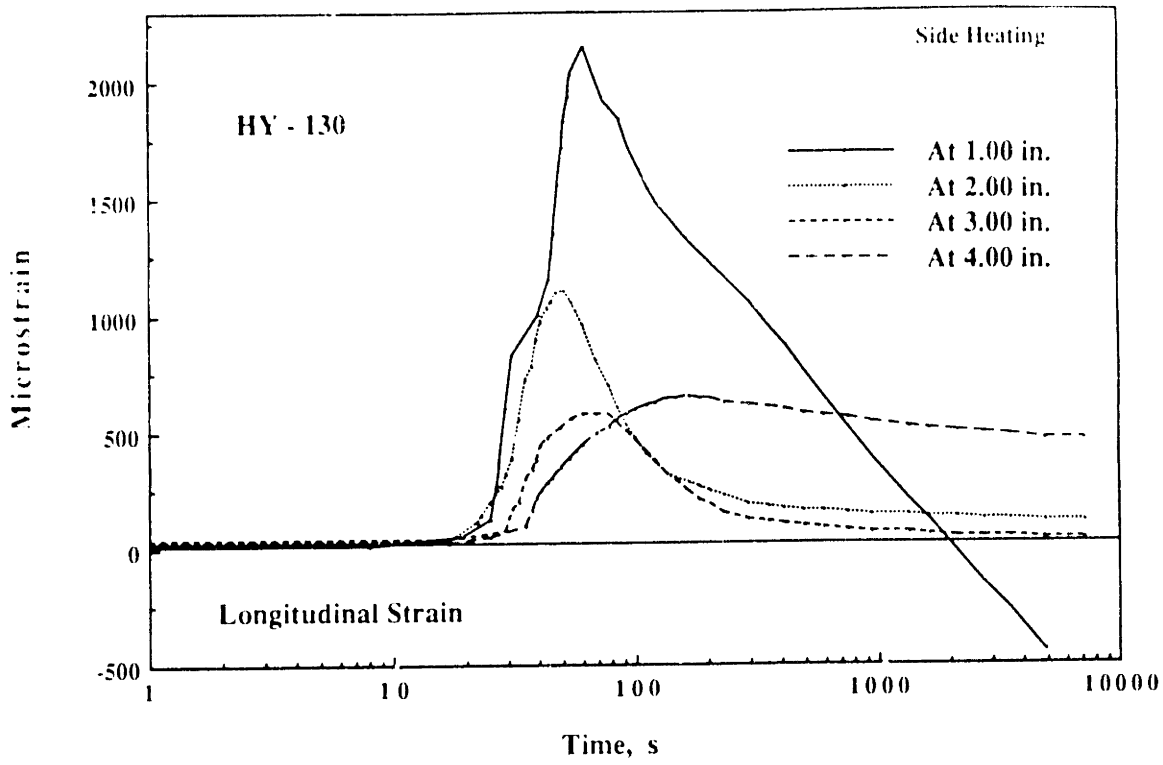

Figure 2-63: Transient Longitudinal Strain Profile for HY-130

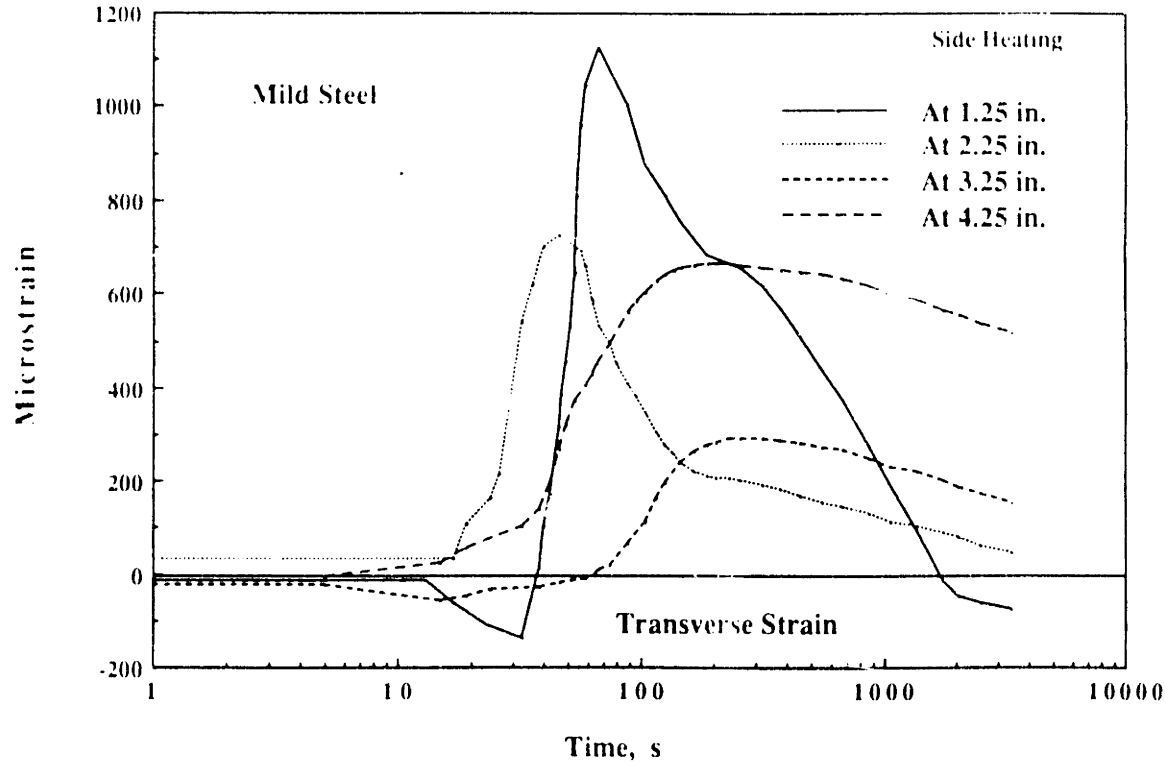

Figure 2-64: Transient Transverse Strain Profile for Low Carbon Steel

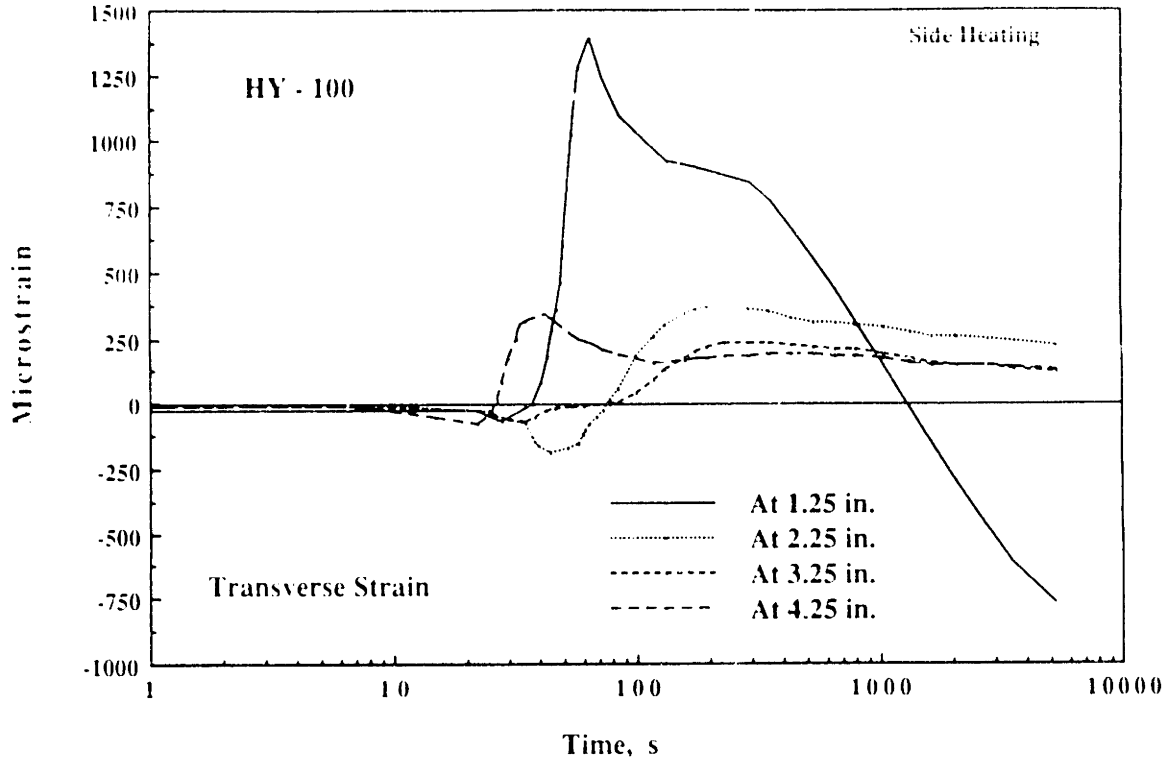

Figure 2-65: Transient Transverse Strain Profile for HY-100

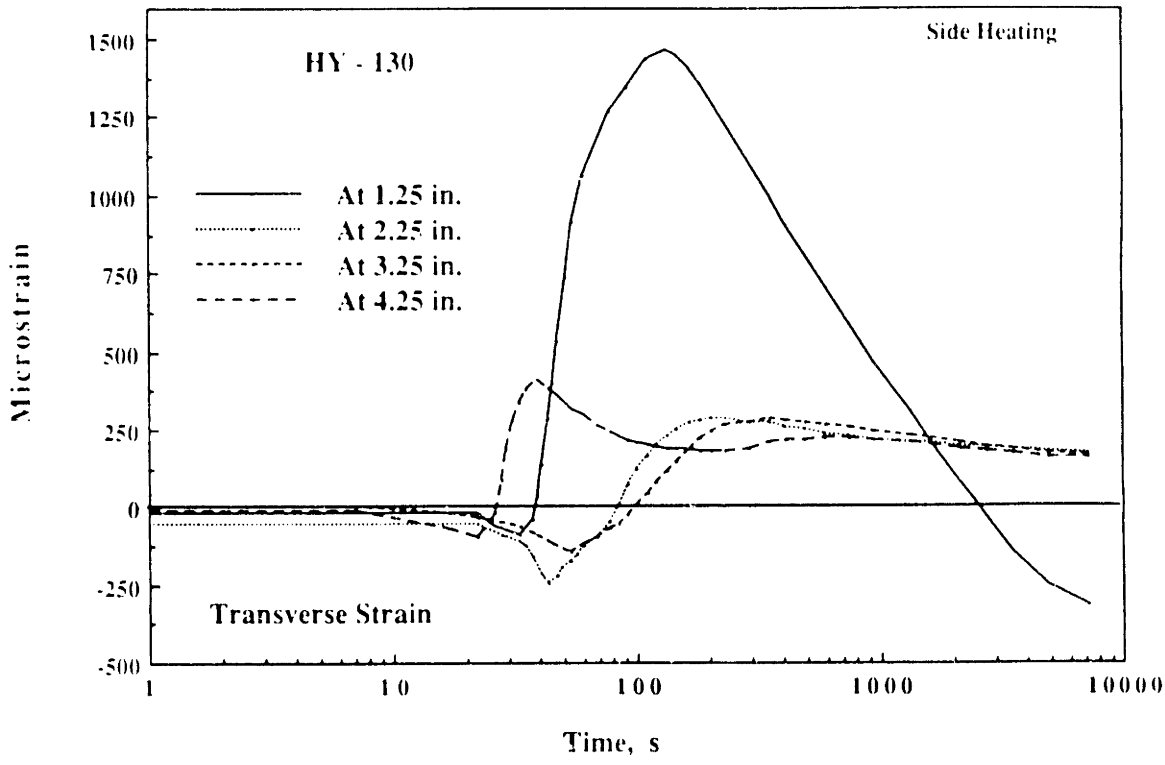

Figure 2-66: Transient Transverse Strain Profile for HY-130

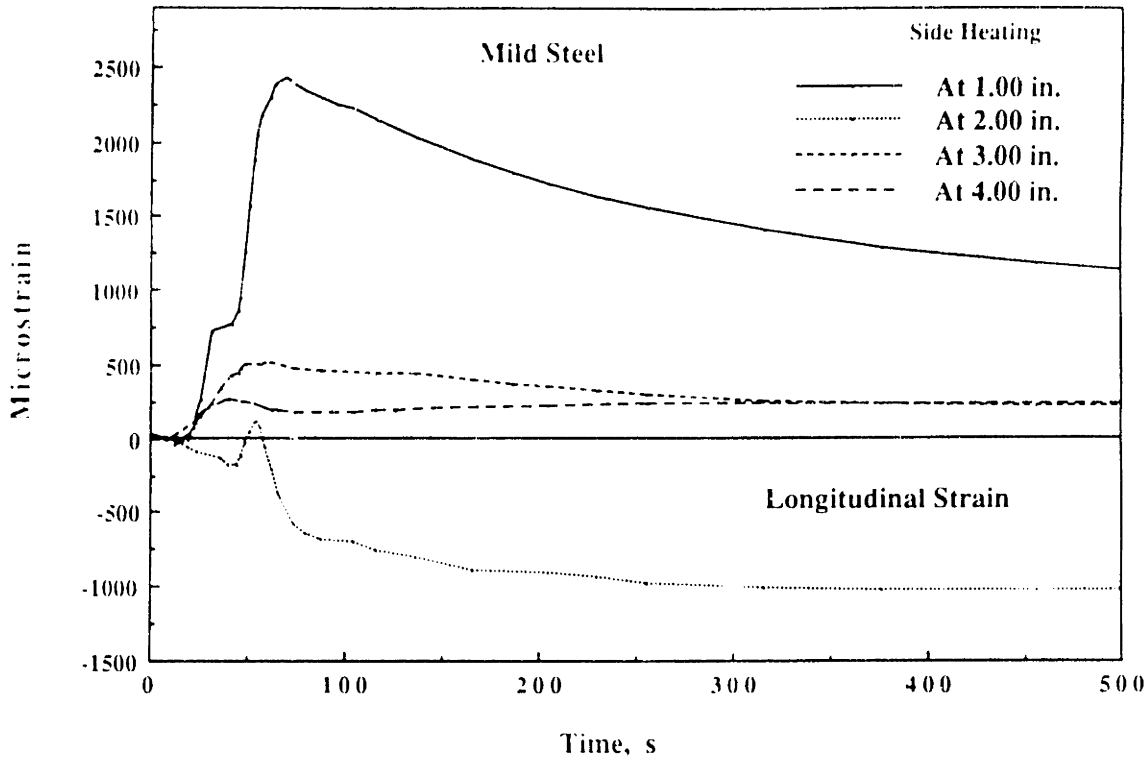

Figure 2-67: Transient Longitudinal Strain Profile for Low Carbon Steel

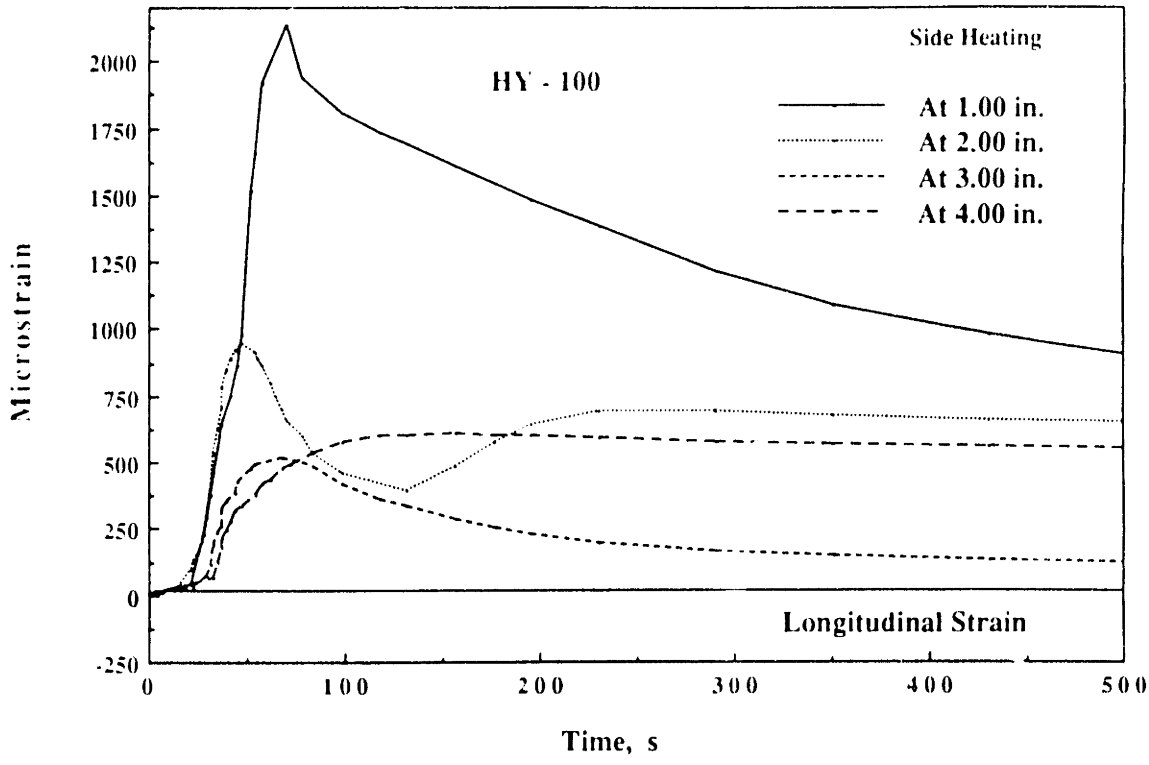

Figure 2-68: Transient Longitudinal Strain Profile for HY-100

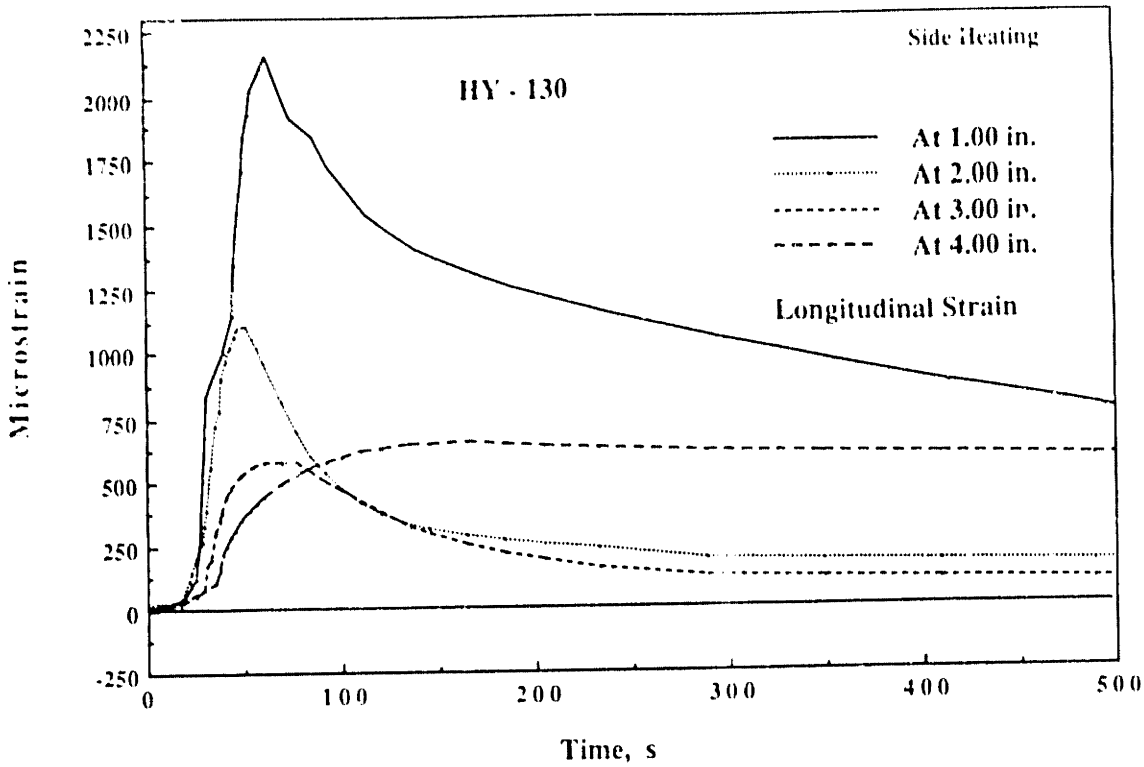

Figure 2-69: Transient Longitudinal Strain Profile for HY-130

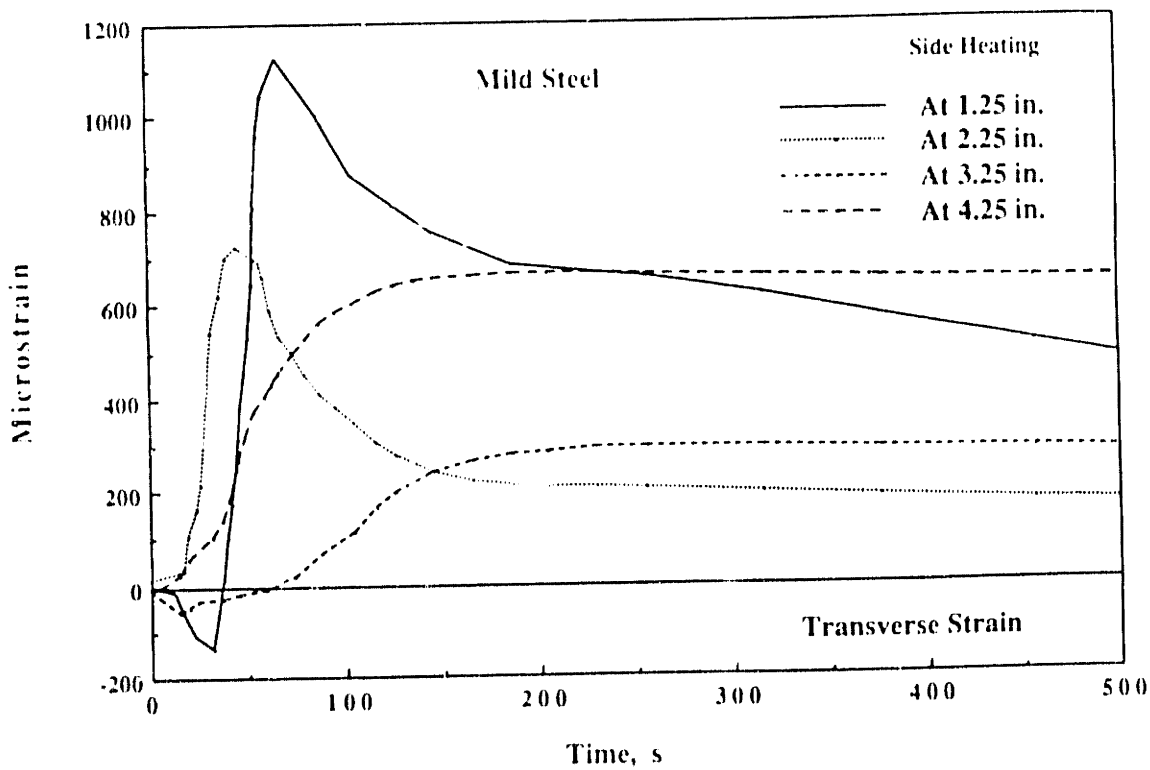

Figure 2-70: Transient Transverse Strain Profile for Low Carbon Steel

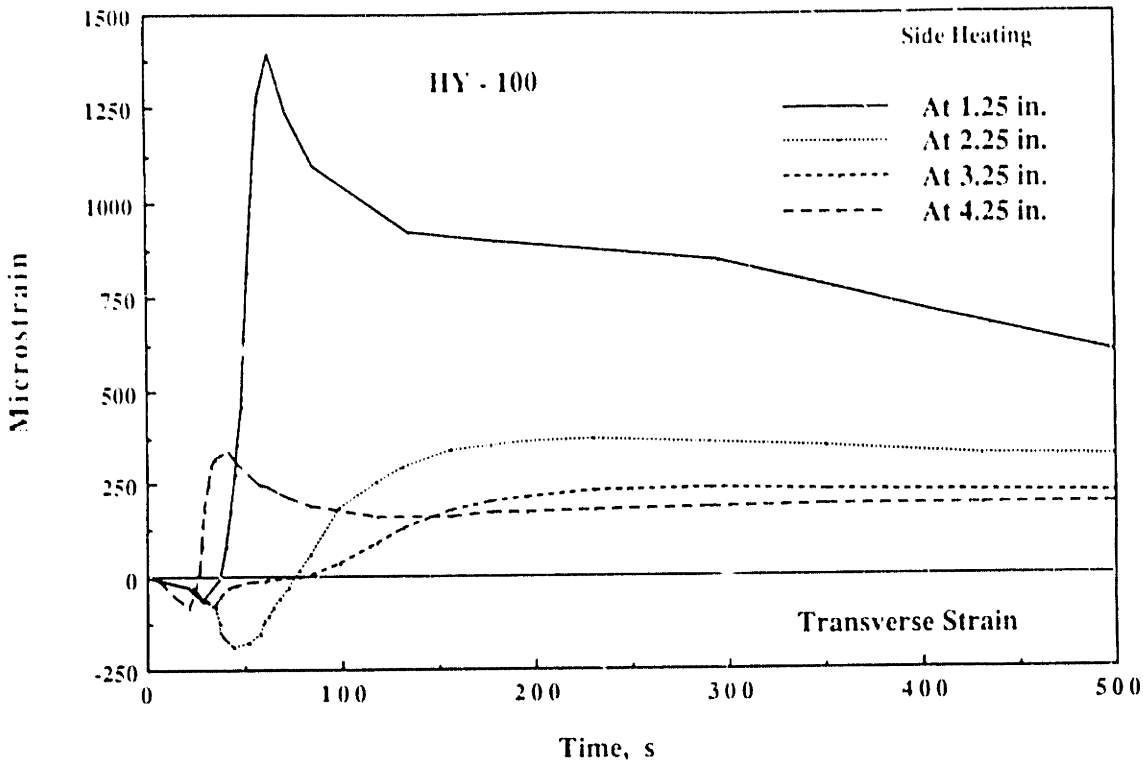

Figure 2-71: Transient Transverse Strain Profile for HY-100

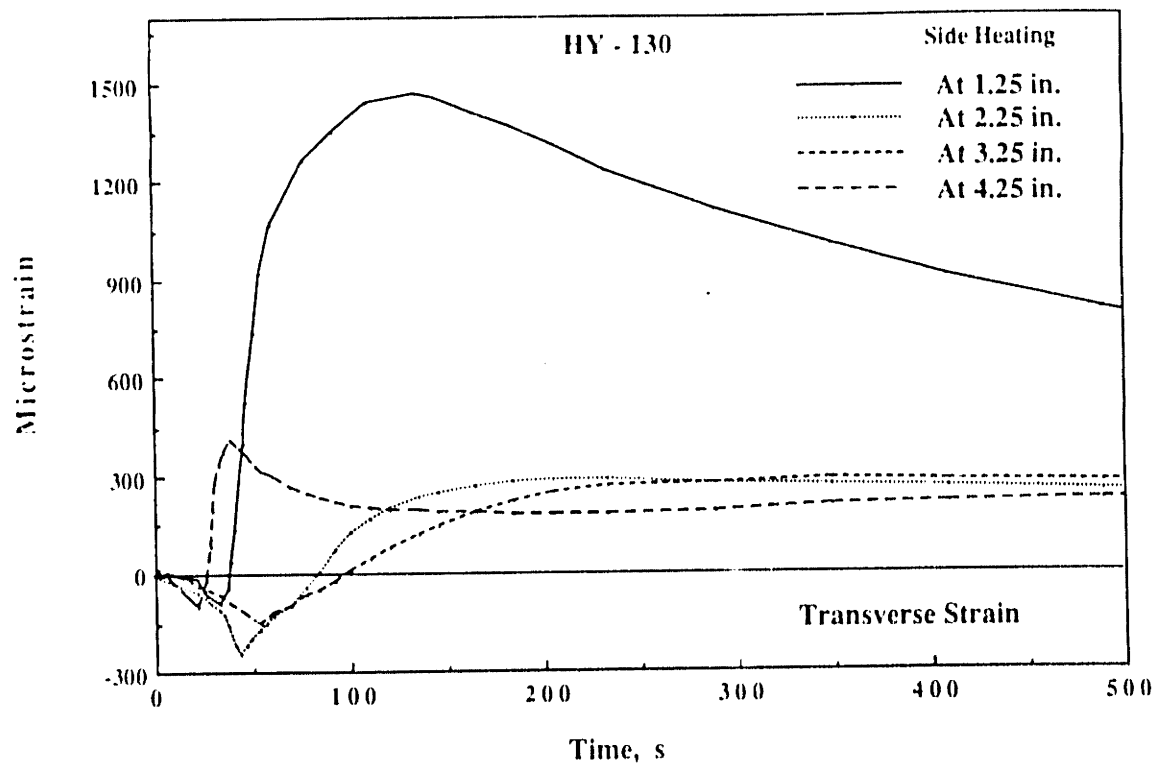

Figure 2-72: Transient Transverse Strain Profile for HY-130

The last part of this set of experiments was conducted to determine the residual stresses. Figures 2-73 to 2-78 show the resulting residual stresses and compare them with those in cases without side heating. Residual stresses were reduced in both longitudinal and transverse directions. For low carbon steel the longitudinal residual stress could be reduced as much as 35% near the weld line and about 33% far away from the weld line. The transverse residual stress could be reduced about 23% near the weld line and 33% far away from the weld line. For HY-100 the longitudinal residual stress was reduced 34% near the weld line and 29% away from the weld line. The transverse residual stress was reduced 33% near the weld line and 37% away from the weld line. For HY-130 the longitudinal residual stress could be reduced about 23% near the weld line and 29% away from the weld line. The transverse strain was reduced 23% near the weld line and 24% away from the weld line.

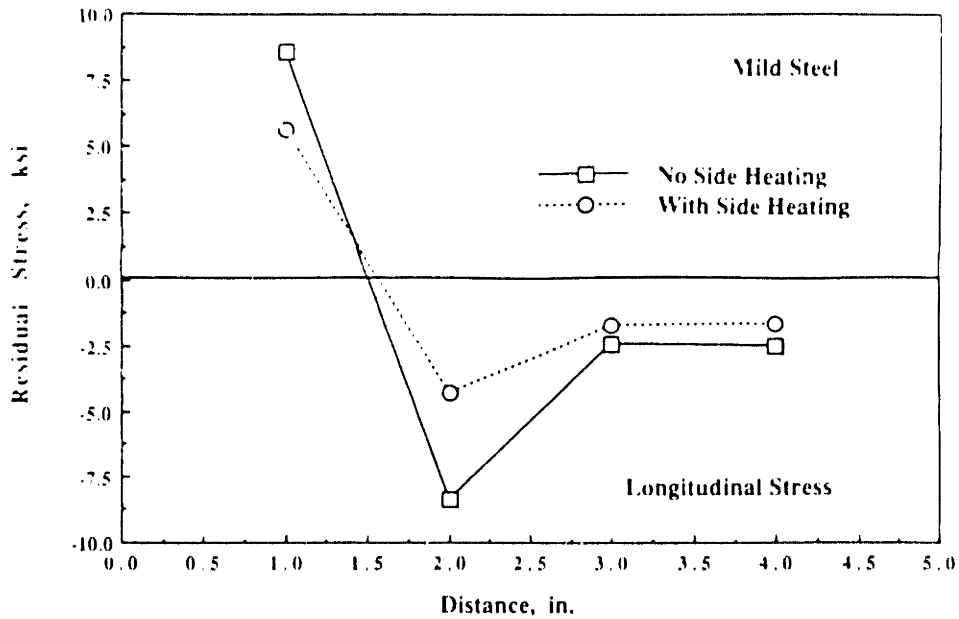

Figure 2-73: Longitudinal Residual Stress Distribution for Low Carbon Steel

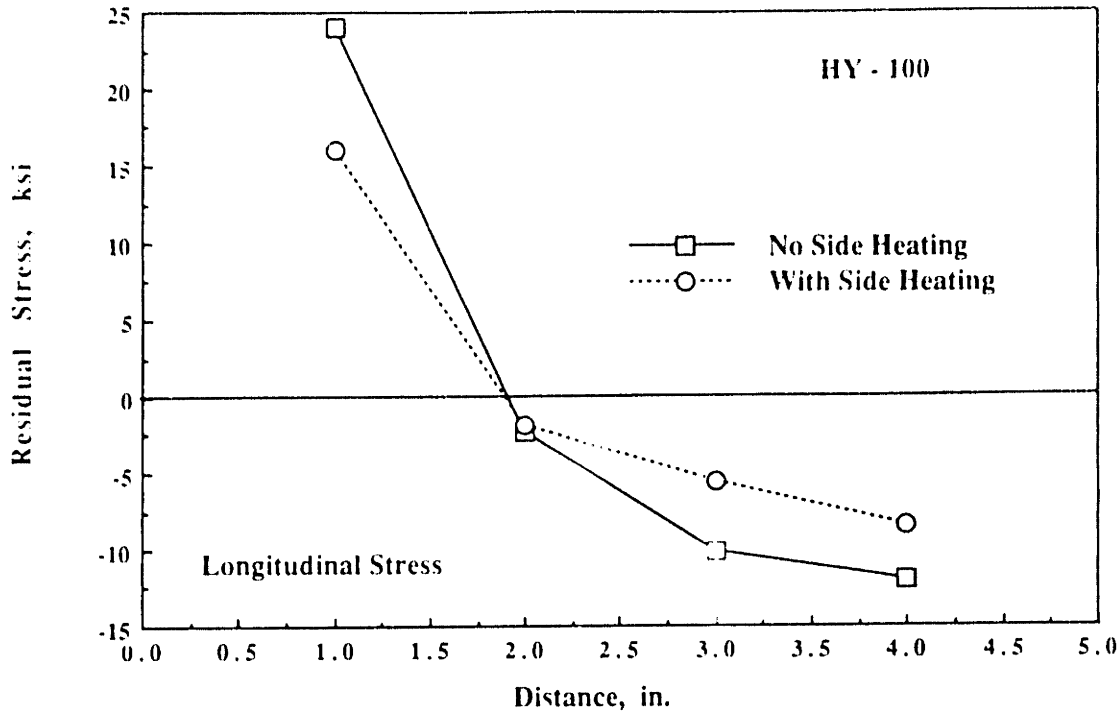

Figure 2-74: Longitudinal Residual Stress Distribution for HY-100

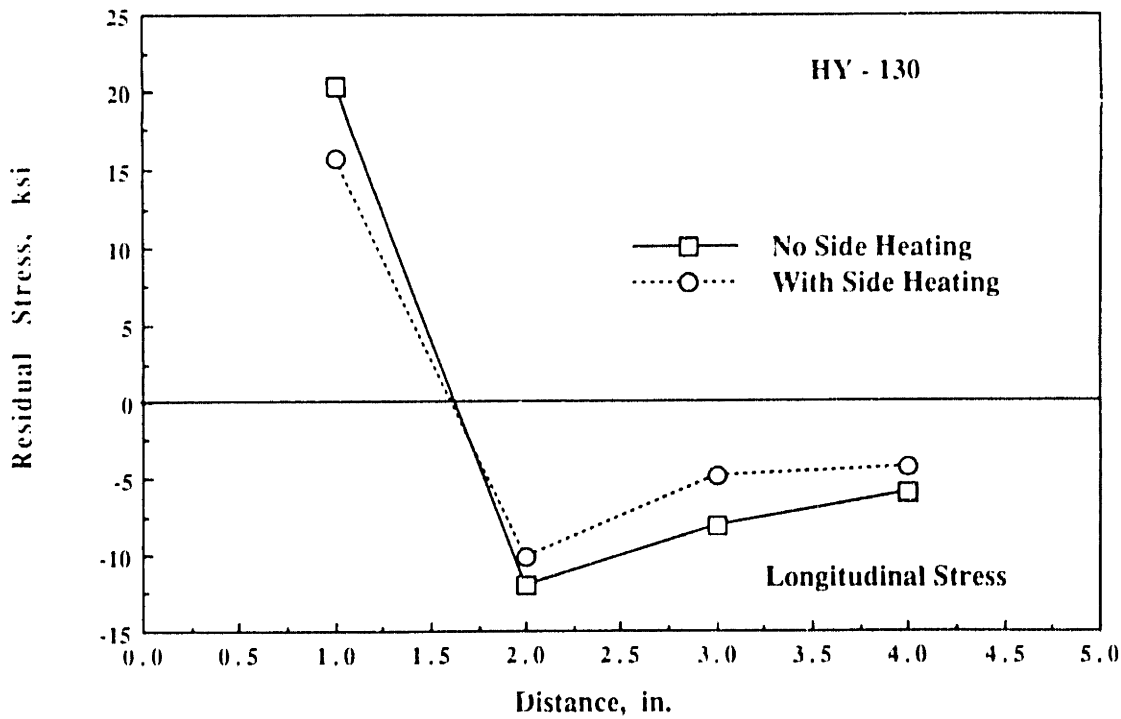

Figure 2-75: Longitudinal Residual Stress Distribution for HY-130

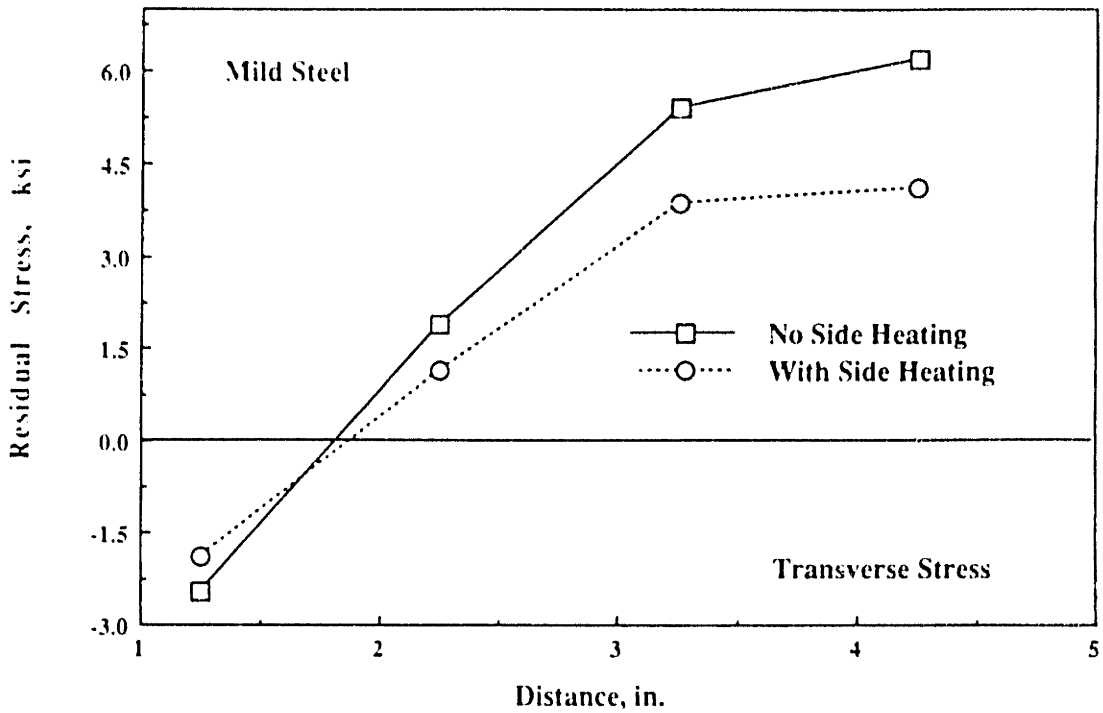

Figure 2-76: Transverse Residual Stress Distribution for Low Carbon Steel

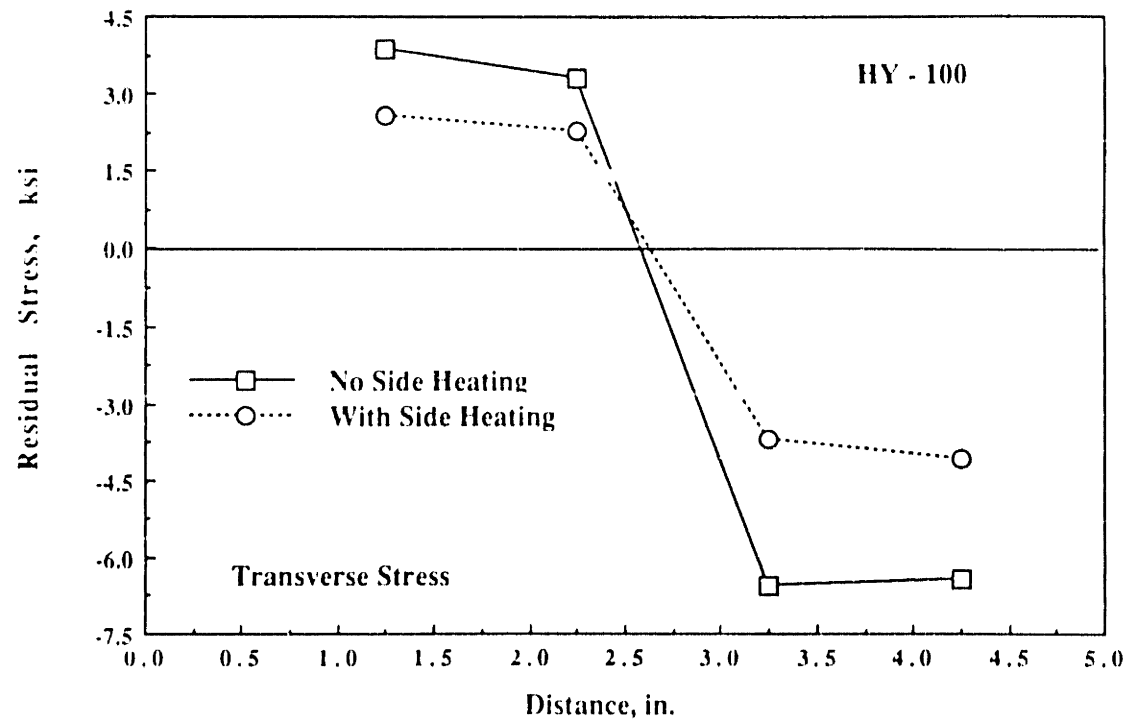

Figure 2-77: Transverse Residual Stress Distribution for HY-100

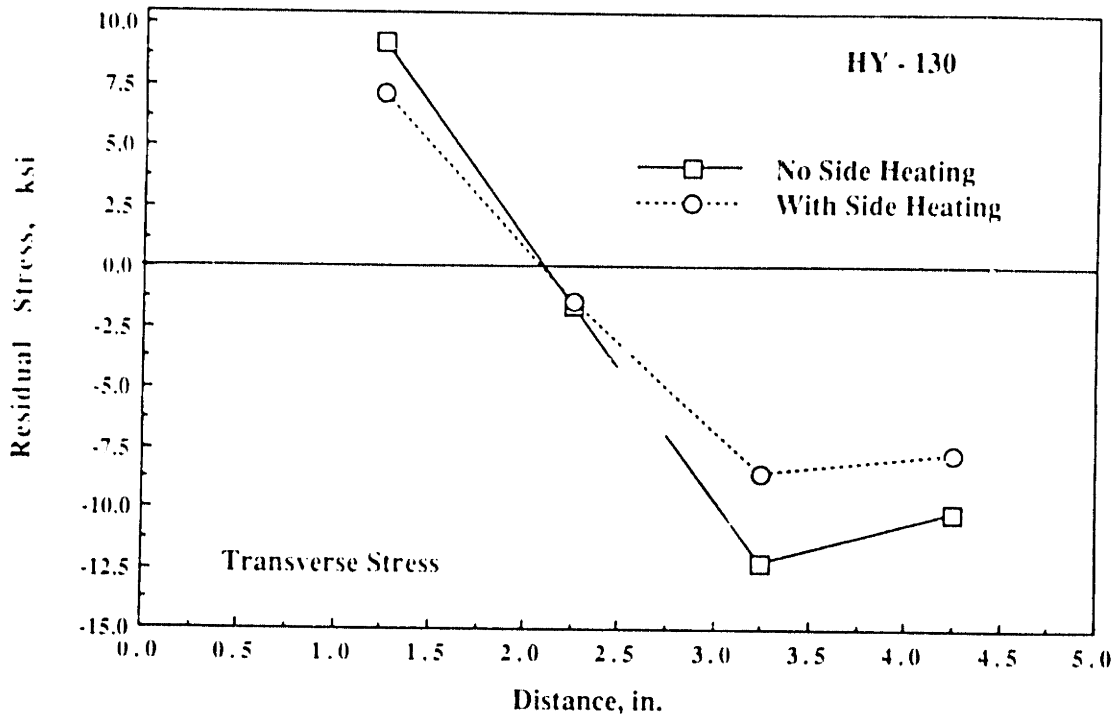

Figure 2-78: Transverse Residual Stress Distribution for HY-130

2.6 Summary

This experimental investigation demonstrated that the side heating technique was indeed effective in reducing both distortion and residual stresses. By heating along with the welding arc far from the weld region at a moderate temperature (200 °F and over), the distortion can be significantly reduced, ranging from 58% for low carbon steel to 44%-48% for HY-100 and HY-130. The residual stresses can be reduced as well, ranging between 23%-34% for all three types of steel. This provides a basis for establishing a method of in-process reduction of distortion and residual stresses during the welding operation.

Chapter 3

Analytical and Numerical Treatment of Heat Flow

3.1 Introduction

Residual stresses and distortion that result from welding have their origin in uneven temperature distribution as well as in the fast heating and cooling rate that occur during the welding operation. Therefore, it is very important to be able to predict temperature distribution during welding. This importance has been recognized for many years by both scientists and engineers working with welding problems. Attempts to solve the problem of heat flow during welding in order to predict temperature distribution can be classified into 3 categories:

1.) Empirical formulas derived from experimental results and knowledge obtained from long years of welding experience.

2.) Analytical solutions derived from the simplified heat conduction equation.

3.) Numerical techniques to solve the nonlinear heat conduction equation.

All of these techniques have some advantages and disadvantages. The empirical formulas can be derived by conducting several experiments and observing factors that influence the temperature distribution during welding. Examples of such parameters are welding heat input, welding speed, heating and cooling rate, thermal properties of material, types of welding process, etc. This analysis obviously consumes a lot of time and has very limited applicability because results depend on several factors, mentioned above, during welding operation. Its accuracy also depends on how well the experiments are performed. The empirical analysis seems to be preferred by practical engineers due to its simplicity and mathematical simplicity. The analytical approach, on the other

hand, requires some mathematical concepts and assumptions in order to simplify the analysis. This is because heat flow during welding is basically the heat conduction in a solid in which the governing equation is highly nonlinear. The analytical approach, therefore, can identify some important parameters but can not guarantee high accuracy of the result. The numerical approach takes advantage of the present fast growing computer technology that makes mathematical operations fast. This approach enables us to include more realistic assumptions in order to improve the accuracy of the results. The analysis, however, does not gain much success due mainly to the prohibitively high computational cost, time, and the insufficient understanding of welding phenomenon, especially near the welding arc.

In this study both analytical and numerical approaches were used to solve the heat transfer problem. For the analytical approach, a three-dimensional finite heat source model developed by Papazoglou [50] was used to calculate the temperature distribution in the weldment. This finite heat source model was later modified to include the secondary heat source; i.e., side heating heat source, to calculate the temperature distribution when the side heating was provided. A finite element method was used to solve the heat transfer problem during welding for the numerical approach. The finite element model for heat transfer analysis was developed and run using Automatic Dynamic Incremental Nonlinear Analysis of Temperature (ADINA-T) finite element program. Results from both the analytical and the numerical approach were then compared with the experimental results.

3.2 Analytical Treatment on Heat Flow Analysis

3.2.1 Literature Review

The differential equation governing the temperature distribution in a solid body can be derived from the energy conservation law and the Fourier equation [48].

$$q_n = -kA\frac{\partial T}{\partial n} \tag{3.1}$$

where n is any direction in space, A is the area normal to n and q_n is the heat transfer rate in any direction. $T(x,y,z,t)$ is the temperature and k is the coefficient of thermal conductivity. If a quantity $\dot{Q}_G$ is defined as the heat generation per unit volume and time, then using the energy conservation concept, the governing equation for heat conduction in a solid is:

$$\rho c\frac{\partial \theta}{\partial t} = \dot{Q}_G + \frac{\partial}{\partial x}(k\frac{\partial \theta}{\partial x}) + \frac{\partial}{\partial y}(k\frac{\partial \theta}{\partial y}) + \frac{\partial}{\partial z}(k\frac{\partial \theta}{\partial z}) \tag{3.2}$$

where

θ = temperature,

t = time,

x, y, z = coordinate system,

ρ = density,

c = specific heat,

k = thermal conductivity,

$\dot{Q}_G$ = heat generated per unit volume and time.

Equation 3.2 can be rewritten as follows:

$$\rho c\frac{\partial \theta}{\partial t} = \dot{Q}_G + k[\frac{\partial^2 \theta}{\partial x^2} + \frac{\partial^2 \theta}{\partial y^2} + \frac{\partial^2 \theta}{\partial z^2}] + \frac{\partial k}{\partial \theta}[(\frac{\partial \theta}{\partial x})^2 + (\frac{\partial \theta}{\partial y})^2 + (\frac{\partial \theta}{\partial z})^2] \tag{3.3}$$

Rosenthal [53] [54] was the first to derive the exact analytical solution for heat flow during welding. His study was essentially an analysis of heat

conduction in a solid due to a moving heat source. He first assumed that welding was performed over a sufficient length so that the temperature distribution around the heat source would not change in the coordinate system moving along with the heat source. This phenomenon is called quasi-stationary or quasi-steady state. In addition, he also made the following assumptions:

1. The physical properties of the conducting medium are constant.

2. No heat losses through the surface of the conducting medium to the surrounding atmosphere.

3. Heat created in electric welding by Joule effect is negligible.

4. No phase changes and the accompanying absorption or release of latent heat in the conducting medium.

5. The conducting medium is infinitely large in the two-dimensional case (line heat source) and semi-infinitely large in the three-dimensional case (point source).

Based on the above assumptions, the highly nonlinear heat conduction equation can be reduced to a linear one as follows:

$$\frac{\partial^2\theta}{\partial w^2} + \frac{\partial^2\theta}{\partial y^2} + \frac{\partial^2\theta}{\partial z^2} = -\frac{v}{\kappa}\left(\frac{\partial\theta}{\partial w}\right) \tag{3.4}$$

where

$w = x - vt$; moving coordinate,

$v =$ welding speed,

$\kappa = \frac{k}{c\rho} =$ thermal diffusivity.

Two exact solutions for line and constant heat sources for the two and three-dimensional cases were derived from Equation 3.4 (see Fig. 3-1 and Fig. 3-2):

$$\theta - \theta_o = \frac{Q}{2\pi kH} e^{-\lambda v w} K_0(\lambda v r) \tag{3.5}$$

$$\theta - \theta_o = \frac{Q}{2\pi k} e^{-\lambda v w} \frac{e^{-\lambda v R}}{R} \tag{3.6}$$

where

θ_0 = initial temperature,

Q = total heat input,

H = plate thickness,

$r = (w^2 + y^2)^{1/2}$,

$R = (w^2 + y^2 + z^2)^{1/2}$,

$\frac{1}{2}\lambda = \kappa$ = thermal diffusivity,

$K_0(x)$ = modified Bessel function of second kind and zero order.

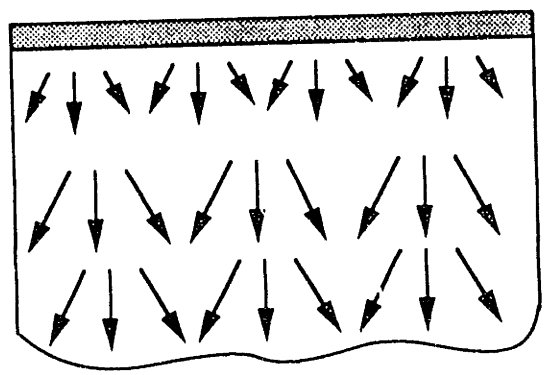

Figure 3-1: Two-Dimensional Heat Flow : Thin Plate

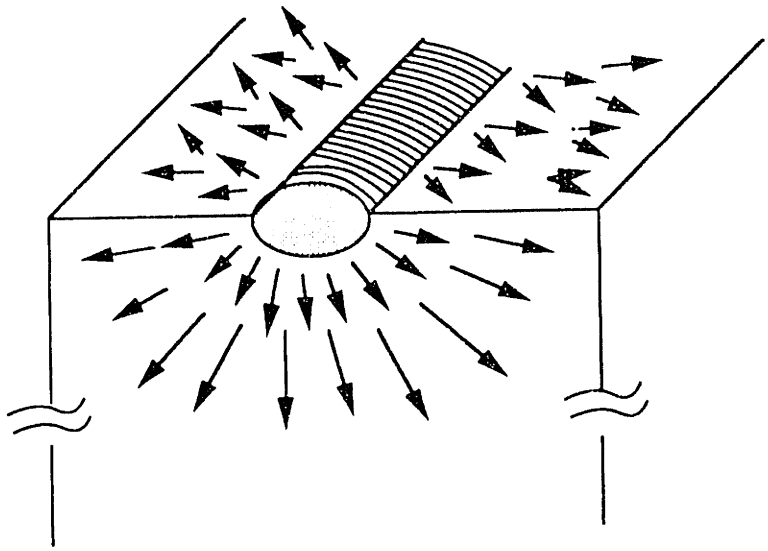

Figure 3-2: Three-Dimensional Heat Flow : Semi-infinite Plate

Heat losses through the surface to the surrounding atmosphere can be taken into account by replacing the factor λw in the Bessel function of Equation 3.5 [53] by:

$$[\,(\lambda w)^2 + \frac{h_1 + h_2}{kH}\,]^{1/2} \tag{3.7}$$

where h_1 and h_2 are the heat transfer coefficients, assumed constant, at the top and bottom of the plate, respectively. Solutions for the case of large but finite thickness and/or finite breadth plates, for example a weld bead lays on a finite thickness plate with no heat losses through surrounding atmosphere can be obtained by using the so-called "image source method" [53]. to Equation 3.6, yielding:

$$\theta - \theta_0 = \frac{Q}{2\pi k} e^{-\lambda v w} \left(\frac{e^{-\lambda w R}}{R} + \sum_{n=1}^{\infty} \left[\frac{e^{-\lambda w R_n}}{R_n} + \frac{e^{-\lambda w R_n'}}{R_n'} \right] \right) \tag{3.8}$$

where

$$R_n = [\,w^2 + y^2 + (2nH - z)^2\,]^{1/2}, \tag{3.9}$$

$$R_n' = [\,w^2 + y^2 + (2nH + z)^2\,]^{1/2}. \tag{3.10}$$

This conventional point heat source closed form solution was later modified to simulate multipass welds by applying the method of images [50]. Figure 3-3 shows the superposition of heat sources necessary to obtain the desired solution. The welding heat source is situated at point O. Two imaginary heat sources T_1 and B_1, being the mirror images of welding heat source with respect to the two surfaces, are added to maintain the adiabatic boundary condition on the top and bottom surface of the plate. These new sources, however, produce heat transfer through the two surfaces. Consequently, new image sources of them should be taken at infinity. For practical purposes, around 30 total imaginary sources are required to obtain the solution. The solution can be expressed by the following equation:

$$\theta = \theta_o + \frac{Q}{4\pi k} e^{-\lambda v w} \left(\frac{e^{-\lambda v R}}{R} + \sum_{n=1}^{\infty} \left[\frac{e^{-\lambda v R_n}}{R_n} + \frac{e^{-\lambda v R_n'}}{R_n'} \right] \right) \tag{3.11}$$

where

$$R_n = (w^2 + y^2 + (OT_n + z)^2)^{1/2},$$

$$R_n' = (w^2 + y^2 + (OB_n - z)^2)^{1/2},$$

$$OT_n = OB_{n-1} + 2F,$$

$$OB_n = OT_{n-1} + 2G.$$

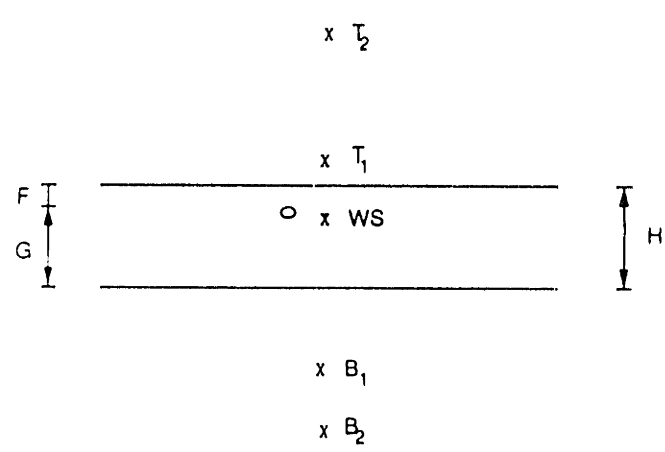

Figure 3-3: Superposition of Heat Sources

This modification helps to locate the point source at any point within the plate thickness as well as to include the effect the joint shape has on temperature distribution. Whereas, in the conventional solution point source it can only be located on the top surface of the plate [50].

Rosenthal and Schmerber [59] tested the two-dimensional solution, Equation 3.5, experimentally. Results obtained from the solution were in good agreement with experimental ones except for the solution in the neighborhood of the arc. This was due to the high temperature in that region which resulted in a large change in material properties. Therefore, the assumption of constant material properties was severely violated. Mahla [30] proposed a solution for the case of a point source moving on the top surface of a semi-infinite conducting medium which is adiabatic along its boundaries as follows:

$$\theta - \theta_o = \frac{Q}{2\pi kR} e^{-\lambda v(w+R)}(1-\gamma) \tag{3.12}$$

where

$\gamma = \frac{\beta}{\lambda v R}(1 + \frac{1}{\lambda v R})$,

$\beta = \frac{(\lambda v)^2}{24}(4p^2 + d^2)$,

$p =$ weld penetration,

$d =$ weld width.

This solution, however, overestimated maximum temperature and cooling rates when compared with experimental results.

Adam [1] developed a solution based on extensive experiments to determine the peak temperature and cooling rate as follows:

$$\frac{1}{T_p - T_o} = \frac{4.13\rho ctY}{H_{net}} + \frac{1}{T_m - T_o} \tag{3.13}$$

$$R = \frac{2\pi k(T_c - T_o)^2}{H_{net}} \tag{3.14}$$

where

T_p = peak temperature, °C,

Y = the distance from the weld fusion boundary,

T_o = initial temperature, °C,

T_m = melting temperature, °C,

H_{net} = net energy input,

t = plate thickness,

R = cooling rate,

T_c = particular temperature of interest.

His solution, however, did not include the effect of latent heat near the heat source region and therefore, the solution yielded a higher temperature than the experimental one. Papazoglou [50] compared the results of the modified point heat source solution (Equation 3.11) with the convention point source (Equation 3.10). His results showed the overestimate of temperature for point source located on the top surface of the plates. The overestimation being even more pronounced in the high temperature region close to the weld centerline. However, he showed good correlation between experimental results and those obtained using the modified approach.

It is necessary to be able to predict the high temperature region as accurately as possible since this region is directly related to the size of the plastic zone and the accompanying residual stresses and distortion. This can be done by treating the temperature dependence of material properties.

Grosh [22] formulated a solution to predict temperature distribution by assuming that thermal conductivity, k, and the product of density and specific heat, ρc, vary in the same manner with temperature so that their ratio, the thermal diffusivity, remains constant. The solution for the two-dimensional case is as follows:

$$\theta = \frac{1}{\gamma}\left[\left\{ \frac{\gamma Q}{\pi k_o H} e^{-\lambda v w} K_o(\lambda v r) + (1+\gamma\theta_o)^2 \right\}^{1/2} - 1 \right] \qquad (3.15)$$

where

$$k = k_0(1 + \gamma\theta),$$

$$\rho c = (\rho c)_0(1 + \gamma\theta).$$

It was found that this linearity assumption is valid only in some aluminum alloys. For other materials, k and ρc cannot be assumed to vary according to the same law.

Nishida [48], and Papazoglou [51] adopted the iteration method to take into account the temperature dependence of material properties. The fundamental heat source solution with material properties at some temperature is used to provide the first approximate solution at a particular point. This temperature is then compared with the initial guess and if the two temperatures disagree by more than 0.5 $^{\circ}C$, new properties are found for a temperature half-way in between. These new values are used to obtain a new temperature estimation. The process is repeated until convergence is reached. It should be pointed out that although this iteration method generally gives good predictions outside the fusion zone, there is no guarantee that it will converge to the correct solution since the approximation used may not satisfy the law of energy conservation. The first temperature estimation is a key point for the success of this process in order to keep the whole temperature range during iteration within the confines of energy conservation law.

3.3 Heat Input

The heat input that enters the plate or section being welded is normally expressed by the formula:

$$Q = \eta_a VI \tag{3.16}$$

where V and I are the arc voltage and current respectively. The coefficient η_a is the so-called arc efficiency. It represents the ratio of the power introduced by the arc into the metal to the total electric arc power. This empirical formula takes into account the various heat losses that occur through electrode tip heating, radiation to the surrounding atmosphere, metal spatter, etc.

In general, the arc efficiency is very much dependent on the welding process used, the penetration achieved, the shielding gas, and many other factors which make it difficult to be predicted. Groove geometry also effects efficiency. A compact arc in a V groove has a greater efficiency than an arc depositing a bead-on-plate weld. Christensen [14] [15] made extensive measurements using the calorimetry method and found approximate ranges of the arc efficiency for various welding processes. Table 3-I is a summary of the values proposed by Christensen [14], Rykalin [55] [56], and Tsai [64].

Table 3-I: Values of Arc Efficiency for Various Processes

	Christensen	Rykalin	Tsai
GMAW	---	0.65-0.85	---
Mild Steel	0.66-0.70	---	0.80-0.90
Aluminum	0.70-0.85	---	---
SAW	0.90-0.99	0.90-0.99	0.85-0.98
SMAW	---	---	---
Mild Steel, AC	0.66-0.85	0.65-0.85	0.55-0.90
GTAW	---	---	---
Mild steel, AC	0.22-0.48	0.20-0.50	---
Mild Steel. DC	0.36-0.46	0.45-0.75	---
Aluminum, AC	0.21-0.43	0.20-0.50	---

Nomenclature

GMAW = Gas Metal Arc Welding

SAW = Submerged Arc Welding

SMAW = Shielded Metal Arc Welding

GTAW = Gas Tungsten Arc Welding

The heat distribution is also important. Rykalin [55] proposed a heat distribution in a form of Gaussian radial heat flux distribution as follows:

$$q(r) = q_0 e^{-Cr^2} \tag{3.17}$$

where

q_0 = maximum heat flux at the center of the heat spot,

C = heat flux concentration coefficient,

r = radial distance from the center of the heat spot.

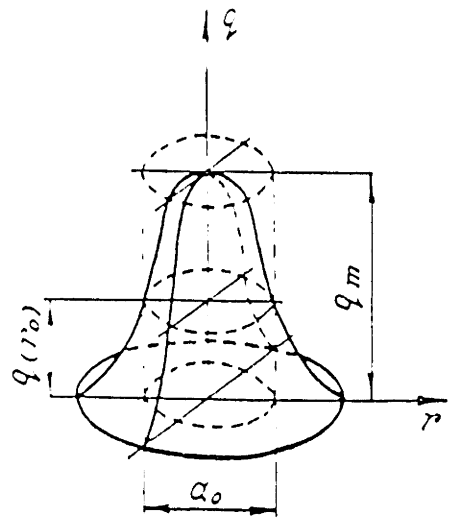

Figure 3-4: Gaussian Radial Heat Flux Distribution

This distributed heat source (Fig. 3-4) has a characteristic that the higher C is, the more concentrated a heat source is and the smaller the diameter d_h of the heat spot. Experimental data on the range of concentration coefficients for various welding processes are shown in Table 3-II [56].

Table 3-II: Experimental Values for the Concentration Coefficient

Welding Process	C, [cm^{-2}]	Polarity, Current
GMAW	1.26-1.32	ac, 550-1100A
SAW	1.00-2.50	ac, 550-1200A
SMAW	1.26-1.32	ac, 550-1100A
GTAW, steel	6.00-14.00	dcsp, 40-200A
Carbon electrode	1.00-3.50	dcsp, 95-2500A

The distance $r_h = \frac{d_h}{2}$ is defined as this at which the heat flux $q(r_h)$ falls to 0.05 of the maximum heat flux q_o. The diameter of the heat spot is then found to be as follows:

$$d_h = 2(\frac{3}{C})^{1/2} \tag{3.18}$$

The expression shows that the diameter of the heat spot is inversely proportional to the square root of the concentration coefficient C.

Tsai [64] modified Equation 3.17 to take into account a moving action of arc which is not radially symmetric but rather distorted backwards. This can be observed using high speed photography technique. He proposed the following equation for the arc heat distribution:

$$q(r,w) = q_o e^{-Cr^2 - \lambda v w} \tag{3.19}$$

In the cylindrical coordinate system, the equation can be written in the following form:

$$q(r,\psi) = q_o e^{-Cr^2 - \lambda v r \cos\psi} \tag{3.20}$$

Equation 3.19 clearly represents the backward distortion of the arc heat distribution; i.e., more heat enters the plate behind the arc than ahead of it, if calculated at a constant radial distance r from the center of the arc column.

3.4 Side Heating Heat Input

The oxyacetylene flame used in this investigation as a side heating source is generally used for brazing, soldering, and pre- and post heating of the weldment. The oxyacetylene flame heats up the metal surface by an intense heat exchange, mainly by force convection. The radiation in the heat exchange is small and seldom exceeds 5-10%. The intensity of the heat exchange increases with increasing differences in temperature between the flame and the surface, as well as with the increased rate of the hot gas flow. This intensity of the heat exchange, being an effective power of the flame, drops as the rise of the metal surface temperature approaches a limit value. The flame efficiency is therefore represented by the ratio of this limit of effective power to the total flame thermal power.

$$\eta_f = \frac{\text{Effective Power of the Flame } (P_{eff})}{\text{Total Flame Thermal Power } (P)} \tag{3.21}$$

Rykalin [57] investigated the flame efficiency and used the Gaussian radial heat distribution to express gas flame heat distribution. He presented the relation between effective power and efficiency of the oxyacetylene flame and acetylene consumption as shown in Fig. 3-5. Table 3-III shows the flame power and heat concentration for different tip sizes of torch TC-49 corresponding to different acetylene consumption rates. Anderson and Stresino [2] did experimental studies on heat transfer from flames impinging on flat plate and cylindrical surfaces. Table 3-IV shows the summary of their results with surface probe and tube probe measurements. The flame efficiency varies from 19% to 59%. Heat distribution is expressed by maximum heat transfer intensity, average heat transfer intensity for a 1/8 inches radius area and heat transfer intensity at about 1/4 inches and 1/2 inches distance from the flame axis.

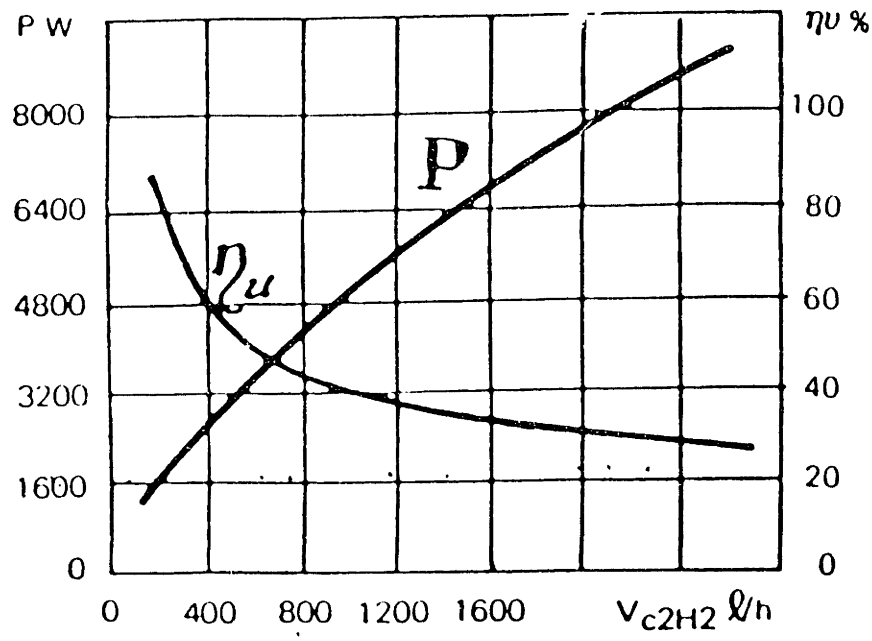

Figure 3-5: Effective Power and Efficiency of the Oxyacetylene Flame versus Acetylene Consumption

Table 3-III: Thermal Characteristic of Oxyacetylene Flame of Standard Torches

Tip Size TC-49	Acetylene Consumption l/hr	Flame Power cal/sec	Efficiency %	Concentration cm^{-2}
1	150	380	72	0.39
2	250	600	68	0.35
3	400	720	51	0.31
4	600	920	44	0.28
5	1000	1270	36	0.23
6	1700	1750	30	0.20
7	2600	2250	25	0.17

Table 3-IV: Flame Efficiencies and Heat Distribution of Various Gas Flame

Test no.	1	2	3	4	5	6	7
A	O_2-H_2	O_2-C_2H_2	O_2-C_2H_2	O_2-C_2H_2	Air-CH_4	Air-CH_4	Air-CH_4
B	Jet	Jet	P.B.	P.B.	P.B.	P.B.	P.B.
C	0.375	0.375	0.070	0.070	0.500	0.625	0.625
D	0.375	0.375	0.40	0.40	0.64	0.80	1.00
E	1100	105	3.7	9.4	2.9	2.9	2.4
F	550	525	13	10.1	21.1	21.1	13.7
G	0.5	5.0	3.5	1.07	1.5	1.5	1.2
H	...	...	0.6	0.3	2.3	2.7	1.5
I	0.5	0.375	0.6	0.3	2.0	2.0	1.5
J	3300	2660	160	200	125	40	5
K	32	28	59	59	43	49	19
L	9.2×10^6	3.6×10^6	6.5×10^5	9.3×10^5	2.6×10^6	2.1×10^6	1.0×10^6
M	6.6×10^6	2.9×10^6	5.7×10^5	6.2×10^5	2.6×10^6	2.1×10^6	8.3×10^5
N	2.8×10^6	1.5×10^6	3.5×10^5	2.4×10^5	2.5×10^6	2.2×10^6	3.6×10^5
O	1.2×10^6	1.0×10^6	2.0×10^5	1.4×10^5	2.4×10^6	2.1×10^6	2.1×10^6

[a] Key to Symbols in Tables 1 and 2

A = Reactants
B = Type of burner—Jet or Postburning (P.B.)
C = Diameter of burner nozzle, in.
D = Flame diameter at probe, in.
E = Fuel rate (C.F.H. at N.T.P.)
F = Oxidant rate (C.F.H. at N.T.P.)
G = Ratio of oxygen to fuel
H = Length of inner cone for postburning flames, in.
I = Distance from burner nozzle to probe, in.
J = Estimated velocity of combustion products, ft/sec
K = Total heat transferred to probe, percent of heat available
L = Maximum heat-transfer intensity at flame axis, Btu/hr-ft²
M = Average heat-transfer intensity for ½-in. radius area around flame axis, Btu/hr-ft²
N = Heat-transfer intensity at ½-in. radial distance from flame axis, Btu/hr-ft²
O = Heat-transfer intensity at ½-in. radial distance from flame axis, Btu/hr-ft²

Test no.	8	9	10	11	12	13	14	15	16	17
A	O_2-H_2	O_2-C_2H_2	O_2-C_2H_2	O_2-C_2H_2	O_2-C_2H_2	O_2-C_2H_2	Air-CH_4	Air-CH_4	Air-CH_4	Air-CH_4
B	Jet	Jet	P.B.	P.B.	P.B.	P.B.	P.B.	P.B.	P.B.	P.B.
C	0.375	0.375	0.070	0.070	0.0465	0.0465	0.500	0.625	0.625	1.375
D	0.375	0.375	0.40	0.40	0.22	0.17	0.64	0.80	1.00	1.5
E	1540	105	4.5	9.4	7.1	2.9	2.9	2.9	2.4	4.1
F	770	525	15.7	10.1	7.6	3.1	21.1	21.1	13.7	31
G	0.5	5	3.5	1.07	1.07	1.07	1.5	1.5	1.2	1.6
H	...	...	0.6	0.3	0.35	0.25	2.25	2.7	2.13	1.0
I	0.1	0	0.6	0.3	0.35	0.25	2.25	2.7	2.13	1.56
J	4600	2660	210	200	330	140	125	40	5	1
L	1.3×10^7	6.3×10^6	1.1×10^6	2.3×10^6	3.5×10^6	1.7×10^6	3.6×10^6	2.8×10^6	1.0×10^6	1.5×10^6
M	7.8×10^6	3.6×10^6	8.8×10^5	1.3×10^6	1.5×10^6	6.7×10^6	2.1×10^6	1.7×10^6	7.8×10^5	5.7×10^5

[b] The probe diameter was 0.055-in. od for the oxyhydrogen jet and 0.036-in. id for all other tests.

3.5 Three-Dimensional Finite Heat Source Model

Papazoglou [50] developed a model for heat transfer analysis by including more realistic assumptions to improve the accuracy of predicting temperature distribution. In his study he assumed the following general assumptions:

1. Quasi-stationary state.
2. Thermal conductivity of the material will be assumed to be a linear function of temperature.
3. Thermal diffusivity of the material will be assumed to be constant.
4. The heat input will be provided by a moving three-dimensional Gaussian radial heat flux distribution (Equation 3.19).
5. Convection and Radiation boundary heat losses will be taken into account through a constant average "effective" heat transfer coefficient.
6. Phase transformation and Joule heating effects will not be included.
7. The initial temperature of the plate, θ_o, can be different from the environmental temperature, θ_e, to allow for preheating.

This model was later modified to include the effect from side heating in this study.

3.5.1 Governing Equation

The governing equation for heat flow during welding (Equation 3.2) in a solid body can be rewritten as follows:

$$\frac{\partial}{\partial x}(k\frac{\partial \theta}{\partial x}) + \frac{\partial}{\partial y}(k\frac{\partial \theta}{\partial y}) + \frac{\partial}{\partial z}(k\frac{\partial \theta}{\partial z}) = \rho c\frac{\partial \theta}{\partial t} - \dot{Q}_G \tag{3.22}$$

now let

$$T = \theta - \theta_o \tag{3.23}$$

Equation 3.22 can be rewritten as:

$$\frac{\partial}{\partial x}(k\frac{\partial T}{\partial x}) + \frac{\partial}{\partial y}(k\frac{\partial T}{\partial y}) + \frac{\partial}{\partial z}(k\frac{\partial T}{\partial z}) = \rho c\frac{\partial T}{\partial z} - \dot{Q}_G \tag{3.24}$$

Using Kirchhoff's transformation

$$u = \frac{1}{k_o}\int_0^T k(T)dT \tag{3.25}$$

where

k_o = thermal conductivity at $T = 0$ or $\theta = \theta_o$

$k(T)$ = thermal conductivity function

Assume linear relation for thermal conductivity function

$$k(T) = k_o(1 + \gamma T) \tag{3.26}$$

then

$$u = \frac{1}{k_o}\int_0^T k_o(1 + \gamma T)dT = T + \frac{\gamma}{2}T^2 \tag{3.27}$$

therefore

$$u = \theta - \theta_o + \tfrac{\gamma}{2}(\theta - \theta_o)^2$$

$$= \tfrac{\gamma}{2}\theta^2 + \theta(1 - \gamma\theta_o) + (\tfrac{\gamma}{2}\theta_o^2 - \theta_o) \text{ or}$$

$$\frac{\gamma}{2}\theta^2 + \theta(1 - \gamma\theta_o) + (\frac{\gamma}{2}\theta_o^2 - \theta_o) - u = 0 \tag{3.28}$$

Solving the above equation, we have

$$\theta = \theta_o + \frac{1}{\gamma}(\sqrt{1 + 2\gamma u} - 1) \tag{3.29}$$

or

$$T = \theta - \theta_o = \frac{1}{\gamma}(\sqrt{1 + 2\gamma u} - 1) \tag{3.30}$$

Furthermore, noting that from Equation 3.25 we have

$$\frac{\partial u}{\partial t} = \frac{k(T)}{k_o}\frac{\partial T}{\partial t} \quad \text{or} \quad \nabla u = \frac{k(T)}{k_o}\nabla T \tag{3.31}$$

therefore

$$\frac{\partial T}{\partial x} = \frac{k_o}{k(T)}\frac{\partial u}{\partial x}, \qquad \frac{\partial T}{\partial y} = \frac{k_o}{k(T)}\frac{\partial u}{\partial y}, \qquad \frac{\partial T}{\partial z} = \frac{k_o}{k(T)}\frac{\partial u}{\partial z}$$

Substituting into Equation 3.24, we have

$$k_o\left[\frac{\partial^2 u}{\partial x^2}+\frac{\partial^2 u}{\partial y^2}+\frac{\partial^2 u}{\partial z^2}\right]=\rho c\frac{k_o}{k(T)}\frac{\partial u}{\partial t}-\dot{Q}_G \tag{3.32}$$

or

$$\nabla^2 u=\frac{\rho c}{k(T)}\frac{\partial u}{\partial t}-\frac{\dot{Q}_G}{k_o} \tag{3.33}$$

Assume $\frac{\rho c}{k(T)}=\frac{1}{\kappa}=$ constant. Therefore

$$\nabla^2 u=\frac{1}{\kappa}\frac{\partial u}{\partial t}-\frac{\dot{Q}_G}{k_o} \tag{3.34}$$

Assume no internal energy generated ($\dot{Q}_G=0$)

$$\nabla^2 u=\frac{1}{\kappa}\frac{\partial u}{\partial t} \tag{3.35}$$

Define moving coordinate $w=x-vt$. Therefore

$$\frac{\partial u}{\partial x}=\frac{\partial u}{\partial w}\frac{\partial w}{\partial x}=\frac{\partial u}{\partial w}\qquad\left[\frac{\partial w}{\partial x}=1\right]$$

$$\frac{\partial u}{\partial t}_{|fix}=\frac{\partial u}{\partial w}\frac{\partial w}{\partial t}+\frac{\partial u}{\partial t}_{|mov}=-v\frac{\partial u}{\partial w}+\frac{\partial u}{\partial t}_{|mov}$$

Equation 3.35 can be rewritten as:

$$\frac{\partial^2 u}{\partial w^2}+\frac{\partial^2 u}{\partial y^2}+\frac{\partial^2 u}{\partial z^2}=\frac{1}{\kappa}\left[-v\frac{\partial u}{\partial w}+\frac{\partial u}{\partial t}_{|mov}\right] \tag{3.36}$$

For quasi-steady state $\frac{\partial u}{\partial t}_{|mov}=0$

$$\frac{\partial^2 u}{\partial w^2}+\frac{\partial^2 u}{\partial y^2}+\frac{\partial^2 u}{\partial z^2}=-\frac{v}{\kappa}\frac{\partial u}{\partial w} \tag{3.37}$$

or

$$\frac{\partial^2 u}{\partial w^2}+\frac{\partial^2 u}{\partial y^2}+\frac{\partial^2 u}{\partial z^2}+\frac{v}{\kappa}\frac{\partial u}{\partial w}=0 \tag{3.38}$$

Define $\bar{u}=u+(\theta_o-\theta_\epsilon)$, Equation 3.38 can be rewritten as:

$$\frac{\partial^2 \bar{u}}{\partial w^2} + \frac{\partial^2 \bar{u}}{\partial y^2} + \frac{\partial^2 \bar{u}}{\partial z^2} + \frac{v}{\kappa}\frac{\partial \bar{u}}{\partial w} = 0 \tag{3.39}$$

Let $\bar{u} = e^{-\frac{v}{2\kappa}w}\phi(w,y,z) + (\theta_o - \theta_e)$. Therefore:

$$\frac{\partial \bar{u}}{\partial w} = e^{-\frac{v}{2\kappa}w}\frac{\partial \phi}{\partial w}(w,y,z) - \frac{v}{2\kappa}e^{-\frac{v}{2\kappa}w}\phi(w,y,z)$$

$$\frac{\partial^2 \bar{u}}{\partial w^2} = e^{-\frac{v}{2\kappa}w}\frac{\partial^2 \phi}{\partial w^2}(w,y,z) - \frac{v}{2\kappa}e^{-\frac{v}{2\kappa}w}\frac{\partial \phi}{\partial w}(w,y,z) + (\frac{v}{2\kappa})^2 e^{-\frac{v}{2\kappa}w}\phi(w,y,z) - \frac{v}{2\kappa}e^{-\frac{v}{2\kappa}w}\frac{\partial \phi}{\partial w}(w,y,z)$$

$$\frac{\partial^2 \bar{u}}{\partial y^2} = e^{-\frac{v}{2\kappa}w}\frac{\partial^2 \phi}{\partial y^2}(w,y,z)$$

$$\frac{\partial^2 \bar{u}}{\partial z^2} = e^{-\frac{v}{2\kappa}w}\frac{\partial^2 \phi}{\partial z^2}(w,y,z)$$

Substituting the above relations into Equation 3.39, we have

$$\frac{\partial^2 \phi}{\partial w^2} + \frac{\partial^2 \phi}{\partial y^2} + \frac{\partial^2 \phi}{\partial z^2} - (\frac{v}{2\kappa})^2\phi = 0 \tag{3.40}$$

Using cylindrical coordinate we have

$$\frac{\partial^2 \phi}{\partial r^2} + \frac{1}{r}\frac{\partial \phi}{\partial r} + \frac{\partial^2 \phi}{\partial z^2} - (\frac{v}{2\kappa})^2\phi = 0 \tag{3.41}$$

$$\bar{u} = e^{-\frac{v}{2\kappa}w}\phi(r,z) + (\theta_o - \theta_e) \tag{3.42}$$

where $r^2 = w^2 + y^2$

Equation 3.41 and 3.42 along with boundary conditions will be used to solve for heat flow analysis.

3.5.2 Heat Input Model for the Welding Torch and Side Heating Torch

The heat input is modeled using the Gaussian radial heat flux distribution with distorted backward compensation (Equation 3.19). For the sake of notation it is rewritten as follow:

$$q(r,w) = q_o e^{-Cr^2} - \frac{v}{2\kappa} w \tag{3.43}$$

In case of side heating, Equation 3.43 is modified to represent the heat input from a side heating torch as follows: (see Fig. 3-6 and Fig. 3-7)

For heating torch position ahead of the welding torch

$$q_s(r,w) = q_{s1} e^{-C(r+R)^2} - \frac{v}{2\kappa}(w - |D|) + q_{s2} e^{-C(r-R)^2} - \frac{v}{2\kappa}(w - |D|) \tag{3.44}$$

For heating torch position behind the welding torch

$$q_s(r,w) = q_{s1} e^{-C(r+R)^2} - \frac{v}{2\kappa}(w + |D|) + q_{s2} e^{-C(r-R)^2} - \frac{v}{2\kappa}(w + |D|) \tag{3.45}$$

where

R = distance, along r - direction, between the welding torch and the side heating torch,

D = distance, along x - direction (welding direction), between the welding torch and the side heating torch.

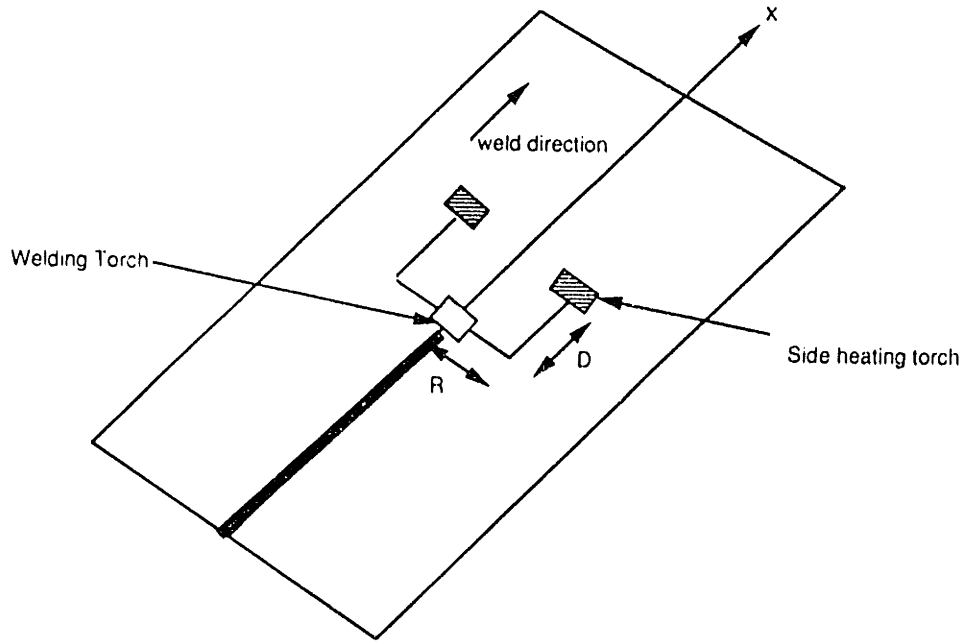

Figure 3-6: Schematic Representation for Welding with Side Heating

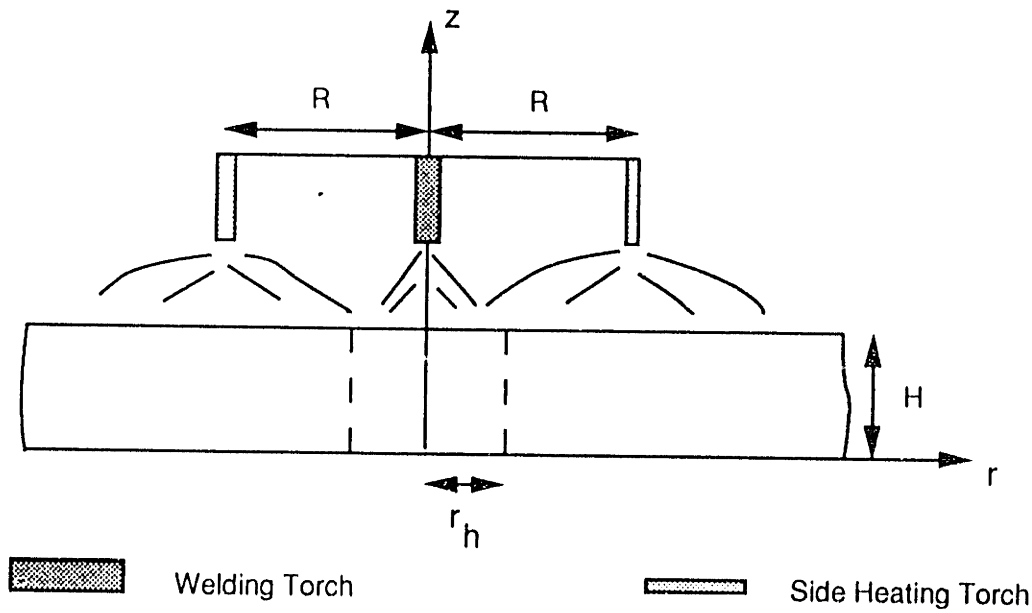

Figure 3-7: Schematic Representation of Geometry for Boundary Condition

The distance r_h that determines the region where both welding heat torch and side heating torch dominate can be calculated by considering only the effect of the welding torch, since outside r_h the plate will be dominated by the side heating torch only. This distance r_h can be calculated from Equation 3.18.

$$r_h = \frac{d_h}{2} = (\frac{3}{c})^{\frac{1}{2}} \tag{3.46}$$

By considering the symmetry of the problem, only half of the plate needs be considered. Therefore, it can be used as well to analyze bead-on-edge welding.

3.5.3 Boundary Conditions

The solution to Equation 3.41 can be divided into an inner solution $\phi^i(r,z)$ for $r < r_h$ and an outer solution $\phi^o(r,z)$ for $r > r_h$ which will be matched on the common boundary $r = r_h$

3.5.3.1 Case Without Side Heating

For Inner Region $r < r_h$

1. $k(\theta^i)\frac{\partial\theta^i}{\partial z} - h_2(\theta^i - \theta_e) = 0$ at $z = 0$ (3.47)

2. $-k(\theta^i)\frac{\partial\theta^i}{\partial z} + q_o e^{-Cr^2} - \frac{v}{2\kappa}w - h_1(\theta^i - \theta_e) = 0$ at $z = H$ (3.48)

3. $\frac{\partial\theta^i}{\partial r} = 0$ at $r = 0$ (3.49)

For Outer Region $r > r_h$

1. $k(\theta^o)\frac{\partial\theta^o}{\partial z} - h_2(\theta^o - \theta_e) = 0$ at $z = 0$ (3.50)

2. $-k(\theta^o)\frac{\partial\theta^o}{\partial z} - h_1(\theta^o - \theta_e) = 0$ at $z = H$ (3.51)

3. $\theta^o \rightarrow \theta_o$ at $r \rightarrow \infty$ (3.52)

For Matching Region $r = r_h$

1. $\theta^i = \theta^o$ (3.53)

2. $\frac{\partial\theta^i}{\partial r} = \frac{\partial\theta^o}{\partial r}$ (3.54)

where h_1 and h_2 are the heat transfer coefficients at the top and bottom surface of the plate. They are defined as follows:

$$h = h_c + \sigma\varepsilon A(\theta^2 + \theta_e^2)(\theta + \theta_e) \tag{3.55}$$

where

h_c = temperature dependent convection coefficient,

σ = Stefan-Boltzman constant,

ε = emissivity of the surface,

A = shape function,

θ_e = environmental temperature.

3.5.3.2 Case With Side Heating

For Inner Region $r < r_h$

$$1.\ k(\theta^i)\frac{\partial\theta^i}{\partial z} - h_2(\theta^i - \theta_e) = 0 \qquad \text{at } z = 0 \tag{3.56}$$

$$2.\ -k(\theta^i)\frac{\partial\theta^i}{\partial z} + [q_o e^{-Cr^2} - \tfrac{v}{2\kappa}w + q_s e^{-C(r-R)^2 - \frac{v}{2\kappa}(w-D)}]$$

$$-h_1(\theta^i - \theta_e) = 0 \qquad \text{at } z = H \tag{3.57}$$

$$3.\ \frac{\partial\theta^i}{\partial r} = 0 \qquad \text{at } r = 0 \tag{3.58}$$

For Outer Region $r > r_h$

$$1.\ k(\theta^o)\frac{\partial\theta^o}{\partial z} - h_2(\theta^o - \theta_e) = 0 \qquad \text{at } z = 0 \tag{3.59}$$

$$2\quad -k(\theta^o)\frac{\partial\theta^o}{\partial z} + [q_s e^{-C(r-R)^2 - \frac{v}{2\kappa}(w-D)}]$$

$$-h_1(\theta^o - \theta_e) = 0 \qquad \text{at } z = H \tag{3.60}$$

$$3.\ \theta^o \to \theta_o \qquad \text{at } r \to \infty \tag{3.61}$$

For Matching Region $r = r_h$

$$1.\ \theta^i = \theta^o \tag{3.62}$$

$$2.\ \frac{\partial\theta^i}{\partial r} = \frac{\partial\theta^o}{\partial r} \tag{3.63}$$

3.5.4 Linearization on Boundary Conditions

Due to the temperature dependence of coefficient k, h_1 and h_2, the boundary conditions as shown above are non-linear, To linearize these boundary conditions, the heat transfer coefficients h_1 and h_2 are assumed to be constant and equal to an average value over the temperature history of the plate. Equations 3.23, 3.25, and 3.42 are then used to linearize boundary conditions to ones having the variable ϕ.

For the case without side heating

From $T = \theta - \theta_o$, we can rewrite Equation 3.47 as follows:

$$k(T^i)\frac{\partial T^i}{\partial z} - h_2(T^i + (\theta_o - \theta_e)) = 0 \tag{3.64}$$

From $\frac{\partial T^i}{\partial z} = \frac{k_o}{k(T)}\frac{\partial u^i}{\partial z}$, we have

$$k(T^i)\frac{\partial T^i}{\partial z} = k(T^i)\frac{k_o}{k(T^i)}\frac{\partial u^i}{\partial z} = k_o\frac{\partial u^i}{\partial z} \tag{3.65}$$

From $T = \frac{1}{\gamma}(\sqrt{1 + 2\gamma u} - 1)$, we have $T^i = \frac{1}{\gamma}(\sqrt{1 + 2\gamma u^i} - 1)$, therefore

$$k_o\frac{\partial u^i}{\partial z} - h_2[T^i(u) + (\theta_o - \theta_e)] = 0 \tag{3.66}$$

Now approximate function for $T^i(u)$ by expanding $k(T)$ in a Taylor series around 0.

$$k(T) = k(0) + Tk'(0) + \frac{T^2}{2}k''(0) + O(T^3) \tag{3.67}$$

Substituting the above into Equation 3.25, we have

$$u = T + \frac{k'}{k_o}\frac{T^2}{2} + \frac{k'}{k_o}\frac{T^3}{6} + O(T^4) \tag{3.68}$$

For the first approximation $u = T + O(T^2)$ or $u \approx T$, therefore we can rewrite Equation 3.66 as follows:

$$k_o\frac{\partial u^i}{\partial z} - h_2[u^i + \theta_o - \theta_e] = 0 \tag{3.69}$$

From $\bar{u} = u + (\theta_o - \theta_e)$ and Equation 3.42, the above expression becomes

$$\frac{\partial \phi^i}{\partial z} = \frac{h_2}{k_o}\phi^i \qquad z = 0\ ,\ r < r_h \qquad (3.70)$$

Working similarly on other boundary conditions, the following equations were derived:

$$\frac{\partial \phi^i}{\partial z} = \frac{q_o}{k_o}e^{-Cr^2} - \frac{h_1}{k_o}\phi^i \qquad z = H,\ r < r_h \qquad (3.71)$$

$$\frac{\partial \phi^i}{\partial r} = 0 \qquad r = 0,\ \text{all } z \qquad (3.72)$$

$$\frac{\partial \phi^o}{\partial z} = \frac{h_2}{k_o}\phi^o \qquad z = 0,\ r > r_h \qquad (3.73)$$

$$\frac{\partial \phi^o}{\partial z} = -\frac{h_1}{k_o}\phi^o \qquad z = H,\ r > r_h \qquad (3.74)$$

$$\phi^o \rightarrow 0 \qquad r \rightarrow \infty,\ \text{all } z \qquad (3.75)$$

$$\phi^o = \phi^i \qquad r = r_h,\ \text{all } z \qquad (3.76)$$

$$\frac{\partial \phi^o}{\partial r} = \frac{\partial \phi^i}{\partial r} \qquad r = r_h,\ \text{all } z \qquad (3.77)$$

For the case with side heating

Using similar procedures as shown previously, the boundary conditions for the case with side heating can be linearized as follows:

$$\frac{\partial \phi^i}{\partial z} = \frac{h_2}{k_o}\phi^i \qquad z = 0,\ r < r_h \qquad (3.78)$$

$$\frac{\partial \phi^i}{\partial z} = \frac{1}{k_o}\left[q_o e^{-Cr^2} + q_s e^{-C(r-R)^2 - \frac{\upsilon}{2\kappa}(-D)}\right] - \frac{h_1}{k_o}\phi^i \qquad z = H,\ r < r_h \qquad (3.79)$$

$$\frac{\partial \phi^i}{\partial r} = 0 \qquad r = 0,\ \text{all } z \qquad (3.80)$$

$$\frac{\partial \phi^o}{\partial z} = \frac{h_2}{k_o}\phi^o \qquad z = 0,\ r > r_h \qquad (3.81)$$

$$\frac{\partial \phi^o}{\partial z} = \frac{1}{k_o}\left[q_s e^{-C(r-R)^2 - \frac{\upsilon}{2\kappa}(-D)}\right] - \frac{h_1}{k_o}\phi^o \qquad z = H,\ r > r_h \qquad (3.82)$$

$$\phi^o \rightarrow 0 \qquad r \rightarrow \infty,\ \text{all } z \qquad (3.83)$$

$$\phi^o = \phi^i \qquad r = r_h\ ,\ \text{all } z \qquad (3.84)$$

$$\frac{\partial \phi^o}{\partial r} = \frac{\partial \phi^i}{\partial r} \qquad r = r_h,\ \text{all } z \qquad (3.85)$$

3.5.5 Solution Procedure

3.5.5.1 Case Without Side Heating

Papazoglou [50] solved Equation 3.41 by using the method of separation of variables along with linearized boundary conditions (Equations 3.70 - 3.77). Details of his analysis can be found in reference [50]. Only the final solution will be presented here as follows:

$$\theta = \theta_o + \frac{1}{\gamma}(\sqrt{1 + 2\gamma e^{-\frac{\upsilon}{2\kappa}w}\phi(r,z)} - 1) \tag{3.86}$$

$$\phi(r,z) = \phi^i(r,z)[u_{-1}(r) - u_{-1}(r-r_h)] + \phi^o(r,z)u_{-1}(r-r_h) \tag{3.87}$$

with $u_{-1}(r-a)$ being the unit step function and

$$\phi^i(r,z) = \sum_{n=1}^{\infty} \frac{2q_o K_n J_0(\delta_n r)[h_2 \sinh(\chi_n z) + k_o \chi_n \cosh(\chi_n z)]}{J_1^2(\delta_n r_h)[k_o \chi_n (h_1+h_2)\cosh(\chi_n H) + (k_o^2 \chi_n^2 + h_1 h_2)\sinh(\chi_n H)]}$$

$$+ C_n K_0(\xi_n r_h)\frac{I_0(\xi_n r)}{I_0(\xi_n r_h)}[\frac{h_2}{\omega_n k_0}\sin(\omega_n z) + \cos(\omega_n z)] \tag{3.88}$$

$$\phi^o(r,z) = \sum_{n=1}^{\infty} C_n K_0(\xi_n r)[\frac{h_2}{k_o \omega_n}\sin(\omega_n z) + \cos(\omega_n z)] \tag{3.89}$$

where

$$C_n = \frac{1}{a_n}\sum_{m=1}^{\infty} \frac{2q_o K_m \delta_m [r_{mn}\tanh(\chi_m H) + s_{mn}]}{(\chi_m^2 + \omega_n^2) J_1(\delta_m r_h)[d_m + e_m \tanh(\chi_m H)]}$$

$$n = 1,2,3..... \tag{3.90}$$

$$a_n = b_n c_n \tag{3.91}$$

$$b_n = \xi_n [K_1(\xi_n r_h) + K_0(\xi_n r_h)\frac{I_1(\xi_n r_h)}{I_0(\xi_n r_h)}] \tag{3.92}$$

$$c_n = \frac{H}{2}(1 + \frac{h_2^2}{\omega_n^2 k_o^2}) + \frac{1}{4\omega_n}(1 - \frac{h_2}{\omega_n^2 k_o^2})\sin(2\omega_n H)$$

$$+ \frac{h_2}{\omega_n^2 k_o}\sin^2(\omega_n H) \tag{3.93}$$

$$d_m = k_o\chi_m(h_1 + h_2) \tag{3.94}$$

$$e_m = k_o^2\chi_m^2 + h_1h_2 \tag{3.95}$$

$$r_{mn} = h_2(\omega_n + \frac{\chi_m^2}{\omega_n})\sin(\omega_nH) + (k_o\chi_m^2 - \frac{h_2^2}{k_o})\cos(\omega_nH) \tag{3.96}$$

$$s_{mn} = \chi_m(k_o\omega_n + \frac{h_2^2}{k_o\omega_n})\sin(\omega_nH) \tag{3.97}$$

$$\xi_n^2 = \omega_n^2 + (\frac{\upsilon}{2\kappa})^2 \tag{3.98}$$

$$(k_o^2\omega_n^2 - h_1h_2)\tan(\omega_nH) = k_o\omega_n(h_1 + h_2) \tag{3.99}$$

$$J_0(\delta_n r_h) = 0 \qquad n = 1,2,3..... \tag{3.100}$$

$$\delta_n^2 = \chi_n^2 - (\frac{\upsilon}{2\kappa})^2 \tag{3.101}$$

$$K_n = \int_0^1 xe^{-Cr_h^2x^2}J_0(\delta_n r_h x)dx \tag{3.102}$$

H is the plate thickness, $J_0(x)$ and $J_1(x)$ are the Bessel functions of first kind and of zero and first order respectively, $I_0(x)$ and $I_1(x)$ are the modified Bessel functions of first kind and of zero and first order respectively. All other variables have been previously defined.

3.5.5.2 Case With Side Heating

The governing Equation 3.41 will be solved using the method of separation of variable along with linearized boundary conditions (Equations 3.78 - 3.85). Let

$$\phi(r,z) = R(r)Z(z) \tag{3.103}$$

Substitute the above equation into Equation 3.41 and rearrange the similar terms. The following two ordinary differential equations can be derived:

$$\frac{1}{R(r)}[R''(r) + \frac{1}{r}R'(r)] - (\frac{\upsilon}{2\kappa})^2 = \mp\omega^2 \tag{3.104}$$

$$-\frac{1}{Z(z)}Z''(z) = \mp\omega^2 \tag{3.105}$$

where the sign of ω^2 will be chosen such that the boundary value problem of the homogeneous direction leads to a characteristic value problem. The constant ω will be determined by boundary conditions.

Inner Solution

Due to the non-homogeneous boundary conditions existing in the r and z direction [$\phi^i = \phi^o$], we need to use the superposition principle to separate boundary conditions by dividing the inner solution into two parts.

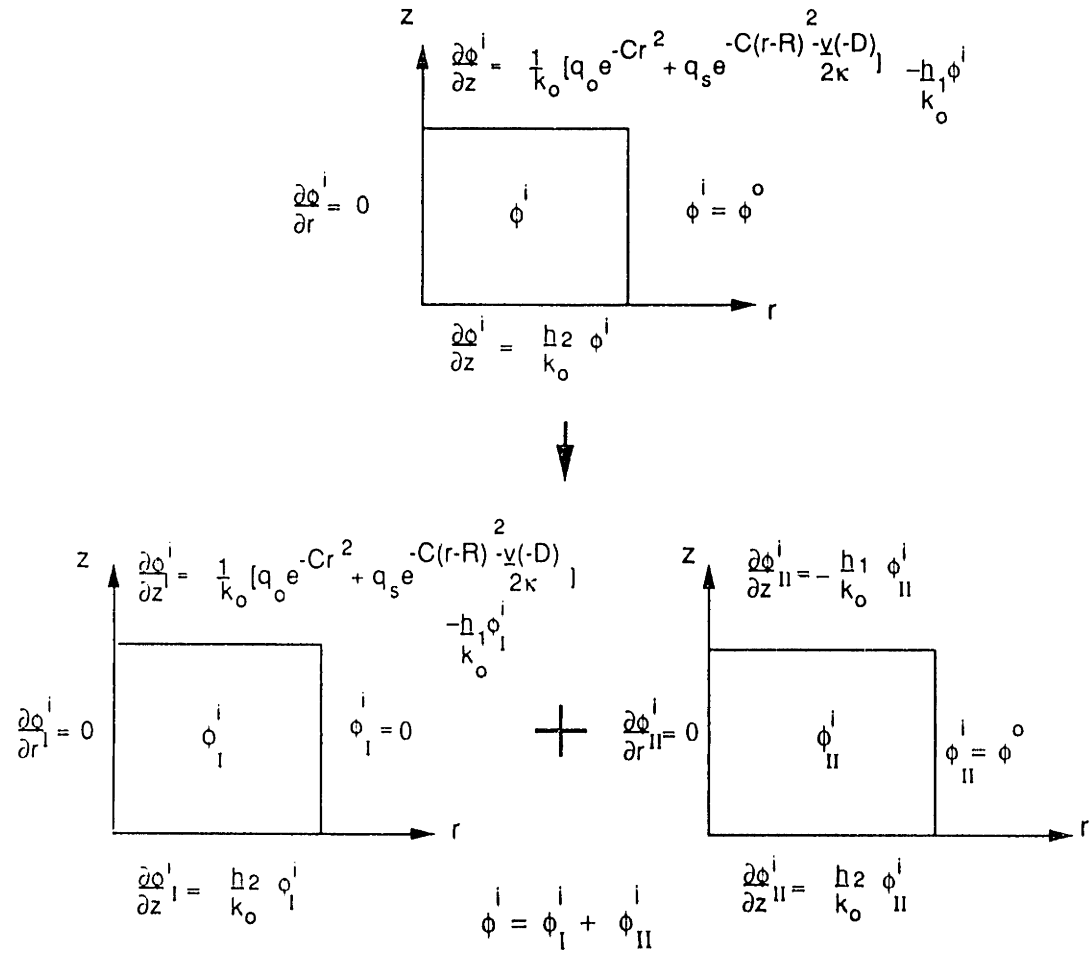

Figure 3-8: Superposition Used for Inner Solution

Solution for ϕ_I^i

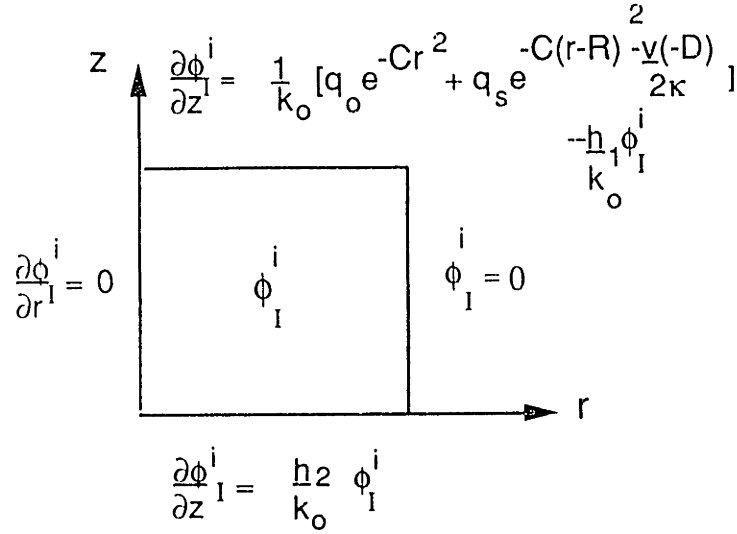

Figure 3-9: Boundary Conditions for ϕ_I^i

The homogeneous direction is in the r direction hence choose $-\omega^2$ in Equations 3.104 and 3.105.

$$R_I^{i''}(r) + \frac{1}{r}R_I^{i'}(r) + (\omega^2 - (\frac{\upsilon}{2\kappa})^2)R_I^i(r) = 0 \tag{3.106}$$

$$Z_I^{i''}(z) - \omega^2 Z_I^i(z) = 0 \tag{3.107}$$

Change $\omega^2 \rightarrow \chi^2$ and let $\delta^2 = \chi^2 - (\frac{\upsilon}{2\kappa})^2$, we have

$$R_I^{i''}(r) + \frac{1}{r}R_I^{i'}(r) + \delta^2 R(r) = 0 \tag{3.108}$$

$$Z_I^{i''}(z) - \chi^2 Z_I^i(z) = 0 \tag{3.109}$$

Boundary Conditions

1. $R_I^{i'}(0) = 0$
2. $R_I^i(r_h) = 0$
3. $Z_I^{i'}(0) - \frac{h_2}{k_o}Z_I^i(0) = 0$
4. $\frac{\partial\phi_I^i}{\partial z}(r,H) = \frac{1}{k_o}[q_o e^{-Cr^2} + q_s e^{-C(r-R)^2 - \frac{\upsilon}{2\kappa}(-D)}]$

$$-\frac{h_1}{k_o}\phi_I^i(r,h)$$

The general solutions for Equations 3.108 and 3.109 are:

$$R_I^i(r) = A_1' J_0(\delta r) + A_2' Y_0(\delta r) \tag{3.110}$$

$$Z_I^i(z) = B_1' \sinh(\chi z) + B_2' \cosh(\chi z) \tag{3.111}$$

where A_1', A_2', B_1', B_2' are constant. J_0 and Y_0 are Bessel functions of first and second kind and of zero order.

From boundary condition (1) and the condition that $Y_1(0) \to \infty$ and $J_1(0) = 0$, we have $A_2' = 0$. Therefore

$$R_I^i(r) = A_1' J_0(\delta_n r)$$

From boundary condition (2), we have

$$J_0(\delta_n r_h) = 0 \qquad \text{for } n = 1, 2, 3 \ldots\ldots$$

Using the above equation, the value of δ_n for each value of n can be found.

By using boundary condition (3), the relation between the constant B_1' and B_2' is as follows:

$$B_1' = \frac{h_2}{k_o \chi_n} B_2'$$

From the above three boundary conditions, we can write the solution of $\phi_I^i(r,z)$ as follows:

$$\phi_I^i(r,z) = \sum_{n=1}^{\infty} D_n J_0(\delta_n r) \left[\frac{h_2}{\chi_n k_o} \sinh(\chi_n z) + \cosh(\chi_n z) \right] \tag{3.112}$$

The coefficient D_n can be found from the last boundary condition as follows:

$$\sum_{n=1}^{\infty} D_n J_0(\delta_n r) \left[\frac{h_2}{\chi_n k_o} \cosh(\chi_n H) + \sinh(\chi_n H) \right] \chi_n$$

$$= \frac{1}{k_o} \left[q_o e^{-Cr^2} + q_s e^{-C(r-R)^2} - \frac{v}{2\kappa}(-D) \right]$$

$$- \frac{h_1}{k_o} \sum_{n=1}^{\infty} D_n J_0(\delta_n r) \left[\frac{h_2}{\chi_n k_o} \sinh(\chi_n H) + \cosh(\chi_n H) \right]$$

Multiply both sides by $r J_0(\delta_m r)$ then integrate from 0 to r_h and use the following orthogonality property of the Bessel function.

$$\int_0^{r_h} r J_0(\delta_n r) J_0(\delta_m r) dr = 0 \qquad \text{if } \delta_n \neq \delta_m$$

$$= \frac{r_h^2}{2} J_1^2(\delta_n r_h) \qquad \text{if } \delta_n = \delta_m \qquad (3.113)$$

We have

$$D_n = \frac{2[q_o K_n + q_s e^{-\frac{\upsilon}{2\kappa}(-D)} Q_n]}{k_o J_1^2(\delta_n r_h)[\frac{h_1 + h_2}{k_o}\cosh(\chi_n H) + (\chi_n + \frac{h_1 h_2}{\chi_n k_o^2})\sinh(\chi_n H)]} \qquad (3.114)$$

where

$$K_n = \int_0^1 e^{-C r_h^2 x^2} x J_0(\delta_n x r_h) dx$$

$$Q_n = \int_0^1 e^{-C(r_h x - R)^2} x J_0(\delta_n x r_h) dx$$

Solution for ϕ_{II}^i

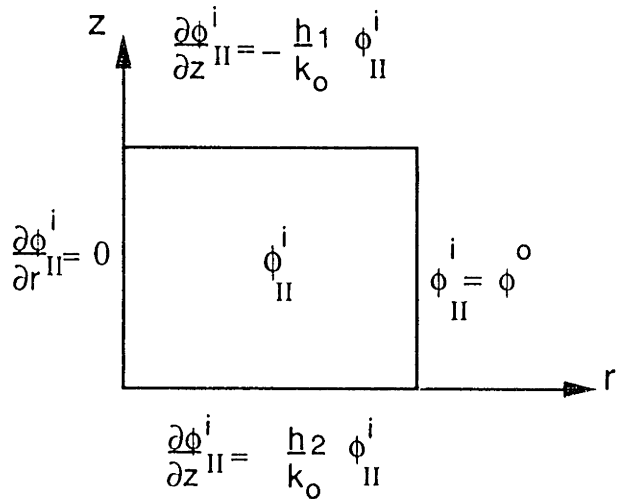

Figure 3-10: Boundary Conditions for ϕ_{II}^i

The homogeneous boundary condition is in the z direction hence choose $+\bar{\omega}^2$ in Equations 3.104 and 3.105.

$$R_{II}^{i\,''}(r) + \frac{1}{r} R_{II}^{i\,'}(r) - (\bar{\omega}^2 + (\frac{\upsilon}{2\kappa})^2) R_{II}^i(r) = 0 \qquad (3.115)$$

$$Z_{II}^{i\,''}(z) + \bar{\omega}^2 Z_{II}^i(z) = 0 \qquad (3.116)$$

Boundary Condition

1. $R_{II}^{i}{}'(0) = 0$

2. $Z_{II}^{i}{}'(0) - \frac{h_2}{k_o} Z_{II}^{i}(0) = 0$

3. $Z_{II}^{i}{}'(H) + \frac{h_1}{k_o} Z_{II}^{i}(H) = 0$

4. $R_{II}^{i}(r_h) Z_{II}^{i}(z) = \phi^o$

The general solutions for Equations 3.115 and 3.116 are

$$R_{II}^{i}(r) = A_1^{"} I_0(\xi r) + A_2^{"} K_0(\xi r) \tag{3.117}$$

$$Z_{II}^{i}(z) = B_1^{"} \sin(\bar{\omega} z) + B_2^{"} \cos(\bar{\omega} z) \tag{3.118}$$

where $\xi^2 = \bar{\omega}^2 + (\frac{\upsilon}{2\kappa})^2$, I_0 and K_0 are modified Bessel functions of first and second kind and of zero order.

From boundary condition (1) and the condition that $K_1(0) \rightarrow \infty$ and $I_1(0) \rightarrow 0$, we have $A_2^{"} = 0$

From boundary condition (2), we have the relation between $B_1^{"}$ and $B_2^{"}$ as follows:

$$B_1^{"} = \frac{h_2}{k_o \bar{\omega}} B_2^{"}$$

From boundary condition (3), we have

$$\tan(\bar{\omega}_h H) = \frac{(h_1 + h_2)\bar{\omega} k_o}{\bar{\omega}^2 k_o^2 - h_1 h_2} \qquad n = 1, 2, 3 \ldots\ldots$$

Finally, the solution for $\phi_{II}^{i}(r, z)$ can be written as follows:

$$\phi_{II}^{i}(r, z) = \sum_{n=1}^{\infty} E_n I_0(\xi_n r) [\frac{h_2}{k_o \bar{\omega}_h} \sin(\bar{\omega}_h z) + \cos(\bar{\omega}_h z)] \tag{3.119}$$

The coefficient E_n will be determined from matching boundary conditions.

Outer Solution

Due to the non-homogeneous boundary conditions existing in the r and z direction, we divide the solution into two parts.

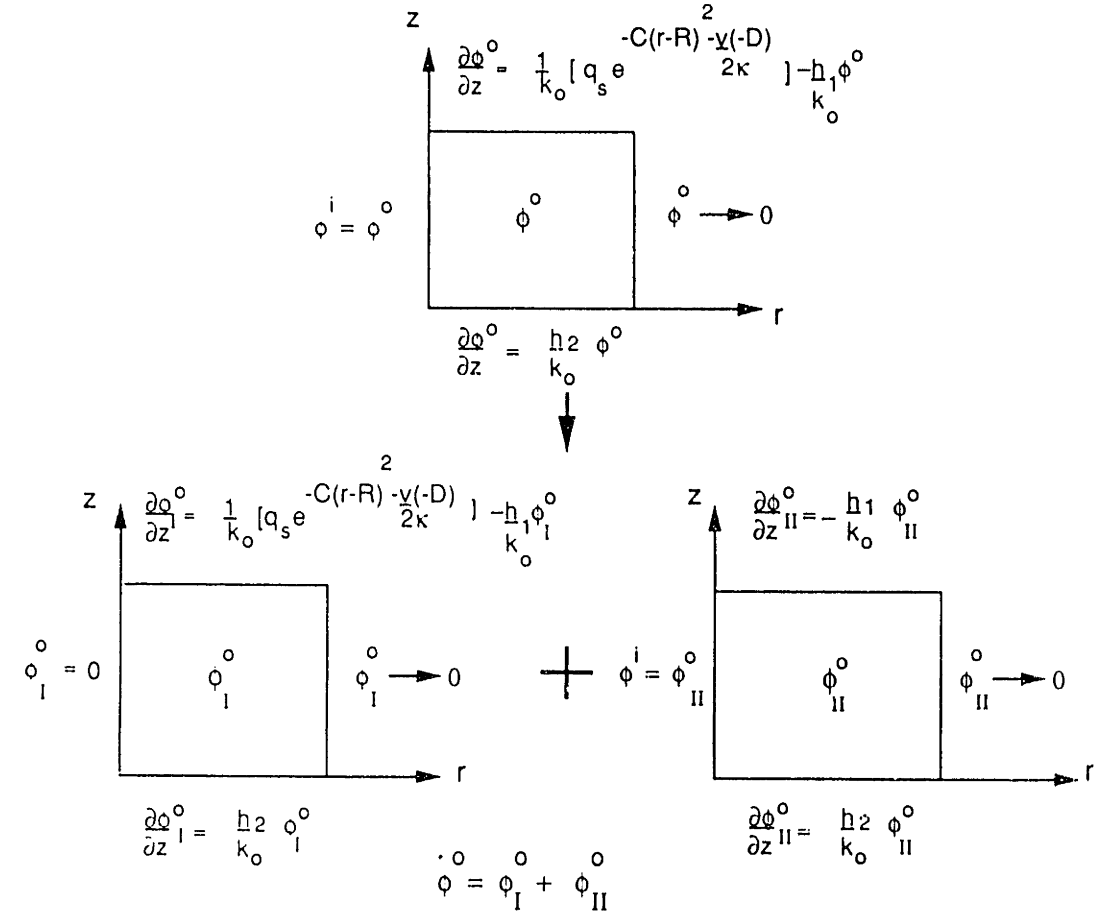

Figure 3-11: Superposition Used for Outer Solution

Solution for ϕ_I^o

The homogeneous direction is in the r direction hence choose $-\omega^2$ in Equations 3.105 and 3.106

$$R_I^{o''}(r) + \frac{1}{r}R_I^{o'}(r) + \xi^2 R_I^o(r) = 0 \tag{3.120}$$

$$Z_I^{o''}(z) - \omega^2 Z_I^o(z) = 0 \tag{3.121}$$

where $\xi^2 = \omega^2 - (\frac{v}{2\kappa})^2$

Boundary Conditions

1. $R_I^o(r_h) = 0$

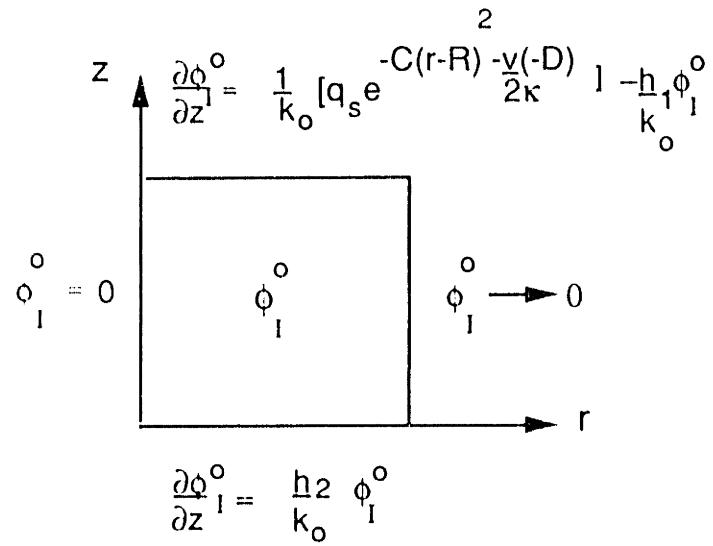

Figure 3-12: Boundary Condition for ϕ_I^o

2. $R_I^o(r) = 0 \qquad \text{as } r \to \infty$

3. $Z_I^{o'}(0) = \frac{h_2}{k_o} Z_I^o(0)$

4. $\frac{\partial \phi_I^o}{\partial z}(r,H) = \frac{1}{k_o} q_s e^{-C(r-R)^2 - \frac{v}{2\kappa}(-D)} - \frac{h_1}{\kappa_o}\phi_I^o(r,H)$

General solutions for Equations 3.120 and 3.121 are:

$$R_I^o(r) = A_1 J_0(\xi r) + A_2 Y_0(\xi r) \tag{3.122}$$

$$Z_I^o(z) = B_1 \sinh(\omega z) + B_2 \cosh(\omega z) \tag{3.123}$$

From boundary condition (2) and using the following properties of Bessel function:

$$J_0(x) \approx \sqrt{\frac{2}{\pi x}} \cos\left(x - \frac{\pi}{4}\right) \qquad \text{for } x \text{ is large}$$

$$Y_0(x) \approx \sqrt{\frac{2}{\pi x}} \sin\left(x - \frac{\pi}{4}\right)$$

we have $A_1 = -A_2$

From boundary condition (1), we have

$$J_0(\xi_n r_h) = Y_0(\xi_n r_h) \qquad n = 1, 2, 3 \ldots\ldots$$

From boundary condition (3), we have

$$B_1 = \frac{h_2}{k_o \omega_n} B_2$$

Therefore the solution is

$$\phi_I^o = \sum_{n=1}^{\infty} F_n [J_0(\xi_n r) - Y_0(\xi_n r)] \left[\frac{h_2}{k_o \omega_n} \sinh(\omega_n z) + \cosh(\omega_n z)\right] \quad (3.124)$$

where F_n can be found by imposing the last boundary condition on the equation above and then multiplying by $\int_{r_h}^{\infty} dr$ on both sides. After performing some necessary integrations we have:

$$F_n = \frac{q_s e^{\frac{-v}{2\kappa}(-D)} C_s}{k_o [X_n - Y_n] [\frac{h_1 + h_2}{k_o} \cosh(\omega_n H) + (\omega_n + \frac{h_1 h_2}{k_o^2 \omega_n}) \sinh(\omega_n H)]} \quad (3.125)$$

where

$$X_n = \int_{r_h}^{\infty} J_0(\xi_n r) dr$$

$$Y_n = \int_{r_h}^{\infty} Y_0(\xi_n r) dr$$

$$C_s = \int_{r_h}^{\infty} e^{-C(r-R)^2} dr$$

Solution for ϕ_{II}^o

The homogeneous direction is in the z direction hence choose $+\omega^2$ in Equations 3.104 and 3.105.

$$R_{II}^{o''}(r) + \frac{1}{r} R_{II}^{o'}(r) - (\omega^2 + (\frac{v}{2\kappa})^2) R_{II}^o(r) = 0 \quad (3.126)$$

$$Z_{II}^{o''}(z) + \omega^2 Z_{II}^o(z) = 0 \quad (3.127)$$

The general solutions for Equations 3.126 and 3.127 are:

$$R_{II}^o(r) = \bar{A}_1 I_0(\bar{\eta} r) + \bar{A}_2 K_0(\bar{\eta} r) \quad (3.128)$$

$$Z_{II}^o(z) = \bar{B}_1 \sin(\eta z) + \bar{B}_2 \cos(\eta z) \quad (3.129)$$

where $\eta = \omega$ and $\bar{\eta}^2 = \eta^2 + (\frac{v}{2\kappa})^2$

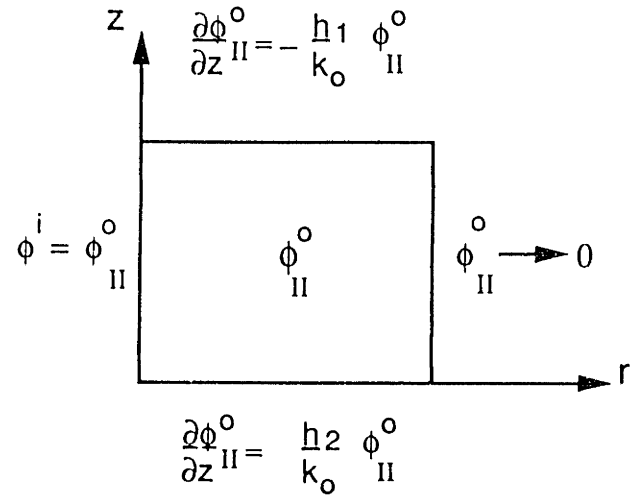

Figure 3-13: Boundary Conditions for ϕ^o_{II}

Boundary Conditions

1. $\phi^o_{II} = \phi^i$ at $r = r_h$
2. $\phi^o_{II}(r) = 0$ as $r \rightarrow \infty$
3. $Z^{o\prime}_{II}(0) = \frac{h_2}{k_o} Z^o_{II}(0)$
4. $Z^{o\prime}_{II}(H) = -\frac{h_1}{k_o} Z^o_{II}(H)$

From boundary condition (2) and the conditions that $I_0(\infty) \rightarrow \infty$ and $K_0(\infty) = 0$, we have $\bar{A}_1 = 0$

From boundary condition (3), we have

$$\bar{B}_1 = \frac{h_2}{k_o \eta} \bar{B}_2$$

From boundary condition (4) and substituting the relation above, we have

$$\tan(\eta H)[k_o^2\eta^2 - h_1 h_2] = (h_1 + h_2) k_o \eta \qquad n = 1, 2, 3 .....$$

Therefore the solution for ϕ^o_{II} is

$$\phi^o_{II} = \sum_{n=1}^{\infty} G_n K_0(\bar{\eta}_n r)\left[\frac{h_2}{k_o \eta_n}\sin(\eta_n z) + \cos(\eta_n z)\right] \tag{3.130}$$

The constant G_n will be determined from matching region conditions.

Matching Region Solution

To complete the solution, the constant E_n and G_n will be found using the conditions at the matching region:

1. $\phi_{II}^{o}(r_h, z) = \phi_{II}^{i}(r_h, z)$
2. $\dfrac{\partial \phi^{o}}{\partial r} = \dfrac{\partial \phi^{i}}{\partial r}$ at $r = r_h$

From condition (1), we have

$$E_n = \frac{K_0(\bar{\eta}_n r_h)\,[\dfrac{h_2}{k_o \eta_n}\sin(\eta_n z) + \cos(\eta_n z)]}{I_0(\xi_n r_h)\,[\dfrac{h_2}{k_o \bar{\omega}_h}\sin(\bar{\omega}_h z) + \cos(\bar{\omega} z)]} G_n$$

Multiply right hand side by $\dfrac{\int_0^H [\frac{h_2}{k_o\eta_n}\sin(\eta_n z) + \cos(\eta_n z)]\,dz}{\int_0^H [\frac{h_2}{k_o\eta_n}\sin(\eta_n z) + \cos(\eta_n z)]\,dz}$

After some complicated integrations, we have:

$$E_n = \frac{K_0(\bar{\eta} r_n) H_n}{I_0(\xi_n r_h)\,\bar{\bar{E}}_n} G_n \qquad \text{for } n = 1, 2, 3 \ldots\ldots$$

where

$$H_n = \frac{H}{2}\left(1 + \frac{h_2^2}{\eta_n^2 k_o}\right) + \frac{1}{4\eta_n}\left[1 - \frac{h_2^2}{\eta_n^2 k_o^2}\right]\sin(2\eta_n H) + \frac{h_2}{\eta_n^2 k_o}\sin^2(\eta_n H)$$

$$\begin{aligned}
\bar{\bar{E}}_n = {} & \frac{h_2^2}{k_o^2 \bar{\omega}_h \eta_n}\left[\frac{\sin(\bar{\omega}_h - \eta_n)H}{2(\bar{\omega}_h - \eta_n)} - \frac{\sin(\bar{\omega}_h + \eta_n)H}{2(\bar{\omega}_h + \eta_n)}\right] \\
& + \frac{h_2}{k_o \bar{\omega}_h}\left[-\frac{\cos(\bar{\omega}_h - \eta_n)H}{2(\bar{\omega}_h - \eta_n)} - \frac{\cos(\bar{\omega}_h + \eta_n)H}{2(\bar{\omega}_h + \eta_n)} + \frac{\bar{\omega}_h}{(\bar{\omega}_h^2 - \eta_n^2)}\right] \\
& + \frac{h_2}{\eta_n k_o}\left[-\frac{\cos(\eta_n - \bar{\omega}_h)H}{2(\eta_n - \bar{\omega}_h)} - \frac{\cos(\eta_n + \bar{\omega}_h)H}{2(\eta_n + \bar{\omega}_h)} + \frac{\eta_n}{(\eta_n^2 - \bar{\omega}_h^2]}\right) \\
& + \left[\frac{\sin(\bar{\omega}_h - \eta_n)H}{2(\bar{\omega}_h - \eta_n)} + \frac{\sin(\bar{\omega}_h + \eta_n)H}{2(\bar{\omega}_h + \eta_n)}\right]
\end{aligned}$$

From boundary condition (2), substitute the relation above and multiply both sides by $\int_0^H [\frac{h_2}{\eta_n k_o}\sin(\eta_n z)+\cos(\eta_n z)]dz$. We can rewrite the boundary condition (2) in the following form:

$$\frac{A_n D_n}{O_n} + \frac{K_0(\bar{\eta}_n r_h)}{I_0(\xi_n r_h)} H_n G_n \xi_n I_1(\xi_n r_h)$$

$$= \frac{B_n \bar{F}_n}{S_n} + (-\bar{\eta}_n) K_1(\bar{\eta}_n r_h) \bar{E}_n G_n \quad (3.131)$$

where

$$A_n = 2[q_o K_n + q_s e^{-\frac{v}{2\kappa}(-D)} Q_n][-\delta_n] J_1(\delta_n r_h)$$

$$B_n = \frac{1}{k_o}[q_s e^{-\frac{v}{2\kappa}(-D)} C_s][-\xi_n J_1(\xi_n r_h) + \xi_n Y_1(\xi_n r_h)]$$

$$O_n = J_1^2(\delta_n r_h)[(h_1 + h_2)\chi_n k_o \cosh(\chi_n H) + (\chi_n^2 k_o^2 + h_1 h_2)\sinh(\chi_n H)]$$

$$D_n = \int_0^H [h_2 \sinh(\chi_n z) + k_o \chi_n \cosh(\chi_n z)] [\frac{h_2}{k_o \eta_n}\sin(\eta_n z) + \cos(\eta_n z)]dz$$

$$\bar{E}_n = \int_0^H [\frac{h_2}{k_o \bar{\omega}_n}\sin(\bar{\omega}_n z) + \cos(\bar{\omega}_n z)]^2 dz$$

$$\bar{F}_n = \int_0^H [\frac{h_2}{k_o \omega_n}\sinh(\omega_n z) + \cosh(\omega_n z)] [\frac{h_2}{\eta_n k_o}\sin(\eta_n z) + \cos(\eta_n z)]dz$$

$$S_n = (X_n - Y_n)[\frac{(h_1+h_2)}{k_o}\cosh(\omega_n H) + (\omega_n + \frac{h_1 h_2}{k_o^2 \omega_n})\sinh(\omega_n H)]$$

therefore

$$G_n = \frac{(\frac{-A_n D_n}{O_n} + \frac{B_n \bar{F}_n}{S_n})}{[\frac{K_0(\bar{\eta}_n r_h)}{I_0(\xi_n r_h)} H_n \xi_n I_1(\xi_n r_h) + \bar{\eta}_n K_1(\bar{\eta}_n r_h)\bar{E}_n]}$$

Summary

Total inner solution $(r < r_h)$ is

$$\phi^i(r,z) = \phi^i_I(r,z) + \phi^i_{II}(r,z) \text{ or}$$

$$\phi^i(r,z) = \sum_{n=1}^{\infty} 2[q_o K_n + q_s e^{\frac{-\upsilon}{2\kappa}(-D)} Q_n]$$

$$\frac{J_0(\delta_n r)[h_2 \sinh(\chi_n z) + k_o \chi_n \cosh(\chi_n z)]}{J_1^2(\delta_n r_h)[(h_1 + h_2) k_o \chi_n \cosh(\chi_n H) + (\chi_n^2 k_o^2 + h_1 h_2)\sinh(\chi_n H)]}$$

$$+ \sum_{n=1}^{\infty} E_n I_0(\xi_n r)\left[\frac{h_2}{k_o \bar{\omega}_n}\sin(\bar{\omega}_n z) + \cos(\bar{\omega} z)\right] \quad (3.132)$$

Total outer solution $(r > r_h)$ is

$$\phi^o(r,z) = \phi^o_I(r,z) + \phi^o_{II}(r,z) \text{ or}$$

$$\phi^o = \sum_{n=1}^{\infty} \frac{\frac{1}{k_o} q_s e^{\frac{-\upsilon}{2\kappa}(-D)} C_s [J_0(\xi_n r) - Y_0(\xi_n r)]\left[\frac{h_2}{k_o \omega_n}\sinh(\omega_n z) + \cosh(\omega_n z)\right]}{(X_n - Y_n)\left[\left(\frac{h_1 + h_2}{k_o}\right)\cosh(\omega_n H) + \left(\omega_n + \frac{h_1 h_2}{k_o^2 \omega_n}\right)\sinh(\omega_n H)\right]}$$

$$+ \sum_{n=1}^{\infty} G_n K_0(\bar{\eta}_n r)\left[\frac{h_2}{k_o \eta_n}\sin(\eta_n z) + \cos(\eta_n z)\right] \quad (3.133)$$

The final solution can be written similarly to the one shown in Equation 3.86 which is

$$\theta = \theta_o + \frac{1}{\gamma}\left(\sqrt{1 + 2\gamma e^{-\frac{\upsilon}{2\kappa}w}\phi(r,z)} - 1\right) \quad (3.134)$$

$$\phi(r,z) = \phi^i(r,z)[u_{-1}(r) - u_{-1}(r - r_h)] + \phi^o(r,z) u_{-1}(r - r_h) \quad (3.135)$$

where $u_{-1}(r-a)$ is the unit step function. ϕ^i and ϕ^o are given by Equations 3.132 and 3.133.

Computer programs were written in FORTRAN77 language to perform necessary calculations for evaluating Equation 3.134.

3.6 Numerical Treatment on Heat Flow Analysis

As mentioned in earlier sections, the analytical solutions cannot very accurately predict the temperature during welding, especially near the weld line. This is primarily due to the highly nonlinear nature of the problem. Nevertheless, such solutions are very useful in providing insight into the problem and allow for extensive parametric analyses due to their low cost. In certain cases the accurate description of temperature distribution is necessary --for example, when a metallurgical characterization of the weld metal and heat affected zone is needed, or when a subsequent stress analysis is required to determine the transient strains and residual stresses. The numerical analysis can play an important role in these cases and ease the mathematical operation through the use of advance computer technology. The effect of size and shape of the heat source can be taken into account in the analysis without too much difficulty as in the analytical method. The temperature effect on thermal properties which leads the problem to a highly nonlinear one can be handled with much less effort. The effect of radiation heat loss from the plate surface can be included as well.

In this study a finite element model for heat flow analysis was developed and run on ADINA-T finite element program. The result from this analysis was then compared with the analytical and experimental results.

3.6.1 Literature Review

The finite element formulation of the heat transfer problem without mechanical coupling was developed by Wilson and Nickell [69] and Becker and Parr [10]. These formulations were based on developing the governing variational principle based on the approach of Gurtis [23]. Oden and Kross [49] presented a nonlinear coupled thermal-elasticity formulation based on energy balance. This comprehensive development applied the first law of

thermodynamics, entropy concepts and free energy to obtain the governing equation. Several types of boundary conditions are considered including specified temperatures and fluxes and convective heat transfer. A finite element formulation for uncoupled problem of heat transfer was developed by Zienkiewicz and Parekh [71]. They applied the Galerkin weighted residual method to the governing differential equation of heat transfer to obtain the finite element equations which can be represented in the following matrix form:

$$[C_T]\{\dot{T}\} + [K_T]\{T\} = \{Q\} \tag{3.136}$$

where

$[C_T]$ is the heat capacity matrix,

$[K_T]$ is the heat conduction matrix,

$\{T\}$ is the column vector of the nodal point temperatures,

$\{\dot{T}\}$ is the time derivative of temperature,

$\{Q\}$ is the column vector of the nodal point heat sources,

The temperature which is transient is determined by means of specific time step schemes. Bathe and co-workers [70] [6] [7] developed a finite element program called ADINA-T which was chosen in this study to solve the welding heat flow problem. This program can take into account temperature dependent material properties as well as nonlinear convection and radiation boundary conditions.

The finite element program for welding problems was developed by Hibbitt and Marcal [24] in 1973 and was used later by other investigators including Hsu [25], and Nickell [46]. At M.I.T. a team headed by Masubuchi had also developed similar programs in the early 1970s [3] [45] [48] [64] [34]. Friedman [20] [19] had also made substantial contributions in the case of GTA welding.

3.6.2 Finite Element Procedure

The governing incremental isoparametric finite element equation for heat conduction analysis has been derived by Bathe [6] and is:

$$({}^{t}K^{k} + {}^{t}K^{c} + {}^{t}K^{r})\Delta\theta^{i} = {}^{t+\alpha\Delta t}Q + {}^{t+\alpha\Delta t}Q^{c}(i-1) + {}^{t+\alpha\Delta t}Q^{r}(i-1) - {}^{t+\alpha\Delta t}Q^{k}(i-1) \quad (3.137)$$

or

$${}^{t}\overline{K}\Delta\theta^{(i)} = {}^{t+\alpha\Delta t}\overline{Q}(i-1) \quad (3.138)$$

where ${}^{t}\overline{K}$ is the effective conductivity matrix at time t consisting of the conductivity, nonlinear convection, and radiation matrices; ${}^{t+\alpha\Delta t}Q$ is the heat flow vector including the effect of surface heat flow inputs, internal heat generation and temperature dependent heat capacity; ${}^{t+\alpha\Delta t}\overline{Q}(i-1)$ is the effective heat flow vector; and $\Delta\theta^{(i)}$ is the increment in the nodal point temperature in iteration i,

$${}^{t+\alpha\Delta t}\theta^{(i)} = {}^{t+\alpha\Delta t}\theta^{(i-1)} + \Delta\theta^{(i)} \quad (3.139)$$

Equation 3.137 is the general incremental heat flow equilibrium equation that is valid for linear and nonlinear analysis. The value of α which is $0 \leq \alpha \leq 1$ was chosen to obtain optimum stability and accuracy in the solution.

3.6.2.1 Boundary Conditions

Convection and radiation boundary conditions are taken into account by including the matrices ${}^{t}K^{c}$ and ${}^{t}K^{r}$ and the vectors ${}^{t+\alpha\Delta t}Q^{c}$ and ${}^{t+\alpha\Delta t}Q^{r}$ in the heat flow equilibrium equations, ie. equation 3.137. Additional external heat flow input on the boundary is specified in ${}^{t+\alpha\Delta t}Q$ as surface heat input. The prescribed temperature conditions can also be specified.

3.6.2.2 Step-By-Step Time Integration

In transient analysis a numerical time integration scheme must be employed. In ADINA-T, a family of one step methods is used, in which

$$ {}^{t+\alpha\Delta t}\dot{\theta} = \frac{({}^{t+\Delta t}\theta - {}^{t}\theta)}{\Delta t} \tag{3.140} $$

$$ {}^{t+\alpha\Delta t}\theta = (1-\alpha){}^{t}\theta + \alpha {}^{t+\Delta t}\theta \tag{3.141} $$

where $0 \le \alpha \le 1$.

This scheme was found to be unconditionally stable for $\alpha \ge \frac{1}{2}$ and to generally give better solution accuracy when $\alpha = 1$ (Euler Backward method). The modified Newton iteration is guaranteed to converge provided the time step Δt is small enough.

3.6.3 Weld Model

In this section all the necessary considerations for the modeling of a bead-on-edge weldment will be discussed.

The heat flow pattern resulting from a moving welding arc is generally three-dimensional; temperature gradients exist through the weldment thickness, as well as in direction parallel and transverse to the arc traveling direction. Let us consider the general heat flow equation (Equation 3.2):

$$ \rho c \frac{\partial \theta}{\partial t} = \dot{Q}_G + \frac{\partial}{\partial x}(k\frac{\partial \theta}{\partial x}) + \frac{\partial}{\partial y}(k\frac{\partial \theta}{\partial y}) + \frac{\partial}{\partial z}(k\frac{\partial \theta}{\partial z}) $$

If the dimensions in the xy-plane are large compared to the thickness so as to be for all practical purposes infinite, the temperature gradient in the thickness direction can be assumed to be zero. In other words, there is no net heat flow across the thickness of the plate. As a consequence, the welding thermal cycle can be analyzed using a two-dimensional transient heat conduction model:

$$ \rho c \frac{\partial \theta}{\partial t} = \dot{Q}_G + \frac{\partial}{\partial x}(k\frac{\partial \theta}{\partial x}) + \frac{\partial}{\partial y}(k\frac{\partial \theta}{\partial y}) \tag{3.142} $$

3.6.3.1 Boundary Conditions

Convection: The linear Newton convection cooling is assumed in the model according to

$$q^s = h(\theta_e - \theta^s) \tag{3.143}$$

where h is the temperature dependent convection coefficient, θ_e is the environmental temperature, and θ^s is the surface temperature at the point under consideration. The estimation of the convection coefficient h in this study is based on semi-empirical studies made by Tsai [64]. Table 3-V provides the value of the temperature dependent convection coefficient h.

Table 3-V: Convection coefficient h

$\theta^s - \theta_e$ [K]	h [W/in^{2}K]
0	0
56	1.1715×10^{-3}
278	5.8575×10^{-3}
556	1.1715×10^{-2}
2778	3.3974×10^{-2}
27778	7.0290×10^{-1}

where θ^s = surface temperature.

θ_e = environmental temperature.

Radiation: In the vicinity of the weld metal, radiation heat losses are significant because of the large difference between the surface and environmental temperature. These losses are modeled according to the quartic Stefan-Boltzman law:

$$q^s = \sigma \varepsilon A(\theta_r^4 - \theta^{s^4}) \tag{3.144}$$

where

σ = Stefan-Boltzman constant,

ε = emissivity of the surface,

A = shape factor,

θ_r = sink temperature,

θ^s = surface temperature.

In this study the shape factor A was taken to be unity and the emissivity coefficient $\varepsilon = 0.8$. The Stefan-Boltzman constant is 3.54375×10^{-11} W/in^{2}K^4.

3.6.3.2 Material Properties

The temperature dependence of the thermal conductivity, k, the specific heat, c, and the density, ρ, of the low carbon steel, HY-100, and HY-130 were shown in Sections 2.2.2, 2.3.2, and 2.3.3. Those values were utilized as input in the finite element heat transfer analysis.

3.6.3.3 Heat Input

The general modeling of heat input during welding was discussed in Sections 3.3 and 3.4, where both its magnitude and distribution were described. The arc efficiency, η_a, and the flame efficiency, η_f, are two of the most important parameters involved. The arc efficiency used in this investigation is 0.5. This value of arc efficiency is small when compared with the values recommended by Christensen [14] for the GMAW process for steel (Table 3-I). Since the investigation was done on bead-on-edge welding, there was no weld configuration that helps to confine the energy dissipation. The heat welding source and side heating heat source were assumed to be the generation of heat from a certain element during a short time. A consistent formulation for the distribution of heat input was adopted [7] assuming uniform distribution in space. Figure 3-14 shows the heat distribution for a welding heat source over 3.667 seconds. This is to simulate the passing of the arc torch traveling at 0.3 inch/second over the distance 1 inch along the weld line.

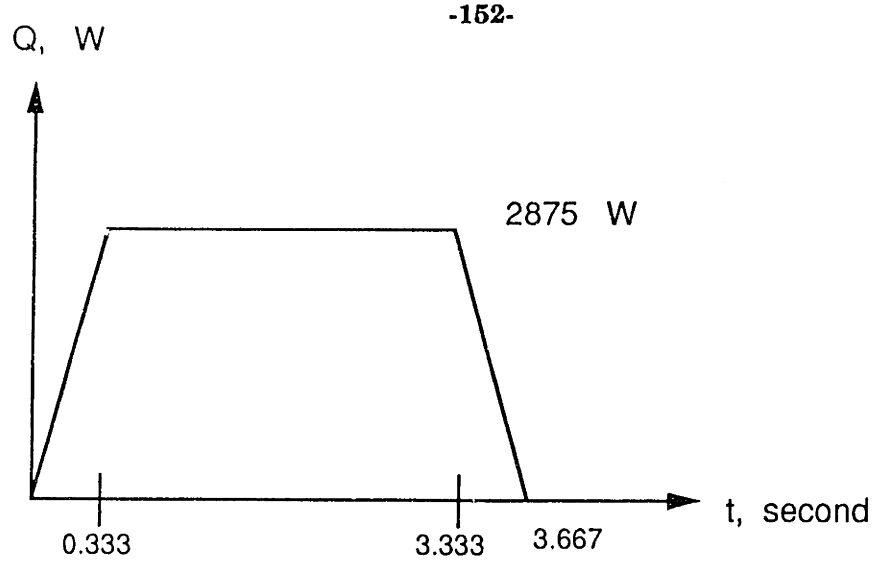

$$Q = \eta_a VI = 0.5 \times 25 \times 230 = 2875 \quad w$$

$$H = \frac{2875}{0.3} = 9583.33 \quad \text{Jule/in.}$$

$$\text{Area} = (0.333 \times 2875) + (3 \times 2875) = 9582.375 \quad \text{Jule/in.}$$

Figure 3-14: Welding Heat Source Distribution

The Gaussian radial heat distribution was assumed for the side heating heat source. From Table 3-III the effective power of acetylene flame was:

$$P_{eff} = \eta_f [\text{ Flame Power }]$$

$$= (0.44)(920)(4.184 \ \frac{W}{cal/sec})$$

$$= 1693.68 \quad W$$

From $q(r) = q_o e^{-Cr^2}$, the total power that could be absorbed by the work piece was:

$$Q = \int_0^\infty q(r) 2\pi r dr$$

$$= 2\pi q_o \int_0^\infty r e^{-Cr^2} dr$$

$$= \frac{\pi q_o}{C}$$

Therefore,

$$q_o = \frac{QC}{\pi} ; \quad C = 1.806 \ \frac{1}{\text{in.}^2} \quad \text{(from Table 3-III)}$$

$$= \frac{(1693.68)(1.806)}{\pi}$$

$$= 973.64 \ \frac{\text{W}}{\text{in.}^2}$$

To calculate the heat distribution for the side heating torch, we had to determine the size of the element that would be used to generate heat. The element with size equal to 1x1.5 inches was defined to match with the circular area of the heat distribution.

$$\pi r^2 = (1)(1.5) = 1.5 \quad \text{inch}^2$$

$$r^2 = 0.4775 \quad \text{inch}^2$$

or

$$r = 0.6910$$

The heat input for the side heating heat source was:

$$Q_s = \int_0^{0.6910} q_o e^{-Cr^2} 2\pi r dr$$

$$= 2\pi q_o \int_0^{0.6910} r e^{-Cr^2} dr$$

$$= (2\pi)(973.64)\left[\frac{-1}{(2)(1.806)}\right][-0.5778]$$

$$Q_s = 978.67 \quad \text{W}$$

This magnitude of heat generation for side heating should be enough to heat the specimen up to 200 °F. This can be verified by using the following relation:

$$Q_s = \dot{m} c [\theta_s - \theta_i]$$

where

c = heat capacity Btu/lbm °F,

θ_s = surface Temperature °F,

θ_i = initial Temperature °F.

$\dot{m} = \rho A v$

$= (0.284)(1.5)(0.5)(0.3)$

$= 0.0639$ lbm/second

Therefore

$$Q_s = (0.0639)(0.110)(200 - 68)(1054.35)$$
$$= 978.25 \quad W$$

Figure 3-15 shows the heat distribution for side heating heat source over 3.667 seconds to simulate the passing of the torch traveling at 0.3 inch/second over the distance 1 inch.

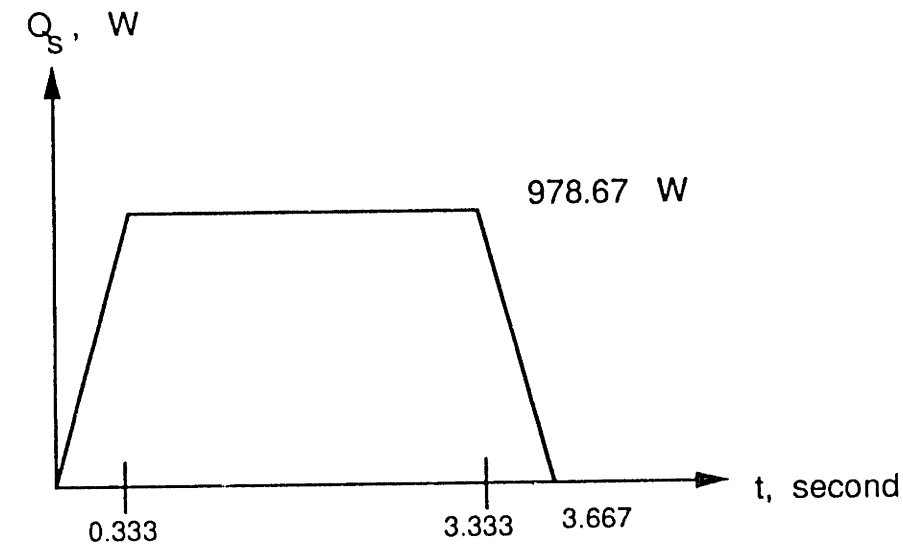

$$H_S = \frac{978.67}{0.3} = 3262.22 \text{ Jule/in.}$$

$$\text{Area} = (0.333 \times 978.67) + (3 \times 978.67) = 3261.91 \text{ Jule/in.}$$

Figure 3-15: Side Heating Heat Source Distribution

Figure 3-16 shows the finite element mesh used in this investigation. A total of 96 4-node isoparametric elements were used. Twelve elements at the top represent the weld metal where the welding heat source generated during a short time. In the case of side heating, twelve elements at the bottom represent the area that generates the heat for side heating.

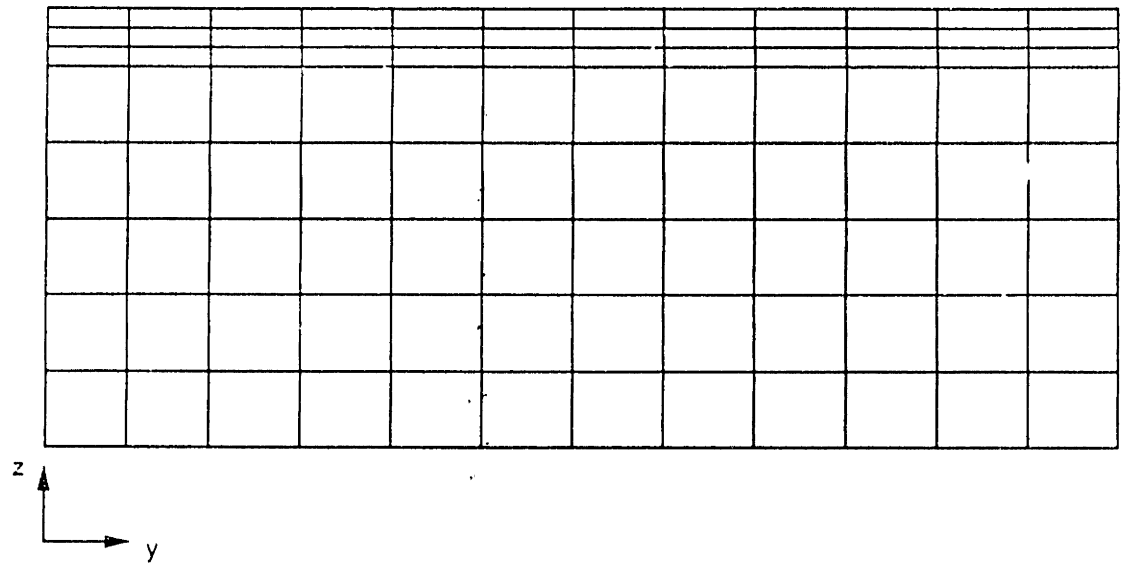

Figure 3-16: Finite Element Mesh for Temperature Analysis

3.7 Comparison of Results

The experimental results were analyzed using both the analytical approach described in Section 3.3 and the finite element program ADINA-T with the model described in Section 3.6. Figures 3-17 to 3-22 show the calculated temperatures and compare them with the experimental results for low carbon steel, HY-100, and HY-130 at two different locations away from the weld line for the case without side heating. The results yield a good correlation with the experimental data. The analytical calculation tends to provide a slight overestimate of peak temperature. This can be attributed to the linear assumption of the thermal conductivity which yields a lower thermal conductivity value than the actual one. At lower temperatures, the difference among all calculations and experiments is not great. At distances close to the

weld line, the analytical calculations predict a slower cooling rate while the finite element calculations yield a higher cooling rate. At distances far away from the weld line the finite element solutions tend to give a slower cooling rate. Heat losses from the specimen surface play an important role in determining the cooling rate. At the lower temperature region, it appears that the constant average heat loss coefficient (from convection and radiation) assumed in the analytical calculation provides a more suitable cooling rate. However, at the high temperature region, the variable heat loss coefficient used in the finite element program provides a better cooling rate. The predicted peak temperature from the finite element approach is also higher than the one obtained from the analytical approach at the distance far away from the weld line.

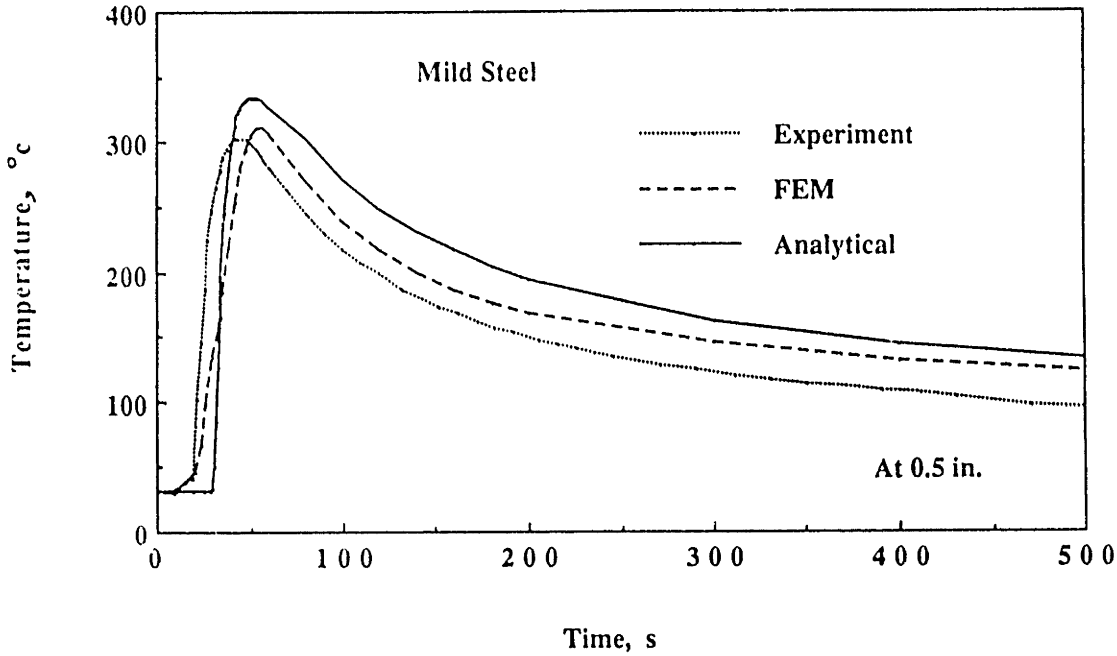

Figure 3-17: Comparison of Temperature History -Calculation Prediction .vs. Experiment Data -for Low Carbon Steel

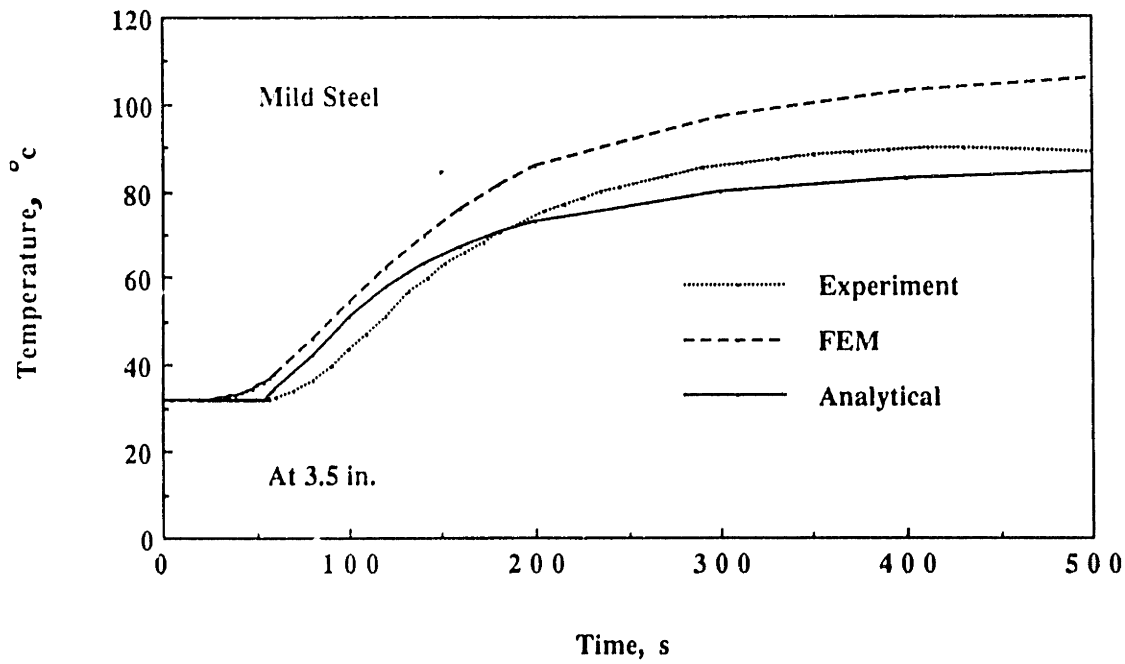

Figure 3-18: Comparison of Temperature History -Calculation Prediction .vs. Experiment Data -for Low Carbon Steel

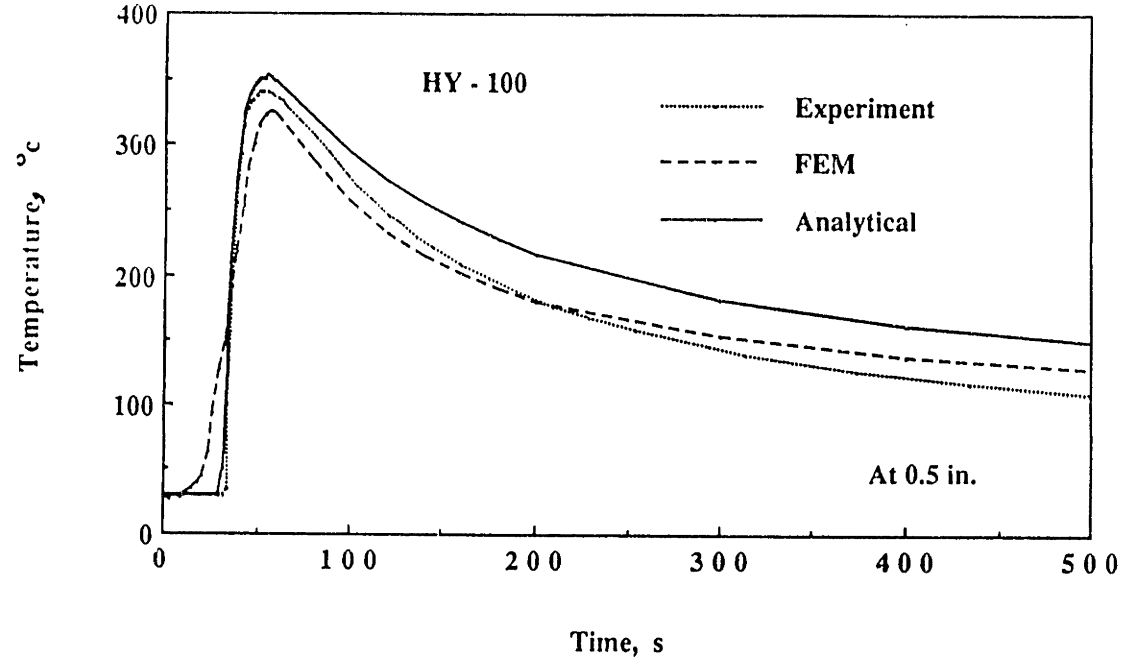

Figure 3-19: Comparison of Temperature History -Calculation Prediction .vs. Experiment Data -for HY-100

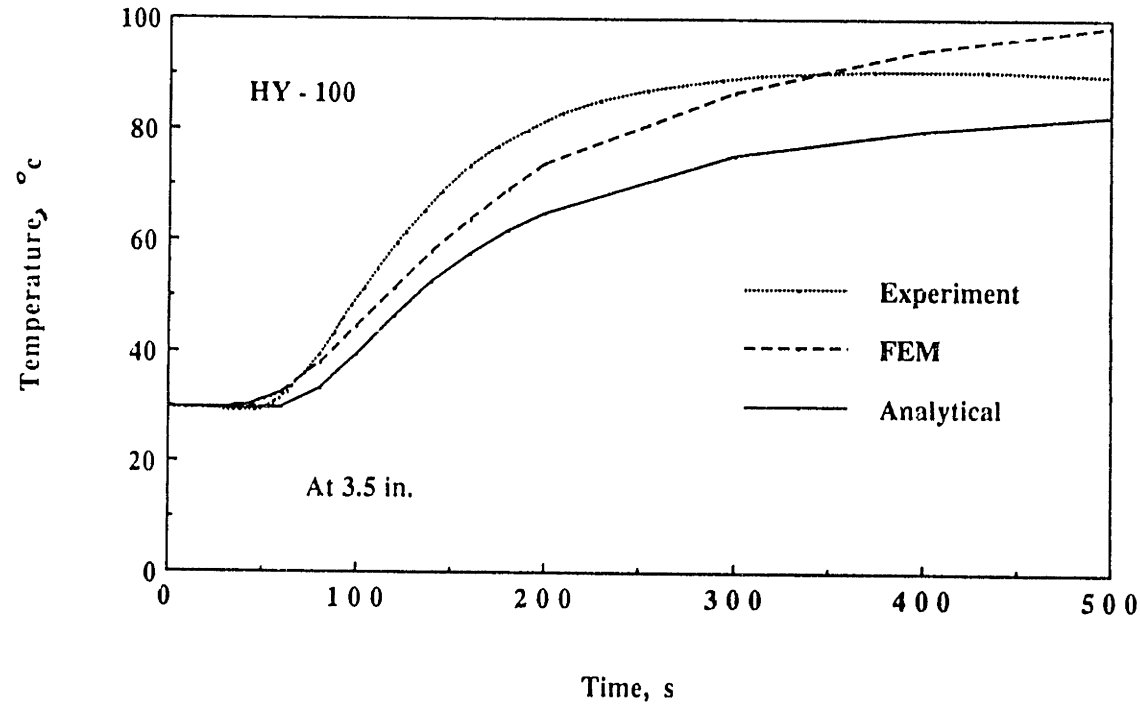

Figure 3-20: Comparison of Temperature History -Calculation Prediction .vs. Experiment Data -for HY-100

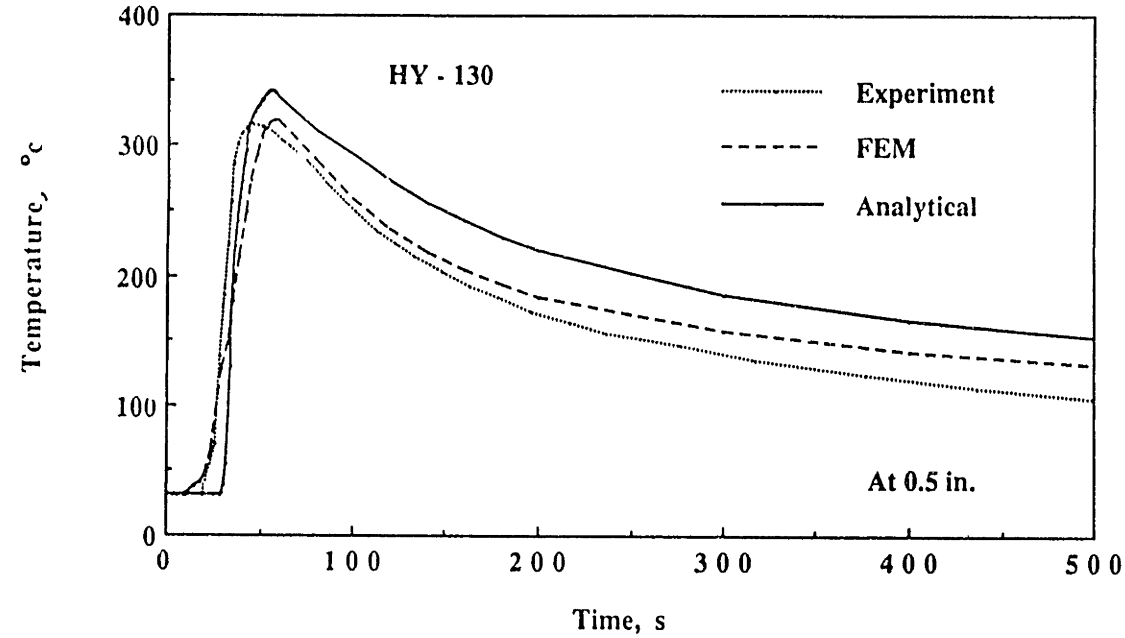

Figure 3-21: Comparison of Temperature History -Calculation Prediction .vs. Experiment Data -for HY-130

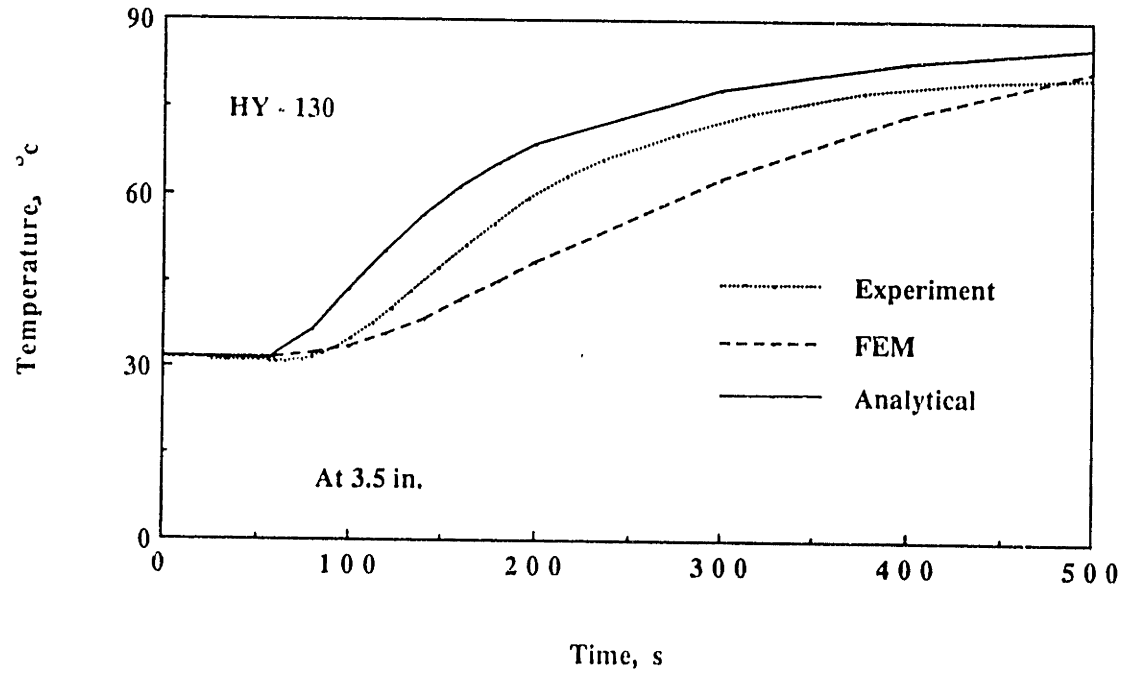

Figure 3-22: Comparison of Temperature History -Calculation Prediction .vs. Experiment Data -for HY-130

Figures 3-23 to 3-28 show the results obtained for the case with side heating. Similar behaviors are observed except that they are more pronounced due to additional heat input from the side heating heat source. The presence of the side heating heat source does not significantly increase the peak temperature at distances close to the weld line. An increase in peak temperature can be observed at the region near the location of the side heating heat source. However, the side heating heat source provides some effects on the cooling rate as described in the previous chapter. These effects also occur in the analysis for both the analytical and numerical approaches. With the side heating heat source applied on the specimen, the cooling rate tends to be slower.

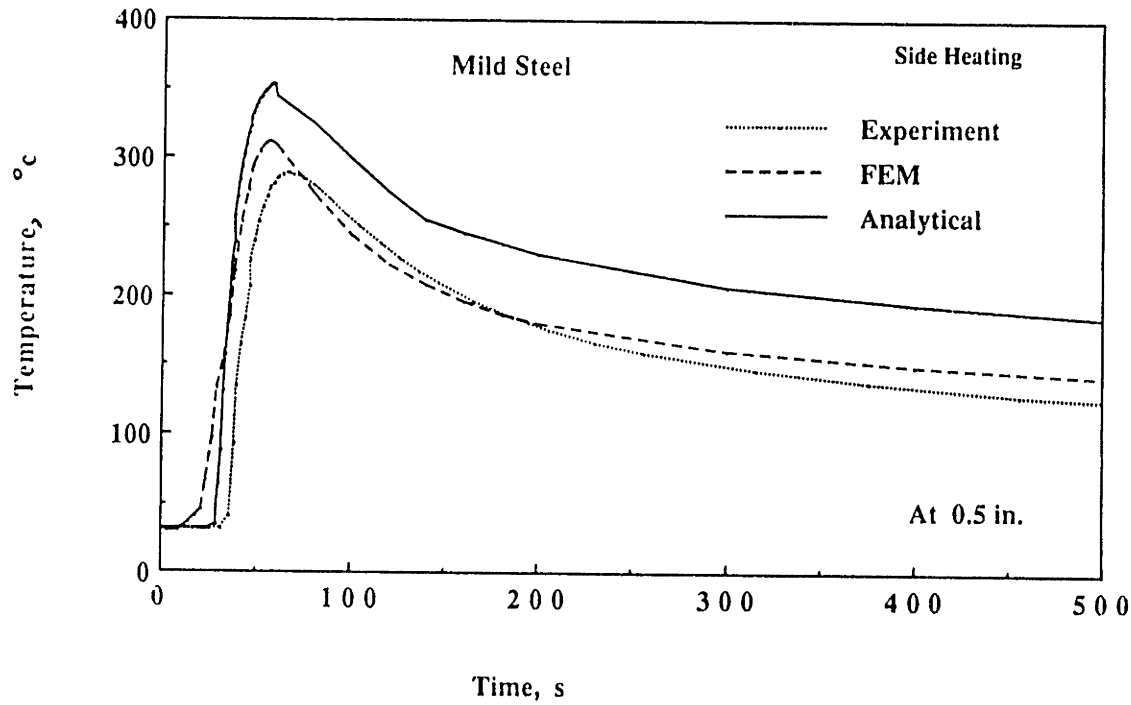

Figure 3-23: Comparison of Temperature History -Calculation Prediction .vs. Experiment Data -for Low Carbon Steel (Side Heating)

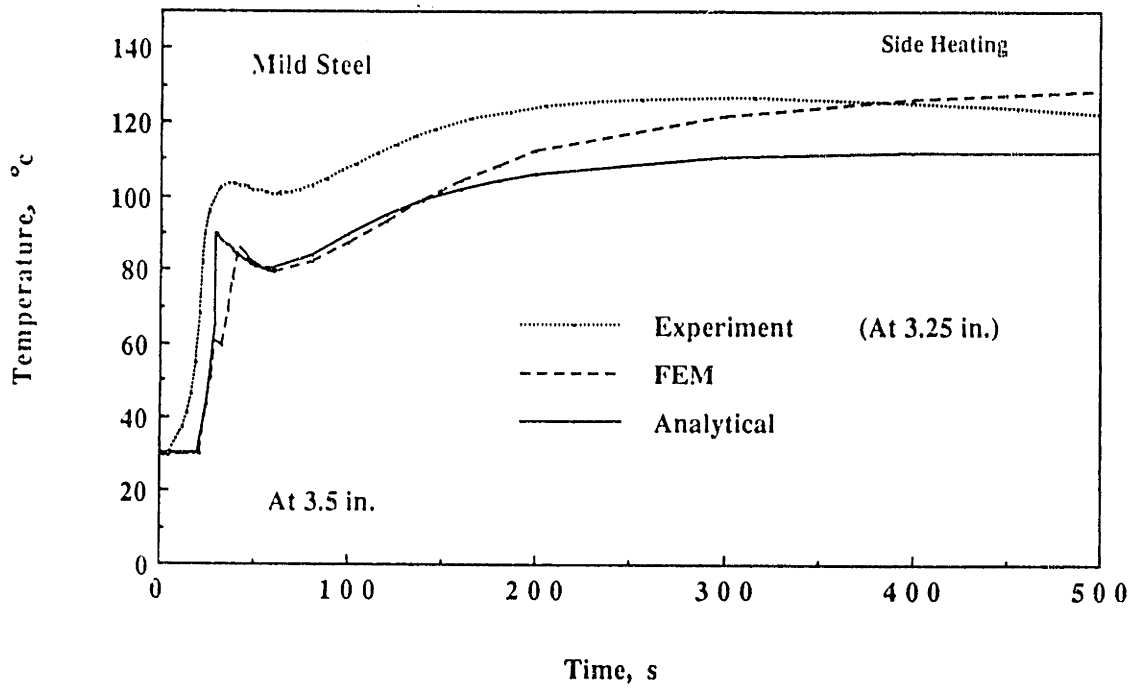

Figure 3-24: Comparison of Temperature History -Calculation Prediction .vs. Experiment Data -for Low Carbon Steel (Side Heating)

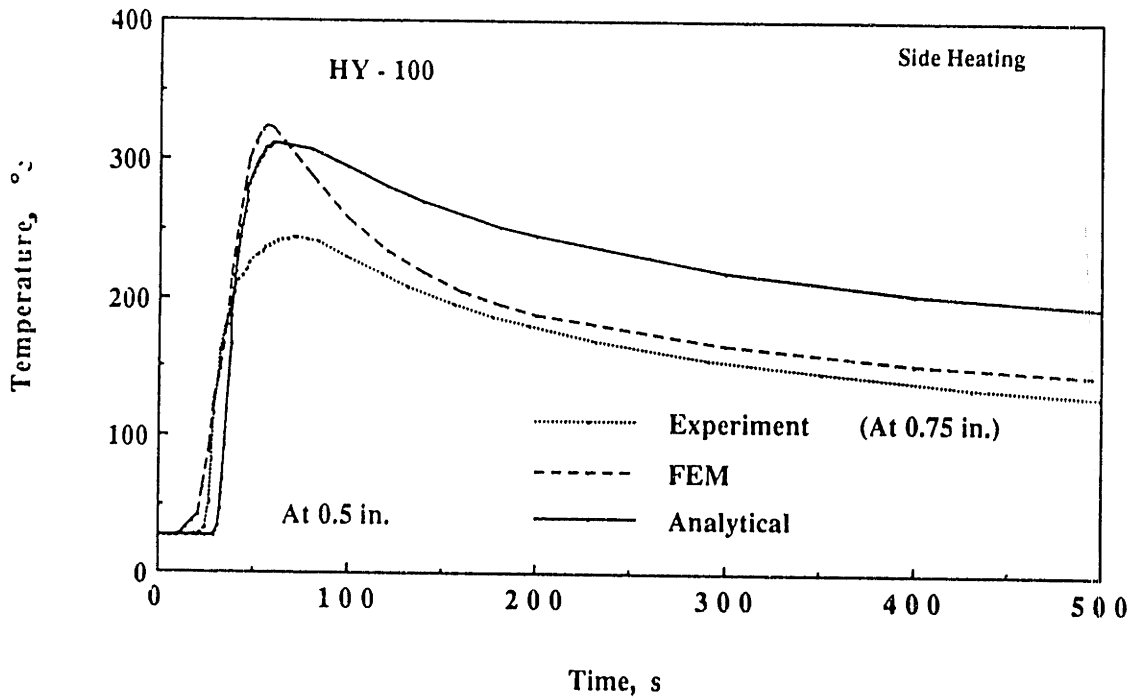

Figure 3-25: Comparison of Temperature History -Calculation Prediction .vs. Experiment Data -for HY-100 (Side Heating)

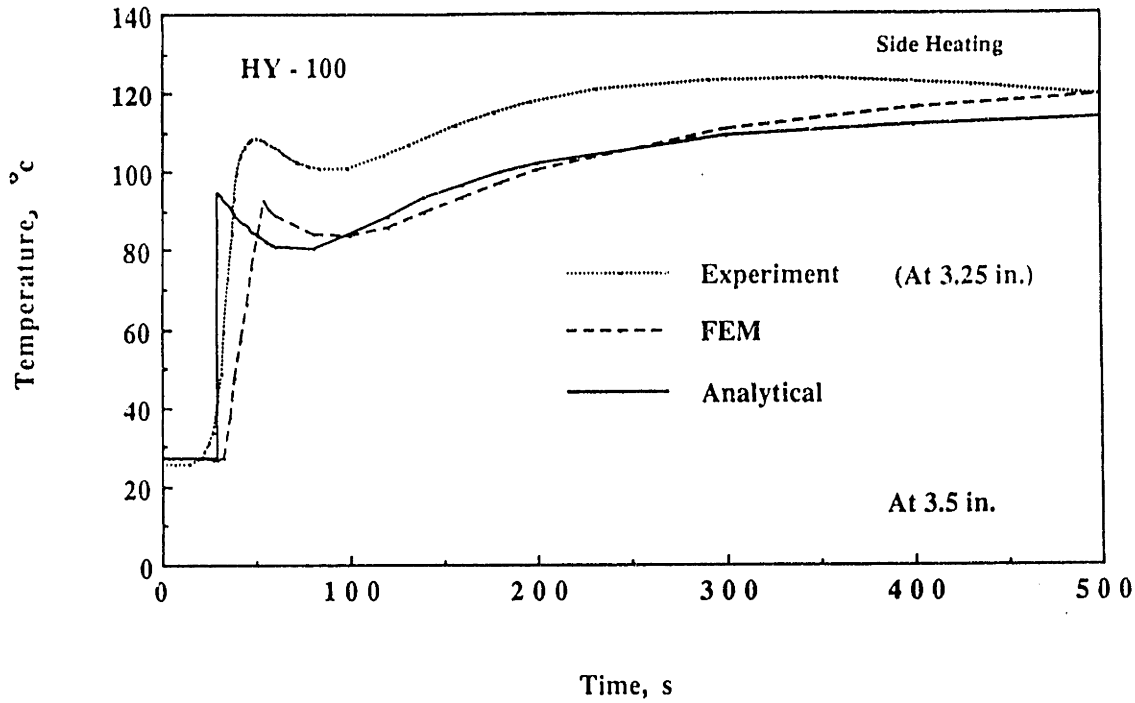

Figure 3-26: Comparison of Temperature History -Calculation Prediction .vs. Experiment Data -for HY-100 (Side Heating)

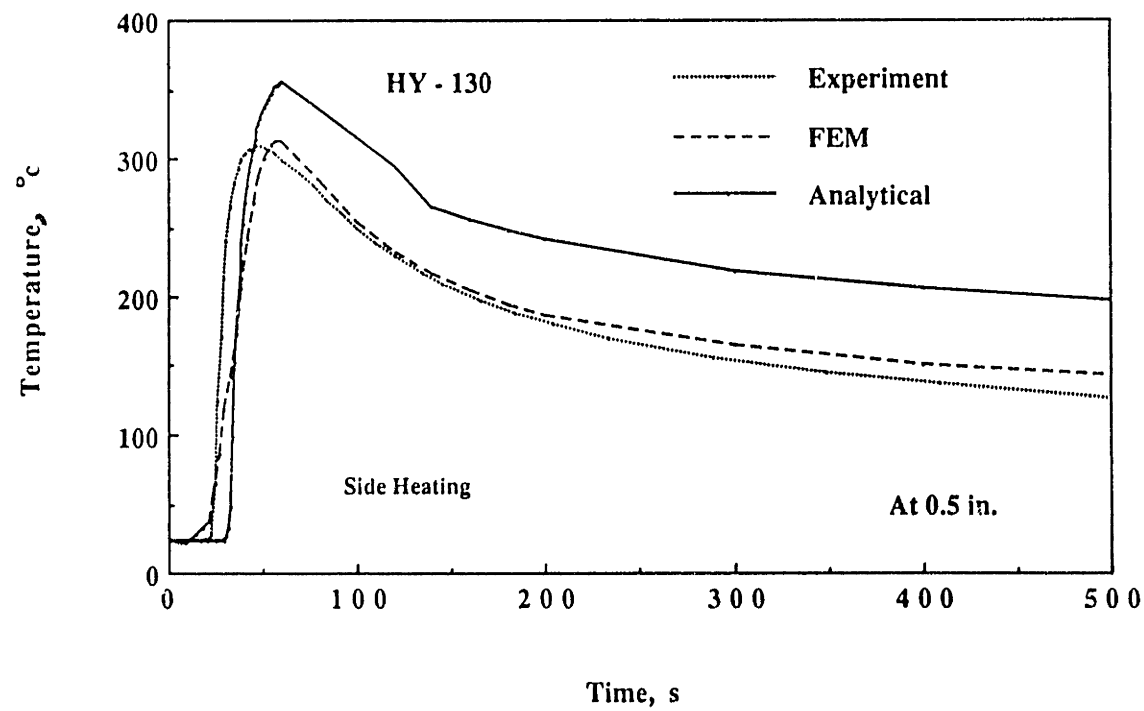

Figure 3-27: Comparison of Temperature History -Calculation Prediction .vs. Experiment Data -for HY-130 (Side Heating)

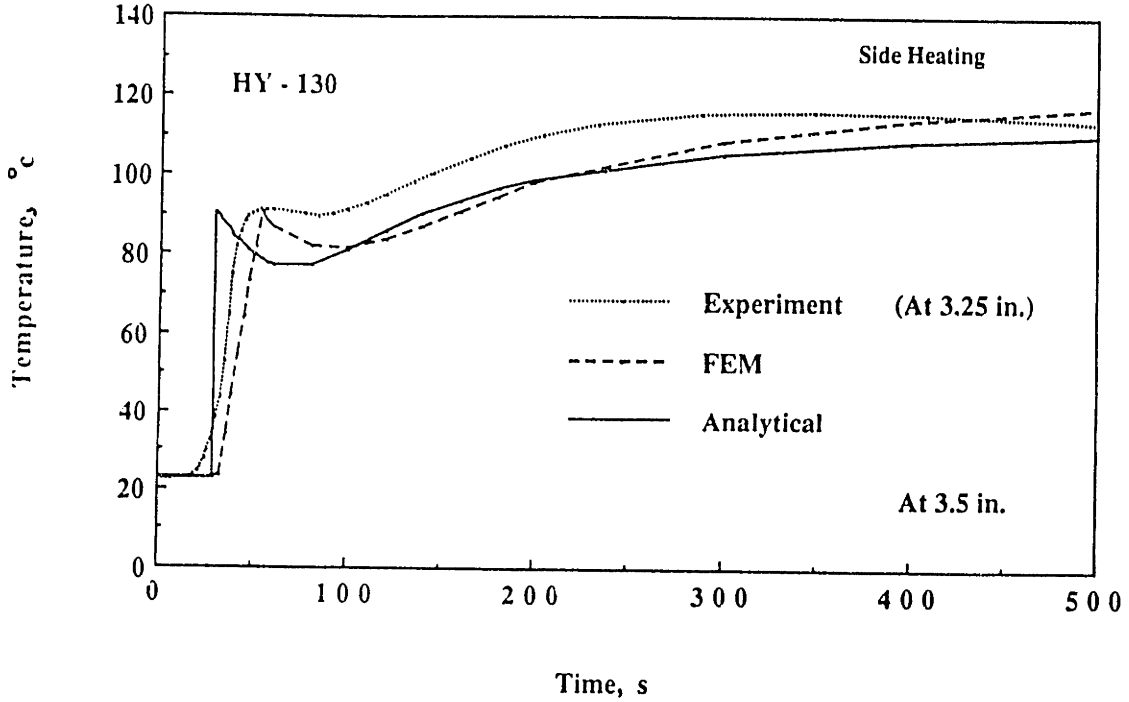

Figure 3-28: Comparison of Temperature History -Calculation Prediction .vs. Experiment Data -for HY-130 (Side Heating)

3.8 Summary

The analysis performed so far gives fairly good agreement with the experimental results. However, it should be noted that welding is a very complex phenomenon and has to deal with many uncertainties involved in estimating several parameters, such as thermal conductivity, heat loss coefficient, etc, which are required as inputs to the solution. The nonlinearity of the phenomenon itself leads to difficulty in finding the accurate solution for general welding processes. A lot of complexities which at present can not be determined accurately also provide difficulty in solving welding problems. Such complexities and nonlinearity are the heat input to the specimen being welded as well as the side heating heat source, the temperature dependence of material at high temperature, the temperature dependence of heat loss coefficient, etc. The improvement in those areas is needed to enhance a good estimation of the temperature distribution during welding.

Chapter 4

Analytical and Numerical Treatment of Stress-Strain-Distortion

4.1 Introduction

In the previous chapter discussion was made on how to predict the uneven temperature distribution that occurs during welding. This uneven temperature is indeed the cause of transient strains and transient stresses and the distortion and residual stresses that remain after welding. To analyze the welding problem which involves both thermal and stress analysis, one should start from the first law of thermodynamics. This means that one would have to solve a problem containing mechanical and thermal coupling. Solving a problem in this way makes the analysis extremely complicated. It is, therefore, necessary to uncouple the thermal and mechanical parts of the welding problem and solve each of them separately. Such an approach was used in this study. By using the temperature distribution predicted based on the techniques described in the previous chapter, the transient strains, transient stresses, distortion, and residual stresses can be calculated.

Two general techniques were used to solve the mechanical problem in this study. One is a simple one-dimensional analytical analysis and the other is a more sophisticated one based on the finite element method. Results from both techniques were then compared with the experimental results.

4.2 Literature Review

Studies on transient thermal stresses during welding started in the 1930s. However, because the computation required for analyzing transient phenomenon is complex, very limited studies were done. Since modern computers became accessible to researchers in the 1960s, more studies have been done to analyze this phenomenon.

The first significant attempt to use a computer in the analysis of thermal stresses during welding was done by Tall [63] in his Ph.D. thesis in 1961. Tall developed a simple program on thermal stresses during bead-on-plate welding along the center line of a strip. In his analysis only the longitudinal stress, σ_x, was considered and was a function of lateral distance only. This kind of analysis was later designated one-dimensional. In 1968, based upon Tall's analysis, Masubuchi [41] developed a FORTRAN program on the one-dimensional analysis of thermal stresses during welding. This program was later modified and improved at M.I.T. [16] [48] [60] [51]. However, due to the complexities of welding problems, particularly the complex effects of inelastic material response and material loading and unloading, this one-dimensional analysis could not be further developed. The attention was then focused on numerical method, especially on the finite element method (FEM) which could be applied to the highly nonlinear inelastic behavior of weld structures.

The first application of the FEM to welding problems was done by Hibbitt and Marcal [24]. In their study a thermo-mechanical model was developed to simulate the GMAW process. This model also accounted for temperature dependent material properties. Several investigators including Nickell and Hibbitt [46], Hsu [25], Lobitz and co-workers [29] later used this model to investigate the welding phenomenon. Friedman [19] developed finite element analysis procedures for calculating stresses and distortion in longitudinal butt welds. Iwaki [42] developed a two-dimensional finite element program for the analysis of thermal stress during bead-on-plate welding. At M.I.T. a team

headed by Masubuchi has also developed a two-dimensional finite element program capable of performing plane strain and plane stress analysis [34]. Muraki [45] developed a two-dimensional finite element program so that thermal stresses during butt welding as well as those during bead-on-plate welding could be analyzed. Papazoglou [50] developed a model that included the effect of phase transformation by using finite element analysis.

Most of the analysis, however, was mainly concentrated on the residual stresses. Very few so far were done on the metal movement of the weldment. Nishida [48] used the one dimensional program to study the transient distortion of a built-up T-shaped beam. He found that the results obtained were greatly affected by the material properties at high temperatures. Shin [61] analyzed two-dimensional out of plane distribution of distortion for the welded panel structures using the finite element method. The results verify that distortion analysis is extremely important in structural design. An optimum design must take into account structural integrity as well as welding fabrication. Satoh [58] and Jonsson [28] did extensive analysis on the root gap changes during welding with and without tack welds. Chang [13] recently used a one-dimensional program to analyze the root gap change during butt welding with and without side heating.

4.3 One-Dimensional Analysis

The method of successive elastic solutions is employed to calculate the transient strains, transient stresses, distortion, and residual stresses in the one-dimensional analysis. The procedure, outlined by Mendelson [43], was first used in the solution of welding problems by Tall [63] and later by Masubuchi [41].

To analyze the stress state at the center cross section of the plate, a narrow strip element perpendicular to the welding is cut out as shown in Fig. 4-1. Both edges of the strip at x and $x + \Delta x$ remain straight --this is an assumption used in the simple beam theory.

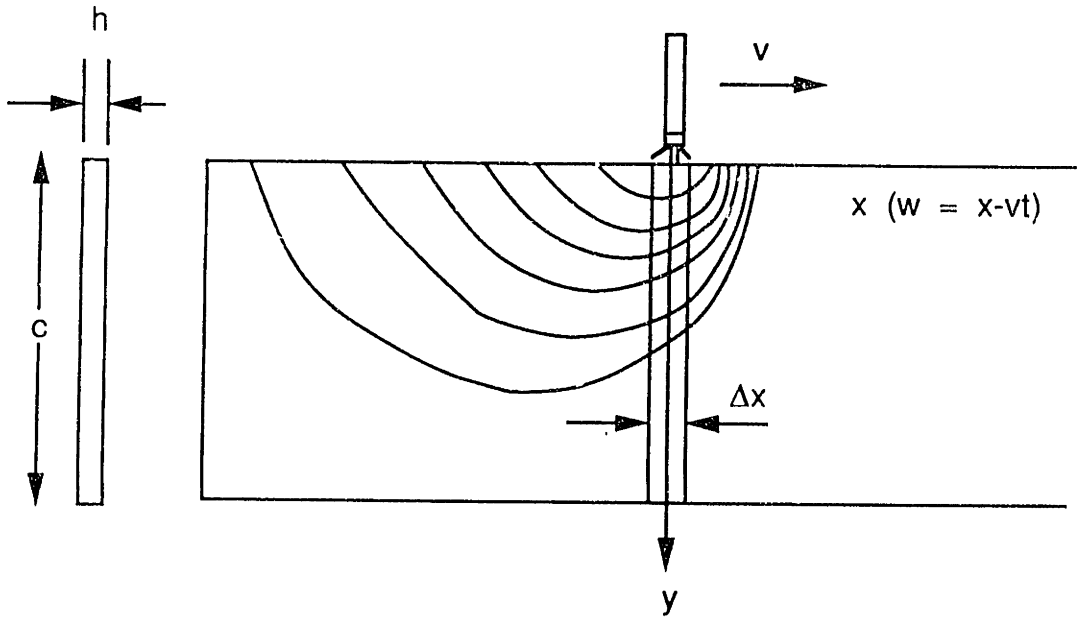

Figure 4-1: Stripped Element for One-dimensional Calculation

A basic assumption inherent in the one-dimensional stress analysis is that $\sigma_y = \tau_{xy} = 0$. The stress equilibrium equation in the absence of any external forces is thereby reduced to a single equation:

$$\frac{\partial \sigma_x}{\partial x} = 0 \tag{4.1}$$

This indicates that σ_x cannot vary in the direction of the weld. It should be pointed out here, however, that the temperature distribution does vary in this direction and consequently σ_x does, too. Hence, the equilibrium conditions are not satisfied by the model. It is further assumed that at time t, the strip is a part of an infinitely long plate subject to the same temperature over its entire length as shown in Fig. 4-2.

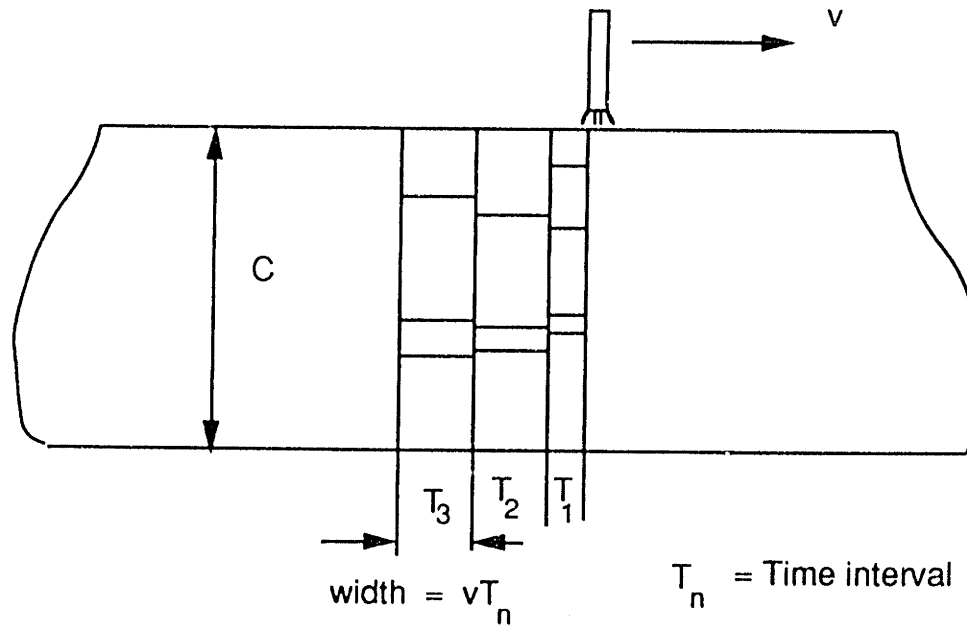

Figure 4-2: Temperature Distribution on One Dimensional Model

If a single longitudinal position is considered, the entire welding process may be divided into a number of time steps. During each time step, the transverse temperature distribution is assumed to remain constant at the observed longitudinal position. At each new time step, the temperature is changed and a new stress distribution is obtained.

Each time step in the fixed system corresponded to a given transverse strip in the moving system. The width of each strip is the product of the length of time step and the speed of the arc [see Fig. 4-2]. The stress at each time step is calculated using the method of successive elastic solutions. The stress-strain relation is used and the strain obtained is also made to satisfy the compatibility equation for one-dimensional analysis.

$$\frac{\partial^2 \varepsilon_x}{\partial y^2} = 0 \tag{4.2}$$

or

$$\varepsilon_x = c_1 + c_2 y \tag{4.3}$$

where c_1 and c_2 are constants to be determined.

Considering an incremental approach at the end of a time interval Δt, the following will hold along the strip:

$$\varepsilon_x = \frac{\sigma_x}{E} + \alpha\Delta\theta + \varepsilon_x^{pl} \tag{4.4}$$

or

$$\sigma_x = E(\varepsilon_x - \alpha\Delta\theta - \varepsilon_x^{pl}) \tag{4.5}$$

where

$\frac{\sigma_x}{E}$ = elastic part of strain, ε_x^{el},

$\alpha\Delta\theta$ = thermal strain, ε_x^{th},

$\Delta\theta$ = $\theta - \theta_o$,

ε_x^{pl} = plastic strain due to previous increment of load.

The global equilibrium equations with no external forces and moments acting on the plate are:

$$\int_0^c \sigma_x dy = 0 \tag{4.6}$$

$$\int_0^c \sigma_x y dy = 0 \tag{4.7}$$

where

c = plate width.

After substituting Equations 4.3 and 4.4 into Equations 4.6 and 4.7, a set of linear equations is obtained for the determination of the unknown coefficients c_1 and c_2. Solving this system and substituting back into Equation 4.3, the following expression is obtained for the total strain:

$$\varepsilon_x = (A_1 - A_2 y)\int_0^c E(\alpha\Delta\theta + \varepsilon_x^{pl})dy - (A_2 - yA_3)\int_0^c E(\alpha\Delta\theta + \varepsilon_x^{pl})ydy \tag{4.8}$$

where

$$A_1 = [\int_0^c Ey^2 dy\,]/B$$

$$A_2 = [\int_0^c Eydy\,]/B$$

$$A_3 = [\int_0^c Edy\,]/B$$

$$B = [\int_0^c Edy\,][\int_0^c Ey^2dy\,] - [\int_0^c Eydy\,]^2$$

Equation 4.8 alone is not enough to solve the problem. A stress-strain relation is needed. At each time step the total strain is first calculated along the strip from Equation 4.8 assuming that no plastic strain exists [$\varepsilon_x^{pl}(y) = 0$]. The mechanical strain ε^m, then, is:

$$\varepsilon^m = \varepsilon_x(y) - \varepsilon_x^{th}(y) = \varepsilon_x(y) - \alpha\Delta\theta(y) \qquad (4.9)$$

Assuming a bilinear stress-strain law (Fig. 4-3), a first approximation of the plastic strain can be obtained as in Fig. 4-4. This value can be used again in Equation 4.8 to obtain a second approximation of the total strain, and the process can be repeated until convergence is reached.

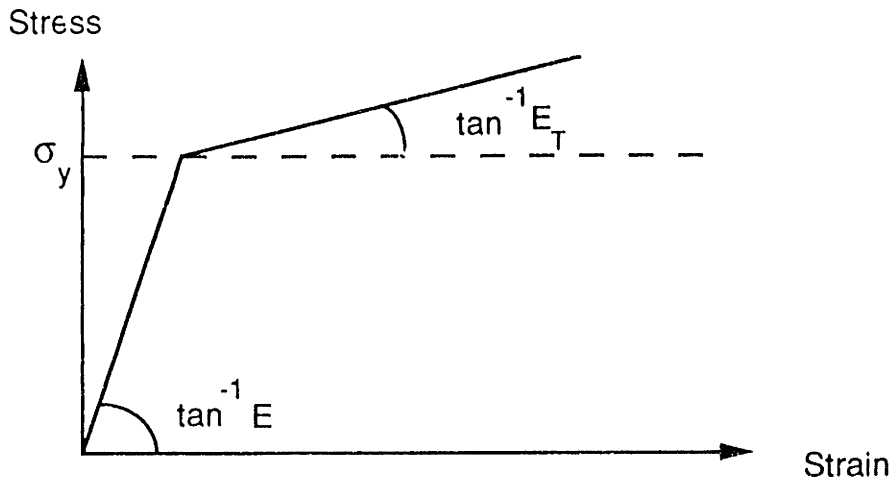

Figure 4-3: Bilinear Stress-strain Relation

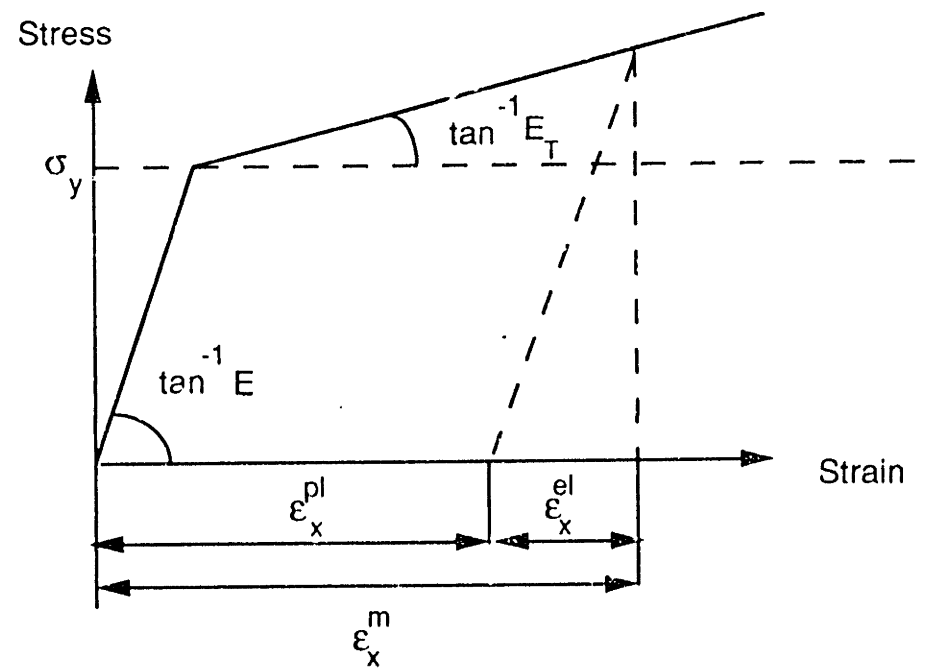

Figure 4-4: Plastic Strain Estimation

During the calculation of the total strains at each time step, the accumulated plastic strains from previous time steps are included to account for possible elastic loading and unloading (Fig. 4-5). This is important in the case of welding, where the complex uneven temperature distribution present in the plate gives rise to complex stress histories.

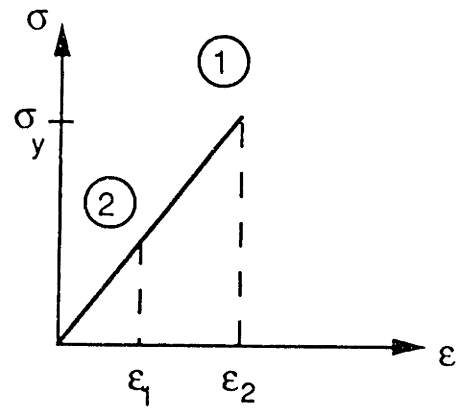

a. Elastic loading and unloading

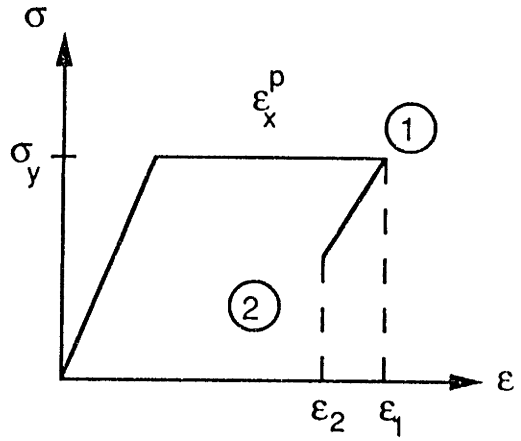

b. Plastic loading -Elastic unloading

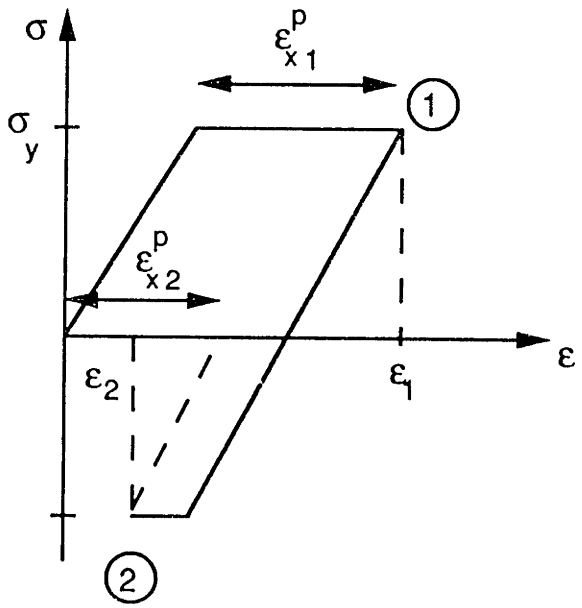

c. Plastic loading - Reverse yielding

Figure 4-5: Loading and Unloading

Once the transient strains are calculated, it is possible to calculate the transient distortion of the weld plates. Figure 4-6 shows the procedure for determining transient distortion at mid-length. Curvature ρ, at a given time, is equal to the quantity c_2 in Equation 4.3. The change of curvature with time t, is shown in Fig 4-6a at the location concerned. The simple beam theory is then used to arrive at:

$$\rho = \frac{\partial^2 w(x)}{\partial x^2} \tag{4.10}$$

where w is the distortion in the y direction at location x.

For a quasi-stationary state it is possible to determine the longitudinal distribution of the curvature at a certain time as shown in Fig. 4-6b. The shape of distortion, w, can be obtained by integrating the ρ-curve along the x direction. If the applied boundary condition is simply support at both ends, the distortion at mid-length can be determined as shown in Fig. 4-8c, by knowing the w-value of three points: the starting edge A, the finish edge B, and the mid-length point M.

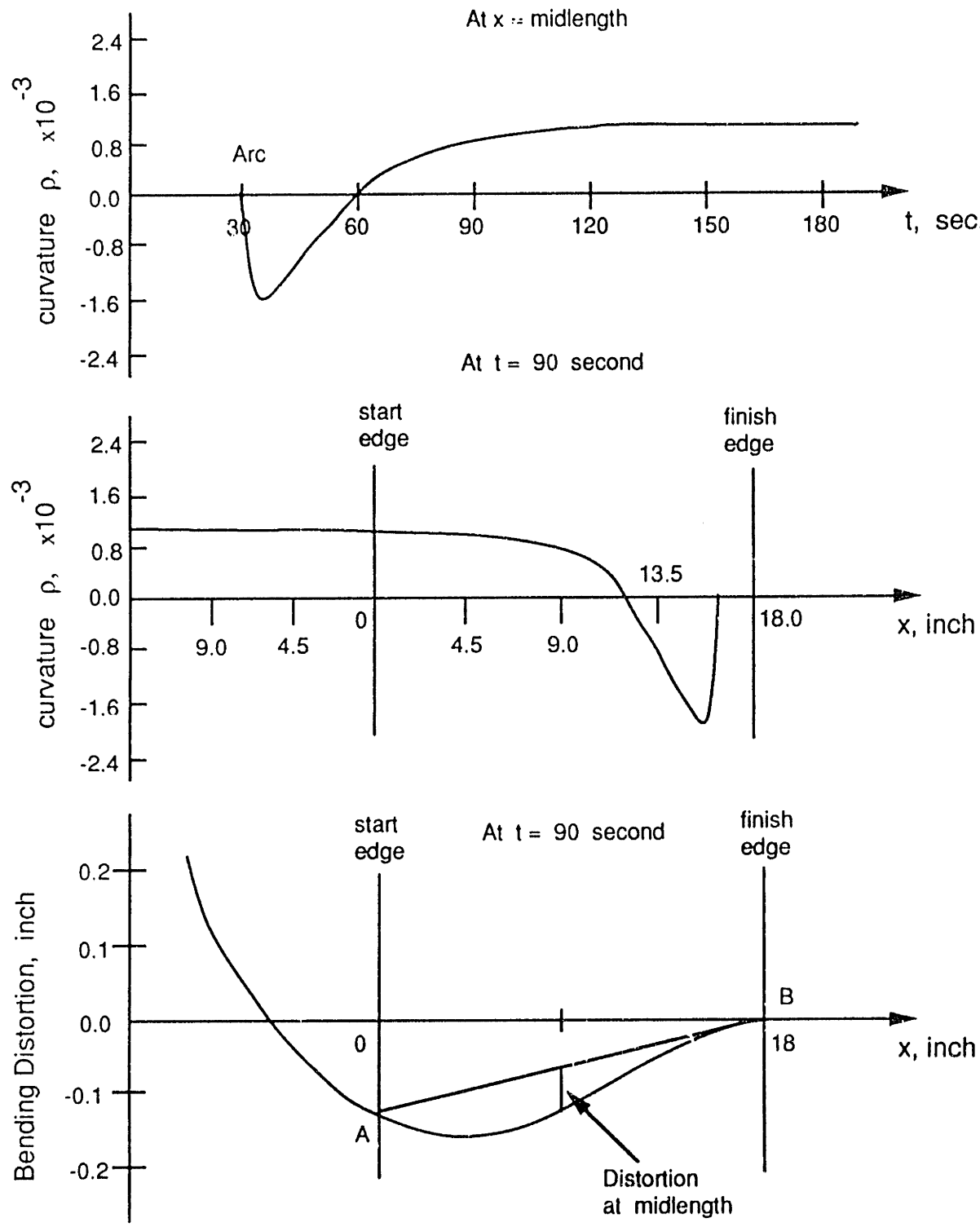

Figure 4-6: Procedure of Calculating Transient Deformation at Mid-length

The computer program was written in FORTRAN to perform the analysis outlined so far. Various integrations are necessary in the stress calculation. In the present program, 21 integration points with unequal intervals were used. The integration schemes used belong to the general group of the Newton-Cotes methods. The program can take into account the temperature dependence of all material properties and any type of strain hardening, and can solve all bead-on-plate, bead-on-edge, and butt welds of flat plates with finite width. The output of each time step consists of the total strain, mechanical strain, plastic strain, and stress at each of the predetermined points located at various transverse distances from the weld line. The distortion is calculated only at the mid-length. The temperature distribution can be input separately or calculated if desired by the same program using the line heat source solution.

4.4 Finite Element Formulation

In order to take the next step in improving the accuracy of the computation, we must take into account the transverse stress, σ_y, whose existence of this stress near the weld line cannot be neglected. To do this, a two-dimensional model should be considered. In the plastic-elastic region, the only possible means is the use of the numerical method. In this study the thermal elastic plastic and creep constitutive model of the multipurpose finite element program ADINA (Automatic Dynamic Increment Nonlinear Analysis) was used to predict the transient strains, transient stresses, distortion, and residual stresses due to welding. The model was developed by Snyder and Bathe [9] in 1980 and is described in the following sections.

4.4.1 Governing Equation

The governing incremental finite element equation for the problem can be written as:

$$^{t+\Delta t}K^{(i-1)}\Delta U^{(i)} = {}^{t+\Delta t}R - {}^{t+\Delta t}F^{(i-1)} \tag{4.11}$$

where

$^{t+\Delta t}K^{(i-1)}$ = tangent stiffness matrix at time $t+\Delta t$ which includes the linear and nonlinear strain stiffness matrices.

$^{t+\Delta t}R$ = vector of externally applied force at time $t+\Delta t$.

$^{t+\Delta t}F^{(i-1)}$ = vector of nodal point force due to element internal stress at time t.

$\Delta U^{(i)}$ = increment in nodal point displacement in iteration i = $[\,{}^{t+\Delta t}U^{(i)} - {}^{t+\Delta t}U^{(i-1)}\,]$.

The term $^{t+\Delta t}F^{(i-1)}$ can be evaluated for the materially nonlinear as follows:

$$^{t+\Delta t}F^{(i-1)} = \int_V {}^tB_L^T\, {}^{t+\Delta t}\sigma^{(i-1)}dV \tag{4.12}$$

where

$^tB_L^T$ = constant strain-displacement transformation matrix.

$^{t+\Delta t}\sigma^{(i-1)}$ = stress vector corresponding to the nodal point displacement $^{t+\Delta t}U^{(i-1)}$.

Equation 4.11 is a linearization of the actual nonlinear continuum mechanics. Therefore, in order to reduce the solution errors, a modified Newton-Raphson iteration is used. The convergence of the iteration can be accelerated using the Aitken method or, in complex material nonlinear cases (such as welding problems), improved using the BFGS (Broyden-Fletcher-Goldfarb-Shanno) matrix updating method [8].

4.4.2 Thermo-Elastic-Plastic and Creep Model

A basic assumption in the formulation of the model is that the infinitesimal total strain tensor can be expressed as the sum of elastic, plastic, thermal and creep strains.

$$ {}^{t}e_{ij} = {}^{t}e_{ij}^{E} + {}^{t}e_{ij}^{P} + {}^{t}e_{ij}^{TH} + {}^{t}e_{ij}^{C} \tag{4.13} $$

where

${}^{t}e_{ij}$ = component of infinitesimal total strain tensor at time t.

${}^{t}e_{ij}^{E}$ = component of infinitesimal elastic strain tensor at time t.

${}^{t}e_{ij}^{P}$ = component of infinitesimal plastic strain tensor at time t.

${}^{t}e_{ij}^{TH}$ = component of infinitesimal thermal strain tensor at time t.

${}^{t}e_{ij}^{C}$ = component of infinitesimal creep strain tensor at time t.

This assumption allows the distinction between time dependence and time independence of inelastic strains. At any time t, the stress is given by the constitutive law for isotropic thermal elastic material for small displacement analysis as follows:

$$ {}^{t}\sigma_{ij} = {}^{t}C_{ijrs}^{E}({}^{t}e_{rs} - {}^{t}e_{rs}^{P} + {}^{t}e_{rs}^{TH} - {}^{t}e_{rs}^{C}) \tag{4.14} $$

where

${}^{t}C_{ijrs}^{E}$ = component of elastic constitutive tensor at time t.

The thermal strains are:

$$ {}^{t}e_{rs}^{TH} = {}^{t}\alpha_{m}({}^{t}\theta - \theta_{R})\delta_{rs} \tag{4.15} $$

where

${}^{t}\alpha_{m}$ = mean coefficient of thermal expansion.

${}^{t}\theta$ = material temperature at time t.

θ_{R} = reference temperature at which thermal strains are zero.

δ_{rs} = Kronecker delta.

The creep strains are neglected in this study since we are only concerned with the no-creep situation.

The situation is more complicated when one tries to find the plastic strains. Even though the elastic theory of isothermal plasticity has been well established [43] [33], the extension of this theory to the non-isothermal case is very difficult. Therefore, the same non-isothermal theory of plasticity will be

used throughout the temperature range encountered in the welding problem. The plastic behavior is described using three fundamental concepts, namely (1) a yield condition which specifies the state of multi-axial stress corresponding to start of plastic flow; (2) a flow rule relating plastic strain increments to the current stresses and the stress increment subsequent to yielding; (3) a hardening rule which specifies how the yield condition is modified during plastic flow.

The general form of the yield or loading function for multiaxial stress condition in non-isothermal condition is;

$$ {}^{t}F = {}^{t}F({}^{t}\sigma_{ij}, {}^{t}\alpha_{ij}, {}^{t}\sigma_{y}) \tag{4.16} $$

where ${}^{t}\alpha_{ij}$ and ${}^{t}\sigma_{y}$ depend on the history of plastic deformation and temperature. For elastic behavior, ${}^{t}F < 0$ and for plastic behavior ${}^{t}F = 0$. As a consequence of Drucker's postulate for stable plastic materials, it can be shown that ${}^{t}F$ describes a convex surface in stress-temperature space. When stress and plastic strain axes are coincident, the infinitesimal plastic strain increment vector is normal to the current yield surface. This latter result can be expressed as:

$$ e_{ij}^{P} = {}^{t}\lambda \frac{\partial {}^{t}F}{\partial {}^{t}\sigma_{ij}} \tag{4.17} $$

where

$$ e_{ij}^{P} = {}^{t+\Delta t}e_{ij}^{P} - {}^{t}e_{ij}^{P} $$

${}^{t}\lambda$ = positive scalar variable.

A hardening rule describes the change in yield surface with continuing plastic deformation. The kinematic hardening mechanism was chosen in this investigation. This is because cyclic plasticity is expected in the welding problem. The isothermal kinematic hardening rule assumes that the size of the yield surface remains constant and that the yield surface can translate as a rigid body in stress space. The translation is a measure of the hardening of the material and the incremental translation is generally assumed to be linearly related to the incremental plastic strain, thus implying a bilinear stress-strain curve.

To extend the rule to non-isothermal conditions it is assumed further that both the size of the yield surface and the hardening of the material (i.e. the translation of the yield surface) can depend on the temperature. The von Mises yield function for non-isothermal kinematic hardening is used and can be written as:

$$ {}^{t}F = \frac{1}{2}({}^{t}s_{ij} - {}^{t}\alpha_{ij})({}^{t}s_{ij} - {}^{t}\alpha_{ij}) - \frac{1}{3}{}^{t}\sigma_y^2 \tag{4.18} $$

where

$${}^{t}\sigma_y = \text{yield stress} = {}^{t}\sigma_y({}^{t}\theta)$$

$${}^{t}\alpha_{ij} = \text{tensor measuring translation of the yield surface} = {}^{t}C\,{}^{t}e_{ij}^{P}$$

$${}^{t}C = \text{hardening parameter} = {}^{t}C({}^{t}\theta)$$

It should be noted here that in ADINA both the von Mises and the Drucker-Prager yield condition have been implemented. The Drucker-Prager yield condition, however, is limited to elastic-perfectly plastic analysis.

A governing incremental stress-strain relation at time $t + \Delta t$ and iteration i can be written as:

$$ {}^{t+\Delta t}\sigma^{(i)} = {}^{t+\Delta t}C^{E}[{}^{t+\Delta t}e^{(i)} - {}^{t\Delta t}e^{P(i)} - {}^{t+\Delta t}e^{TH(i)}] \tag{4.19} $$

where

$$ {}^{t+\Delta t}e^{P(i)} = {}^{t}e^{P} + \int_{t}^{t+\Delta t(i)} d^{t+\Delta t}e^{P} \tag{4.20} $$

It is very important to get the accurate integration of Equation 4.20. The α-method was used with $\alpha = 1$ correspond to the Euler backward (implicit) method. This implicit scheme can provide considerably better stability characteristics through equilibrium iterations. Two intervals of the time step are used. One is for the formation of a new tangent stiffness matrix, and the other is for the equilibrium iteration. The accuracy of the integration is enhanced with the use of subincrements in each time step. This is an important feature considering the rapidity with which some of the solution variables and material parameters vary with time during welding.

4.5 Weld Model Using the FEM

In this section all the necessary considerations for modeling the bead-on-edge weldment will be discussed. They include the geometry and boundary condition, the material properties, and the solution strategy.

4.5.1 Boundary Condition

The whole specimen is modeled using the two-dimension 4-node solid element. The plane stress assumption is used. This assumption implies that the stress is uniform in the thickness direction. In other words, σ_y, σ_z, and τ_{yz} are functions of y and z and $\sigma_x = \tau_{yx} = \tau_{zx} = 0$. This is rationalized by the fact that, for relatively thin plate, the stress field is set off during welding; i.e. the stresses at cross section y at time t are not the same as the stresses at cross section $y + \Delta y$ at time $t + \Delta t$, provided that $\Delta y = v\Delta t$ where v = welding speed (Fig. 4-7). This approach also allows the calculation of in-plane distortion ahead of the welding arc.

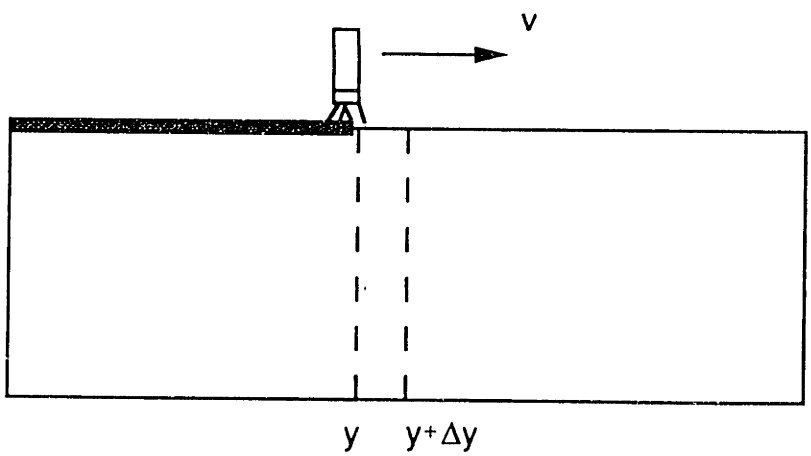

Figure 4-7: Typical 2-D Plane Stress Field

The boundary conditions used in the analysis should be such so as to allow free expansion of the specimen in the transverse direction to the weld. At the same time the specimen should be properly restrained to eliminate possible modes of rigid body motions, otherwise the stiffness matrix will not be positive definite. The finite element mesh along with the boundary condition used in the analysis is shown in Fig. 4-8.

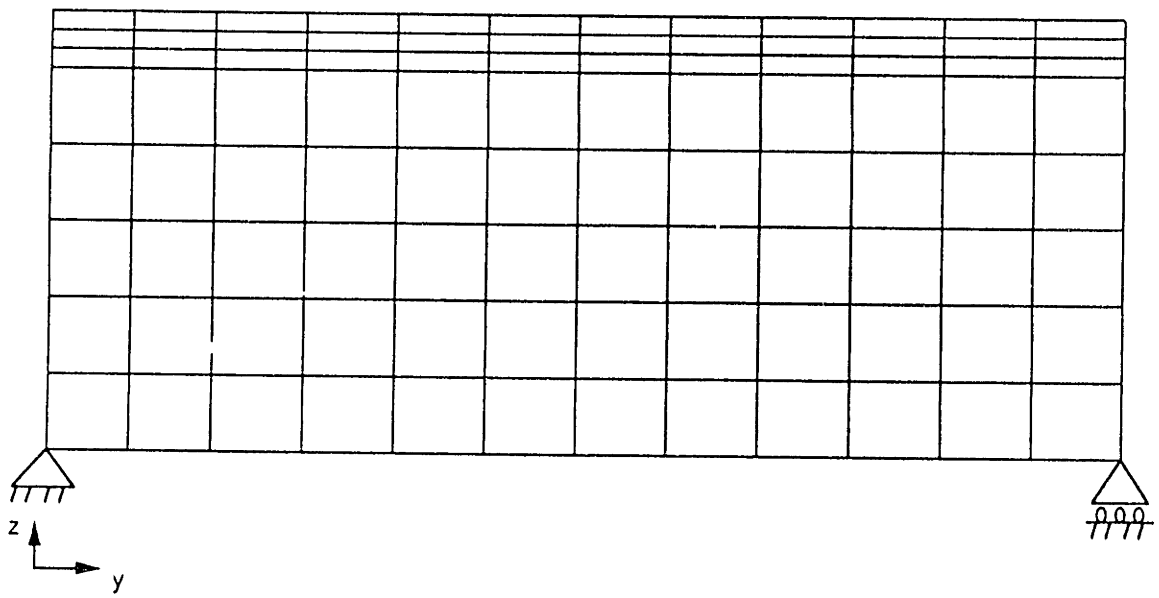

Figure 4-8: Finite Element Mesh and Boundary Conditions

4.5.2 Material Properties

The temperature dependence of the Young's modulus E, Poisson's ratio ν, yield stress σ_y, strain hardening or tangent modulus E_T, and thermal expansion coefficient α, are all the required inputs for the thermo-elastic- ıstic and creep material model incorporated in ADINA. This dependence has ɔen described in chapter 2 and the values shown there were used in this analysis. It should be pointed out here, however, that at the liquidus temperature the material does not have any strength, since all its mechanical properties are zero. But zero properties cannot be entered as inputs to the program. These zero properties

cause numerical instabilities. It was observed in the early stage of this analysis that the convergence of the equilibrium equation could not be reached for certain tolerance values (described in next section) in the finite element program. Therefore, to avoid this behavior, very small values for E, σ_y, and E_T are used above the liquidus temperature.

4.5.3 Solution Procedure

For nonlinear incremental stress analysis in which solutions depend very much on the iteration process, the accuracy and the convergence characteristic of the solution is therefore important. This importance is even more pronounced when one tries to solve the welding problem which involves highly nonlinear material behavior. Some suggestions for solving such a problem were provided by Bathe and Cimento [8].

As mentioned earlier, the solution of the incremental equation can be found using either the modified Newton-Raphson iterative technique (with or without the Aitken acceleration) or the BFGS matrix updating method. Papazoglou [50] reported an increase in unstable behavior signals on several occasions in the out of balance loads when using the Newton-Raphson technique at the initial steps of his analysis. He concluded that these unstable behavior signals were caused by the sudden stiffening of the welded structure during elastic unloading from the plastic stage at several integration points. This behavior was not observed when using the BFGS update. Following this, the BFGS updating method was used for this investigation. The relative displacement tolerance used to measure equilibrium iteration convergence was set to be 0.00001, which is one one-hundredth of the default value. This is because of the plasticity involved in the problem. The relative force and moment tolerance used to measure equilibrium iteration convergence was set to be equal to the default value, 0.05. The tolerance used to measure line search convergence was set to be equal to the default value, 0.5. In addition, iteration and stiffness

deformation were required at each time step to assure the accuracy of the solution. This is required because of the complex material behavior.

4.6 Comparison of the Results

Figures 4-9 to 4-11 show the calculated distortion for the case with side heating at the mid-length of the specimen compared with the experimental results. The 1-D analytical analysis tends to shift the peak distortion further away from the one predicted by finite element method and experiment. Furthermore, the 1-D analytical analysis tends to overestimate the peak distortion. This result can be attributed to the higher temperature as well as slower cooling rate calculated from the analytical analysis. A good correlation can be obtained between the results from finite element calculation and experimental data. The degree of good correlation, however, varies with different materials. This can be attributed to the accuracy of the material property data obtained at elevated temperatures for each material.

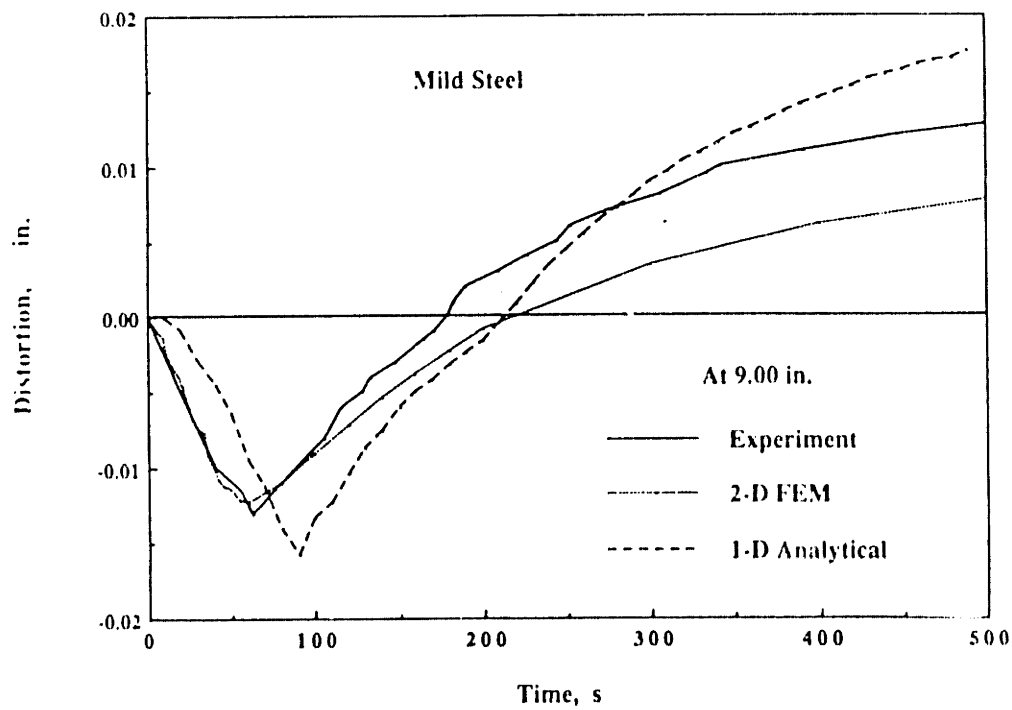

Figure 4-9: Comparison of Distortion --Calculation .vs. Experiment for Low Carbon Steel

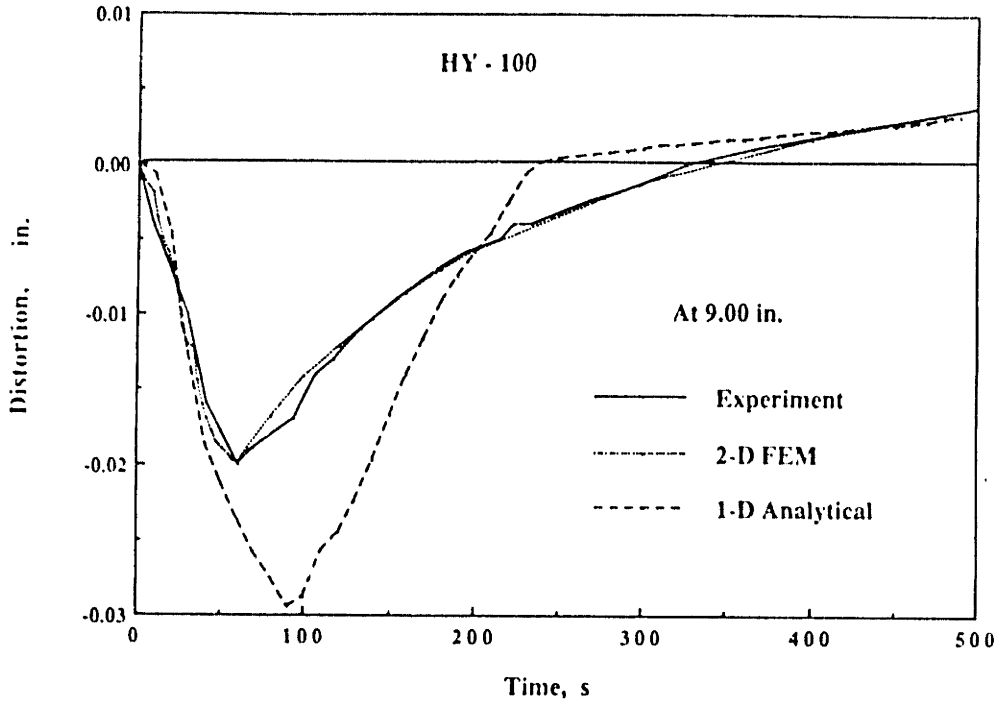

Figure 4-10: Comparison of Distortion --Calculation .vs. Experiment for HY-100

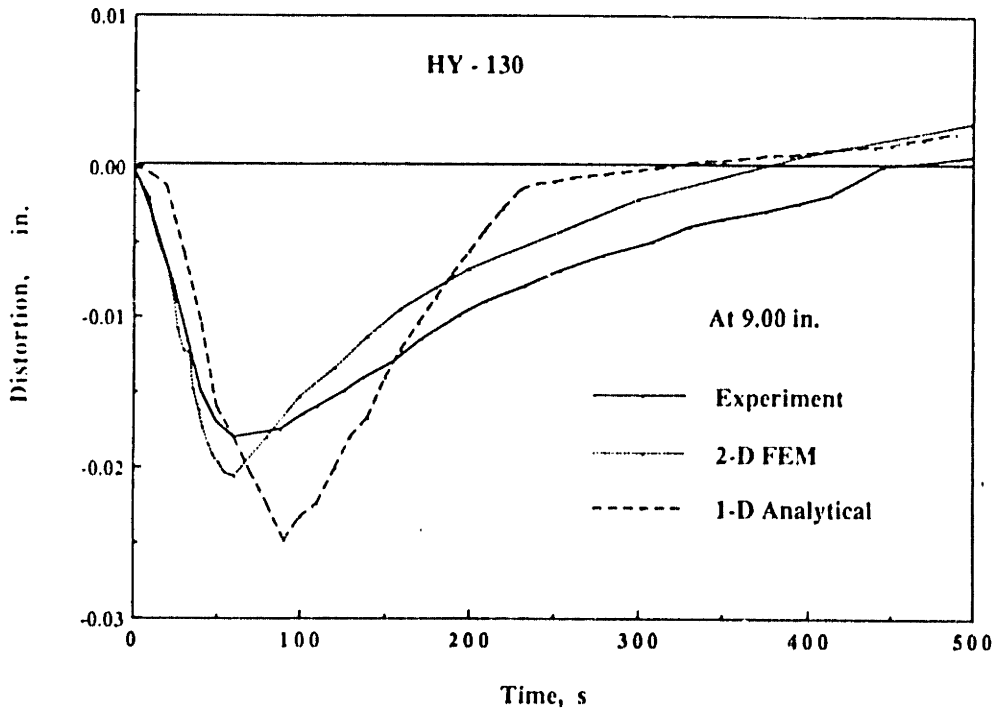

Figure 4-11: Comparison of Distortion --Calculation .vs. Experiment for HY-130

Figures 4-12 to 4-20 show the calculated distortion for the case with side heating. Similar behavior can be observed. The difference between the finite element calculation and the experimental data occurs during the time that the specimen started to cool down. A good correlation, however, is observed during welding. The 1-D analytical analysis tends to delay and overestimate the peak distortion in all cases. Nevertheless, it provides bending behavior similar to that of the specimen.

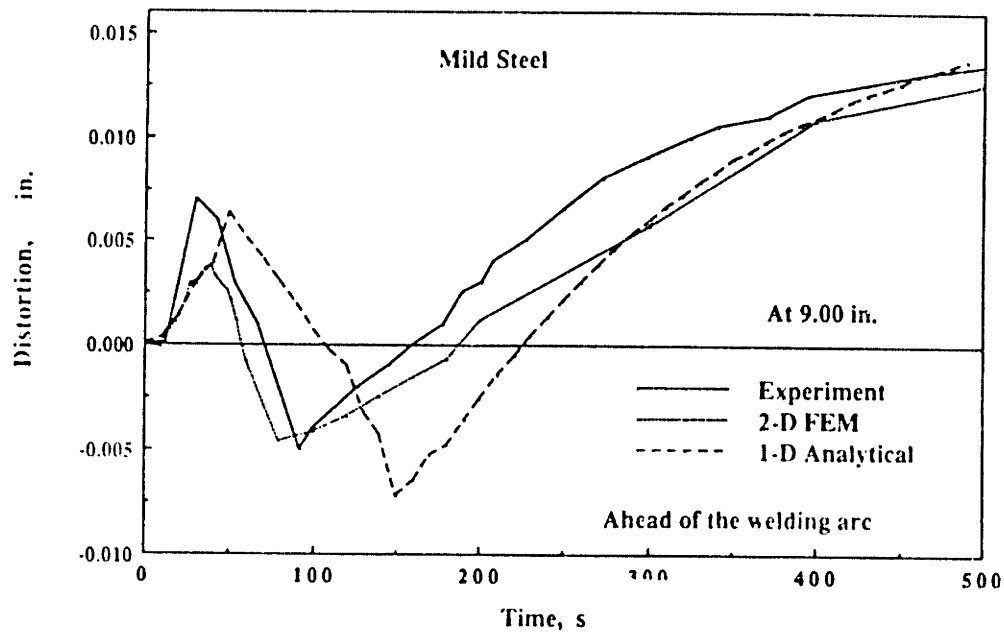

Figure 4-12: Comparison of Distortion --Calculation .vs. Experiment for Low Carbon Steel (Ahead)

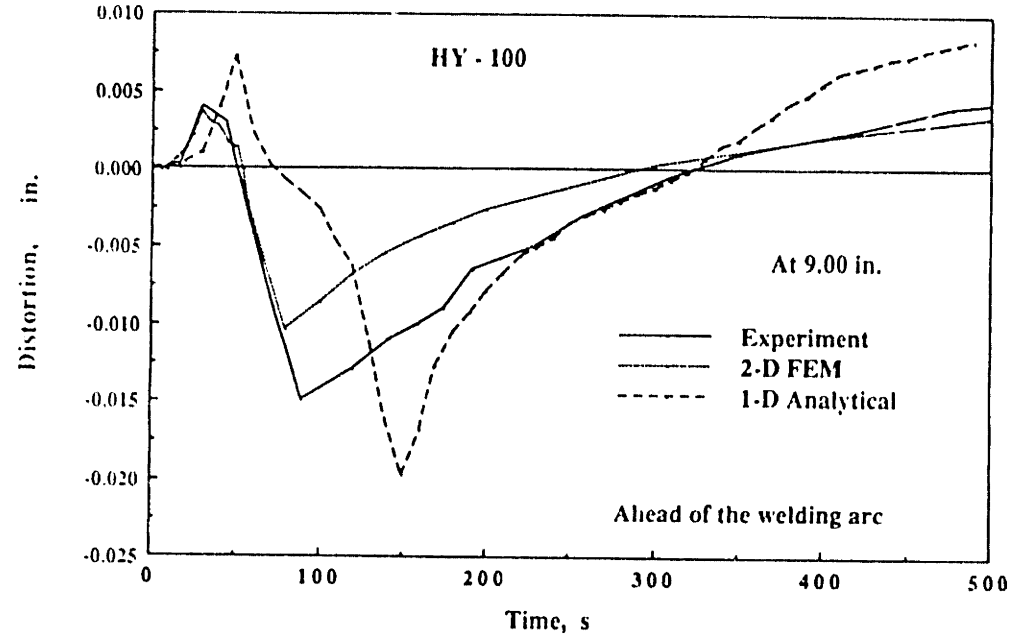

Figure 4-13: Comparison of Distortion --Calculation .vs. Experiment for HY-100 (Ahead)

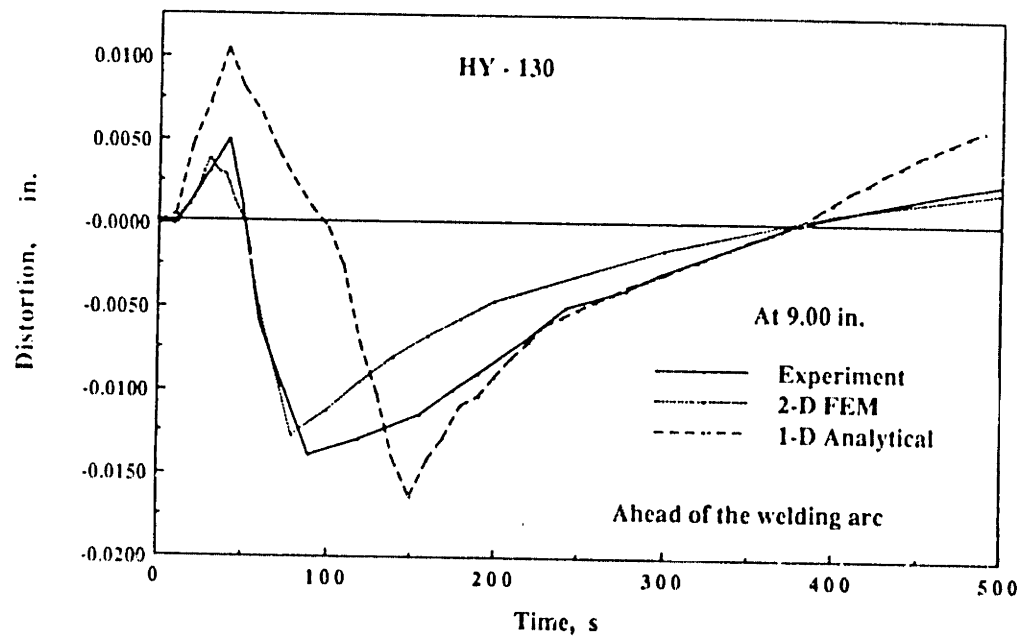

Figure 4-14: Comparison of Distortion --Calculation .vs. Experiment for HY-130 (Ahead)

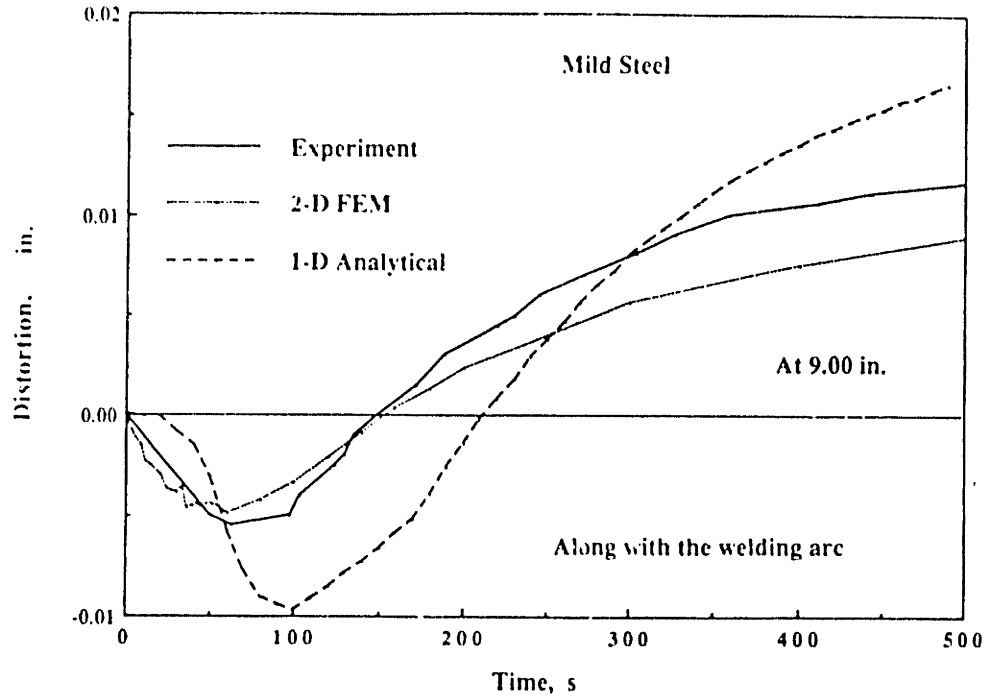

Figure 4-15: Comparison of Distortion --Calculation .vs. Experiment for Low Carbon Steel (Along)

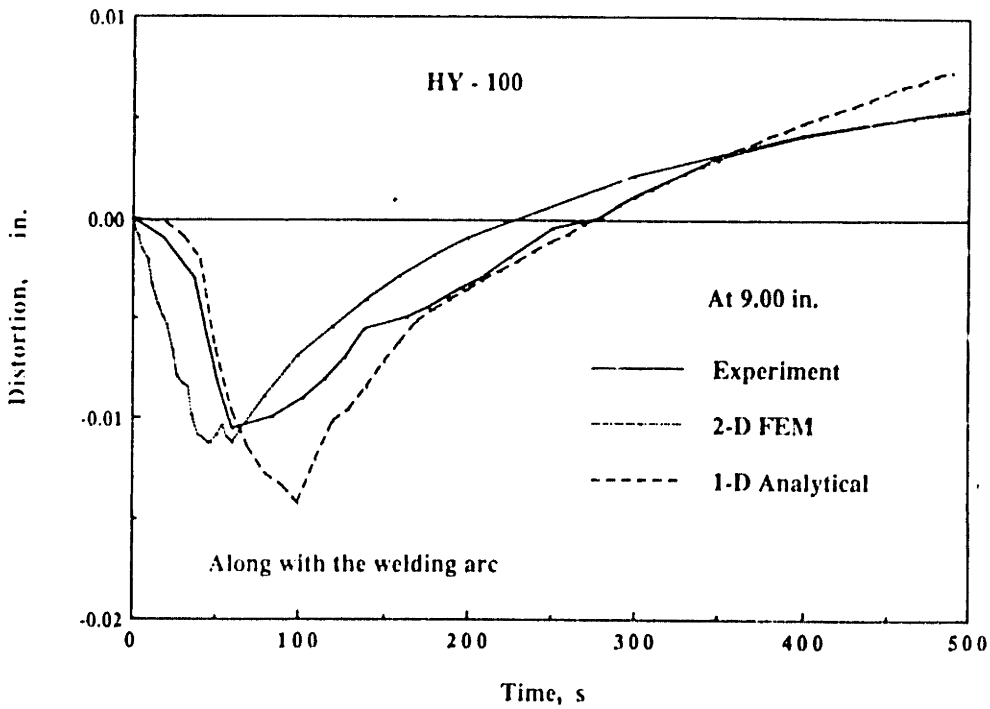

Figure 4-16: Comparison of Distortion --Calculation .vs. Experiment for HY-100 (Along)

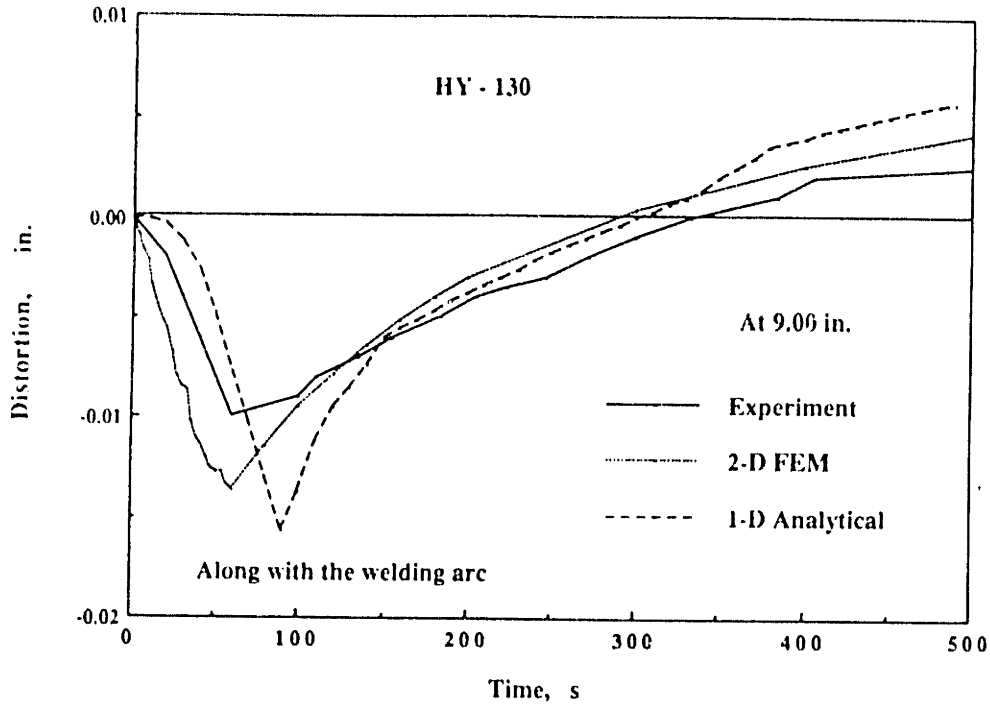

Figure 4-17: Comparison of Distortion --Calculation .vs. Experiment for HY-130 (Along)

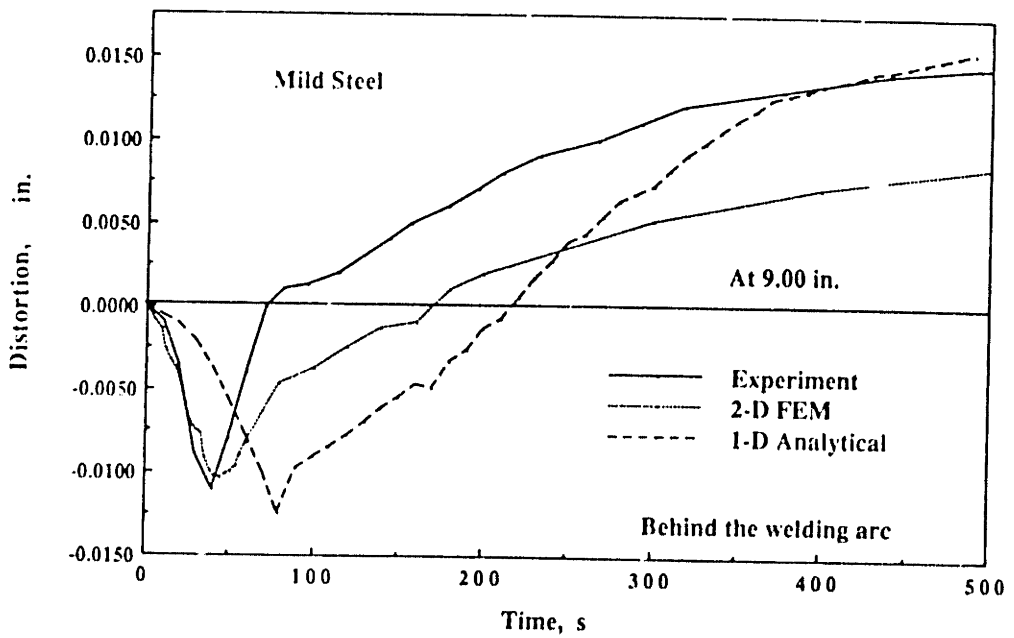

Figure 4-18: Comparis on of Distortion --Calculation .vs. Experiment for Low Carbon Steel (Behind)

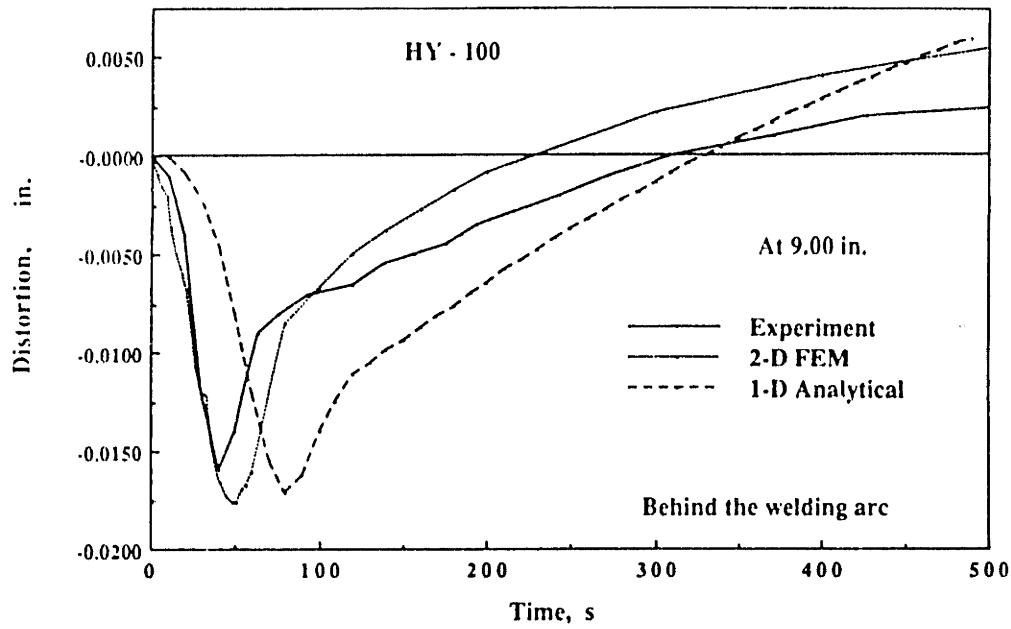

Figure 4-19: Comparison of Distortion --Calculation .vs. Experiment for HY-100 (Behind)

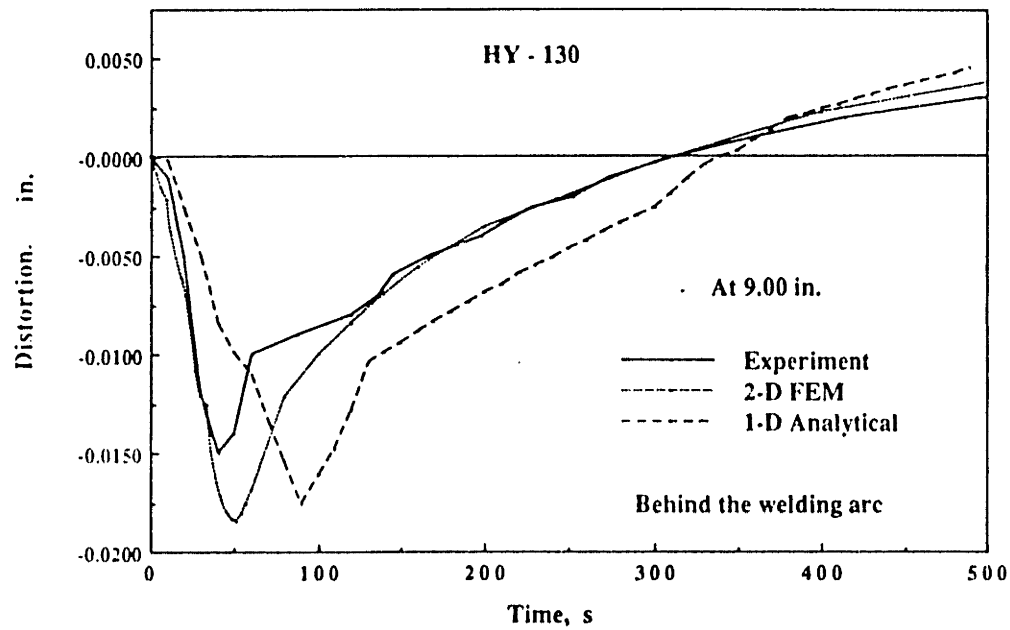

Figure 4-20: Comparison of Distortion --Calculation .vs. Experiment for HY-130 (Behind)

Figures 4-21 to 4-32 show the comparison of the strain profile obtained from experiment and analysis for the case without side heating at positions 1.00 and 4.00 inches away from the weld line. It should be noted that the results from finite element analysis were obtained at the Gaussian integration points which are not exactly the same location as one in the experiment. Similar strain profiles are observed for all experiments and analyses. The analyses show good agreement if one takes into account the various assumptions involved in modeling the complex welding problem. The results show also a relatively good correlation between the calculated data from the one-dimension analysis and the one from experiment. This clearly indicates that the longitudinal stress is the principle stress that dominates during bead-on-edge welding, and the assumption of neglecting transverse stress is sufficiently justified.

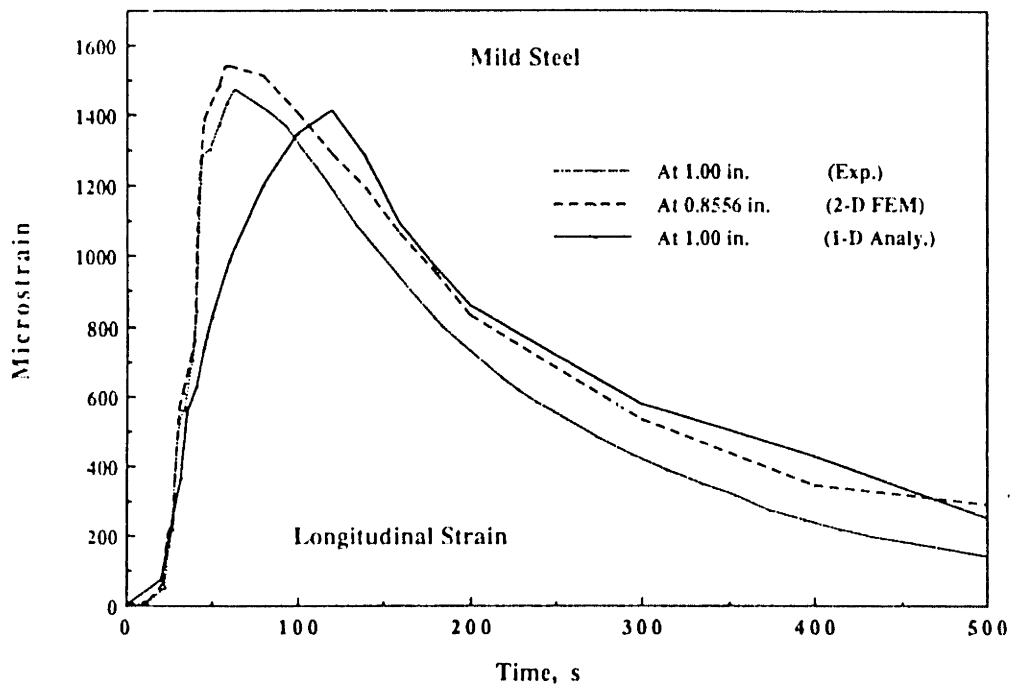

Figure 4-21: Comparison of Longitudinal Strain Profile --Calculation .vs. Experiment for Low Carbon Steel at 1.00 inch

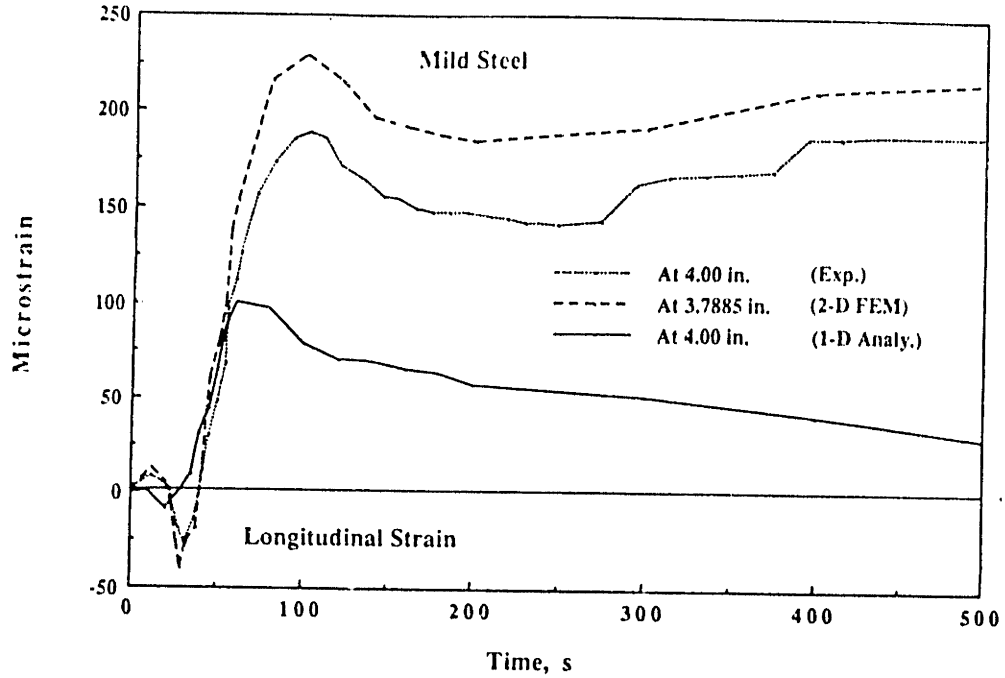

Figure 4-22: Comparison of Longitudinal Strain Profile --Calculation .vs. Experiment for Low Carbon Steel at 4.00 inches

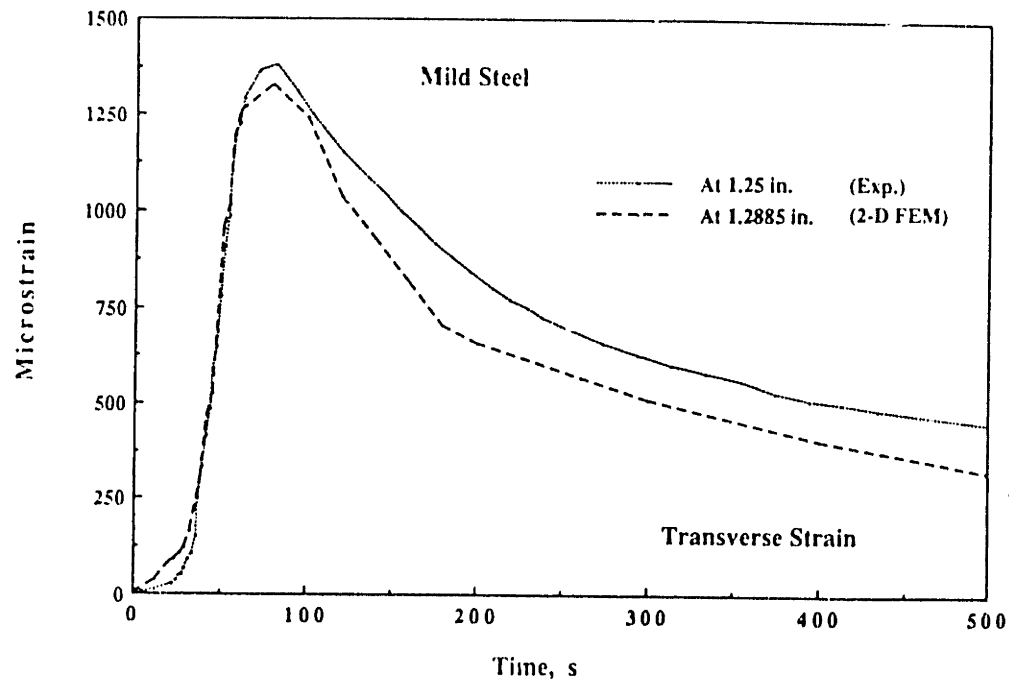

Figure 4-23: Comparison of Transverse Strain Profile --Calculation .vs. Experiment for Low Carbon Steel at 1.25 inches

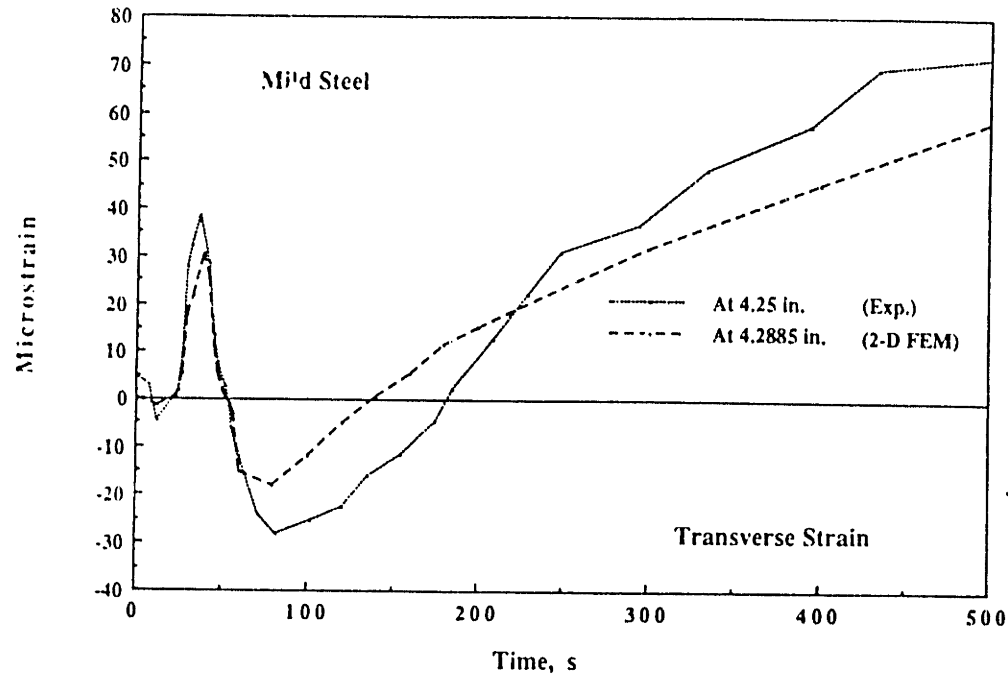

Figure 4-24: Comparison of Transverse Strain Profile --Calculation .vs. Experiment for Low Carbon Steel at 4.25 inches

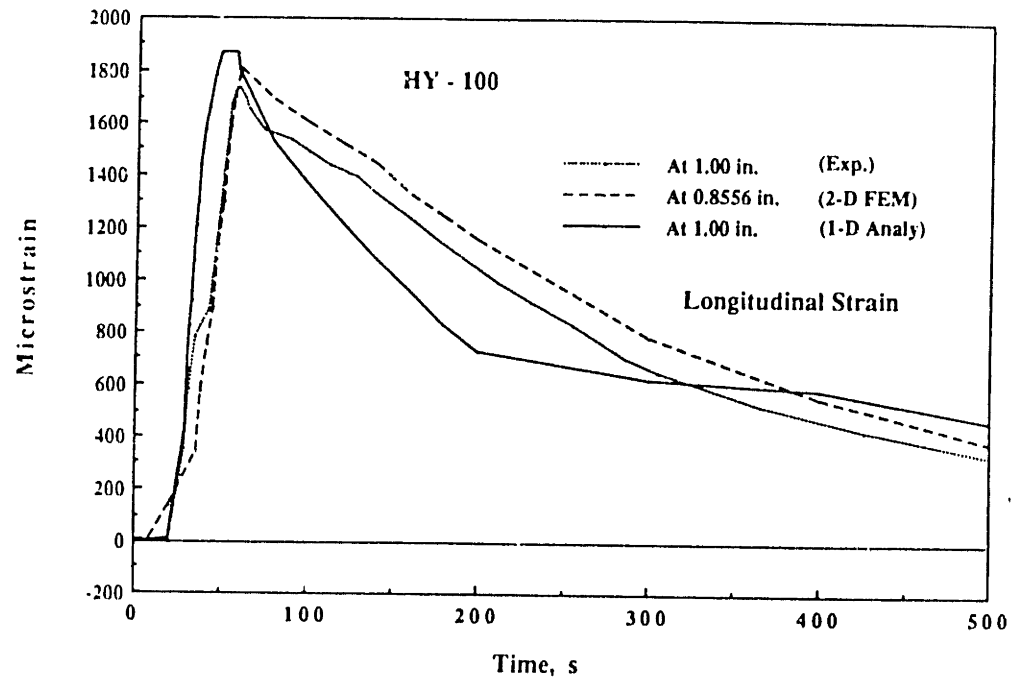

Figure 4-25: Comparison of Longitudinal Strain Profile --Calculation .vs. Experiment for HY-100 at 1.00 inch

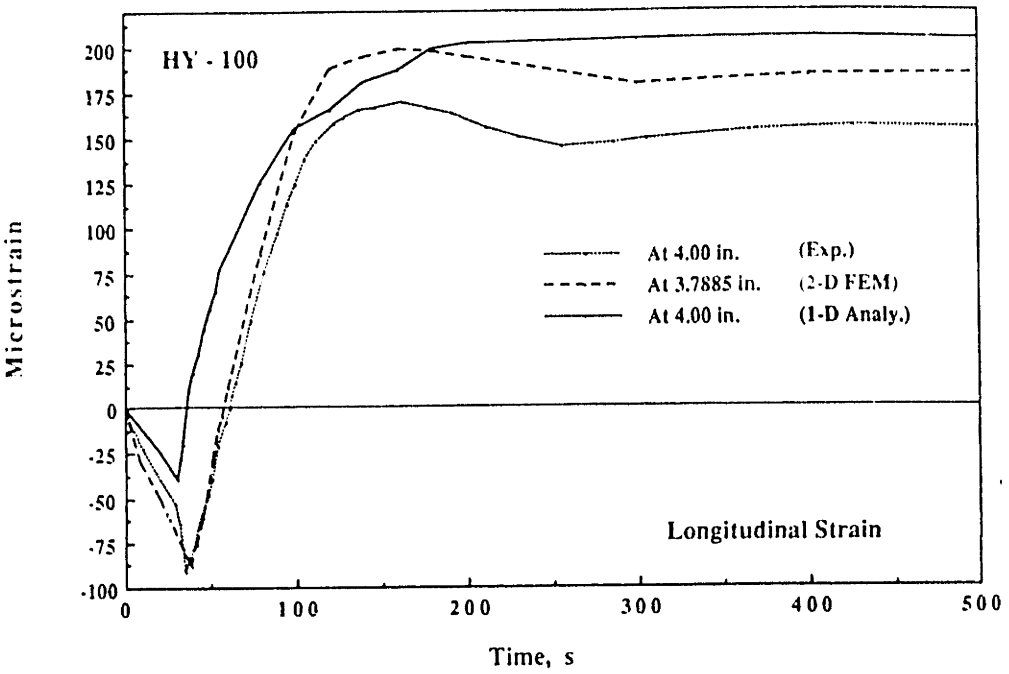

Figure 4-26: Comparison of Longitudinal Strain Profile --Calculation .vs. Experiment for HY-100 at 4.00 inches

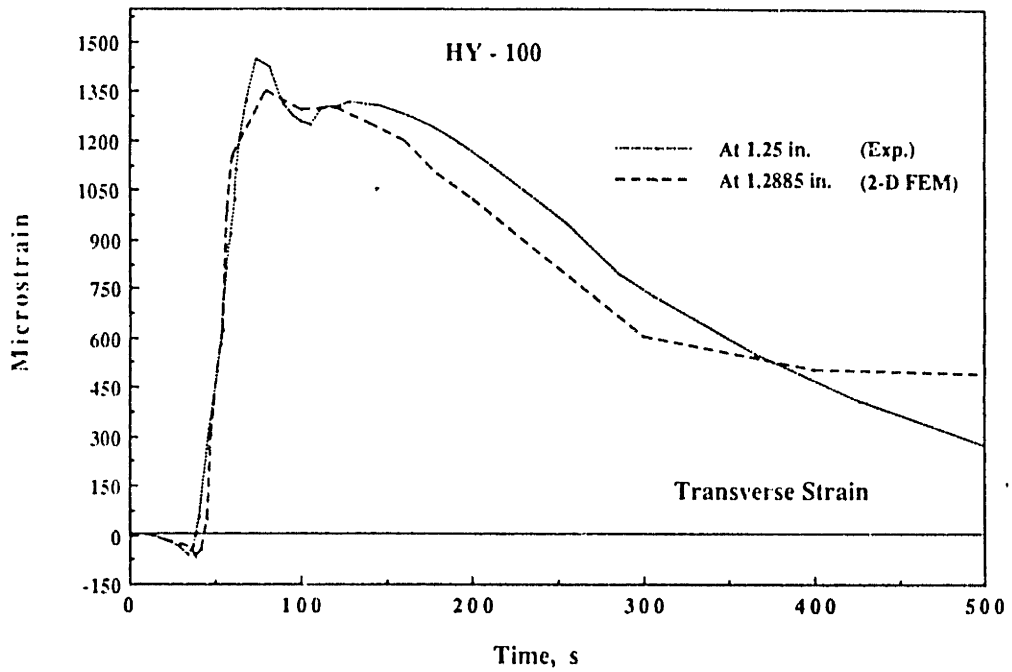

Figure 4-27: Comparison of Transverse Strain Profile --Calculation .vs. Experiment for HY-100 at 1.25 inches

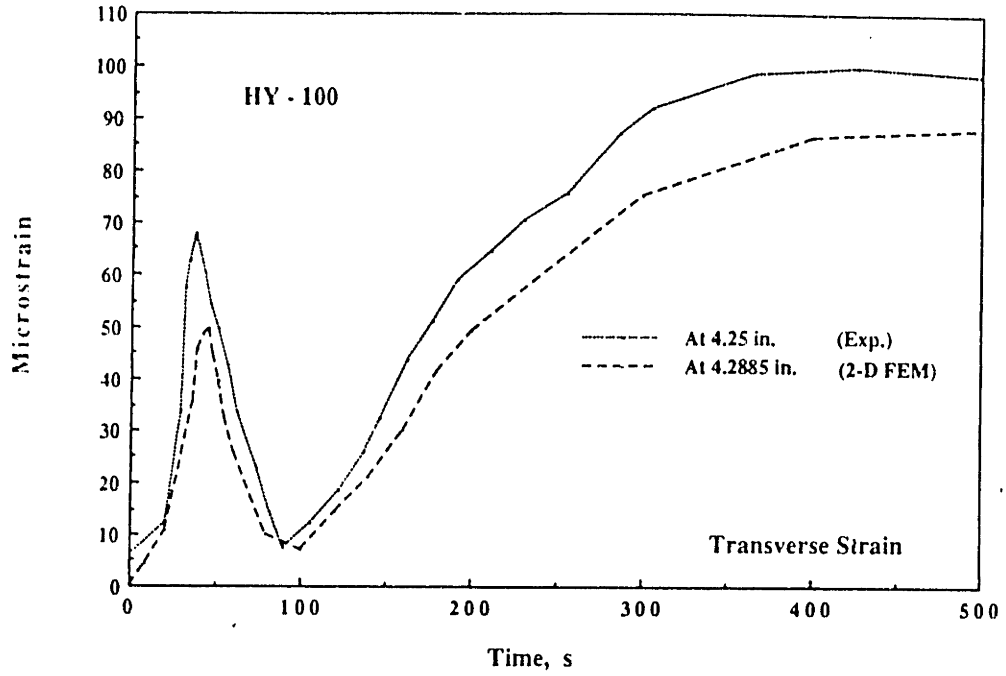

Figure 4-28: Comparison of Transverse Strain Profile --Calculation .vs. Experiment for HY-100 at 4.25 inches

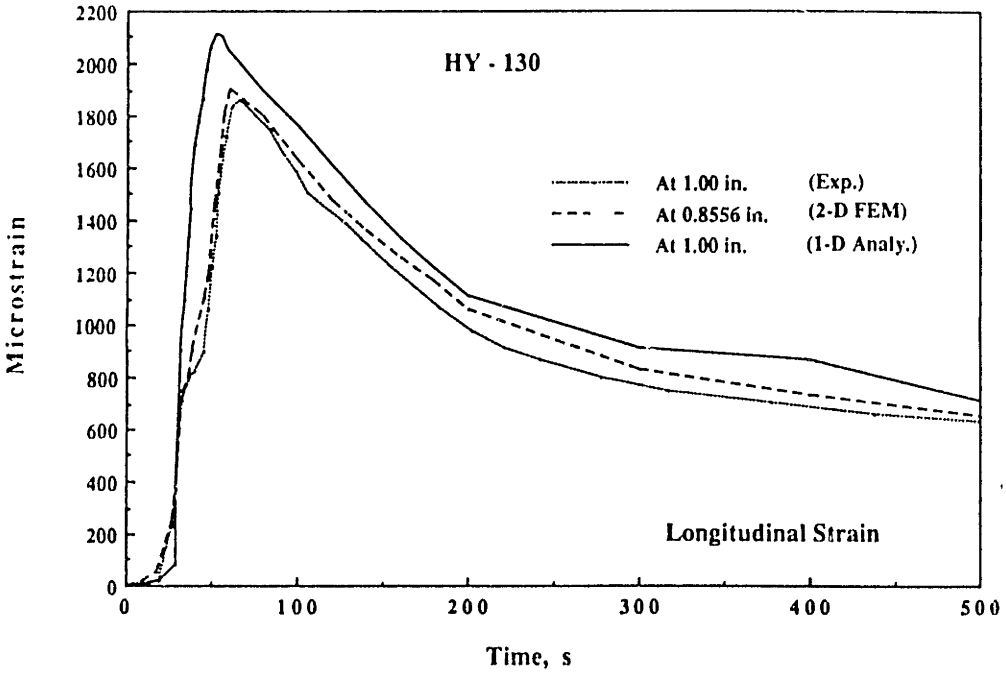

Figure 4-29: Comparison of Longitudinal Strain Profile --Calculation .vs. Experiment for HY-130 at 1.00 inch

Figures 4-12 to 4-20 show the calculated distortion for the case with side heating. Similar behavior can be observed. The difference between the finite element calculation and the experimental data occurs during the time that the specimen started to cool down. A good correlation, however, is observed during welding. The 1-D analytical analysis tends to delay and overestimate the peak distortion in all cases. Nevertheless, it provides bending behavior similar to that of the specimen.

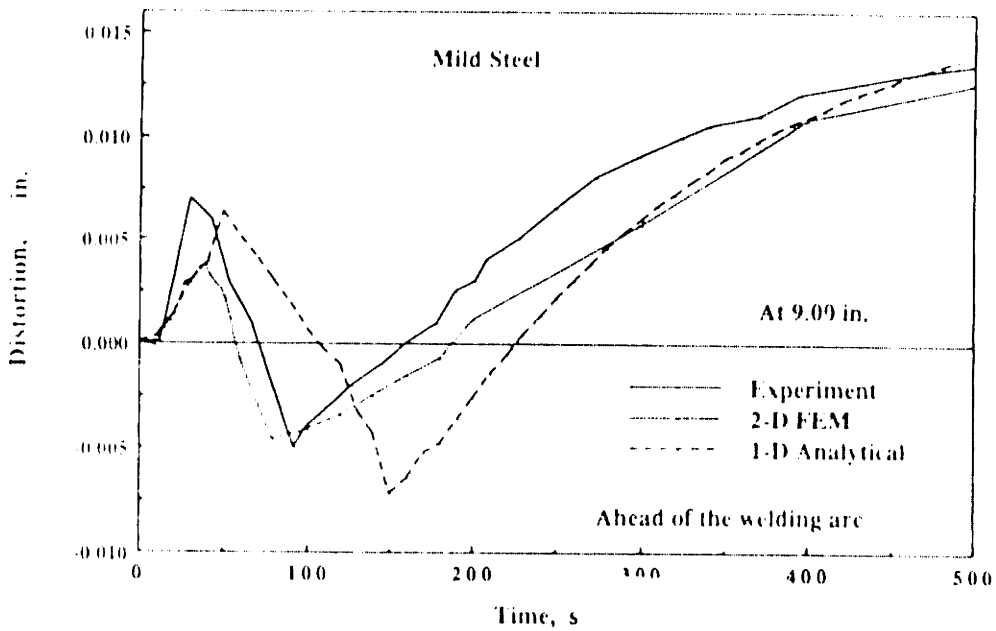

Figure 4-12: Comparison of Distortion --Calculation .vs. Experiment for Low Carbon Steel (Ahead)

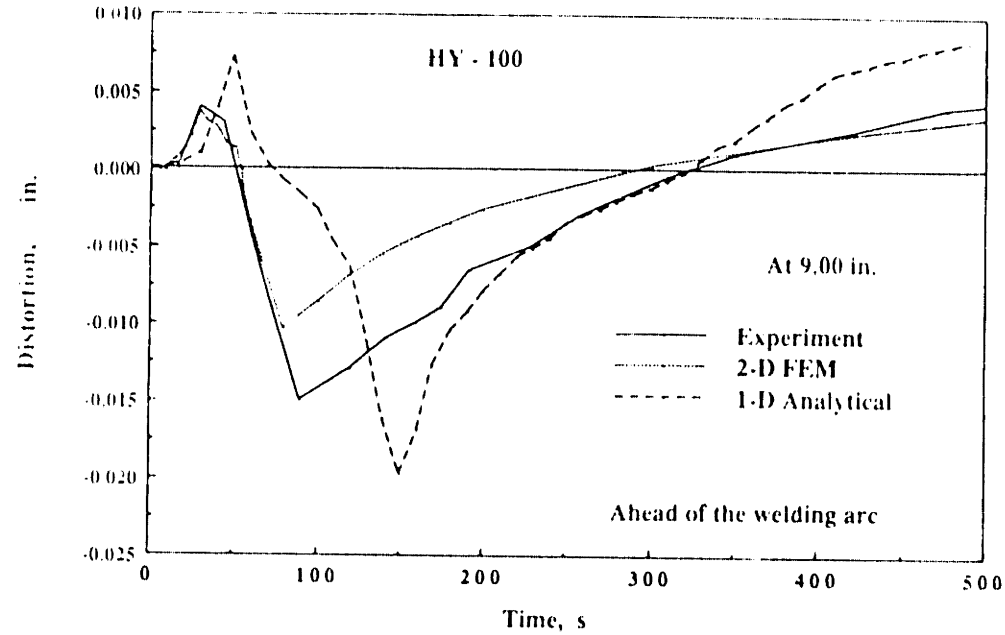

Figure 4-13: Comparison of Distortion --Calculation .vs. Experiment for HY-100 (Ahead)

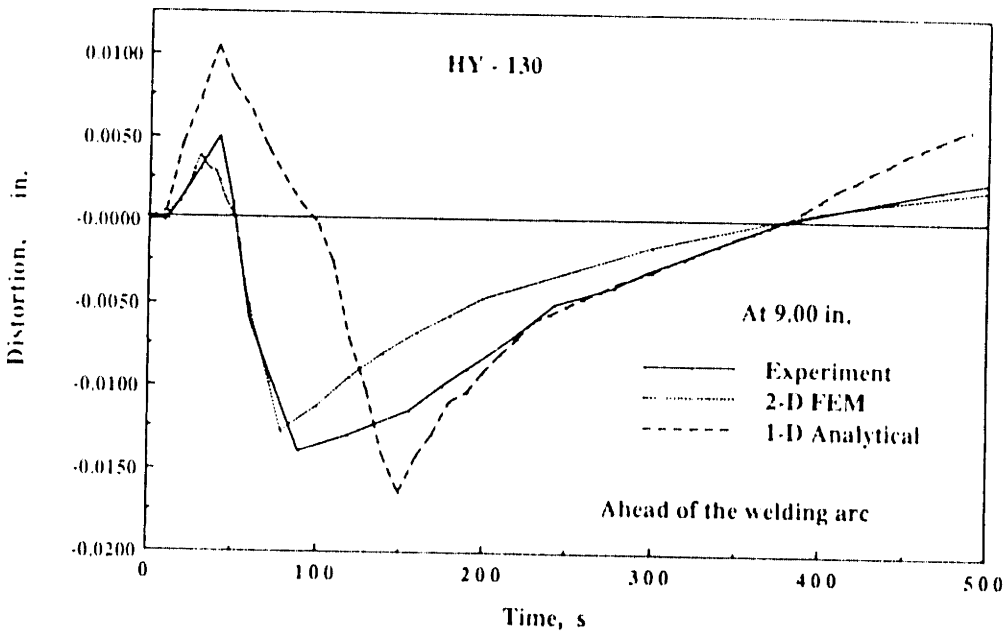

Figure 4-14: Comparison of Distortion --Calculation .vs. Experiment for HY-130 (Ahead)

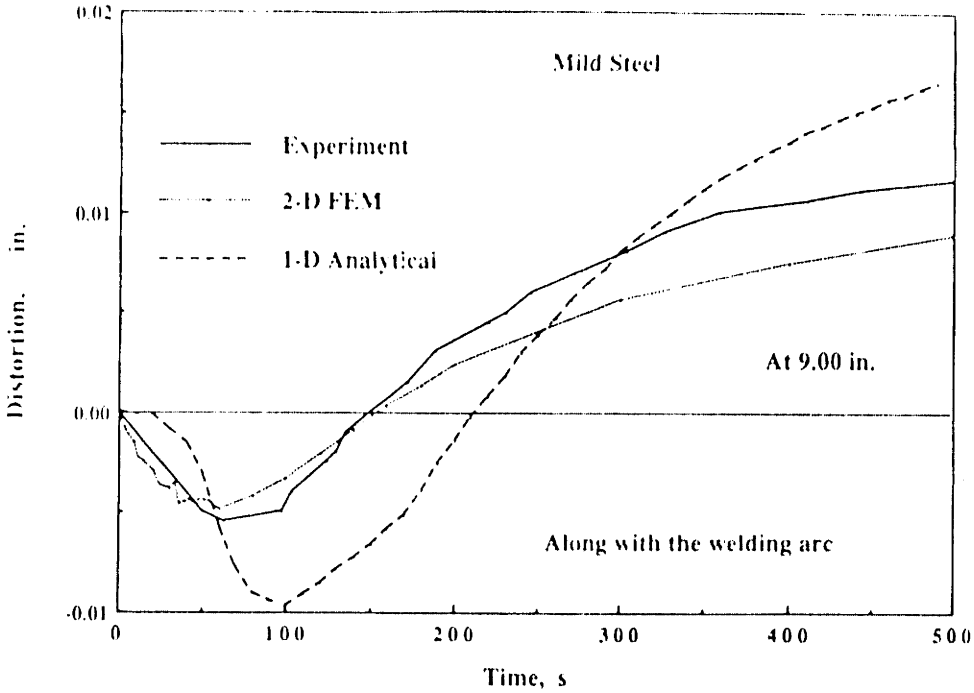

Figure 4-15: Comparison of Distortion --Calculation .vs. Experiment for Low Carbon Steel (Along)

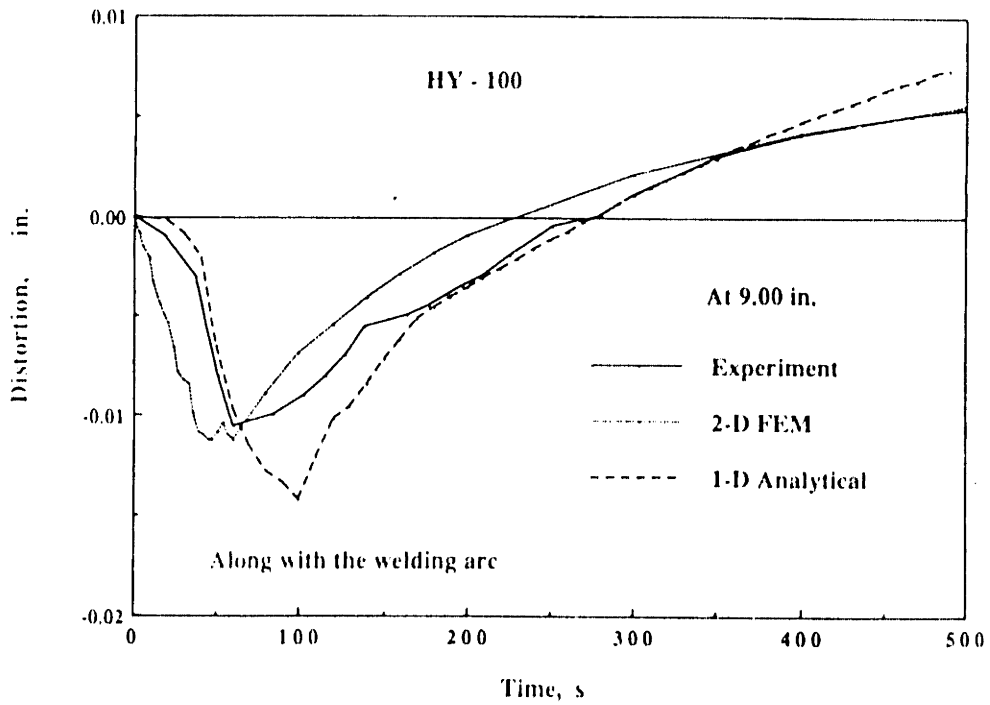

Figure 4-16: Comparison of Distortion --Calculation .vs. Experiment for HY-100 (Along)

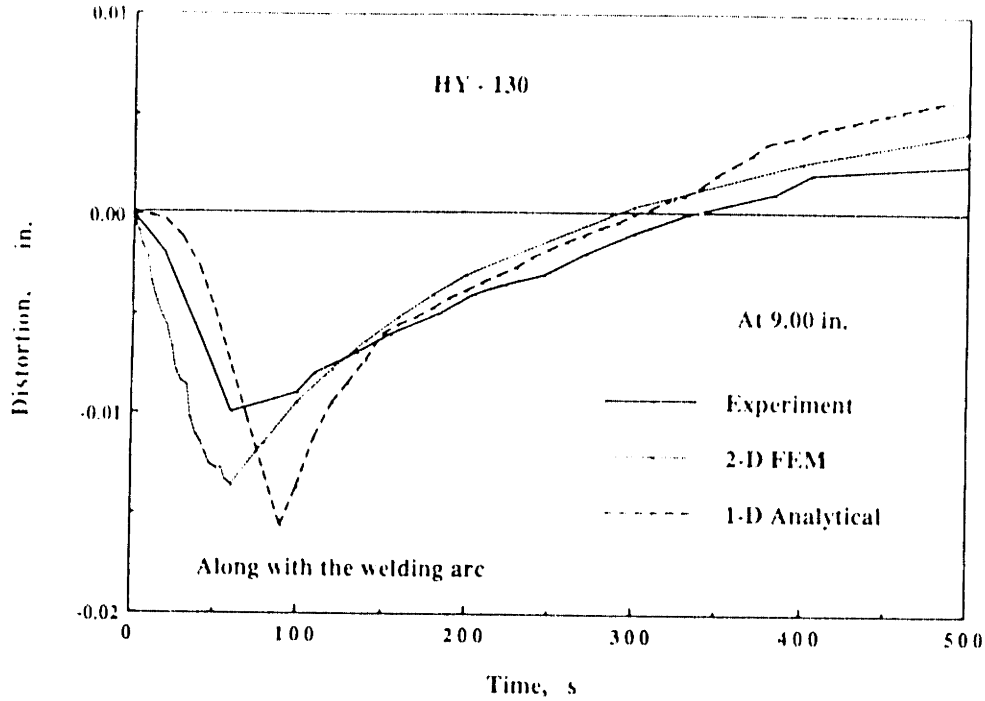

Figure 4-17: Comparison of Distortion --Calculation .vs. Experiment for HY-130 (Along)

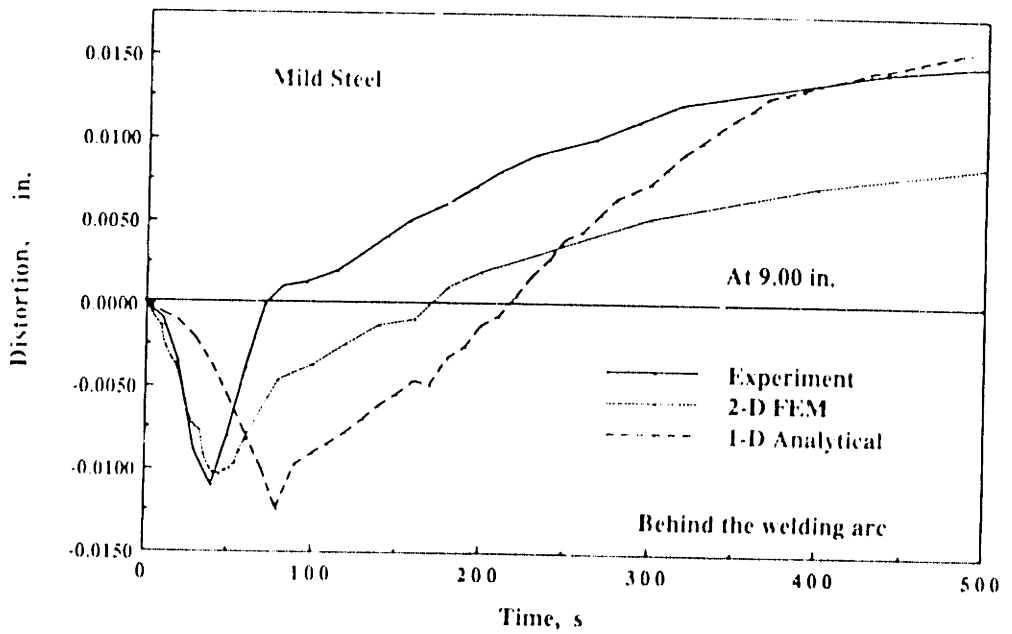

Figure 4-18: Comparison of Distortion --Calculation .vs. Experiment for Low Carbon Steel (Behind)

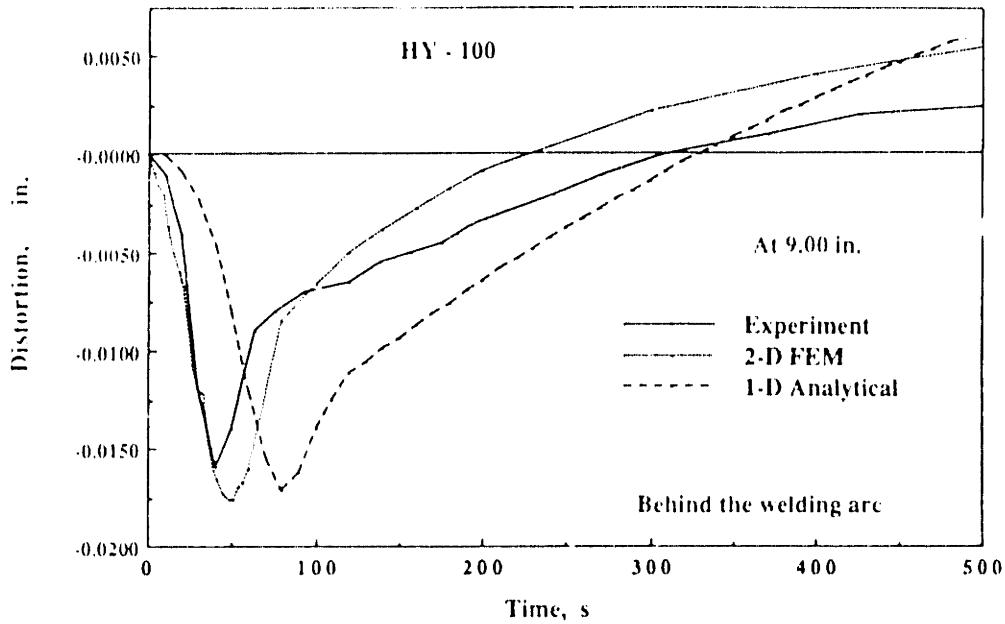

Figure 4-19: Comparison of Distortion --Calculation .vs. Experiment for HY-100 (Behind)

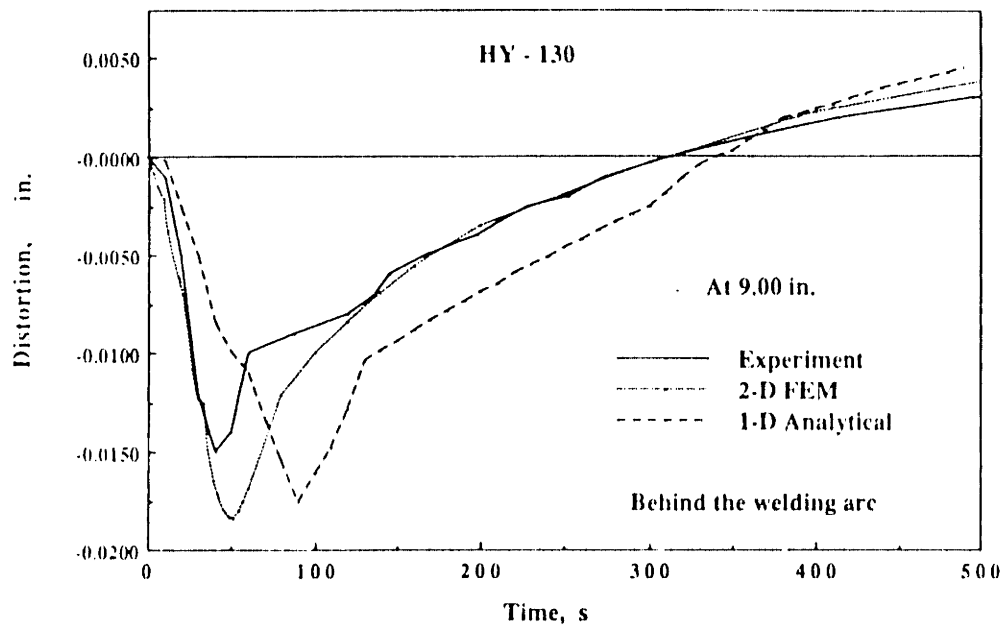

Figure 4-20: Comparison of Distortion --Calculation .vs. Experiment for HY-130 (Behind)

Figures 4-21 to 4-32 show the comparison of the strain profile obtained from experiment and analysis for the case without side heating at positions 1.00 and 4.00 inches away from the weld line. It should be noted that the results from finite element analysis were obtained at the Gaussian integration points which are not exactly the same location as one in the experiment. Similar strain profiles are observed for all experiments and analyses. The analyses show good agreement if one takes into account the various assumptions involved in modeling the complex welding problem. The results show also a relatively good correlation between the calculated data from the one-dimension analysis and the one from experiment. This clearly indica ' that the longitudinal stress is the principle stress that dominates during bead-on-edge welding, and the assumption of neglecting transverse stress is sufficiently justified.

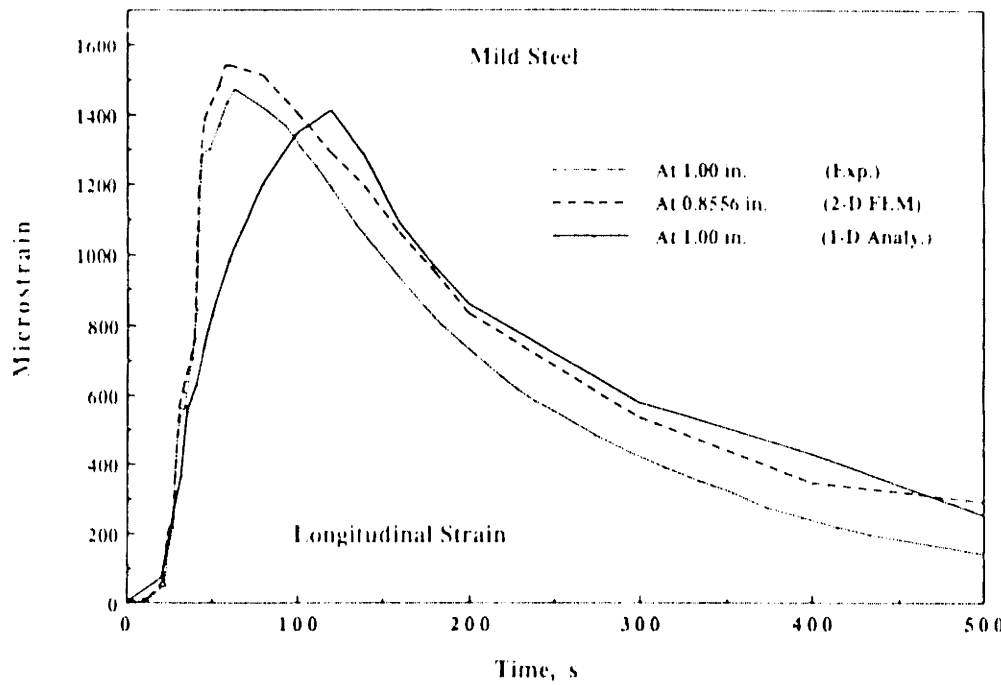

Figure 4-21: Comparison of Longitudinal Strain Profile --Calculation .vs. Experiment for Low Carbon Steel at 1.00 inch

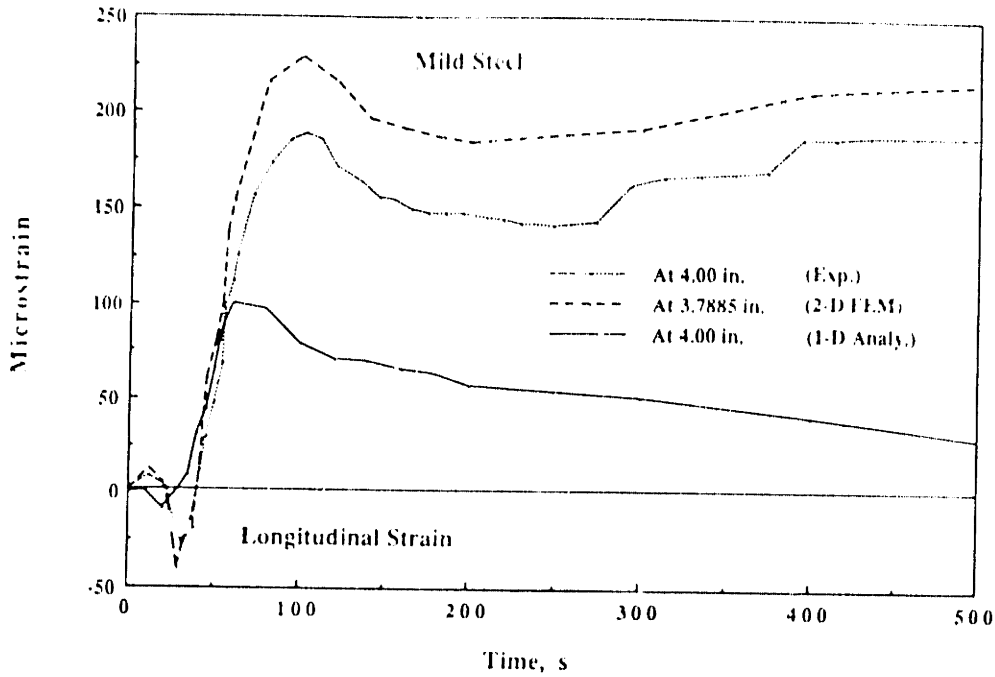

Figure 4-22: Comparison of Longitudinal Strain Profile --Calculation .vs. Experiment for Low Carbon Steel at 4.00 inches

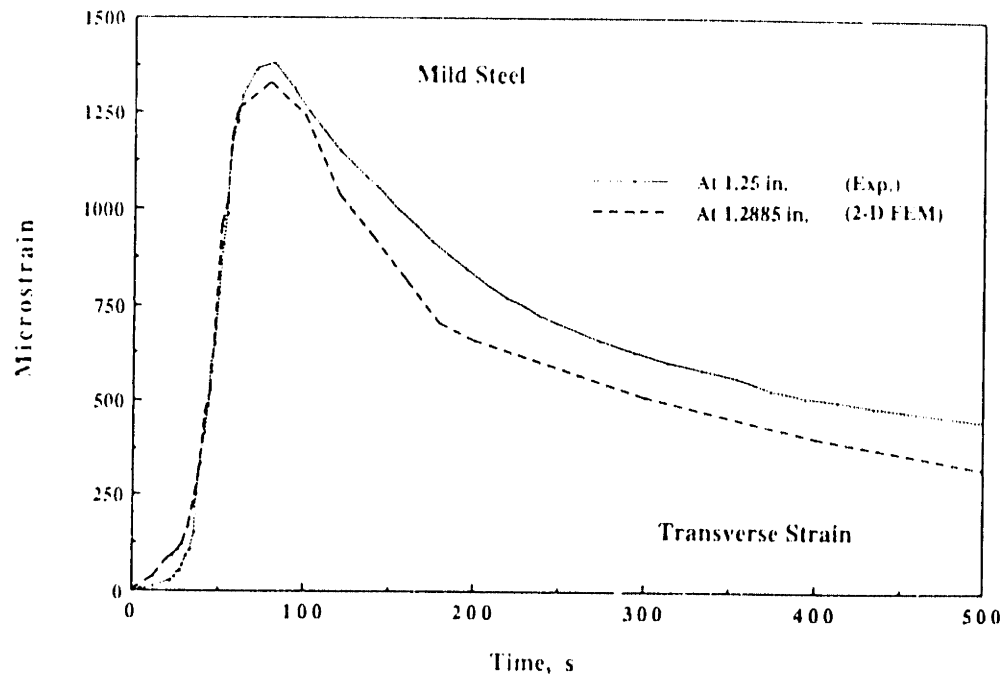

Figure 4-23: Comparison of Transverse Strain Profile --Calculation .vs. Experiment for Low Carbon Steel at 1.25 inches

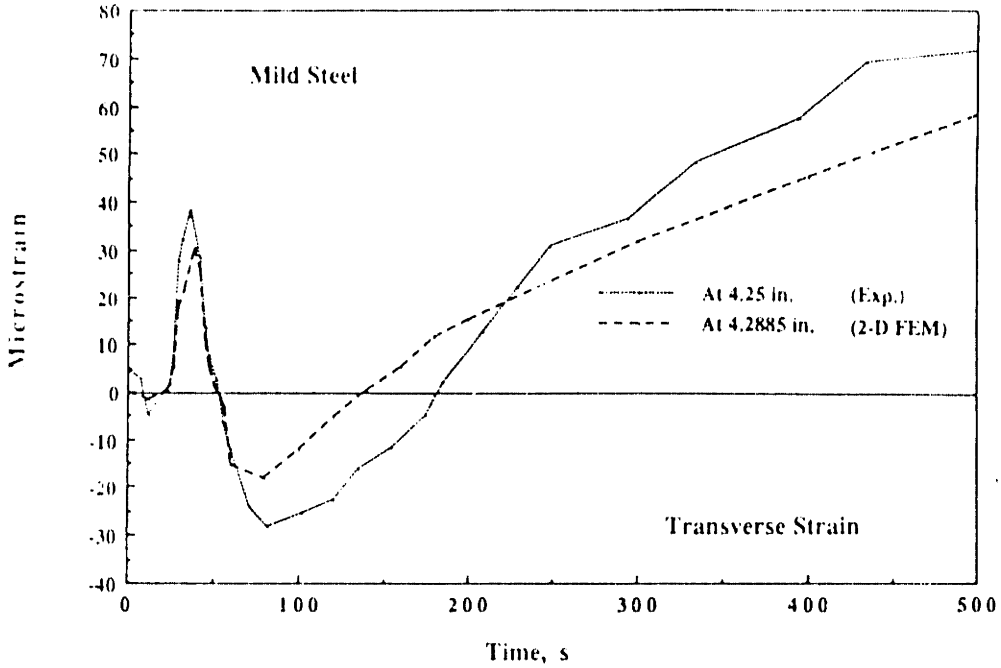

Figure 4-24: Comparison of Transverse Strain Profile --Calculation .vs. Experiment for Low Carbon Steel at 4.25 inches

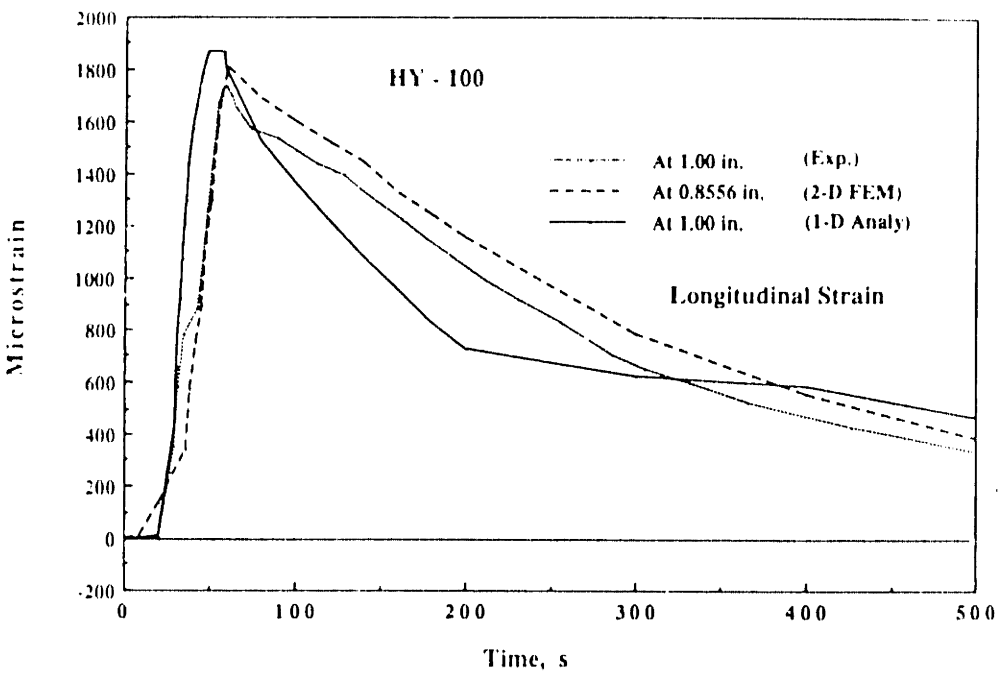

Figure 4-25: Comparison of Longitudinal Strain Profile --Calculation .vs. Experiment for HY-100 at 1.00 inch

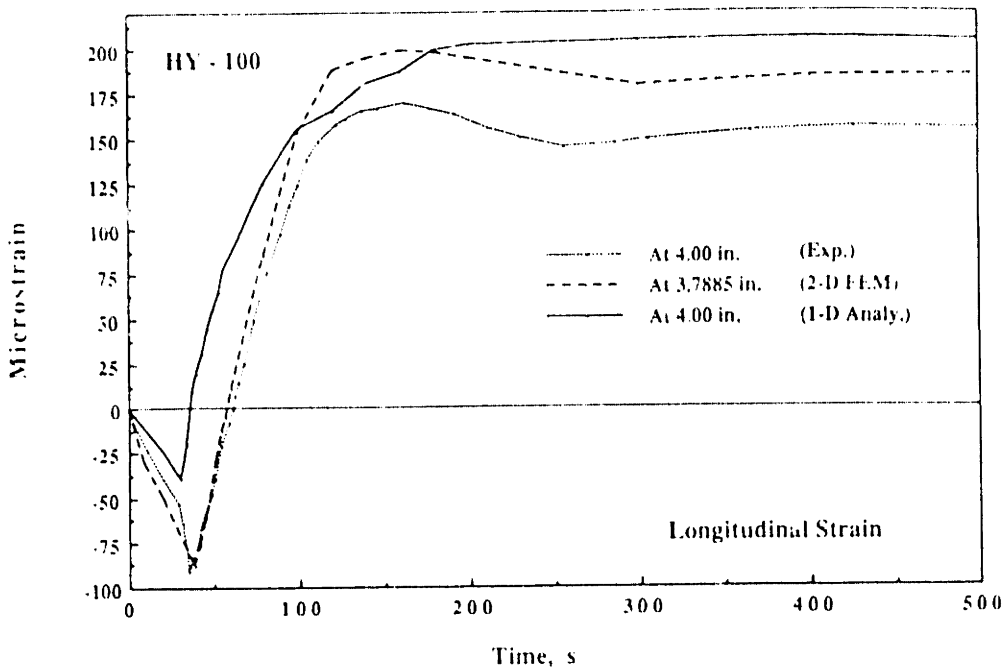

Figure 4-26: Comparison of Longitudinal Strain Profile --Calculation .vs. Experiment for HY-100 at 4.00 inches

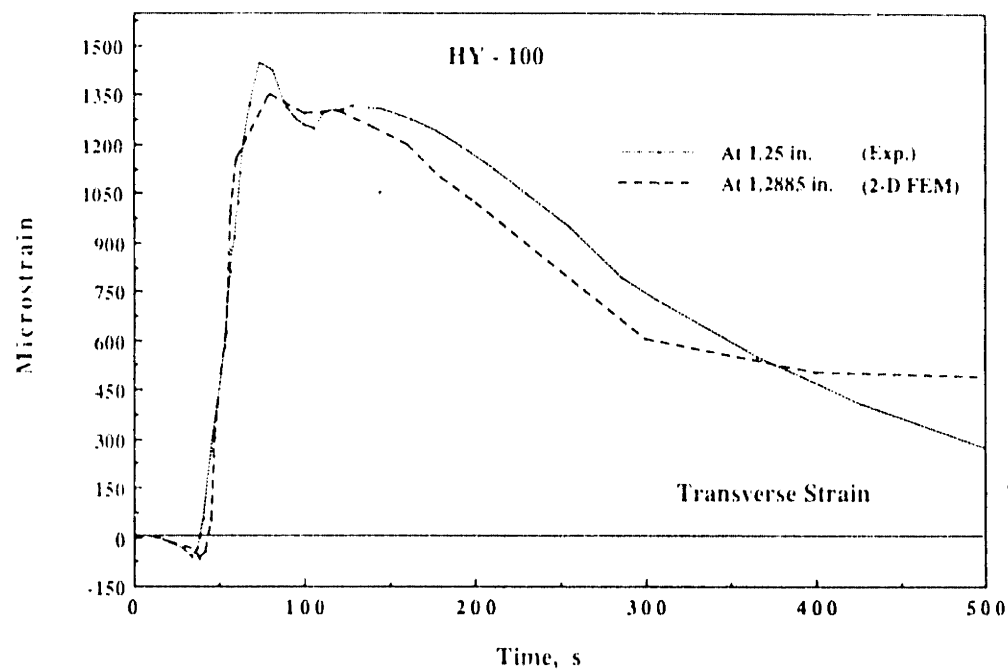

Figure 4-27: Comparison of Transverse Strain Profile --Calculation .vs. Experiment for HY-100 at 1.25 inches

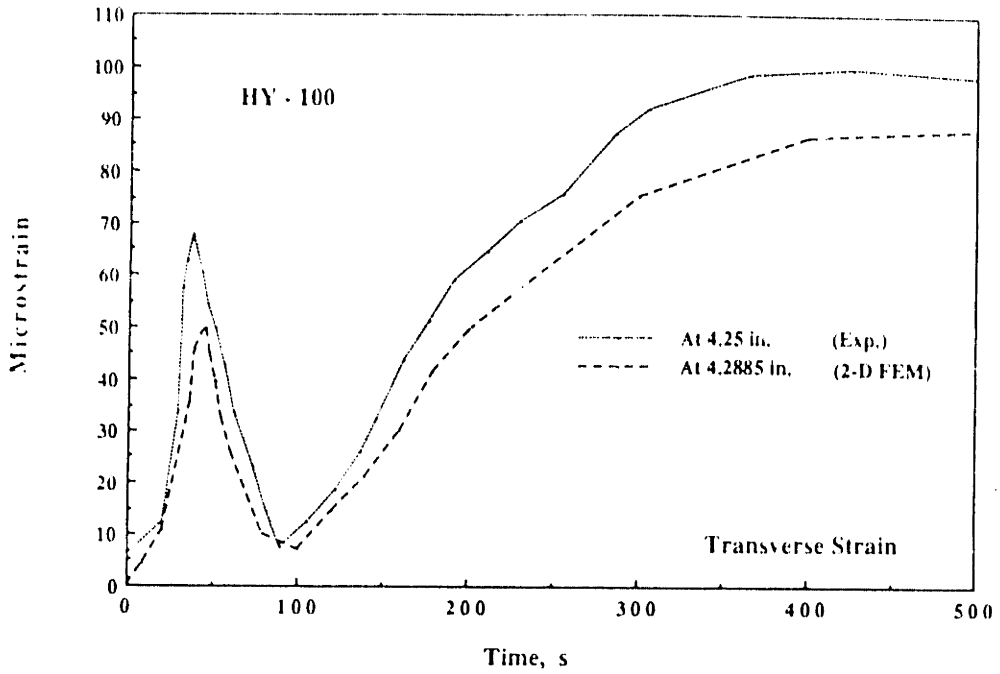

Figure 4-28: Comparison of Transverse Strain Profile --Calculation .vs. Experiment for HY-100 at 4.25 inches

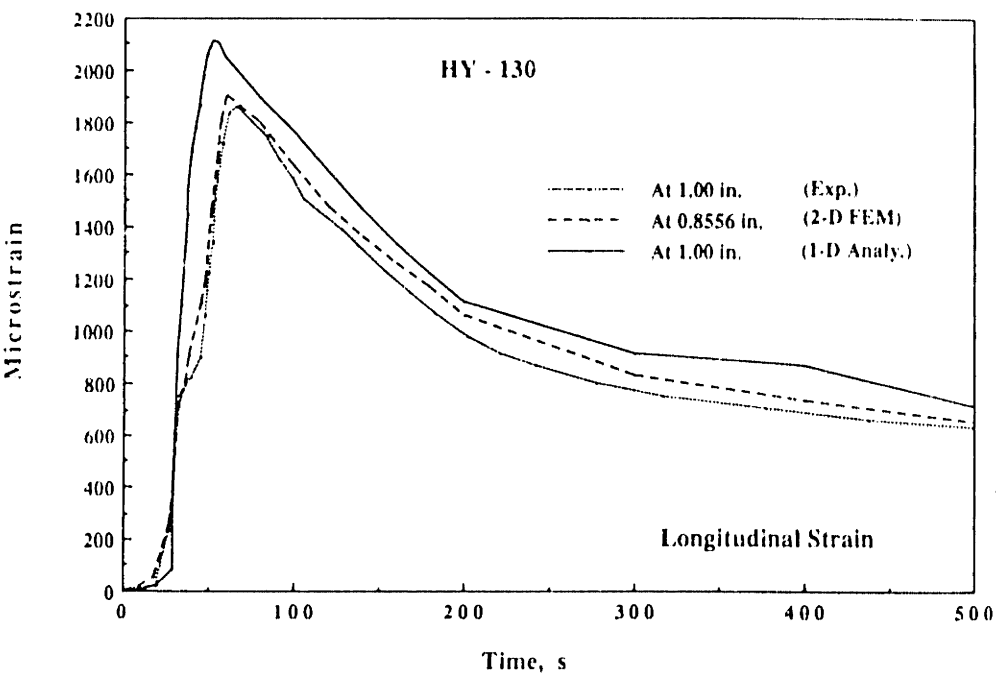

Figure 4-29: Comparison of Longitudinal Strain Profile --Calculation .vs. Experiment for HY-130 at 1.00 inch

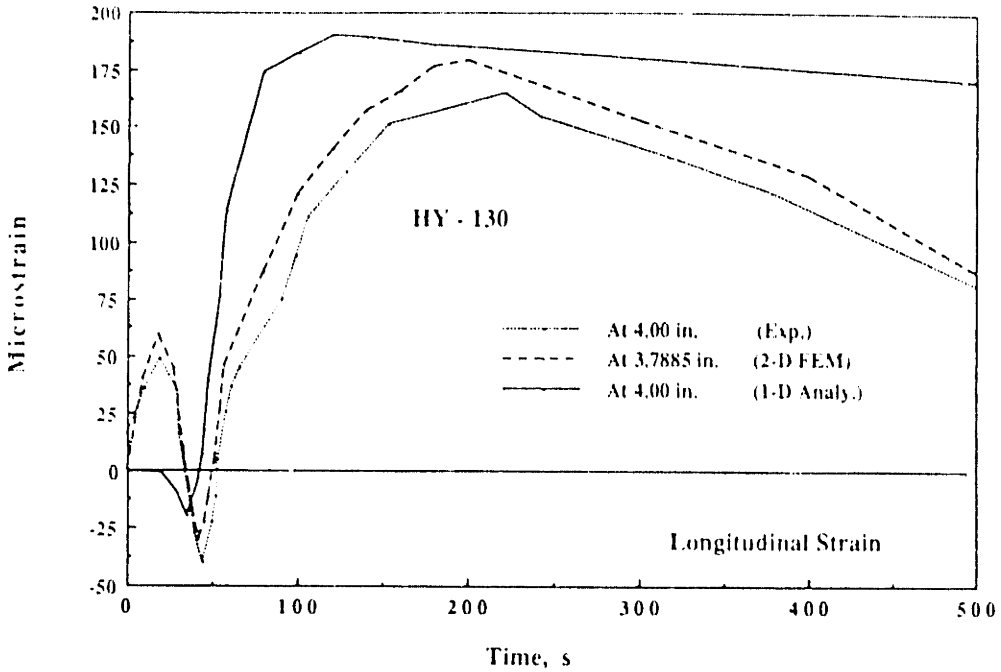

Figure 4-30: Comparison of Longitudinal Strain Profile --Calculation .vs. Experiment for HY-130 at 4.00 inches

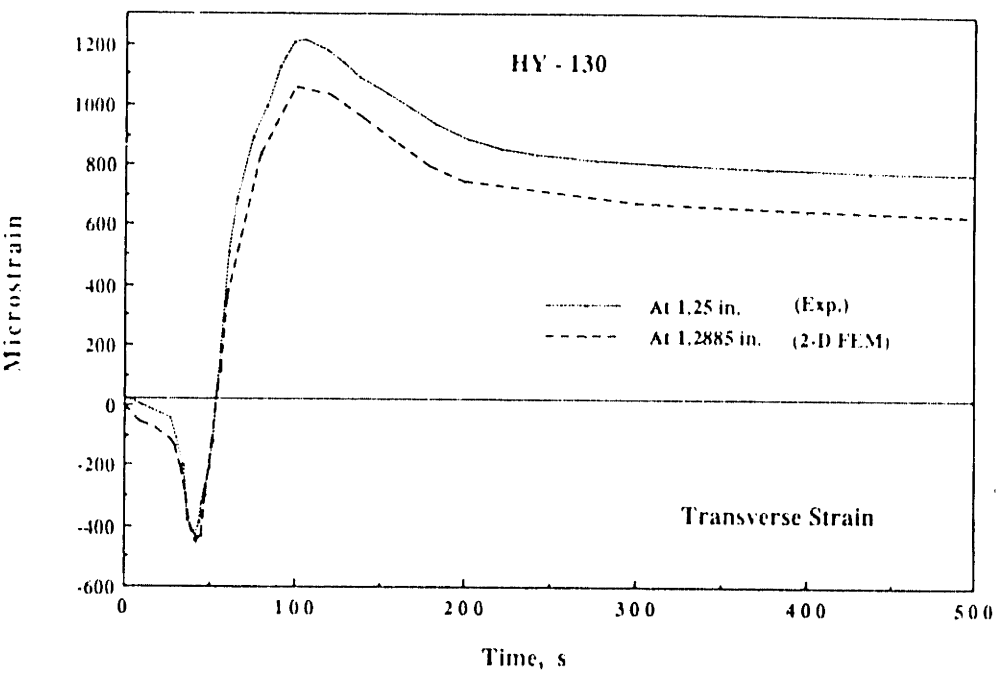

Figure 4-31: Comparison of Transverse Strain Profile --Calculation .vs. Experiment for HY-130 at 1.25 inches

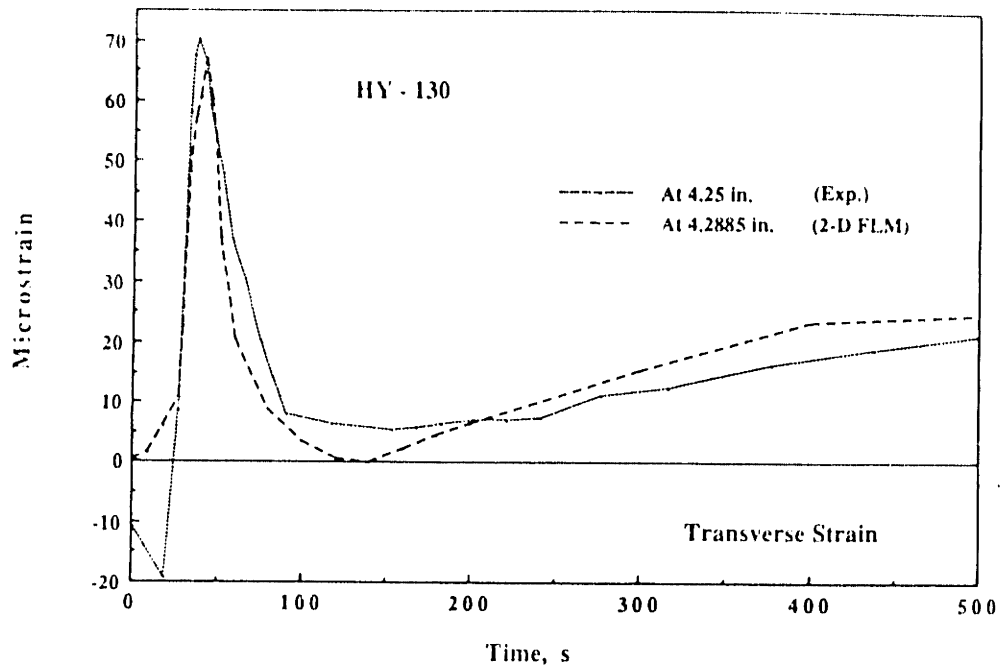

Figure 4-32: Comparison of Transverse Strain Profile --Calculation .vs. Experiment for HY-130 at 4.25 inches

The comparison between experiment data and calculated results for the strain history for the case with side heating at point 1.00 and 4.00 inches away from the weld line is shown in Figs. 4-33 to 4-44. An increase in strain during welding is observed in the analysis as well as in the experiment. A good correlation is obtained in all cases except that an underestimate of strain occurs for low carbon steel at 1.00 inch in the one-dimensional analysis.

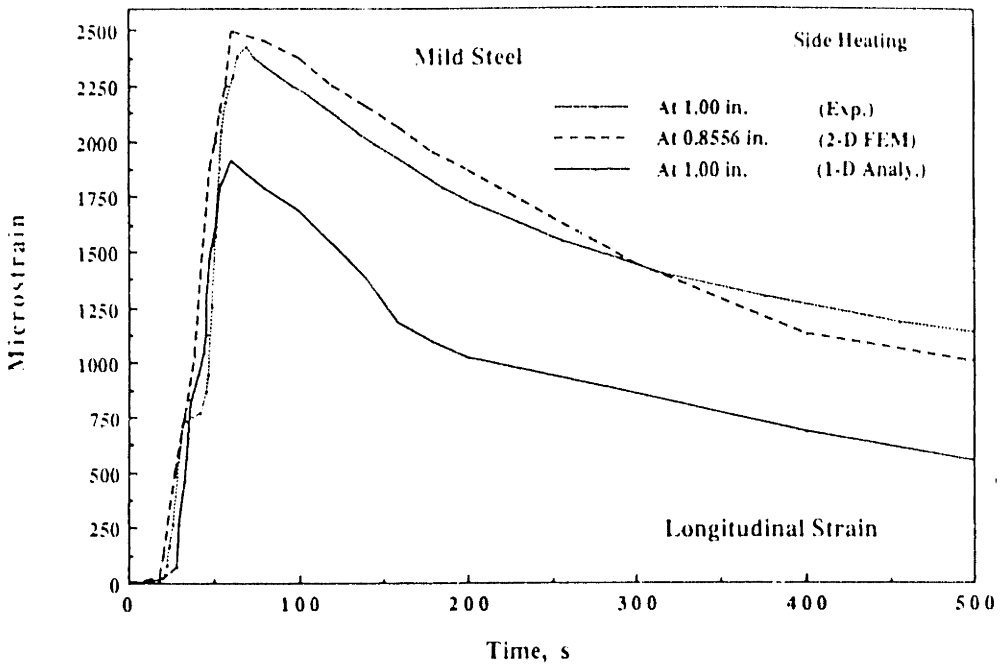

Figure 4-33: Comparison of Longitudinal Strain Profile --Calculation .vs. Experiment for Low Carbon Steel at 1.00 inch (Side Heating)

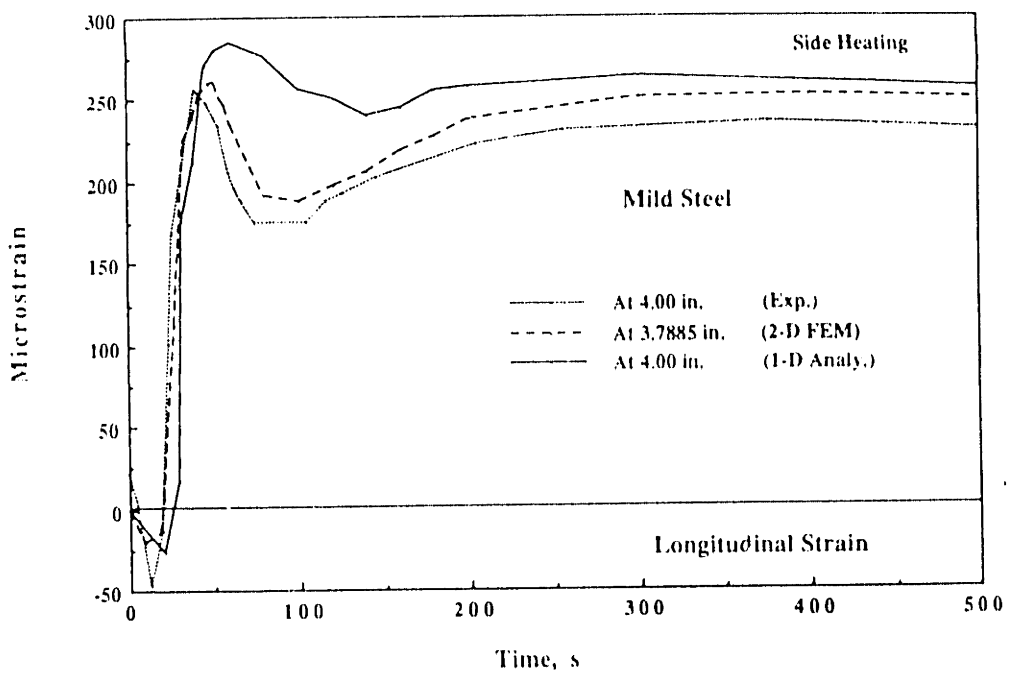

Figure 4-34: Comparison of Longitudinal Strain Profile --Calculation .vs. Experiment for Low Carbon Steel at 4.00 inches (Side Heating)

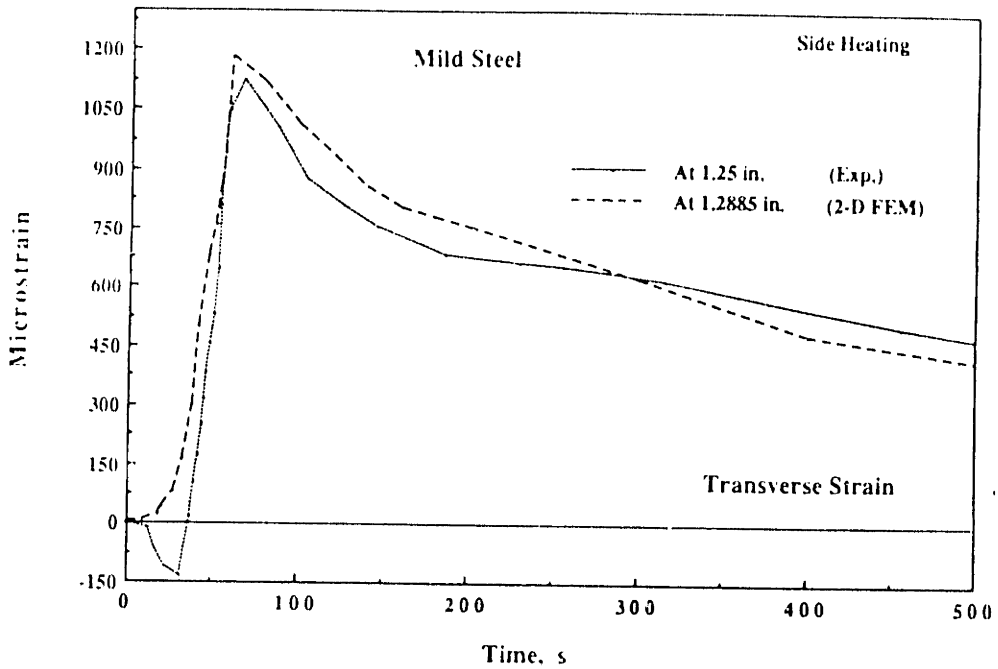

Figure 4-35: Comparison of Transverse Strain Profile --Calculation .vs. Experiment for Low Carbon Steel at 1.25 inches (Side Heating)

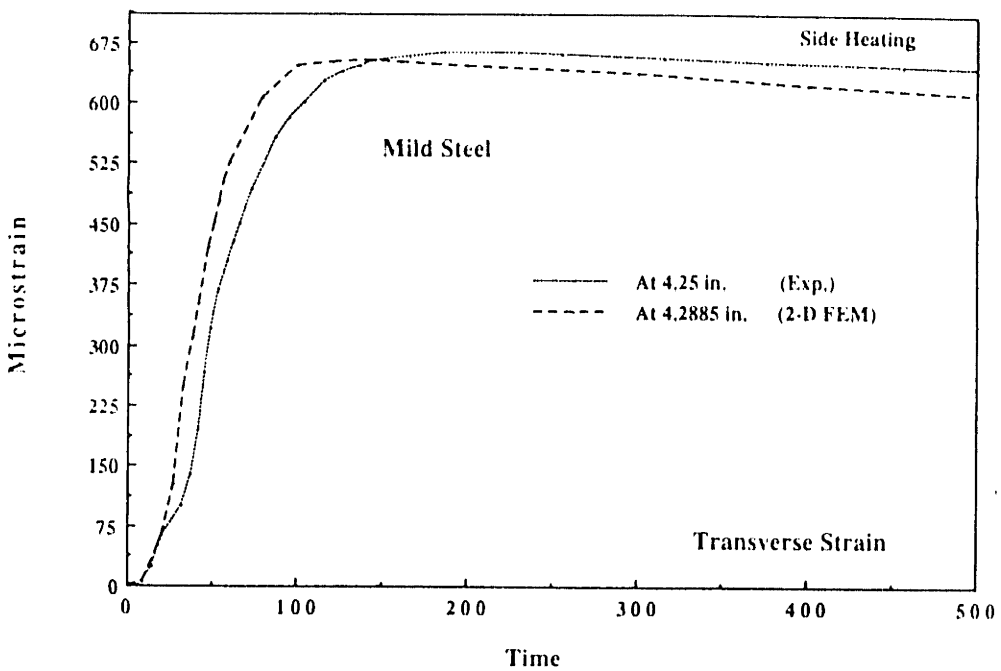

Figure 4-36: Comparison of Transverse Strain Profile --Calculation .vs. Experiment for Low Carbon Steel at 4.25 inches (Side Heating)

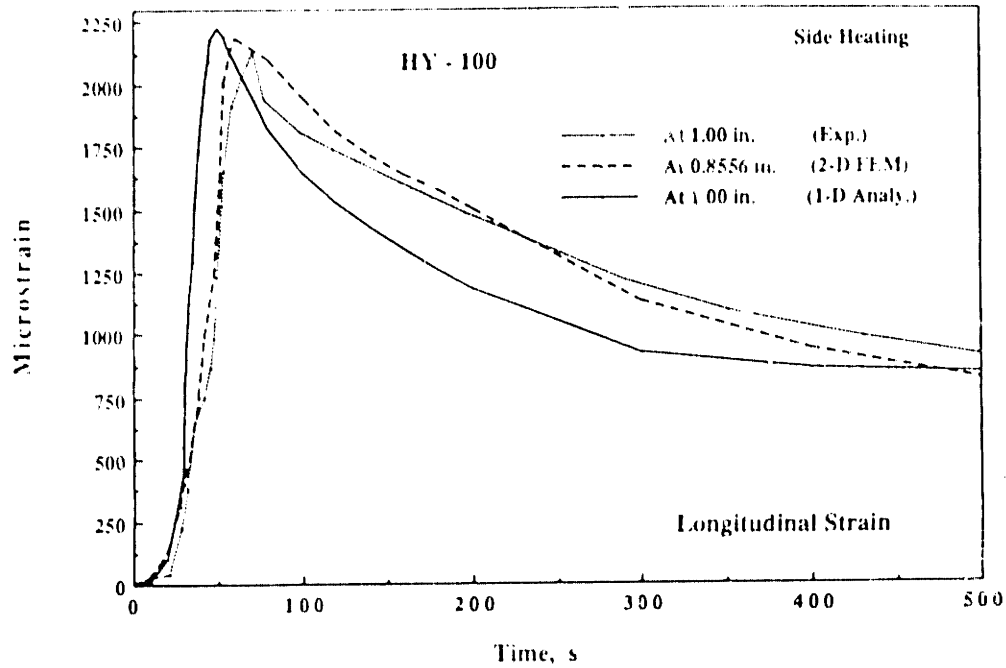

Figure 4-37: Comparison of Longitudinal Strain Profile --Calculation .vs. Experiment for HY-100 at 1.00 inch (Side Heating)

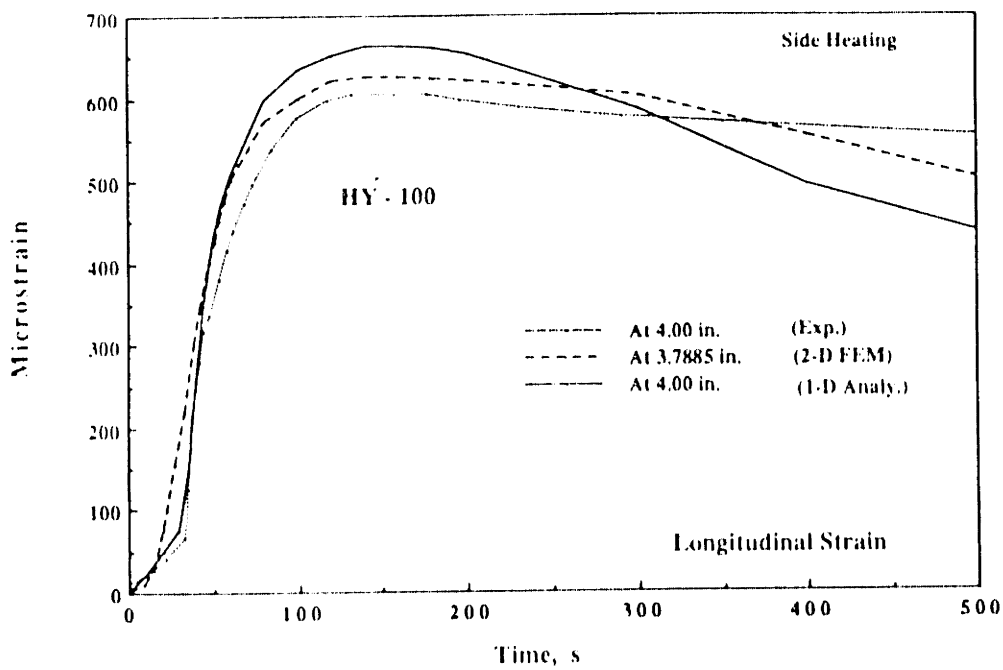

Figure 4-38: Comparison of Longitudinal Strain Profile --Calculation .vs. Experiment for HY-100 at 4.00 inches (Side Heating)

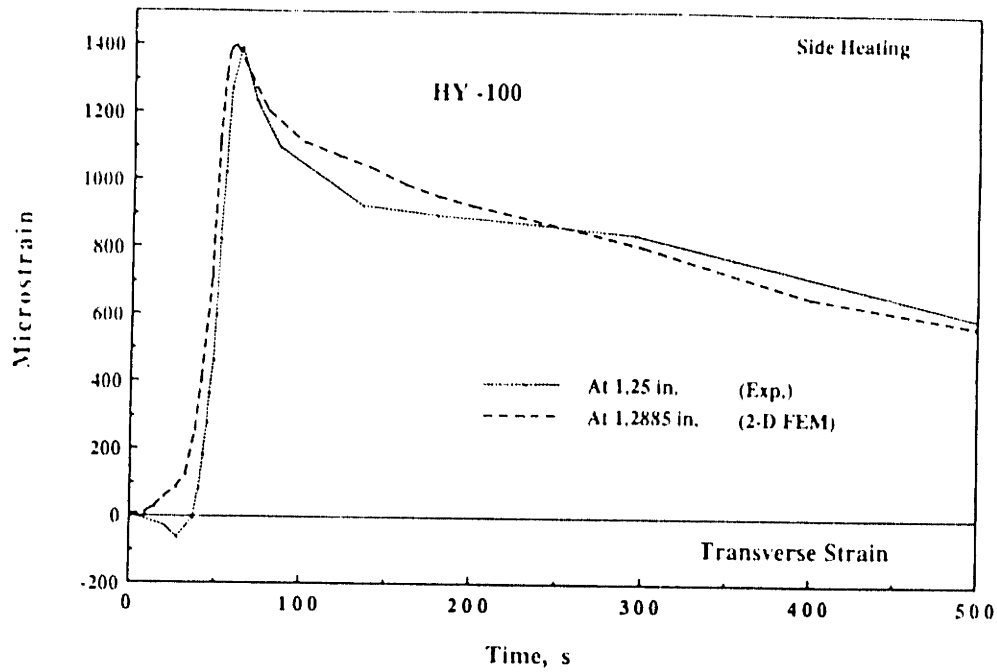

Figure 4-39: Comparison of Transverse Strain Profile --Calculation .vs. Experiment for HY-100 at 1.25 inches (Side Heating)

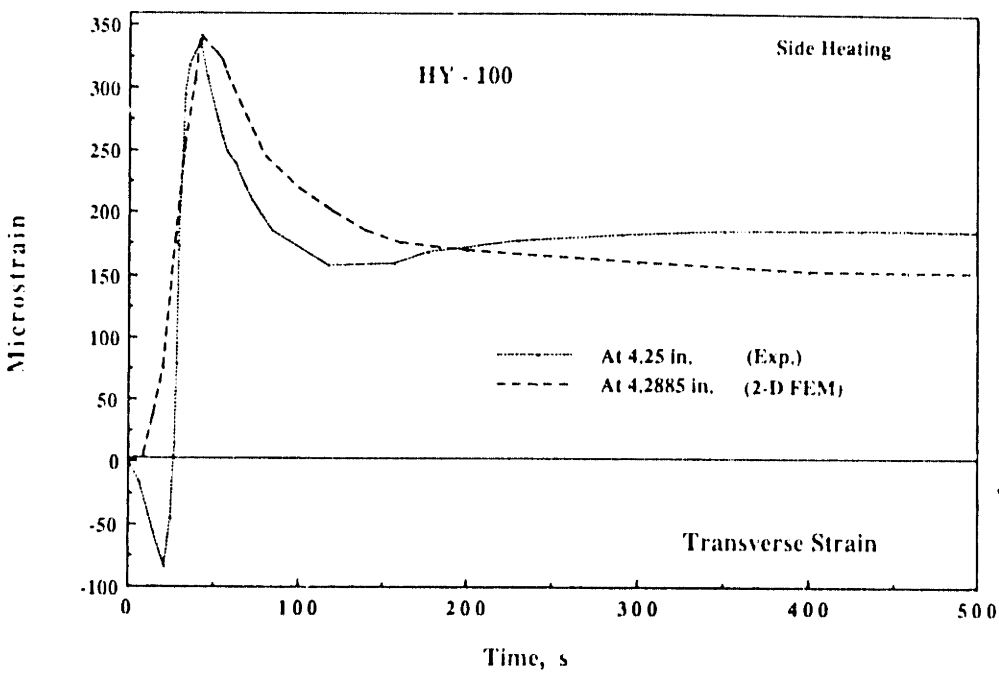

Figure 4-40: Comparison of Transverse Strain Profile --Calculation .vs. Experiment for HY-100 at 4.25 inches (Side Heating)

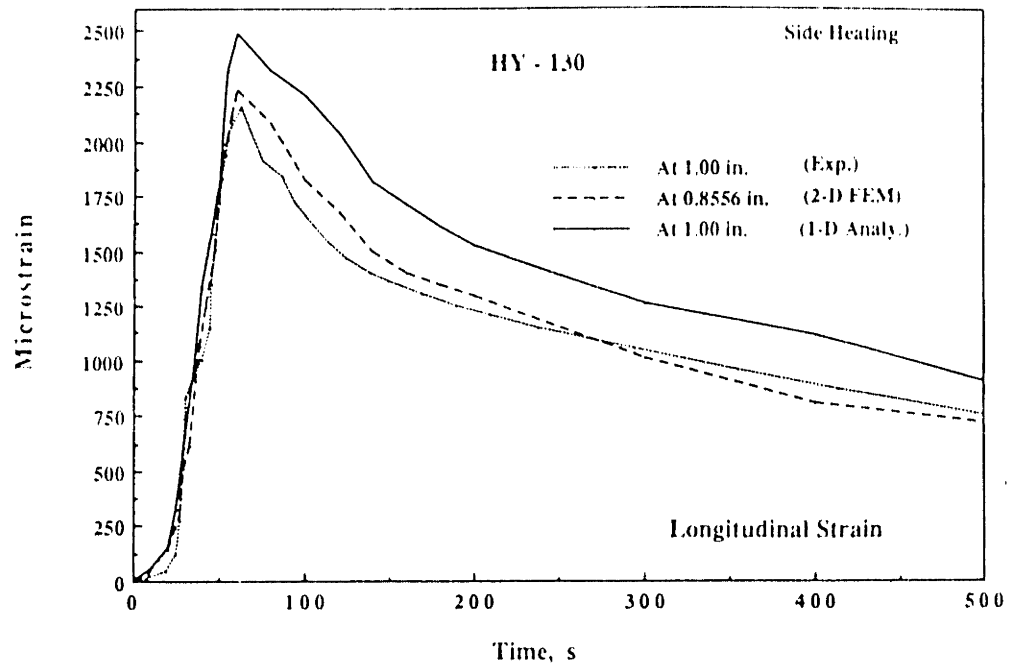

Figure 4-41: Comparison of Longitudinal Strain Profile --Calculation .vs. Experiment for HY-130 at 1.00 inch (Side Heating)

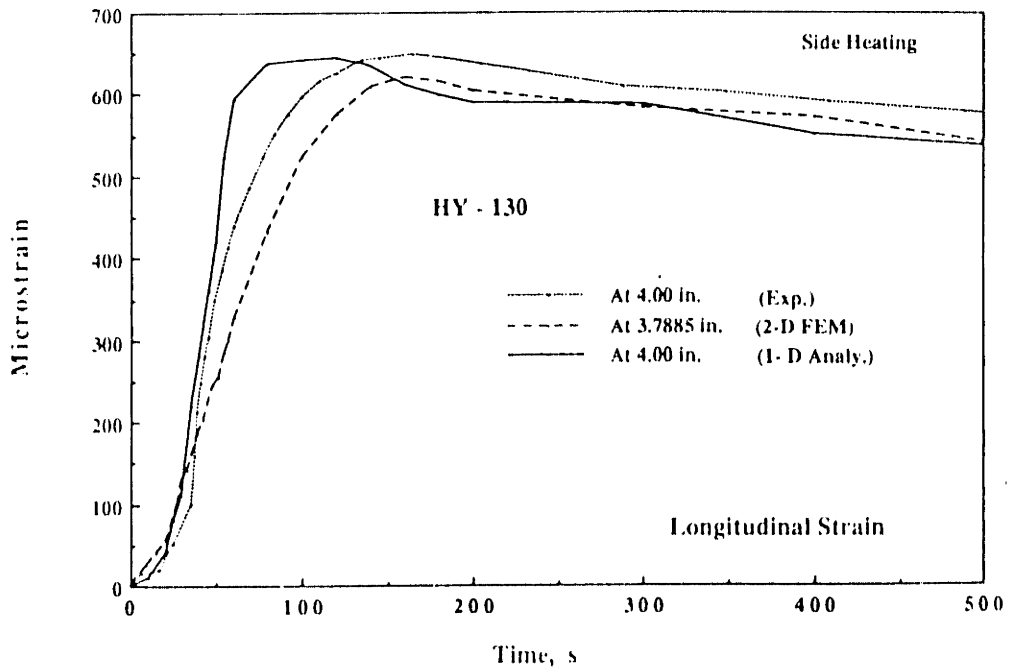

Figure 4-42: Comparison of Longitudinal Strain Profile --Calculation .vs. Experiment for HY-130 at 4.00 inches (Side Heating)

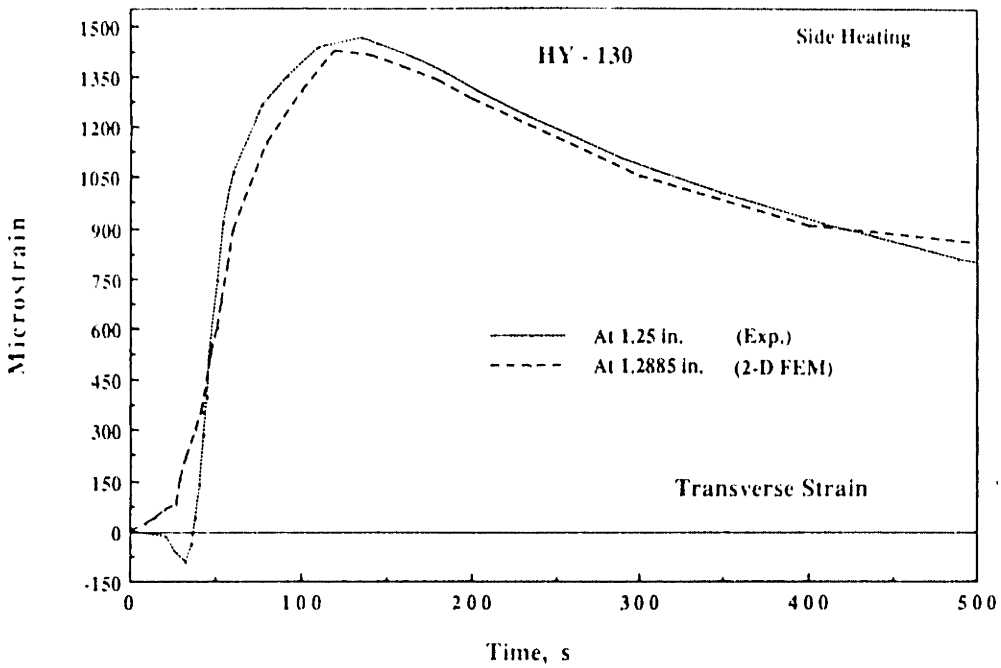

Figure 4-43: Comparison of Transverse Strain Profile --Calculation .vs. Experiment for HY-130 at 1.25 inches (Side Heating)

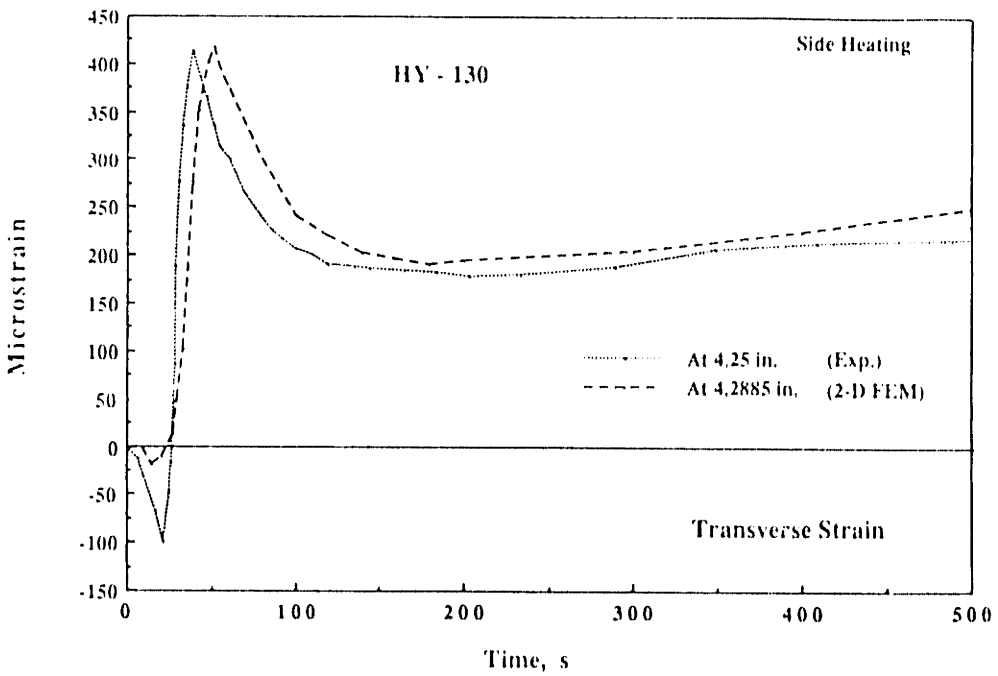

Figure 4-44: Comparison of Transverse Strain Profile --Calculation .vs. Experiment for HY-130 at 4.25 inches (Side Heating)

Finally, the calculated residual stresses from the analyses are compared with those obtained from the experiments. The results are plotted in Figs. 4-45 to 4-50 for the case without side heating and in Figs. 4-51 to 4-56 for the case with side heating. Good residual stress prediction is obtained from finite element analysis. The one-dimensional analysis tends to predict higher compressive residual stresses. The reduction of residual stresses in the case with side heating is observed as well in the analyses. This confirms the results obtained from the experiment. From the analyses it was found that high transverse residual stress does exist in regions very close to the weld line. The magnitude of this transverse residual stress decreases rapidly, however, as the distance increases.

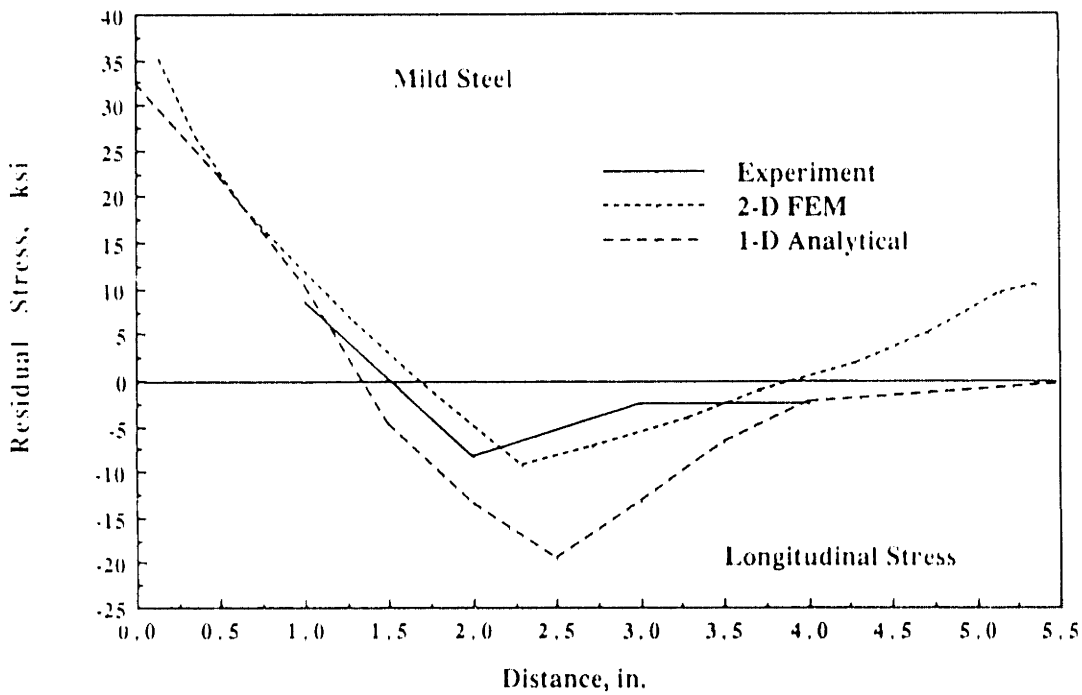

Figure 4-45: Comparison of Longitudinal Residual Stress --Calculation .vs. Experiment for Low Carbon Steel

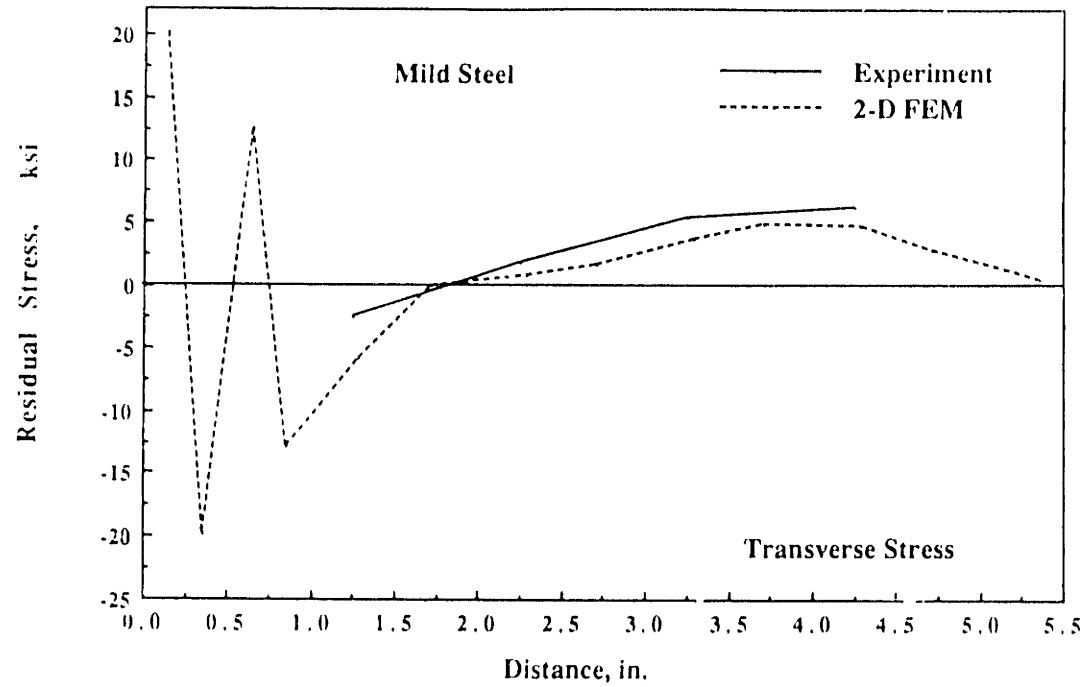

Figure 4-46: Comparison of Transverse Residual Stress --Calculation .vs. Experiment for Low Carbon Steel

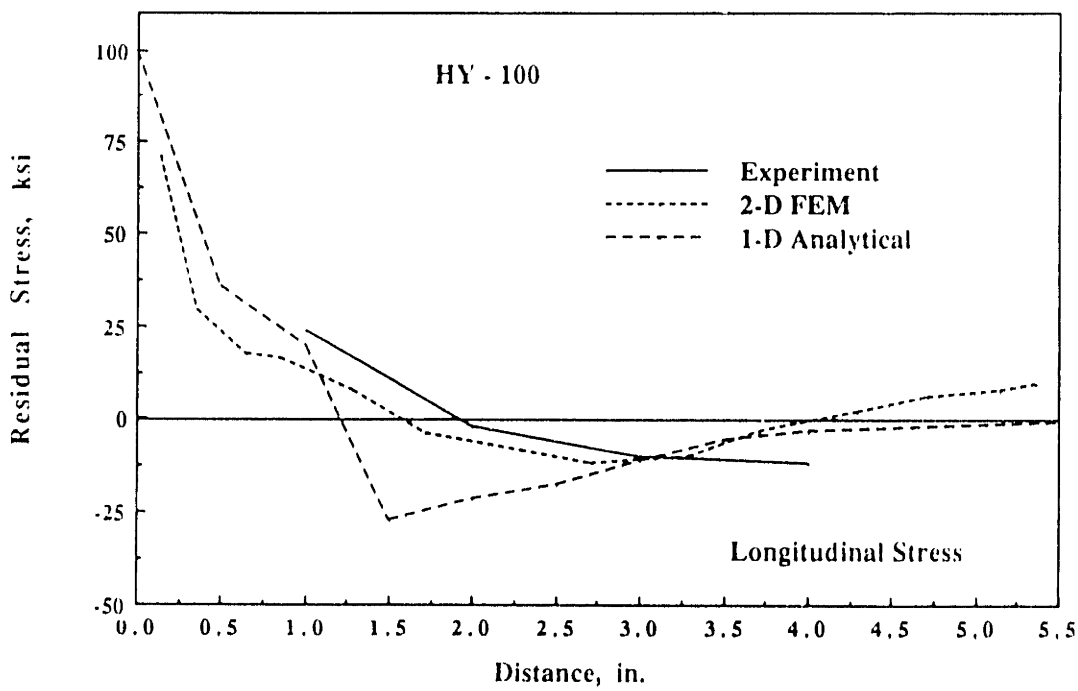

Figure 4-47: Comparison of Longitudinal Residual Stress --Calculation .vs. Experiment for HY-100

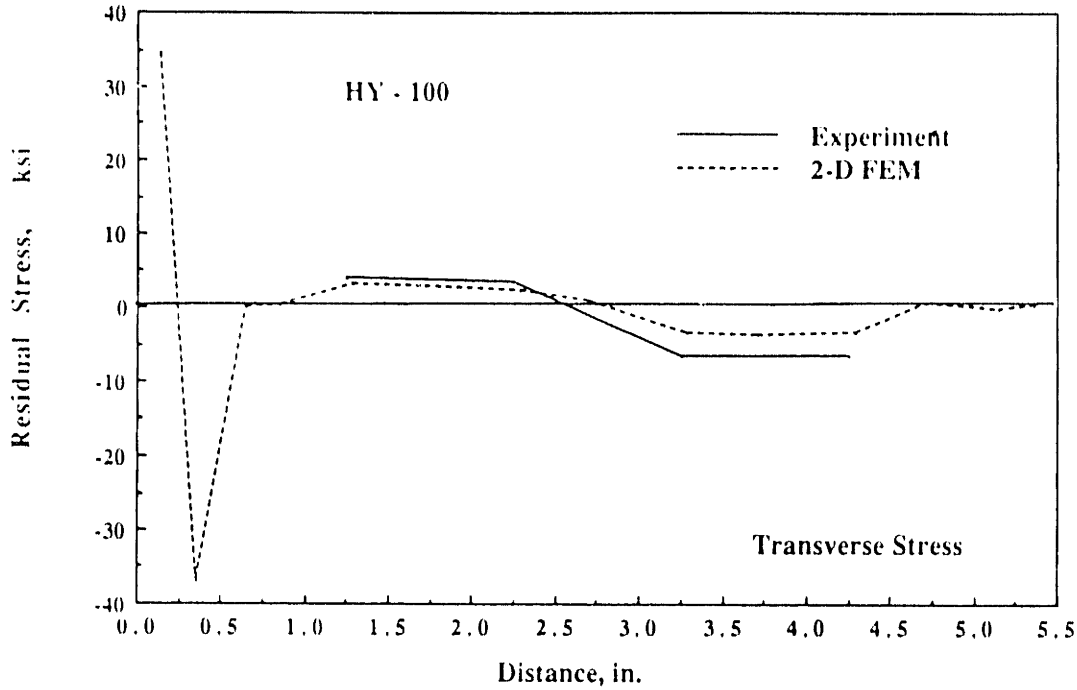

Figure 4-48: Comparison of Transverse Residual Stress --Calculation .vs. Experiment for HY-100

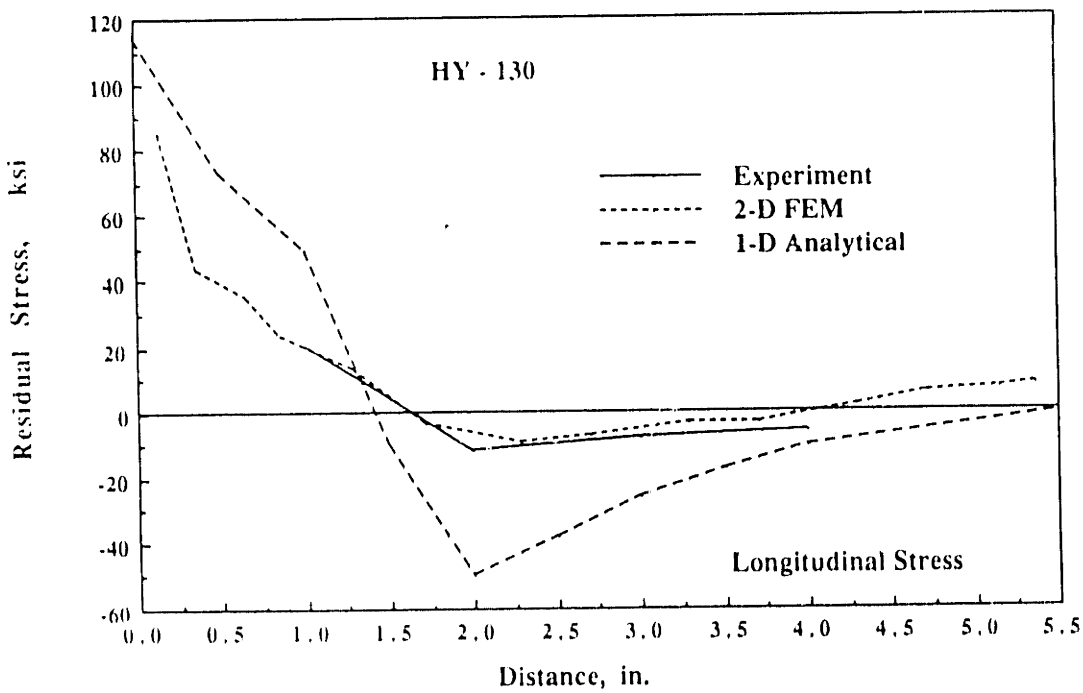

Figure 4-49: Comparison of Longitudinal Residual Stress --Calculation .vs. Experiment for HY-130

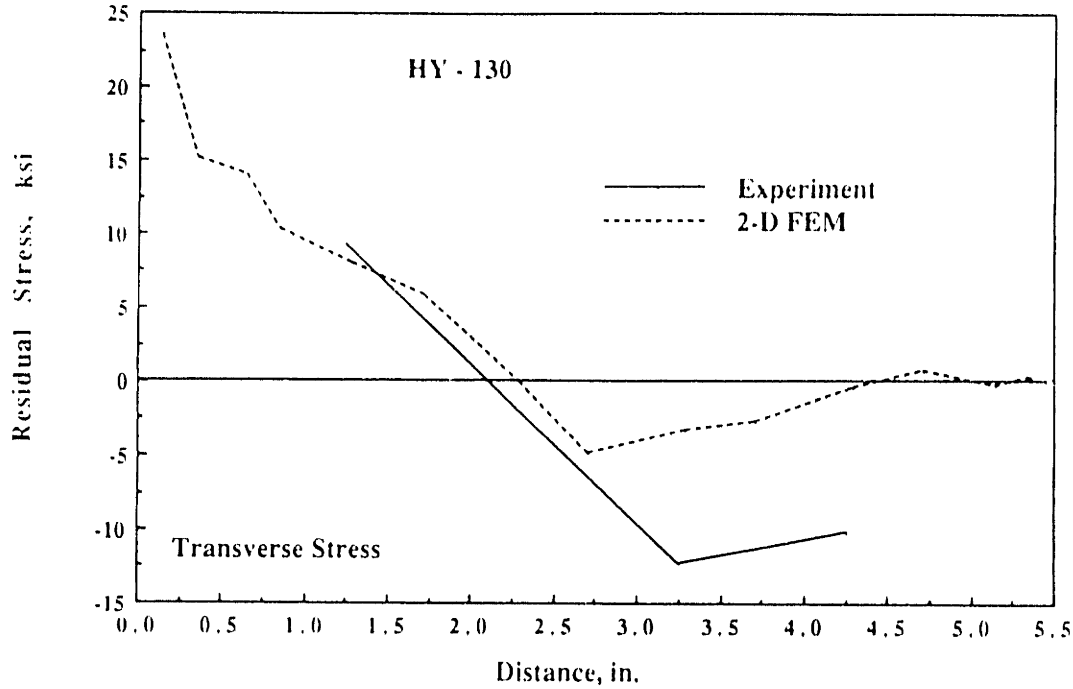

Figure 4-50: Comparison of Transverse Residual Stress --Calculation .vs. Experiment for HY-130

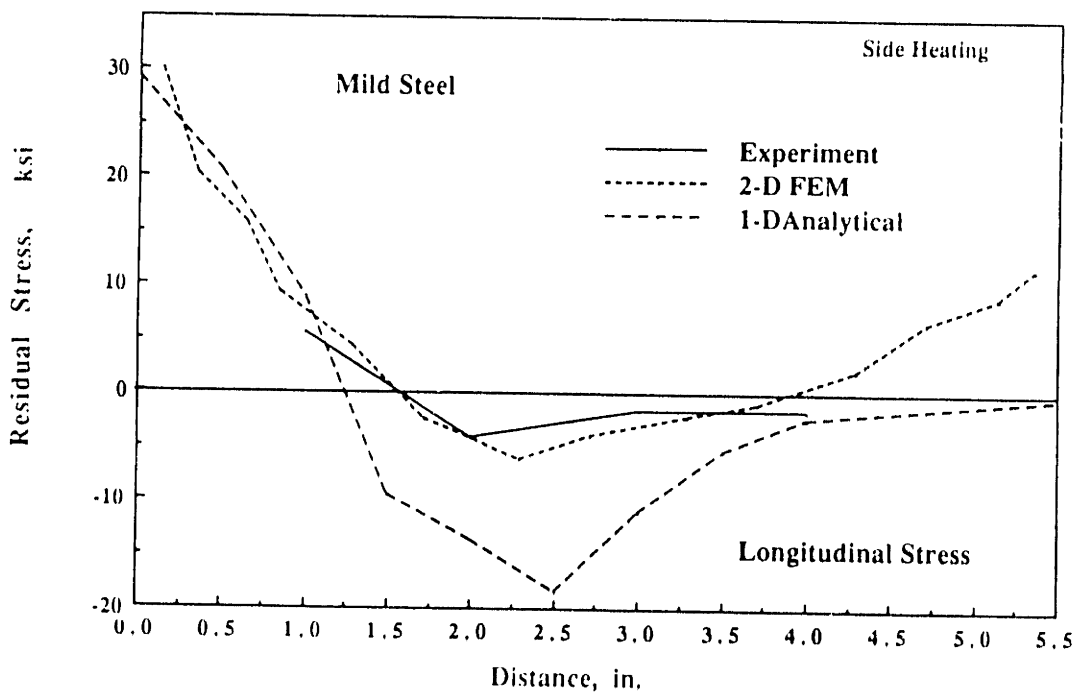

Figure 4-51: Comparison of Longitudinal Residual Stress --Calculation .vs. Experiment for Mild Steel (Side Heating)

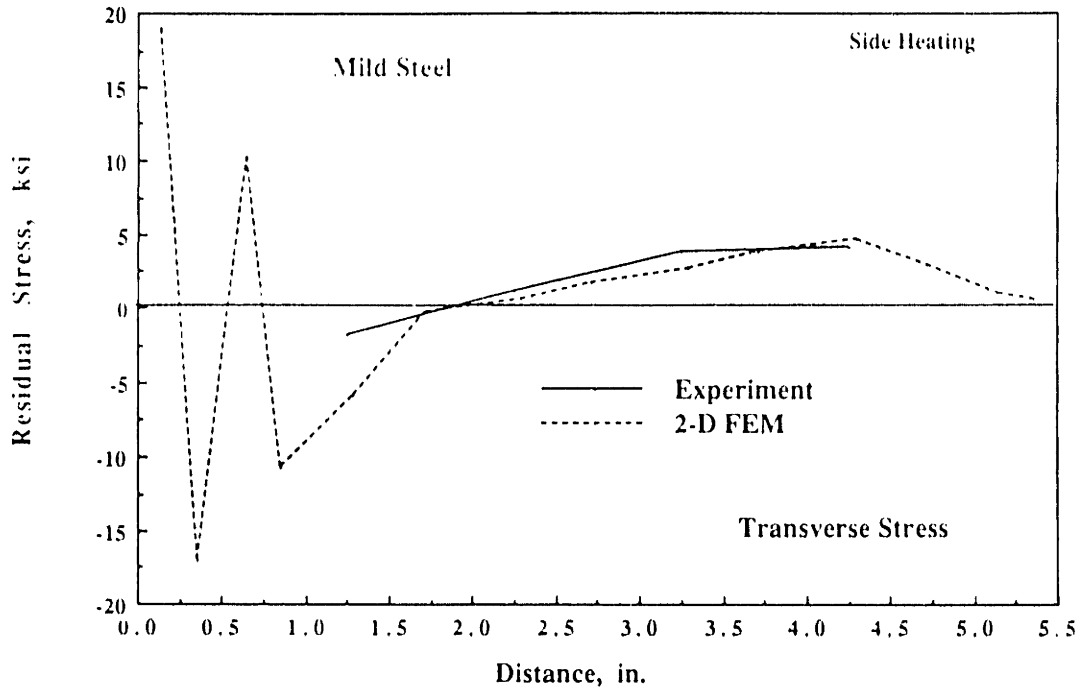

Figure 4-52: Comparison of Transverse Residual Stress --Calculation .vs. Experiment for Low Carbon Steel (Side Heating)

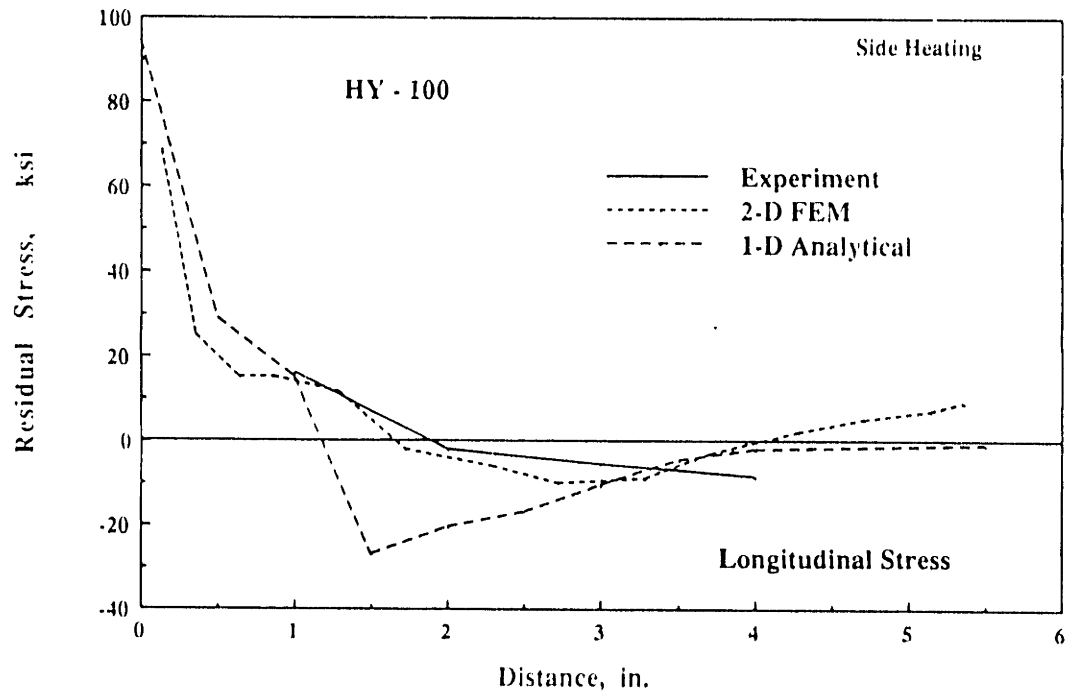

Figure 4-53: Comparison of Longitudinal Residual Stress --Calculation .vs. Experiment for HY-100 (Side Heating)

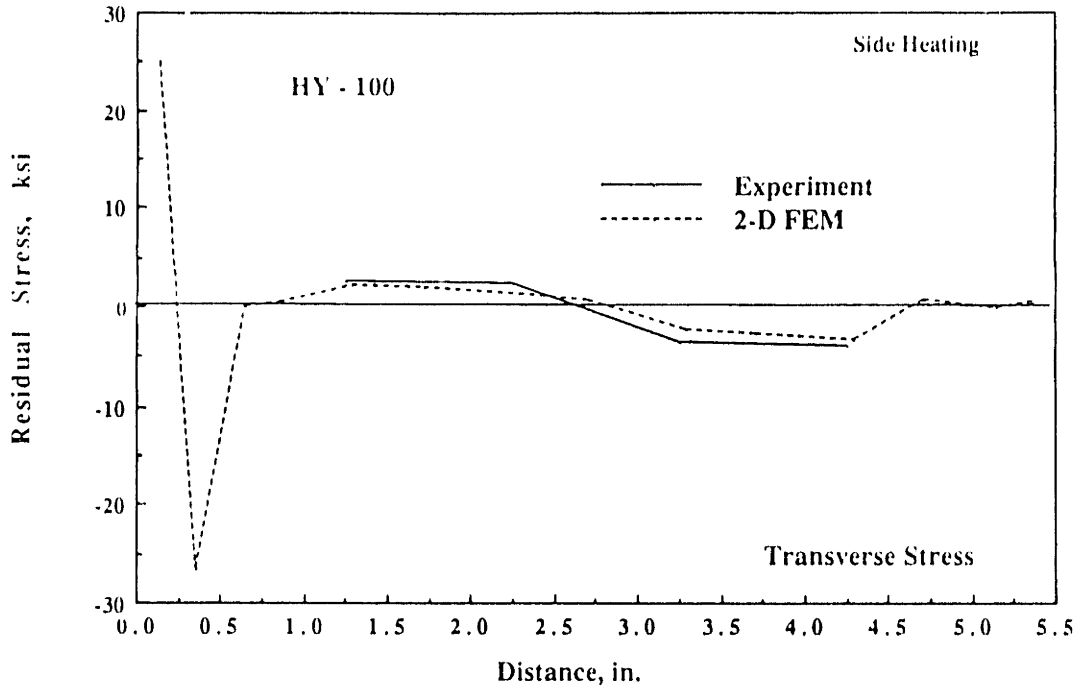

Figure 4-54: Comparison of Transverse Residual Stress --Calculation .vs. Experiment for HY-100 (Side Heating)

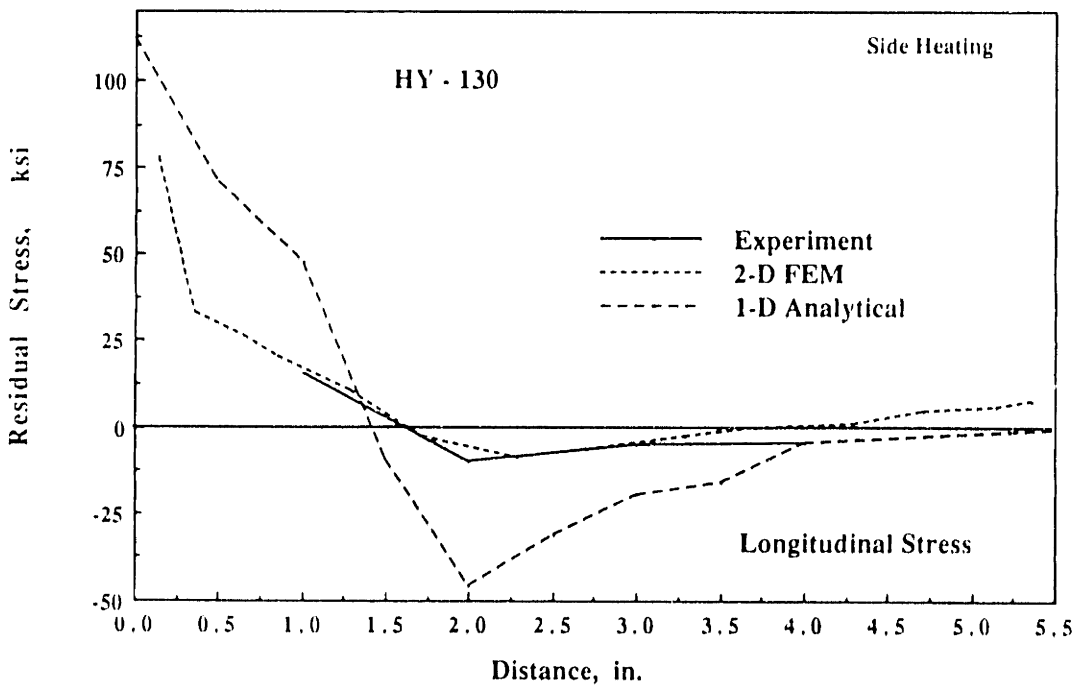

Figure 4-55: Comparison of Longitudinal Residual Stress --Calculation .vs. Experiment for HY-130 (Side Heating)

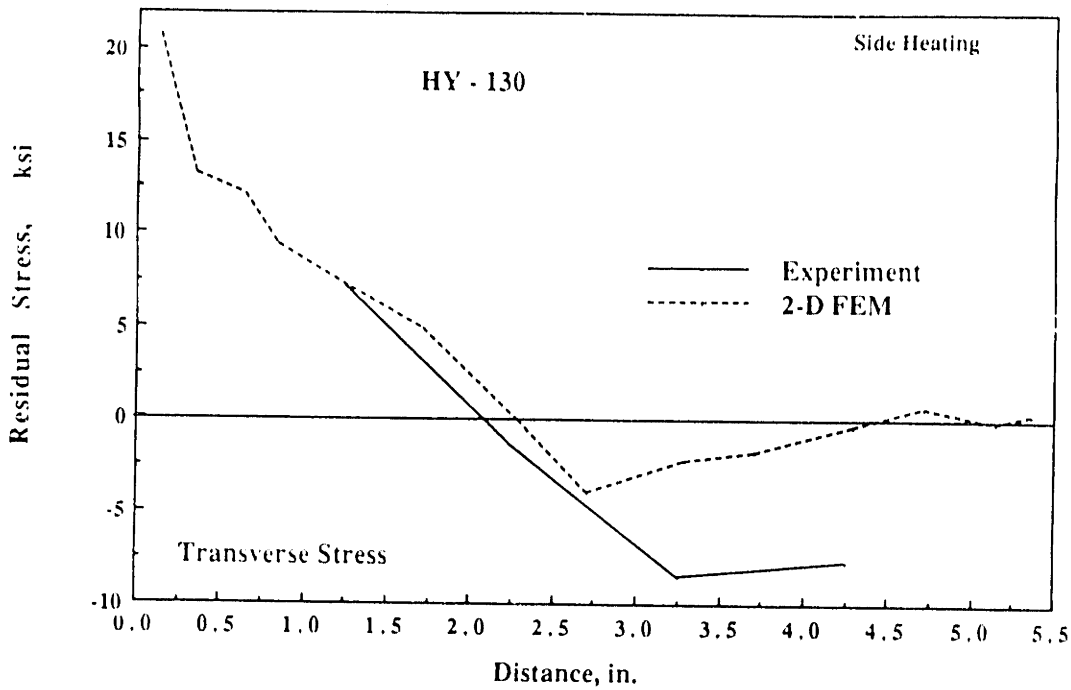

Figure 4-56: Comparison of Transverse Residual Stress --Calculation .vs. Experiment for HY-130 (Side Heating)

4.7 Summary

In summation, the same physical behavior of the specimen in the experiments can be obtained from the analysis. The discrepancy between the calculated results and the experimental data can be attributed to the accuracy of the input data such as material properties, heat source distribution, finite element mesh, assumptions made in the analysis, etc. It should be mentioned that the phase transformation does not include in both one-dimension analysis and finite element analysis for this investigation. This will be the case, however, when poor agreement is observed between experimental data and calculated results. Nevertheless, it is another source of error as well. The analysis does predict the reduction in both distortion and residual stresses when the side heating source is present. This confirms not only the experimental results but also the effectiveness of the side heating technique.

Chapter 5

Concept on Reduction of Residual Stress and Distortion

5.1 Introduction

In this chapter, some discussions will be pursued on observation and the conclusions arrived at during the experiments. Concepts on improving the effectiveness of the side heating technique to reduce residual stresses and distortion will also be presented. The use of thermal stress relief on high strength steel after welding was investigated using the model developed in the previous chapter. The objective is to find an appropriate combination using the present side heating technique along with other existing techniques such as low temperature localized heating to effectively reduce residual stresses and distortion.

5.2 Distortion in Weldment in Various Materials

It was found from this investigation that the maximum distortion during welding of HY-130 and HY-100 was higher than the maximum distortion during welding of low carbon steel (see Fig. 5-1). However, the final distortion of HY-100 and HY-130 was much less than that of low carbon steel. The final distortion at mid-length for all three steels for the welding condition without side heating is shown in Table 5-I.

Table 5-I: Distortion at Mid-Length

Material	Distortion, in.
Low carbon steel	0.015
HY - 100	0.007
HY - 130	0.004

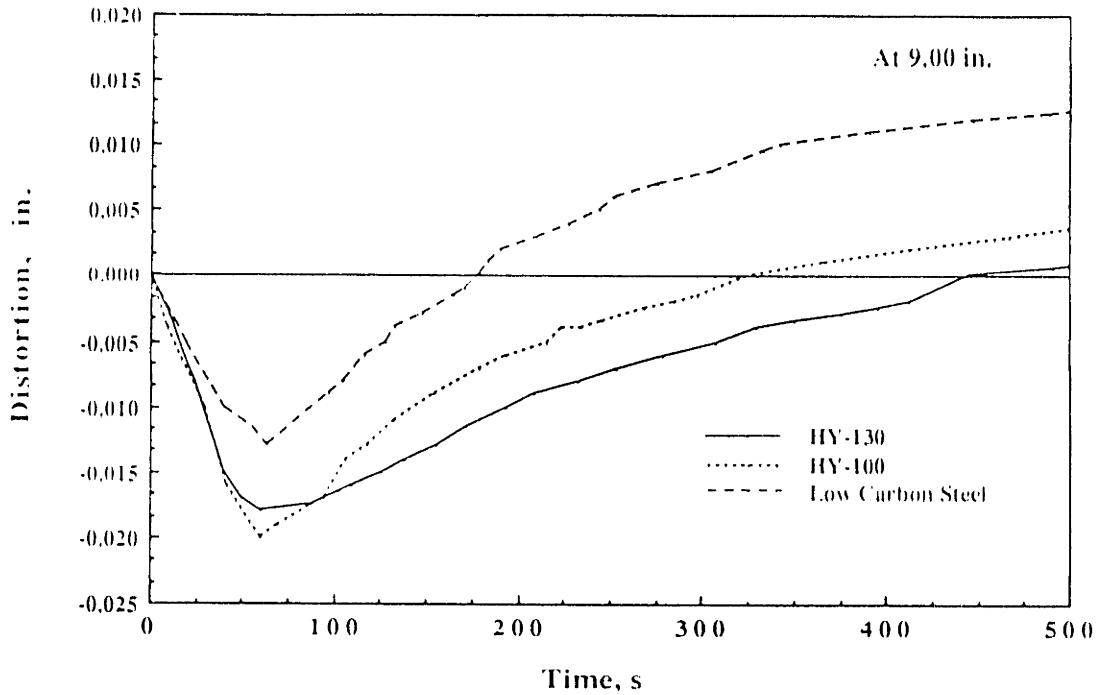

Figure 5-1: Distortion Comparison

This phenomenon of distortion resulted from two basic mechanisms, both of which developed stresses through changes in temperature. First, the strain developed in the base material during welding exceeded the yield condition and plastic upsetting occured. For most structural materials, yielding easily occurs during welding because the yield stress is a decreasing function of temperature. At high temperature, plastic deformation occurs at lower stress levels. As temperature reaches the melting point of the material, the yield stress is comparatively low or zero and plastic behavior is easily achieved. Second, after welding was completed and the specimen cooled down, stress resulted from shrinkage of weld metal occurred. In addition, yield stress started to develop on all three steels as shown in Fig. 5-2. The difference in temperature created different yield stress development throughout the specimen. This yield stress development combined with the stress resulted from shrinkage of weld metal provided an internal bending moment. This bending moment is opposite to the thermal bending moment that resulted from the thermal effect during welding

which caused distortion. Higher yield stress development in HY-130 and HY-100 provided higher internal bending moment thus resulted in lower distortion since the specimen started to bend in the opposite direction.

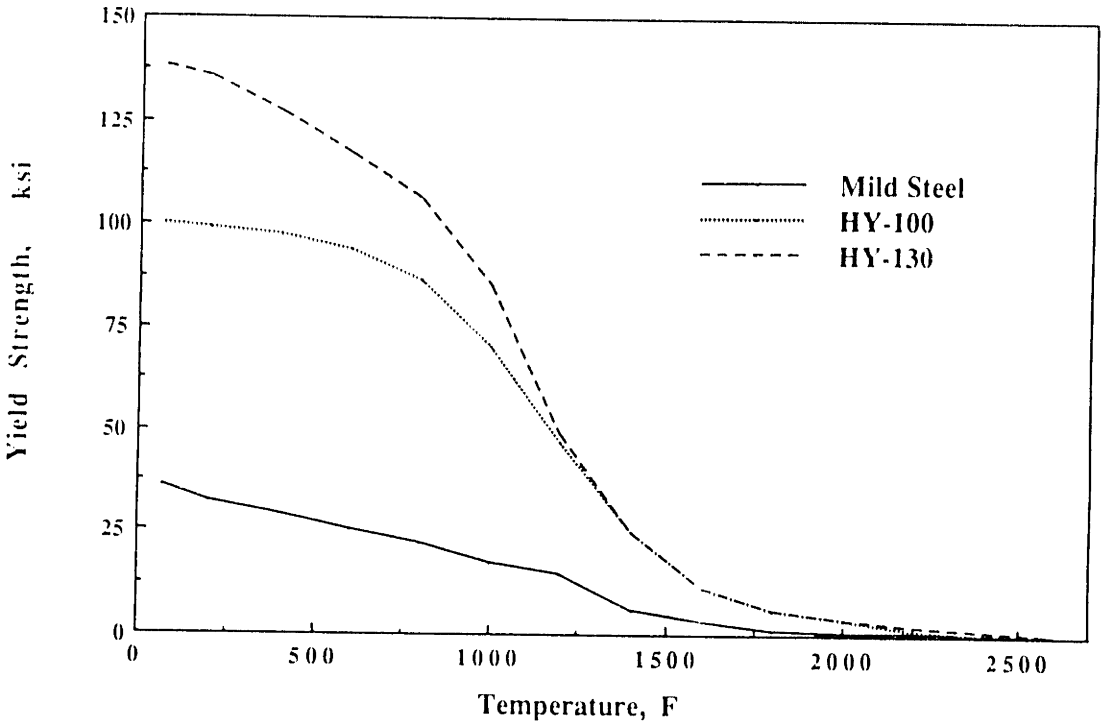

Figure 5-2: Yield Stresses at Elevated Temperature

The shrinkage of the weld along the edge also caused compressive stresses in the region near the weld line. The high shrinkage of the weld which happened in high strength steel enabled high compressive stress to develop near the weld line. As a result, tensile residual stresses which were produced near the weld are lower than the yield stress at room temperature for high strength steel. This can be the reason why the residual stresses in high strength steel are not as high as yield strength as opposed to those in low carbon steel. However, to find a complete answer to this problem one has to study also the microstructural change of the material near the weld which is totally changed due to the high temperature at that location. The phase transformation in that area should be taken into account to study the effect of transformation behavior to the state of stress in addition to the shrinkage behavior near the weld.

The physical behavior of distortion mentioned above indicated that in-process control of distortion and reduction of residual stresses and distortion during welding for high strength steel like HY-130 and HY-100 can be accomplished by providing a stronger side heating heat source than the one for low carbon steel in order to reduce the high distortion during welding. However, the risk of material degradation due to this strong heat source should be taken into consideration. This is important for high strength steel due to high response of this steel to the thermal effect. Therefore, it makes the technique more complicate to be implemented for high strength steel than for low carbon steel. On the other hand, reduction of distortion after welding for high strength steel should be less complicated than that in low carbon steel due to the lower final distortion in high strength steel.

5.3 Maximum Longitudinal Strain in Weldments of Various Materials

Under the same welding conditions, it was observed that the maximum longitudinal strain tends to increase as the yield stress increases. Figure 5-3 shows the result of maximum longitudinal strain observed at 1.00 inch from the weld line for three steels used in this investigation. This observation was confirmed by comparing the result from Hwang's study [26]. Hwang did the bead on edge welding on stainless steel, low carbon steel, and titanium. The difference in magnitude can be attributed to the different sizes of specimens, welding conditions, etc. used in the investigation.

Longitudinal residual stress is the main stress of concern since this residual stress can be as high as the yield stress in low carbon steel or 50-60% of the yield stress in high strength steel. In order to precisely control and reduce this stress during the in-process control of welding, it is necessary to follow the longitudinal strain history during and after welding. High rate of strain change which occurred in high strength steel during welding indicated that the sensing

device implemented in the in-process control of welding should be highly sensitive to detect the rapid change of strain during welding. It should be mentioned that the high rate of strain change accompanied with the high rate of temperature rise during welding provide a difficult task for any contact sensing devices to work well in such a situation. Any non-contact sensing devices such as optical or laser measuring devices would probably be used in this situation provided that improvement in feeding back data from such devices has to be made to ensure the real time control of the process.

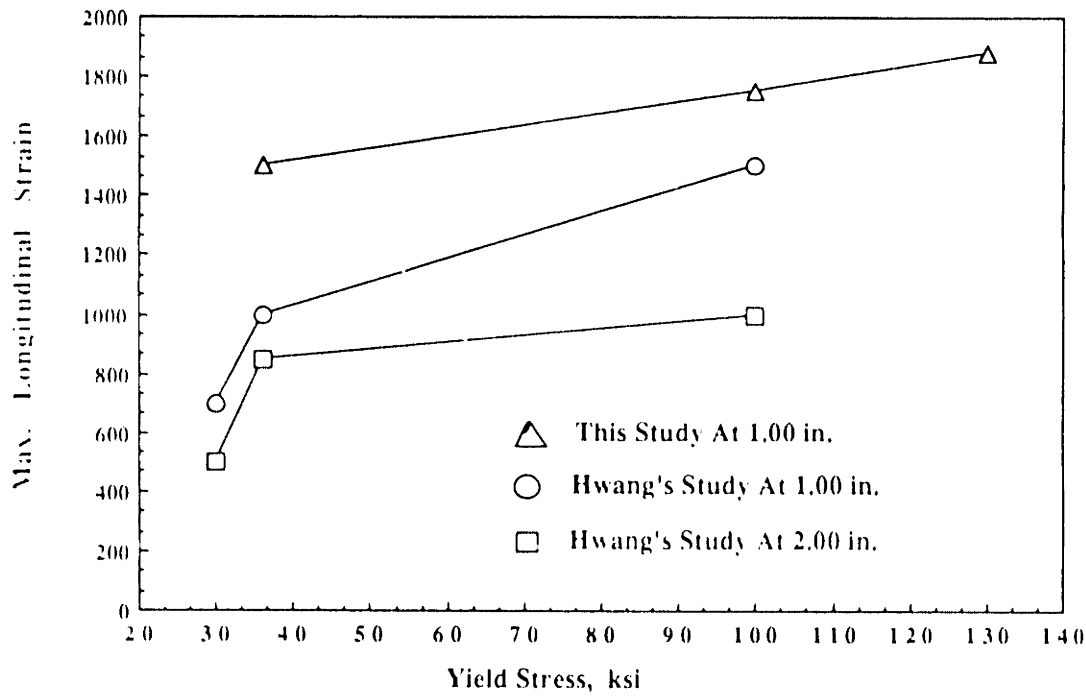

Figure 5-3: Maximum Longitudinal Strain observed at 1 inch from weld line

5.4 Size of Plastic Zone

It is well established that residual stresses and distortion are closely related to the development of a plastic zone near the weld. If there is a method to limit the extent of the plastic zone, residual stresses and distortion can be reduced. Figure 5-4 and Fig. 5-5 show the development of plastic zone for the case without side heating and with side heating for HY-130, respectively. The

observed location is at 8.683 inches. The calculation was done using the model for finite element program described in the previous chapter.

In Fig. 5-4 the material along the weld line first experienced plastic deformation when the welding arc approached a distance about 0.283 inch away. The plastic zone extended outwards as far as 0.447 inches as the arc approached. In Fig. 5-5 with side heating, the material along the weld line experienced plastic deformation at a distance about 0.583 inches away. The plastic zone extension was limited to about 0.303 inches from the the weld line. This clearly indicates that by providing side heating to the weldment during welding, the plastic deformation can be controlled and the size of the plastic zone can be reduced. It should be noted here that values indicated in Fig. 5-4 and Fig. 5-5 are approximate values due to the size of the element used in finite element mesh.

Even though it is possible to determine the plastic zone using the numerical technique such as finite element method, it is very difficult to control the size of plastic zone when one implements the side heating technique into the in-process control of welding. This is because the time required for the calculation is long and it will be too late to adjust the side heating condition for appropriate control of plastic zone. One solution to this problem is to perform extensive calculations to collect data for each welding task and store them into database. This data can then be recalled for comparing when needed.

It should also be noted that the effective stress was used in ADINA to describe the stress state of the material under the combined loading situation. Similarly, one can also use the effective strain to describe the strain state of the material. It will be useful to determine this effective strain and use this to determine how far the material will go beyond the elastic limit when welding. This is because it is feasible to measure strain change while the material is being welded. It is believed that the material should only slightly exceed the elastic limit since welding at each particular point happens for a very short time. However, other factors such as high heat input can also push the material far into the plastic region as well.

Another comment is that in the case that involves thermal effect such as welding, stress is not only a function of strain but also a function of temperature as well. This is because both elastic modulus and tangent modulus are functions of temperature. Therefore, to try to follow either stress or strain state in elastic or plastic region, one has to deal with temperature-strain or temperature-stress coordinate. This means one has to follow along the loading or unloading path in 3D and not in 2D plane.

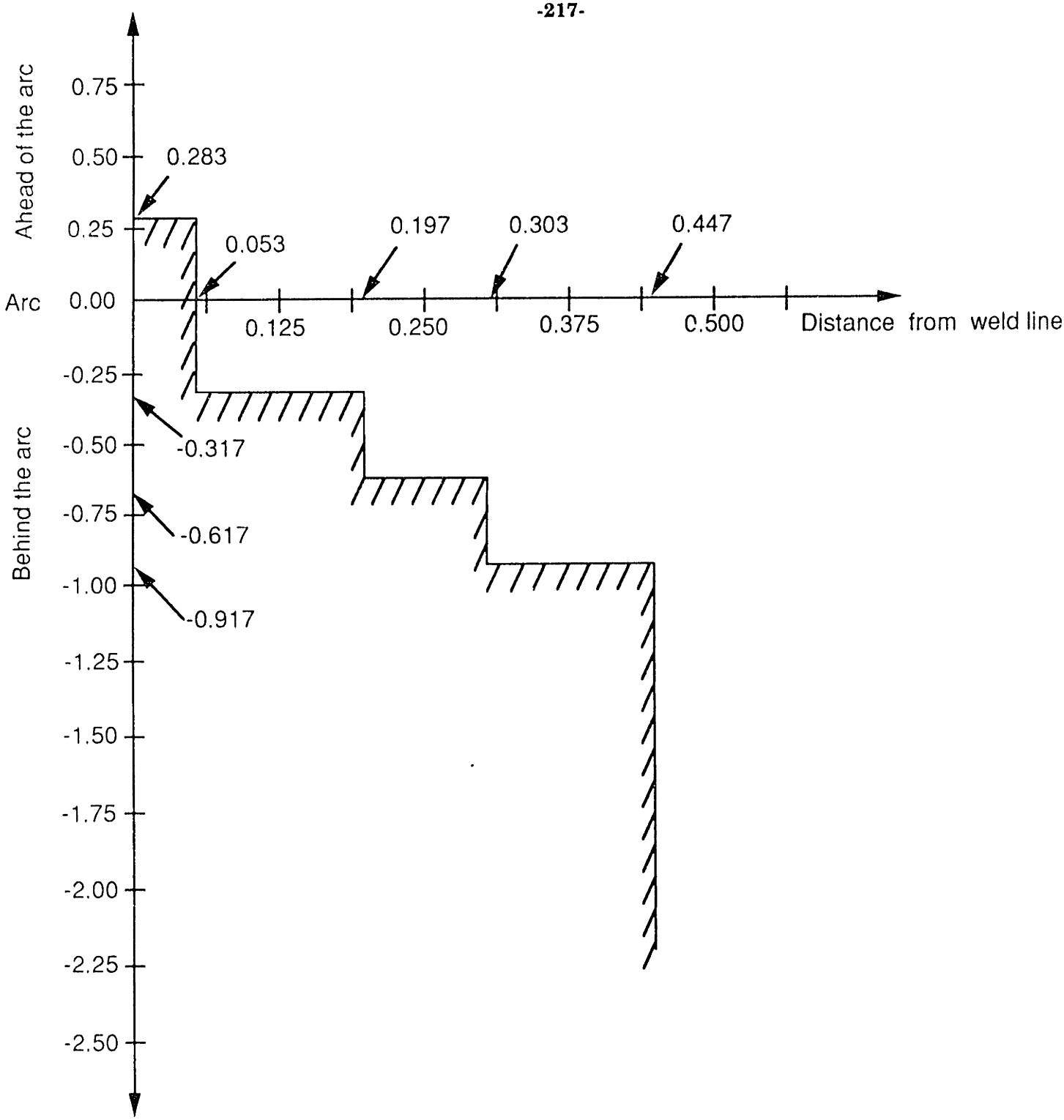

Figure 5-4: Development of Plastic Zone for the Case without Side Heating

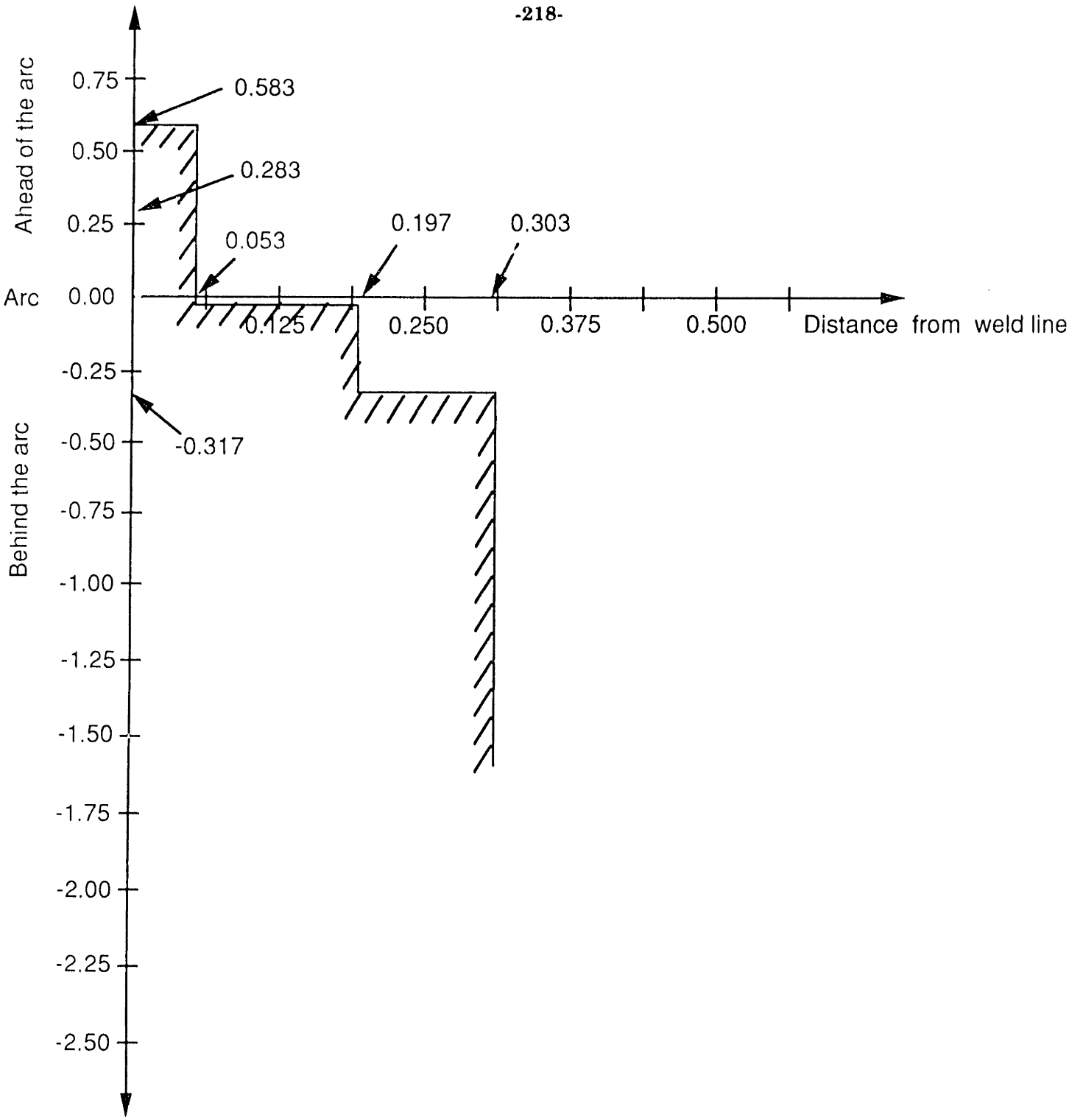

Figure 5-5: Development of Plastic Zone for the Case with Side Heating

5.5 Low Temperature Localized Stress Relief

In this section, low temperature localized stress relief was used to further reduce residual stress and distortion when the welding was completed. This low temperature localized heating is not a new concept. It was introduced by Greene in 1949. Greene [21] suggested this method and reported to have reasonable success on T-2 tankers, penstocks, large field-erected tanks and pressure vessels. However, at that time the only way to be sure that residual stress had actually been reduced was through destructive methods of stress measurement. Therefore, this technique is no longer used. Today, however, the availability of high speed computers allows us to simulate and analyze the possible combination of welding and stress relief techniques.

Low temperature localized stress relief was introduced for use on structures that were too large to be stress relieved by other techniques such as uniform heating in furnaces. The procedure is to use oxyacetylene torches to progressively heat bands on the weldment to 350 to 400 °F (175 to 205 °C) after the weldment cools down. By properly performing this process, partial reduction in residual stresses is possible. However, the overall performance of the structure treated by this method has not been well studied yet.

To study the effectiveness of low temperature localized stress relieving technique, four weldings with different low temperature localized stress relieving techniques were simulated and run using ADINA. They were as follows:

1.) Preheat the plate to 200 ° F and then weld it.

2.) Weld the plate without side heating and wait until the plate cools down. Then heat the plate with the same amount of flame used in side heating at 0.5 inches away from the weld line. The heat band is 1 inch wide.

3.) Weld the plate with side heating and apply the same stress relief technique as in 2.

4.) Weld the plate with side heating and apply the same stress relief technique as in 2 except that the location to be heated is at 3.5 inches from the weld line.

Material used in this simulation was HY-130. Welding conditions and side heating conditions for each simulation were the same as those in Chapter 2. The magnitude of heat used in low temperature localized stress relief was the same as that used for side heating.

Figure 5-6 shows the predicted temperature profile of the weldment during welding for the case of preheating. The maximum temperature observed at 0.5 inches away from the weld line is higher than that shown in Fig. 2-14. This is due to the higher initial temperature of the base plate.

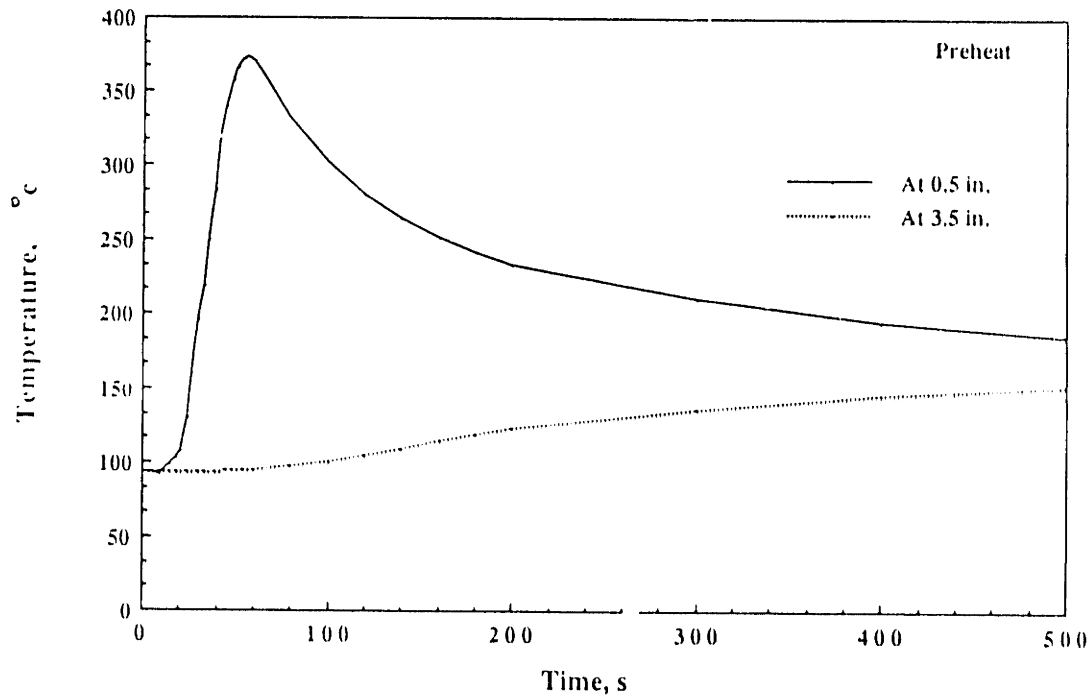

Figure 5-6: Temperature Profile for Preheating

Figure 5-7 shows the temperature profile of the weldment for the case without side heating during the low temperature treatment at 0.5 inches from the weld line.

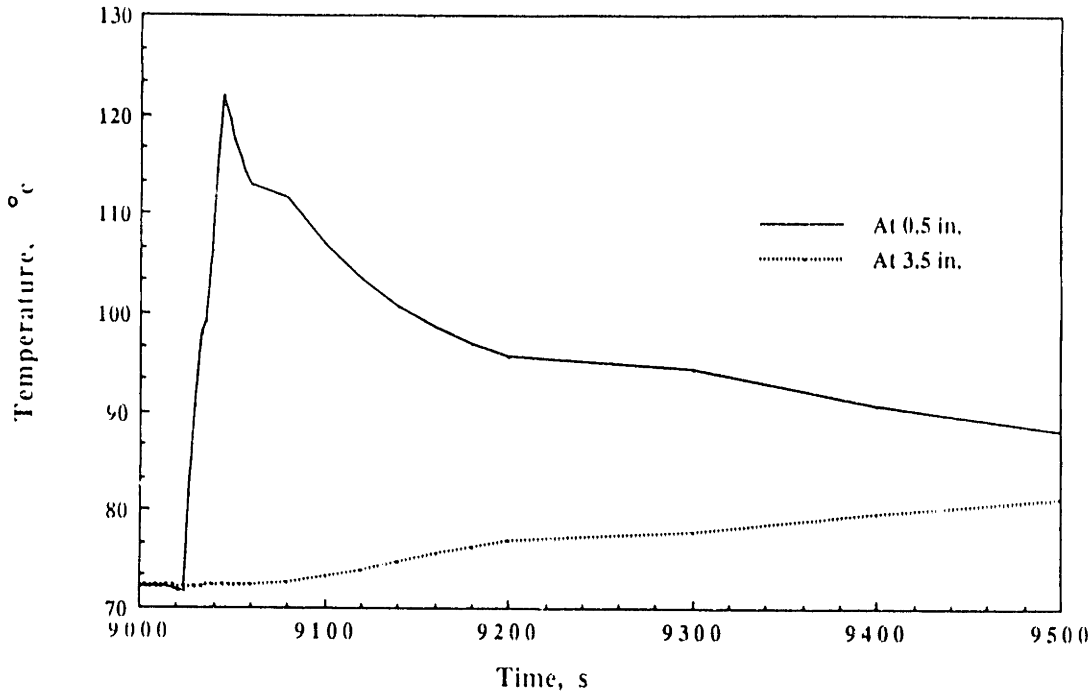

Figure 5-7: Temperature Profile during Low Temperature Treatment at 0.5 inches from the weld line for no side heating case

Figures 5-8 to 5-9 show the temperature profile of the weldment for the case with side heating during the low temperature treatment at 0.5 inches and 3.5 inches from the weld line, respectively.

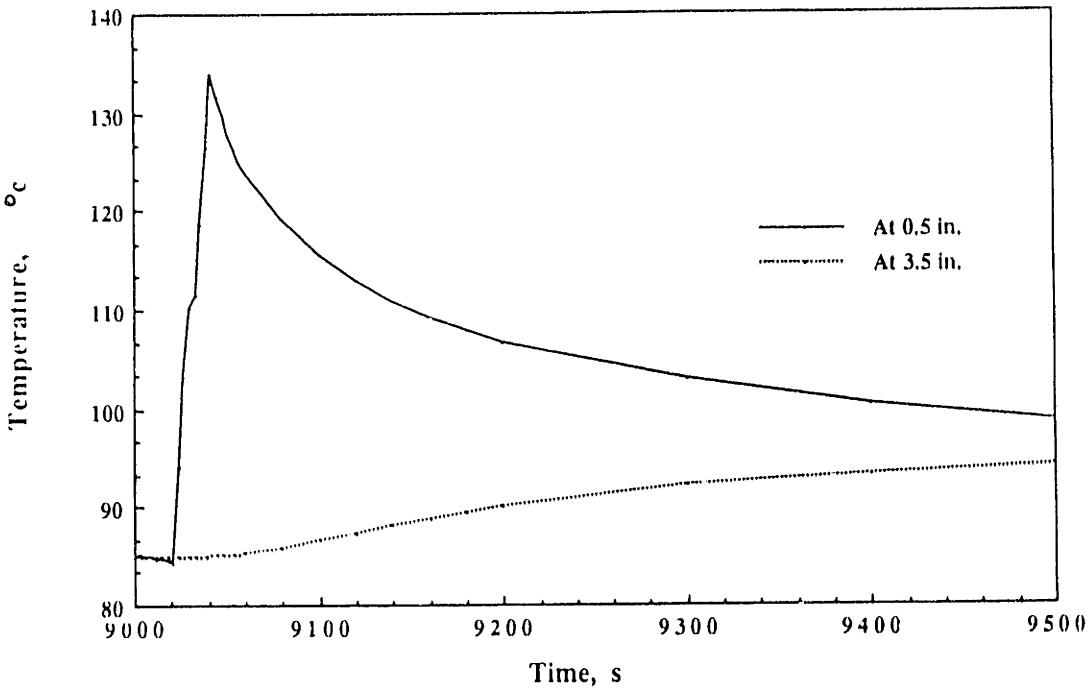

Figure 5-8: Temperature Profile during Low Temperature Treatment at 0.5 inches from the weld line for side heating case

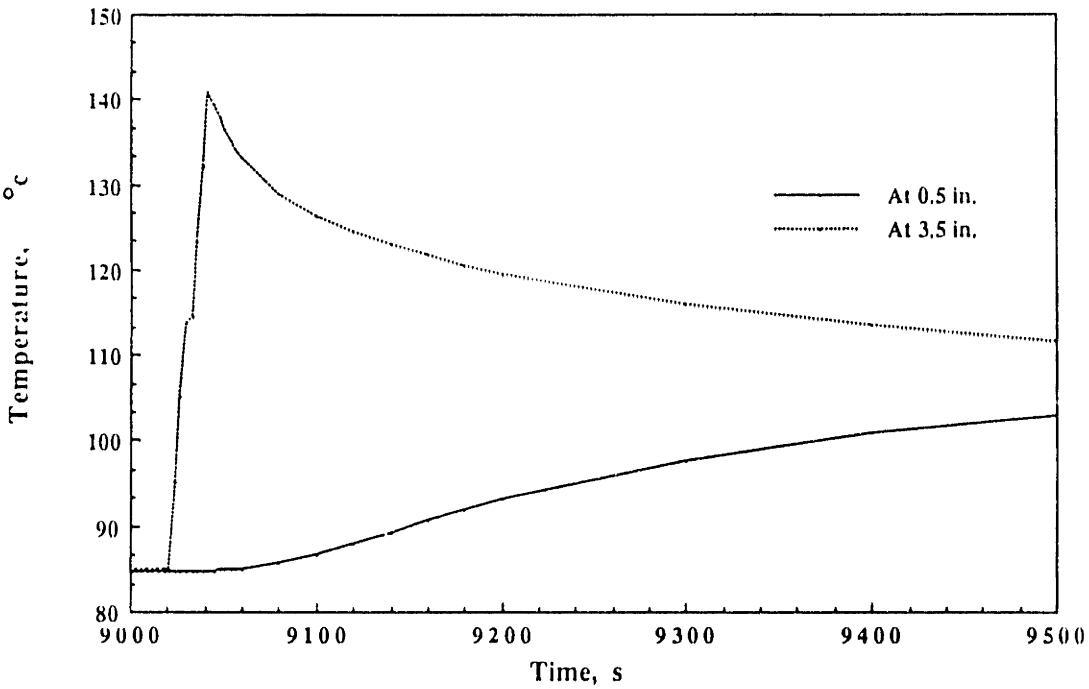

Figure 5-9: Temperature Profile during Low Temperature Treatment at 3.5 inches from the weld line for side heating case

Figure 5-10 shows the distortion profile during welding for the case of preheating and side heating when placing the side heating torch along with the welding torch. It shows clearly that the distortion during welding for the case with side heating is much less than that for the preheating case.

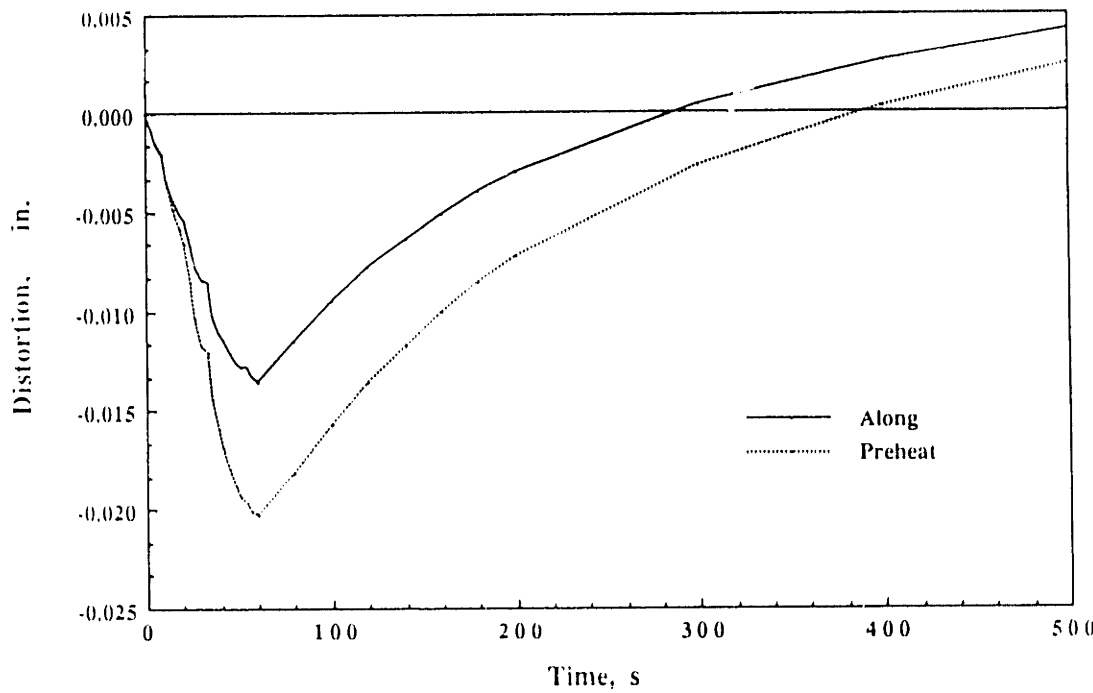

Figure 5-10: Comparison of Distortion Profile between the Side Heating Case and Preheating Case

Figure 5-11 shows the distortion profile during the low temperature treatment. In Fig. 5-11, No. 1 indicates the distortion profile for the case with side heating and low temperature treatment at 3.5 inches from the weld line, No. 2 indicates the distortion profile for the case without side heating and low temperature treatment at 0.5 inches from the weld line, No. 3 indicates the distortion profile for the case with side heating and low temperature treatment at inches from the weld line. It was found that by performing low temperature treatment at a position far away from the weld line, the distortion increased (curve no. 1). The distortion, however, decreased when performing low temperature treatment at a position near the weld line (curve no. 2 and 3)

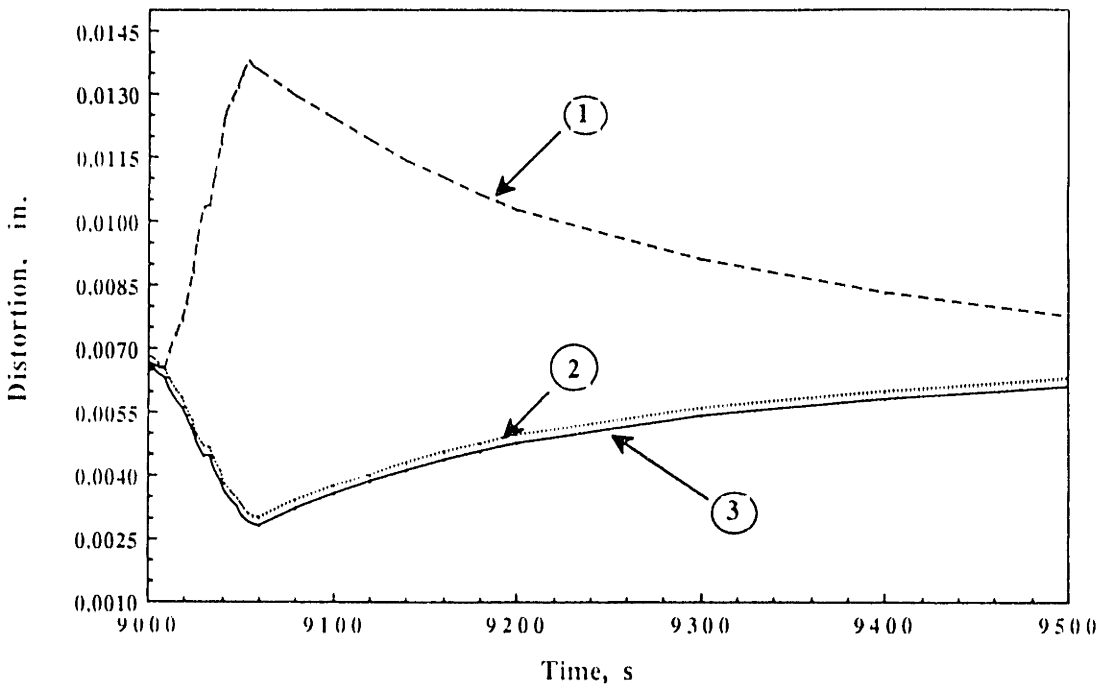

Figure 5-11: Comparison of Distortion Profile

Figures 5-12 to 5-15 show the residual stresses distribution along the transverse direction to the weld line for 6 cases which are as follows:

1.) Welding only.

2.) Preheating before welding.

3.) Welding without side heating and performing low temperature treatment near the weld line (0.5 inches).

4.) Welding with side heating.

5.) Welding with side heating and performing low temperature treatment away form the weld line (3.5 inches).

6.) Welding with side heating and performing low temperature treatment near the weld line (0.5 inches).

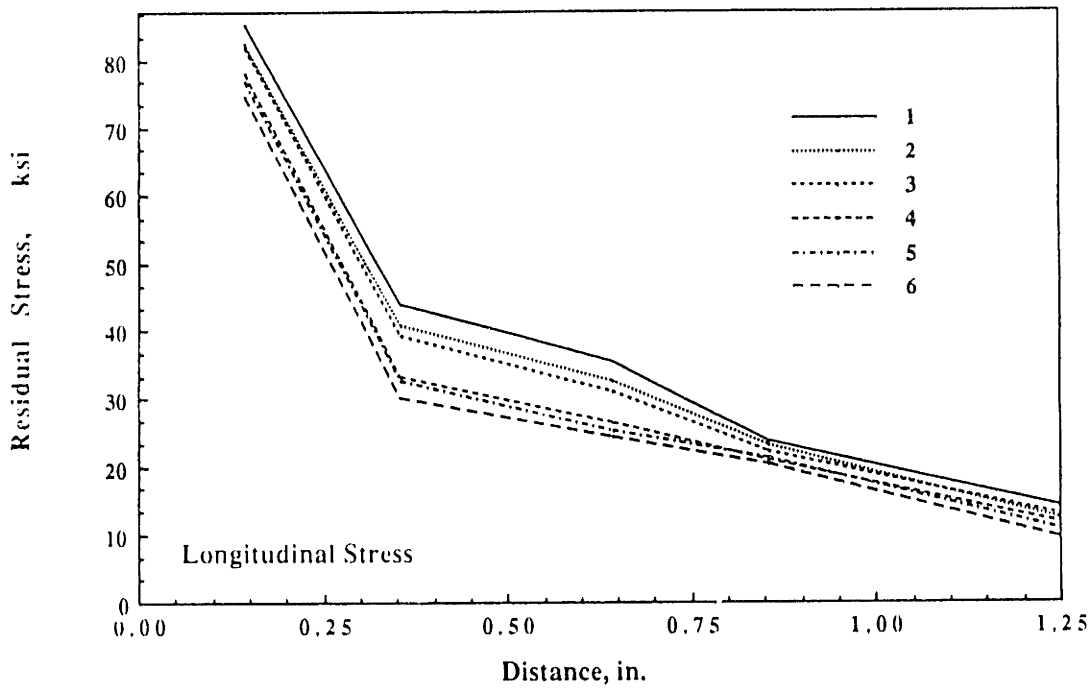

Figure 5-12: Comparison of Longitudinal Residual Stress I

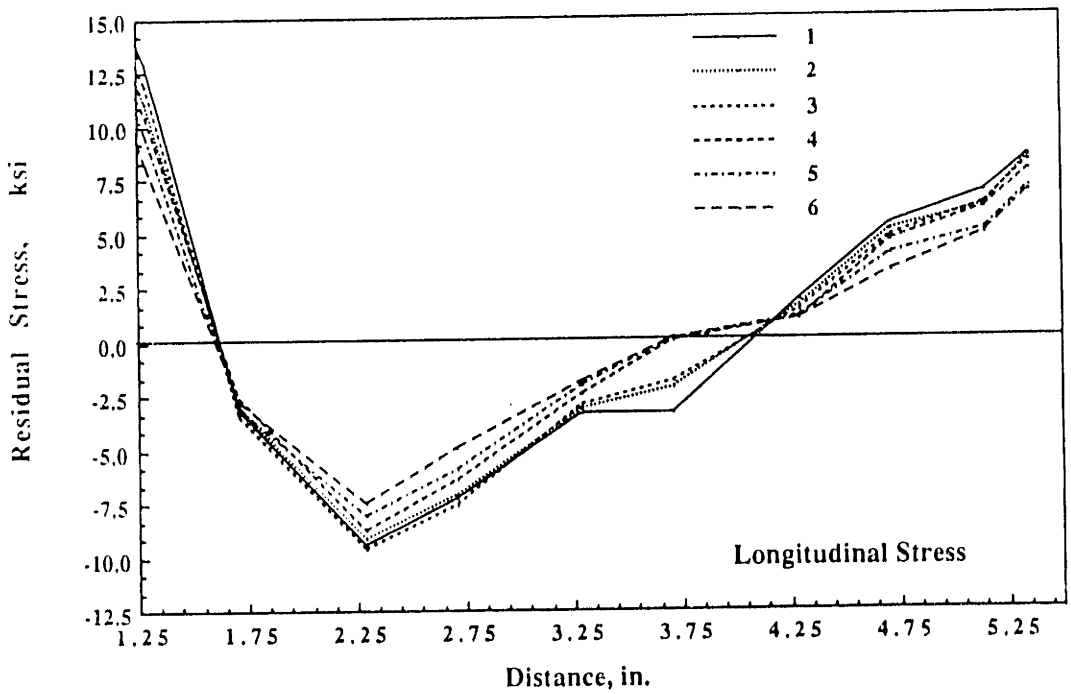

Figure 5-13: Comparison of Longitudinal Residual Stress II

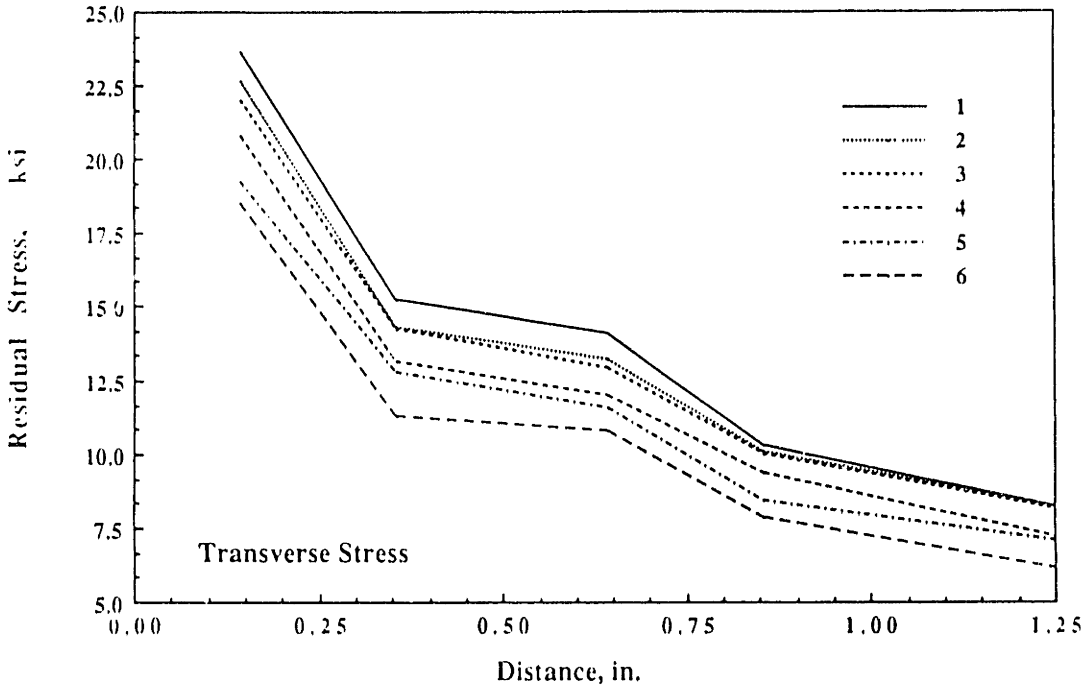

Figure 5-14: Comparison of Transverse Residual Stress I

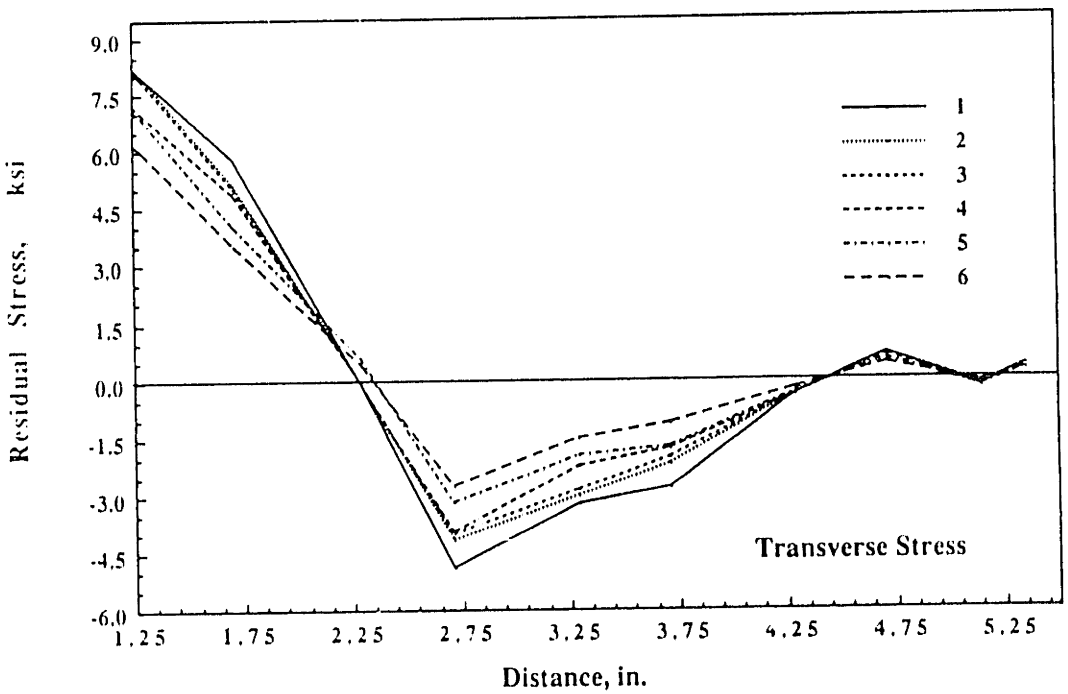

Figure 5-15: Comparison of Transverse Residual Stress II

By combining both side heating technique used during welding and low temperature stress relief used after welding, the residual stresses can be more effectively reduced. The simulation also showed that the amount of stress relief is strongly related to the position where the low temperature stress relief was performed. The process effectiveness increases when being performed near the weld line and is less effective when being performed away from the weld line.

The reduction of residual stress shown above, however, was not so high at the location near the weld line where high residual stress existed. It was then decided to use a stronger heat input in order to raise the temperature up to 400 ^{0}F which is the upper limit of the temperature recommended by Greene. The heat band was increased to 3 inches and covered also the weld line.

Figure 5-16 shows the temperature distribution during and after treatment at 0.5 inches and 2.5 inches from the weld line.

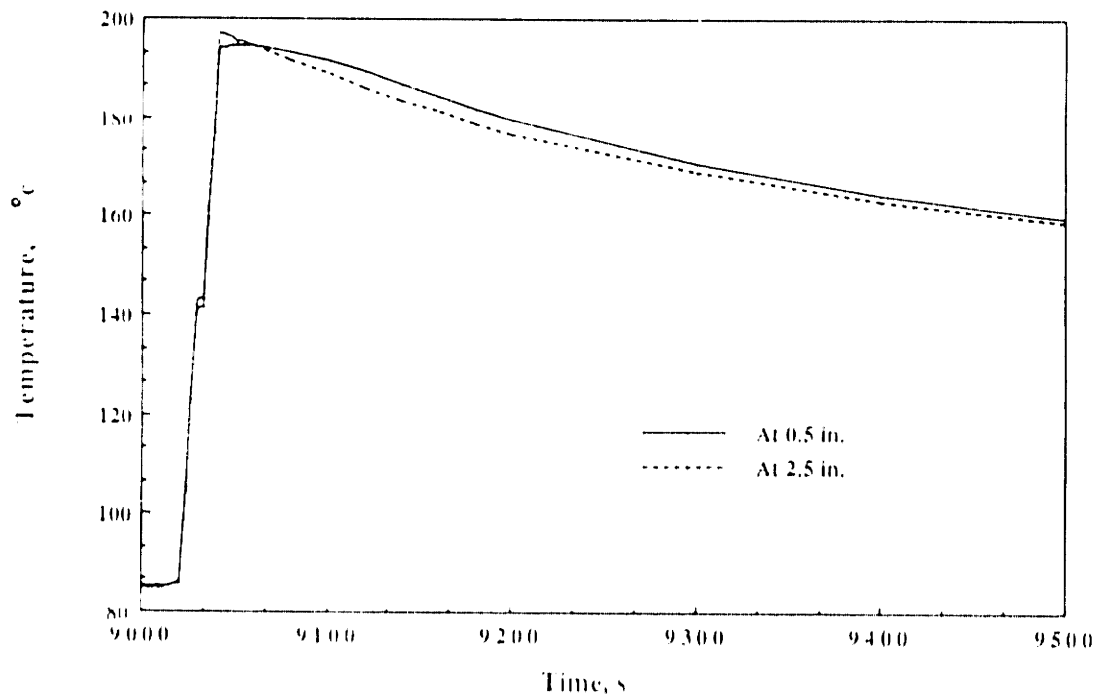

Figure 5-16: Temperature Profile during Low Temperature Treatment

Figure 5-17 shows the distortion profile during the treatment. It can be seen that the distortion is reduced more aggressively than in previous cases due to stronger heat input. This distortion profile indicates that the specimen experiences complex bending behavior, i.e., at the beginning the specimen bent upward, then bent downward during the treatment and then bent upward again during cooling.

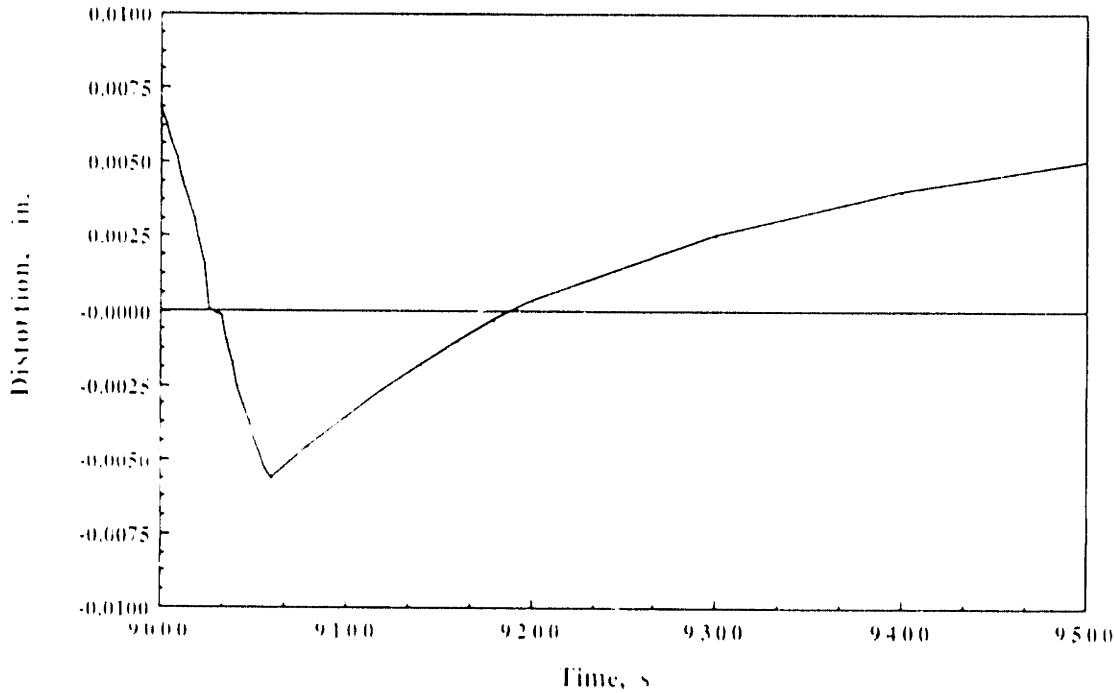

Figure 5-17: Distortion Profile during Low Temperature Treatment

Figures 5-18 to 5-19 show the residual stress distribution along the transverse direction to the weld line for this case compared with case no. 1 and 6 in Figs. 5-12 to 5-15 (no. 1 and no.2 in Figs. 5-18 to 5-19). The residual stress was further reduced in both directions. However, fluctuation of residual stress distribution occurred at a distance away from the weld line. The residual stress was greatly reduced at this region. This may be because of the already low residual stress distribution in that region.

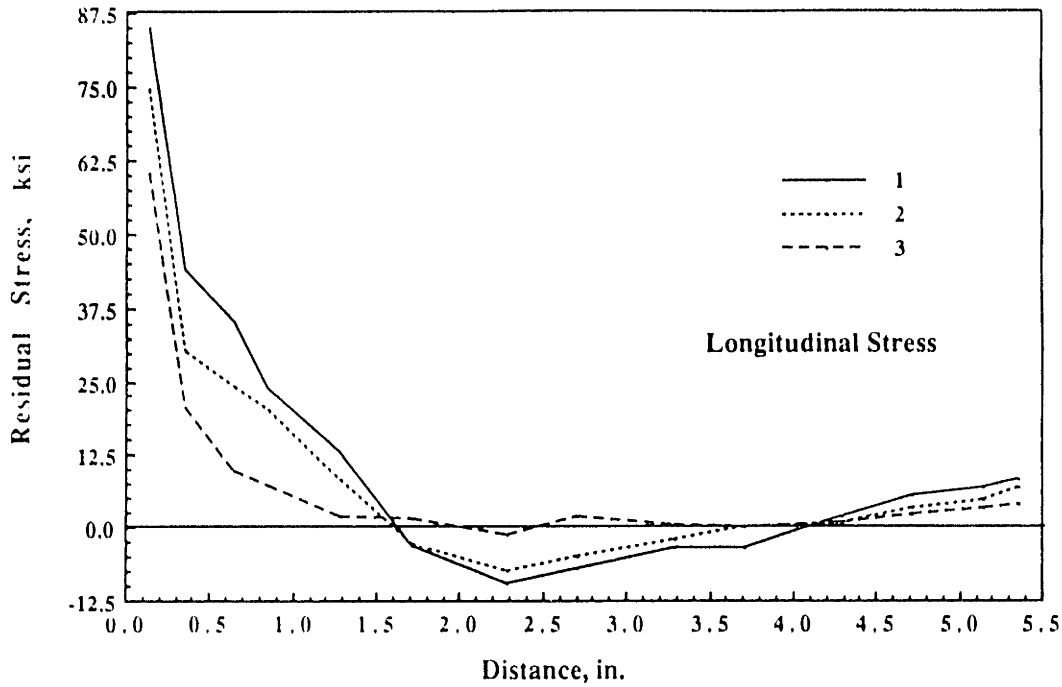

Figure 5-18: Comparison of Longitudinal Residual Stress

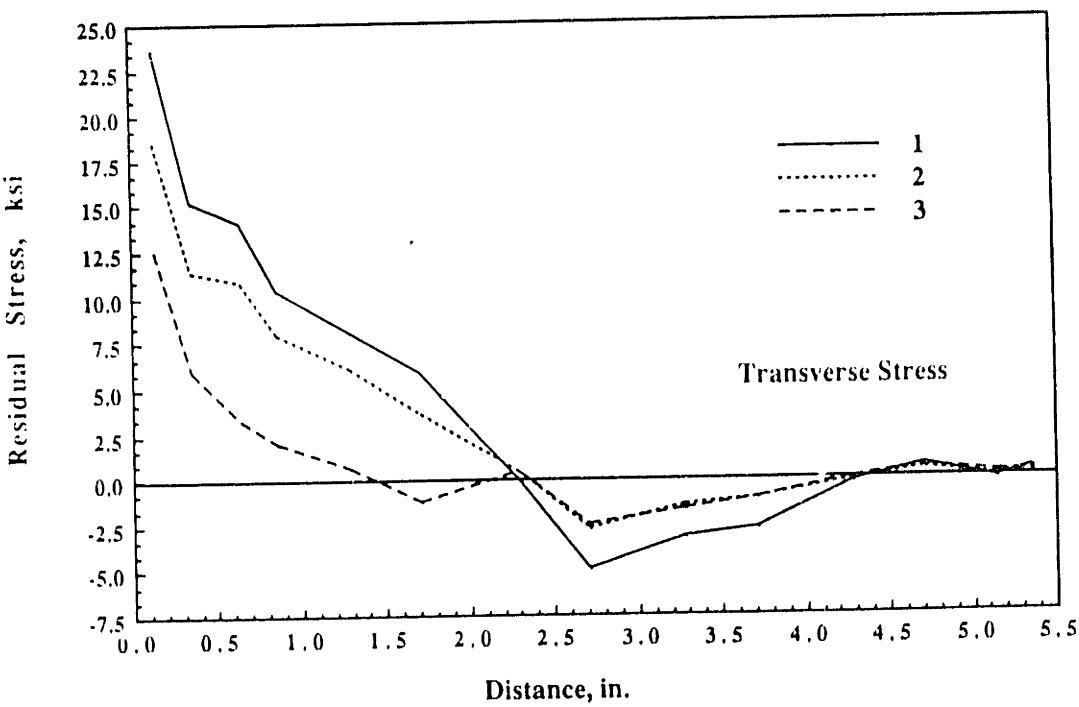

Figure 5-19: Comparison of Transverse Residual Stress

5.6 Summary

The study suggested that by taking advantage of other post-weld stress relieving techniques such as low temperature localized stress relief, the residual stresses can be more effectively reduced. The study also confirmed the effectiveness of this low temperature stress relieving technique. Even though this technique is rarely used due to the lack of appropriate non-destructive methods of stress measurement it provides some attractive features such as feasibility to be used in the field with simple operation and low cost as well as the ability to be used on large structures. However, much study is needed to be done to further investigate the usefulness of such a technique as well as parameters involved. Distortion that happened during this treatment should be taken into consideration and, in fact, this effect was not discussed in Greene's paper. Another point that is needed to be considered is the metallurgical effect from this low temperature stress relief to the structure especially when being performed at the weld. The effectiveness of this technique may be attributed to the metallurgical change inside the specimen. However, this is beyond the scope of this study.

Chapter 6

Conclusion and Future Study

It was found from the experiment and analysis that residual stresses and distortion can be significantly reduced by providing side heat with low magnitude and low concentration to the weldment in the region away from the weld line during the welding process. This provides a means to control and reduce residual stresses and distortion during the in-process control welding.

Conventionally, these residual stresses and distortion can be reduced by performing either pre- or post-weld treatment after the welding is completed and the weldment cools down. This, however, is not the effective way to reduce residual stresses and distortion as mentioned earlier in Chapter 1 and sometimes it is impossible to do any treatment when the welding is completed especially for large structures.

The investigation confirmed the validity of the theory of using opposing thermal force to reduce residual stresses and distortion during welding. The distortion which causes the metal movement on the weldment could be reduced and thereby allow more weldability to the weldment. In addition to residual stress reduction, the tendency for a weldment to crack can also be reduced, especially for high strength steels such as HY-130.

By applying other post-weld treatments such as low temperature localized stress relief, residual stress and distortion can be further reduced. The simulation showed that to obtain the best effectiveness of such a process the low temperature localized stress relief should be performed near or at the the weld line after the material cools down.

As far as metal movement is concerned, this investigation showed that the metal movement can be modified or adjusted. A possibility of controlling the metal movement during in-process control welding was also discussed. However,

the metal movement must be quantified before implementing this technique into the process. A direct approach to measure the metal movement by dial gage reading may not be appropriate when structures being welded are complex. For residual stress reduction, the method of determining the transient strains which are being formed during welding is a must. The difficulty is that the welding process happens in a very short time and the process of forming transient strains is very complex. This makes the analysis very complicated. A one-dimensional method can be used to calculate transient strains in a short time but limitation of the method due to its nature prevents high accuracy of the results obtained from the calculation. The finite element method provides more accurate results but takes a much longer time to perform the calculation. The empirical method may be the best choice to implement in the in-process control to determine the transient strains. However, to be able to come up with such a methodology, a great deal of work is needed to collect enough data for any particular cases.

As far as the accuracy of the analysis is concerned, the non-steady factors must be taken into consideration for heat transfer analysis. Material properties of steels at high temperature must be determined with good accuracy. Magnitude and concentration of flame used for side heating must be well studied. It is important to have an accurate model of side heating flame which includes the motion of the flame torch that moves along with the welding torch so that the dynamic effect from the flame can be included. For stress-strain analysis, phase transformation should be included to simulate the solidification process which should yield a better prediction of the development of the plastic zone and provide more understanding of how material behaves in microscopic scale as well as the stress or strain state of the material. Finally, to assure the effectiveness of the side heating technique, material degradation due to side heating must be examined to assure the quality of the weldment. Experimental verification is needed for this point.

To implement the side heating technique in the in-process control welding,

sensor is very important. This is because it is the only way to know how the weldment being treated behaves while the treatment is being performed. Probing changes of distortion can be done using an electric dial gage. An optical or laser measuring device may be used but converting any signals from such devices for measurement has to be very fast in order to have a real time control with the welding process itself. Probing changes of temperature can be done using suitable thermocouples. However, for residual stresses it is very difficult to probe any change in residual stresses.

It should also be cautioned that application of the side heating technique to other types of material requires further investigation. This is because not all materials can obtain the benefit from this technique. Aluminum, for example, cannot be treated by this technique due to its low melting point temperature which may lead to severe material degradation. Titanium and some other high strength steels such as HSLA 100, T-1 alloy steel will be interesting materials to test the effectiveness of side heating technique for future work.

Appendix A
Data Acquisition Program

```
 10      !data acquisition program
 20      !for 10 channels temp. and strain measurement
 30      !version 1.0   ;   last modified : 03/15/1989
 40      !by Chirdpun  Vitooraporn
 50      !
 60      Sys_init("none",130)
 70      Sched_init(25)
 80      Sched_config(1,"Set",1,"y")
 90      Sched_config(2,"Dbas",2,"y")
100      Sched_config(3,"C",3,"y")
110      Sched_config(4,"Ref",4,"y")
120      Sched_config(5,"Init",5,"y","i","r",5,"00:00:01")
130      Sched_config(6,"Mes",6,"y")
140      Sched_config(7,"Fir",7,"y","i","r",60,"00:00:01")
150      Sched_config(8,"F",8,"y")
160      Sched_config(9,"Sec",9,"y","i","r",30,"00:00:01")
170      Sched_config(10,"S",10,"y")
180      Sched_config(11,"Th",11,"y","i","r",20,"00:00:01")
190      Sched_config(12,"T",12,"y")
200      Sched_config(13,"Fou",13,"y","i","r",10,"00:00:01")
210      Sched_config(14,"Fo",14,"y")
220      Sched_config(15,"Fif",15,"y","i","r",10,"00:00:01")
230      Sched_config(16,"Fi",16,"y")
240      Sched_config(17,"Six",17,"y","i","r",10,"00:00:01")
250      Sched_config(18,"Si",18,"y")
260      Sched_config(19,"Sev",19,"y","i","r",10,"00:00:01")
270      Sched_config(20,"Se",20,"y")
280      Sched_config(21,"Eig",21,"y","i","r",5,"00:00:01")
290      Sched_config(22,"Ei",22,"y")
300      Sched_config(23,"Nin",23,"y","i","r",10,"00:00:01")
310      Sched_config(24,"Ni",24,"y")
320      Sched_config(25,"Pr",25,"y")
330      on cycle 1 call select_job
340  idle:goto idle
350      end
360      !*************************************************************
370      sub  select_job
380         on  fnSched_job+2 gosub done,none,Set,Dbas,C,Ref,Init,Mes,
         Fir,F,Sec,S,Th,T,Fou,Fo,Fif,Fi,Six,Si,Sev,Se,Eig,Ei,Nin,Ni,Pr
390      subexit
400      !*************************************************************
410  none:
420      return
430      !*************************************************************
440  Set:
450      output 709;"set timedate";timedate
460      return
470      !*************************************************************
480  Dbas:
490      dim data_def$[80]
500      print "setting database record.............."
510      arch_open("meas_rec",70,1)        !data file "meas_rec"
```

```
520       data_def$="data reading from slot 0 and slot 4 "
530       book_def("data_rec"," chanel|distance|temperature c|  ch. |
          dis. |strain micro","ch_vect|dit_vect|hp-ib|chs_vect|dis_vect
          |hp-ib",data_def$)
540       !*******************************************************
550       integer chantemp(0:7),chanstrain(0:7),n
560       real dit(0:7),dis(0:7)
570       !
580       data 0,1,2,3,4,5,6,7
590       read chantemp(*)
600       data 0,1,2,3,4,5,6,7
610       read chanstrain(*)
620       save_ivect(chantemp(*),"ch_vect")
630       save_ivect(chanstrain(*),"chs_vect")
640       !
650       data 1,1.25,2,2.25,3,3.25,4,4.25
660       read dis(*)
670       data 0.5,1.5,2.5,3.25,0,0,0,0
680       read dit(*)
690       save_rvect(dis(*),"dis_vect")
700       save_rvect(dit(*),"dit_vect")
710       print "done !!!"
720       return
730       !*******************************************************
740   C:
750       print "setting HP_3852A  ....."
760       output 709;"reset;blockout off;outbuf on; sysout on"
770       print "done"
780       return
790       !*******************************************************
800   Ref:
810       print  "initial reference strains are being collected"
820       output 709;"real str_ref(8)"
830       output 709;"confmeas strun 400,-407 use 600 into str_ref"
840       print "done !!!"
850       print " "
860       print "initial data are being collected......"
870       return
880       !*******************************************************
890   Init:
900       output 709;"use 600"
910       output 709;"confmeas tempk 000,-007  ; confmeas strq 400,-407
          ref str_ref  gf 1.97e-6"
920       Sched_info(5,n,a$,s$,Read_number)
930       Pagelabel$="init read # "&val$(Read_number)
940       Page_store("data_rec",709,Pagelabel$)
950       return
960       !*******************************************************
970   Mes:
980       print"done"
990       print "  "
1000      input "press return when you are ready to begin the process",
          iid$
```

```
1010      print "data collecting process is now active....please wait"
1020      return
1030      !*********************************************************
1040  Fir:
1050      output 709; "use 600"
1060      output 709; "confmeas tempk 000,-007; confmeas strq 400,-407
          ref str_ref gf 1.97e-6"
1070      Sched_info(7,n,a$,s$,Read_number)
1080      Pagelabel$="1 sec read # "&val$(Read_number)
1090      Page_store("data_rec",709,Pagelabel$)
1100      return
1110      !*********************************************************
1120  F:
1130      print "sucessful completetion for first reading period !!!"
1140      return
1150      !*********************************************************
1160  Sec:
1170      output 709; "use 600"
1180      output 709; "confmeas tempk 000,-007; confmeas strq 400,-407
          ref str_ref gf 1.97e-6"
1190      Sched_info(9,n,a$,s$,Read_number)
1200      Pagelabel$="5 sec read # "&val$(Read_number)
1210      Page_store("data_rec",709,Pagelabel$)
1220      wait 4
1230      return
1240      !*********************************************************
1250  S:
1260      print "sucessful completetion for second reading period !!!"
1270      return
1280      !*********************************************************
1290  Th:
1300      output 709; "use 600"
1310      output 709; "confmeas tempk 000,-007; confmeas strq 400,-407
          ref str_ref gf 1.97e-6"
1320      Sched_info(11,n,a$,s$,Read_number)
1330      Pagelabel$="20 sec read # "&val$(Read_number)
1340      Page_store("data_rec",709,Pagelabel$)
1350      wait 22
1360      return
1370      !*********************************************************
1380  T:
1390      print "sucessful completetion for third reading period !!!"
1400      return
1410      !*********************************************************
1420  Fou:
1430      output 709; "use 600"
1440      output 709; "confmeas tempk 000,-007; confmeas strq 400,-407
          ref str_ref gf 1.97e-6"
1450      Sched_info(13,n,a$,s$,Read_number)
1460      Pagelabel$="50 sec read # "&val$(Read_number)
1470      Page_store("data_rec",709,Pagelabel$)
1480      wait 57
1490      return
```

```
1500      !*****************************************************
1510  Fo:
1520      print "sucessful completetion for fourth reading period !!!"
1530      return
1540      !*****************************************************
1550  Fif:
1560      output 709; "use 600"
1570      output 709; "confmeas tempk 000,-007; confmeas strq 400,-407
          ref str_ref gf 1.97e-6"
1580      Sched_info(15,n,a$,s$,Read_number)
1590      Pagelabel$="100 sec read # "&val$(Read_number)
1600      Page_store("data_rec",709,Pagelabel$)
1610      wait 115
1620      return
1630      !*****************************************************
1640  Fi:
1650      print "sucessful completetion for fifth reading period !!!"
1660      return
1670      !*****************************************************
1680  Six:
1690      output 709; "use 600"
1700      output 709; "confmeas tempk 000,-007; confmeas strq 400,-407
          ref str_ref gf 1.97e-6"
1710      Sched_info(17,n,a$,s$,Read_number)
1720      Pagelabel$="200 sec read # "&val$(Read_number)
1730      Page_store("data_rec",709,Pagelabel$)
1740      wait 231
1750      return
1760      !*****************************************************
1770  Si:
1780      print "sucessful completetion for sixth reading period !!!"
1790      return
1800      !*****************************************************
1810  Sev:
1820      output 709; "use 600"
1830      output 709; "confmeas tempk 000,-007; confmeas strq 400,-407
          ref str_ref gf 1.97e-6"
1840      Sched_info(19,n,a$,s$,Read_number)
1850      Pagelabel$="400 sec read # "&val$(Read_number)
1860      Page_store("data_rec",709,Pagelabel$)
1870      wait 463
1880      return
1890      !*****************************************************
1900  Se:
1910      print "sucessful completetion for seventh reading period !!!"
1920      return
1930      !*****************************************************
1940  Eig:
1950      output 709; "use 600"
1960      output 709; "confmeas tempk 000,-007; confmeas strq 400,-407
          ref str_ref gf 1.97e-6"
1970      Sched_info(21,n,a$,s$,Read_number)
1980      Pagelabel$="900 sec read # "&val$(Read_number)
```

```
1990        Page_store("data_rec",709,Pagelabel$)
2000        wait 1044
2010        return
2020        !*********************************************************
2030    Ei:
2040        print "sucessful completetion for eightth reading period !!!"
2050        return
2060        !*********************************************************
2070    Nin:
2080        output 709; "use 600"
2090        output 709; "confmeas tempk 000,-007; confmeas strq 400,-407
            ref str_ref gf 1.97e-6"
2100        Sched_info(23,n,a$,s$,Read_number)
2110        Pagelabel$="1500 sec read # "&val$(Read_number)
2120        Page_store("data_rec",709,Pagelabel$)
2130        wait 1741
2140        return
2150        !*********************************************************
2160    Ni:
2170        print "sucessful completetion for nineth reading period !!!"
2180        return
2190        !*********************************************************
2200    Pr:
2210        print "printing results from data_rec.....please wait"
2220        printer is 26
2230        arch_dir("meas_rec","data_rec")
2240        !
2250        for i=1 to 5
2260          Pagelabel$="init read # "&val$(i)
2270          Page_print("meas_rec","data_rec",Pagelabel$)
2280        next i
2290        for i=1 to 60
2300          Pagelabel$="1 sec read # "&val$(i)
2310          Page_print("meas_rec","data_rec",Pagelabel$)
2320        next i
2330        for i=1 to 30
2340          Pagelabel$="5 sec read # "&val$(i)
2350          Page_print("meas_rec","data_rec",Pagelabel$)
2360        next i
2370        for i=1 to 20
2380          Pagelabel$="20 sec read # "&val$(i)
2390          Page_print("meas_rec","data_rec",Pagelabel$)
2400        next i
2410        for i=1 to 10
2420          Pagelabel$="50 sec read # "&val$(i)
2430          Page_print("meas_rec","data_rec",Pagelabel$)
2440        next i
2450        for i=1 to 10
2460          Pagelabel$="100 sec read # "&val$(i)
2470          Page_print("meas_rec","data_rec",Pagelabel$)
2480        next i
2490        for i=1 to 10
2500          Pagelabel$="200 sec read # "&val$(i)
```

```
2510        Page_print("meas_rec","data_rec",Pagelabel$)
2520      next i
2530      for i=1 to 10
2540        Pagelabel$="400 sec read # "&val$(i)
2550        Page_print("meas_rec","data_rec",Pagelabel$)
2560      next i
2570      for i=1 to 5
2580        Pagelabel$="900 sec read # "&val$(i)
2590        Page_print("meas_rec","data_rec",Pagelabel$)
2600      next i
2610      for i=1 to 10
2620        Pagelabel$="1500 sec read # "&val$(i)
2630        Page_print("meas_rec","data_rec",Pagelabel$)
2640      next i
2650      printer is 1
2660      return
2670      !************************************************
2680  Done:
2690      arch_close
2700      stop
2710  subend
```

References

[1] Adams, C. M.,Jr.
Cooling rate and peak temperature in fusion welding.
Welding Journal 37:97s-104s, 1958.
Research Supplement.

[2] Anderson, J.E. and Stesino, E.F.
Heat Transfer from Flames Impinging on Flat and Cylindrical Surfaces.
J. of Heat Transfer (ASME) :49-54, February, 1963.

[3] Andrews, J.B., Arita, M., and Masubuchi, K.
Analysis of Thermal Stresses and Metal Movement During Welding.
Technical Report NASA CR-61351, The G.G. Marshall Space Flight Center, NASA, 1970.

[4] Apps, R. and Milner, D.
Heat Flow in Argon-Arc Welding.
British Welding Journal 2(10):475-485, 1955.

[5] Barnes, P. K.
Reduction of Residual Stresses and Distortion in Girth-Welded Pipes.
Master's thesis, M.I.T., June, 1987.

[6] Bathe, K.J.
ADINAT - A Finite Element Program for Automatic Dynamic Incremental Nonlinear Analysis of Temperature.
Technical Report 82448-5, Dept. of Mechanical Engineering, M.I.T., May, 1977.

[7] Bathe, K.J., and Khoshgoftaar, M.R.
Finite Element Formulation and Solution of Nonlinear Heat Transfer.
J. of Nuclear Eng. and Design 51:389-401, 1979.

[8] Bathe, K.J., and Cimento, A.P.
Some practical procedures for the solution of nonlinear finite element equation.
J. of Comp. Meth. in Appl. Mech. and Eng. 22:59-85, 1980.

[9] Snyder, M.D., and Bathe, K.J.
A Solution Procedure for Thermo-Elastic-Plastic and Creep Problems.
J. of Nuclear Eng. and Design 64:49-80, 1981.

[10] Becker, E.B., and C.H. Parr.
Application of Finite Element Method to Heat Conduction in Solids.
Technical Report S-117, Rohm and Haas Redstone Research Laboratories, 1967.

[11] Brick, R.M., Pense, A.W., and Gordon, R.B.
Structure and Properties of Engineering Materials.
McGraw-Hill Book Co., 1977.

[12] Masubuchi, K. and Chang, I.H.
Hybrid Experimental-Analytical Approach for Controlling Distortion and Residual Stresses in Weldments.
In *International Conference on Computational Engineering Science*, pages viii 1-4. Springer Verlag, 1988.

[13] Chang, I.H.
Analysis and Control of Root Gap Change During Butt Welding.
Ph.D. thesis, M.I.T., April, 1988.

[14] Christensen, N. and Davies, V. and Gjermundsen, K.
Distribution of Heat Around Finite Moving Sources.
Technical Report CA-91-508-EVC-378, U.S. Army, September, 1959.

[15] Christensen, N. and Davies, V. and Gjermundsen, K.
The Distribution of Temperature in Arc Welding.
British Welding Journal 12(1):54-75, 1965.

[16] DeBiccari, A.
A Control of Distortion and Residual Stresses in Girth-Welded Pipes.
Ph.D. thesis, M.I.T., July, 1986.

[17] Degarmo, et. al.
The Effect of Weld Length Upon Residual Stresses of Unrestrained Butt Welds.
Welding Journal 25(8):485s-486s, 1946.
Research Supplement.

[18] Eagar, T. and Tsai, N.S.
Temperature Fields Produced by Traveling Distributed Heat Sources.
Welding Journal 62(12):346s-355s, 1983.

[19] Friedman, E.
Numerical Simulation of the Gas Tungsten Arc Welding Process.
In *Proceeding of Numerical Modeling of Manuf. Process*, pages 35-47. ASME, 1977.

[20] Friedman, E.
Thermodynamical Analysis of the Welding Process Using the Finite Element Method.
J. of Pressure Vessel Technology :206-213, August, 1975.

[21] Greene, T.W. and Holzbaur, A.A.
Controlled Low-temperature Stress Relieving.
Welding Journal 25(3):1715-1855, March, 1946.
Research Supplement.

[22] Grosh, R.J., and Trabant, E.A.
Arc Welding Temperatures.
Welding Journal 35:396s-400s, 1956.

[23] Gurtis, M.E.
Variational Principles for Linear Initial Value Problems.
Quart. Appl. Mech. 22(3), 1964.

[24] Hibbit, H.D., and Marcal, P.V.
A Numerical Thermo-mechanical Model for the Welding and Subsequent Loading of a Fabricated Structure.
Technical Report N00014-67-A-019-0006, Dept. of the Navy, March, 1972.

[25] Hsu, M.B.
Analysis of Welds by the Finite Element Method.
In *Proc. of Numerical Modeling of Manuf. Processes*, pages 97-115. ASME, 1977.

[26] Hwang, Jye Suan.
Residual Stresses in Weldment in High Strength Steels.
Master's thesis, M.I.T., February, 1976.

[27] Jackson, C.E., and Shrubsall, A.E.
Energy Distribution in Electric Welding.
Welding Journal 29:231s-241s, 1950.
Research Supplement.

[28] Jonsson, M., Karlsson, L and Lindgren L-E.
Simulations of Tack Welding Procedures in Butt Joint Welding of Plates.
Welding Journal :296s-301s, 1985.

[29] Lobitz, D.W.,, McClure, J.D., and Nickell, R.E.
Residual Stresses and Distortion in Multipass Welding.
In *Proceeding of Numerical Modeling of Manuf. Process*, pages 81-96. ASME, 1977.

[30] Malha, E. and Rowland, M. and Shook, C. and Doan, G.
Heat Flow in Arc Welding.
Welding Journal 20(10):559s-568s, 1941.
Research Supplement.

[31] *Welder's Handbook for Welding HY80, HY100, and HY130*
General Dynamics Corporation, 1975.

[32] Masubuchi, K. and D.C. Martin.
Investigation of Residual Stresses by Use of Hydrogen Cracking.
Welding Journal 40(12):401s-418s, 1966.
Research Supplement.

[33] Martin, J.B.
Plasticity: Fundamentals and General Results.
M.I.T. Press, Cambridge, 1975.

[34] Masubuchi, K.
Numerical Analysis of Stresses, Strains, and other Effects produced by Welding.
Technical Report Document X-1087-85, A.W.S., 1985.

[35] Masubuchi, K.
Analysis of Welded Structures.
Pergamon Press, 1980.

[36] Masubuchi, K.
Control of Distortion and Shrinkage During Welding.
Welding Research Council Bulletin 149, April, 1970.

[37] Masubuchi, K. and Agapakis, J.E.
Analysis and Control of Residual Stresses, Distortion, and Their Consequences.
In *Trends in Welding Research in the United States*, pages 153-172. American Society of Metals, November 16-18, 1981.

[38] Masubuchi, K., et. al.
Research on High-Strength Steels with an Improvement Against Weld Cracking -Evaluation of Weld Cracking Sensitivities.
In *The First OMAE Specialty Symposium on Offshore and Arctic Frontiers*, pages 429-437. ASME, 1986.

[39] Masubuchi, K.
Advances in Analysis and Control of Residual Stresses and Distortion.
In *The 1987 Annual Convention of the American Welding Society*. American Welding Society, April, 1987.

[40] Masubuchi, K.
Materials for Ocean Engineering.
M.I.T. Press, 1970.

[41] Masubuchi, K., Simons, F.B., and Monroe, R.E.
Analysis of Thermal Stresses and Metal Movement During Welding.
Battelle Memorial Institute, 1968.

[42] Masubuchi, K., and Iwaki, T.
Thermo elastic analysis of orthotropic plastic by the finite method.
J. of the Society of Naval Architects of Japan 130:195-204, 1971.

[43] Mendelson, A.
Plasticity : Theory and Application.
Macmillan, New York, 1968.

[44] Chang, I.H., Miyachi, H., and Masubuchi, K.
Instrumentation, Measurement, and Analysis for Controlling Residual Stresses and Metal Movement -Especially Reducing Joint Mismatch and Force Acting on Tack Welds During Butt Welding.
In *The Fifth Symposium on Energy Engineering Sciences, Instrumentation, Diagnostic, and Material Behavior*, pages 161-167. Argonne National Laboratory, June, 1987.

[45] Muraki, T., Bryan, J.J., and Masubuchi, K.
Analysis of Thermal Stresses and Metal Movement During Welding, Part II: Comparison of Experimental Data and Analytical Results.
J. of Eng. Materials and Technology :85-91, January, 1975.

[46] Nickell, R.E., and Hibbitt, H.D.
Thermal and Mechanical Analysis of Welded Structure.
J. of Nuclear Engineering and Design 32:110-120, 1975.

[47] Nippes, E.F., and Savage, W.F.
Residual Stresses in Welded Titanium Plates.
Welding Journal 37(10):433s-439s, 1958.
Research Supplement.

[48] Nishida, M.
Analytical Prediction of Distortion in Welded Structures.
Master's thesis, M.I.T., March, 1976.

[49] Oden, J.T., and D.A. Kross.
Analysis of General Coupled Thermo-elasticity problems by the finite element method.
In *The Second Conference on Matrix Methods in Structural Mechanic.* ASME, October, 1968.

[50] Papazoglou, V.J.
Analytical Techniques for Determining Temperatures, Thermal Strains, and Residual Stresses During Welding.
Ph.D. thesis, M.I.T., May, 1981.

[51] Papazoglou, V.J.
Computer Programs for the One Dimension Analysis of Thermal Stresses and Thermal Movement During Welding.
Technical Report N00014-75-C-0469, Office of Naval Research, 1977.

[52] Roberts, D.K., and Wells, A.A.
Fusion Welding of Aluminum Alloys, Part V: A mathematical examination of the effect of the bounding planes on the temperature distribution due to welding.
British Welding Journal :553-560, December, 1954.

[53] Rosenthal, D.
Mathematical Theory of Heat Distribution During Welding and Cutting.
Welding Journal 20(5):220s-234s, 1941.
Research Supplement.

[54] Rosenthal, D.
The Theory of Moving Sources of Heat and its Application to Metal Treatment.
Transactions ASME :849-866, November, 1946.

[55] Rykalin, N. N.and Nikolaev, A.
Welding Arc Heat Flow.
Welding in the World :112-132, September, 1971.

[56] Rykalin, N. N.
Calculation of Heat Processes in Welding.
Lecture presented before the A.W.S. , April, 1961.

[57] Rykalin, N.N.
Energy Sources Used for Welding.
Welding in the World 12:227-247, 1974.

[58] Satoh, K, Terasaki, T. and Nohara, K.
Changes of Root Gap during Welding in Case of Butt Weld Joint.
J. Japanese Welding Society 50:76-82, 1981.

[59] Rosenthal, D. and Schmerber, R.
Thermal Study of Arc Welding.
Welding Journal 17(4):208s, 1948.
Research Supplement.

[60] Serotta, M.D.
Reduction of Distortion in Weldment.
Master's thesis, M.I.T., March, 1975.

[61] Shin, D.B.
Finite Element Analysis of Out-of-Plane Distortion of Panel Structures.
Master's thesis, M.I.T., May, 1972.

[62] Soete, W.
Measurement and relaxation of residual stresses.
Welding Journal 28(8):354s-364s, 1949.
Research Supplement.

[63] Tall, L.
Residual Stresses in Weld Plates -A Theoretical Study.
Welding Journal 43(1):10s-23s, 1964.
Research Supplement.

[64] Tsai, C.L.
Parametric Study on Cooling Phenomena in Underwater Welding.
Ph.D. thesis, M.I.T., September, 1977.

[65] Ueda, Y., and Yamakawa, T.
Analysis of Thermal Elastic-Plastic Stress and Strain Analysis During Welding By Finite Element Method.
Transaction of J.W.S. 2:90-100, September, 1971.

[66] Ueda, Y., and Yamakawa, T.
Thermal Stress Analysis of Metals with Temperature Dependent Mechanical Properties.
In *Proceeding of International Conference on Mech. Behavior of Materials*, pages 10-20. JWS, 1971.

[67] Ueda, Y., and Fukuda, K.
Analysis of Welding Stress Relieving by Annealing Based on Finite Element Method.
Technical Report IIW Doc X-773-75, A.W.S., 1975.

[68] Wells, A.
Heat Flow in Welding.
Welding Journal 31(6):263s-267s, 1952.
Research Supplement.

[69] Wilson, E.L., and R.E. Nickell.
Application of the Finite Element Method to Heat Conduction Analysis.
J. of Nuclear Eng. and Design 4(3):276-286, October, 1966.

[70] Wilson, E.L., Bathe, K.J., and Peterson, F.E.
Finite Element Analysis of Linear and Non Linear Heat Transfer.
J. of Nuclear Eng. and Design 29:110-124, 1974.

[71] Zienkiewicz, O.C., and C.J. Parekh.
Transient Field Problems: Two Dimensional and Three Dimensional Analysis of Isoparametric Finite Elements.
Int. J. for Numerical Methods in Engineering 2(1):61-71, 1970.